LIQUID ALUMINIUM CORROSION CHARACTERISTICS OF CAST IRON AND STEEL

A Thesis

Submitted to the Department of Mechanical Engineering

University of Canterbury

By

Mandeep Singh Sidhu

IN PARTIAL FULFILLMENT OF THE REQUIREMENTS FOR THE

DEGREE OF DOCTOR OF PHILOSOPHY

IN

MECHANICAL ENGINEERING

2012

Preface

This thesis is submitted as a partial requirement for the degree of Doctor of Philosophy in Mechanical Engineering in the University of Canterbury. This research was conducted under the supervision of Professor Milo V. Kral in the Department of Mechanical Engineering, University of Canterbury, between October 2007 and August 2011.

A part of this work has been published in:

M.S. Sidhu, M.V. Kral, Erosion of Ferrous Alloys by Liquid Aluminum, Light Metals, TMS Annual Meeting, Seattle, WA, USA, (2010) 325-330.

Acknowledgements

Numerous individuals contributed to make the realization of this project possible. Firstly, the author wishes to express his gratitude to Professor Milo V. Kral, in addition to his generous offer of PhD research, his patience, steadfast encouragement, and personal support will long be appreciated. The author expresses his heartfelt thanks to Dr. Catherine Bishop for providing insight, guidance and sharing her wealth of knowledge in writing this thesis.

I want to thank New Zealand Aluminium Smelters and Blaine Morch for providing, not only the financial support, but also the useful information pertaining to this project. I also greatly appreciate the cooperation of Eric Colins and Eric Jack from Buchanan Foundry, and Ian Close from Casting Shop for preparing the cast iron compositions.

Also, I want to thank work-shop staff; Scott Amies, Ken Brown, David Read and Jim McLean for fabricating the parts of test set ups and test specimens, and for allowing me to operate the workshop machines. I am thankful to Kevin Stobbs and Mike Flaws for their help in laboratory work and electron microscopy. A very special thanks to Julian

Philips - departmental electronics technician - his timely help in repairing and preparing the parts of the test set ups is highly appreciated. I also thank fellow students; Takanori Sato, Daniel Drabble, Karl Buchanan and Pawan Kumar for helping whenever I asked.

I am also thankful to Members of the University of Canterbury Materials Engineering Group (MEG): Dr. Mark Staiger, Emeritus Professor Les Erasmus, Mike Flaws, and Kevin Stobbs; MEG visitors, Dr. Chris Hutchinson and Professor Anil Saigal; and fellow MEG students, for all their help, discussions and comments.

A special thanks to my wife, Rupinder. Without her encouragement and sacrifices, I could never have undertaken such a daunting task. Thanks to my parents for their love and continual encouragement, but especially to my father whose drive and determination have always been an inspiration to me. I am thankful everyone else too; my teachers, relatives, colleagues and friends, who motivated me and inspired me throughout my life.

Abstract

Cast iron and steel alloys are commonly used for tooling and structural components in Al production, Al die-casting and the aluminizing industry due to their favourable properties including high strength, good formability and low cost. However, the liquid Al corrosion of these materials is one of the crucial concerns in maintaining the efficient production.

Al is produced by the electrolytic smelting of alumina. Cast iron and/or cast steel pipes - commonly known as ‘tapping pipes’ - are used to extract the liquid Al produced by smelting. Tapping pipes mainly degrade by material loss because liquid Al reacts with nearly all metals. Failure of tapping pipes is a significant contributor to the maintenance expenses; therefore, the primary aim of this research is to develop a material to enhance the life time of tapping pipes.

Various test methods were developed in order to examine the effect of molten Al environment on cast iron and steel alloys. The corrosion resistance of these alloys was determined under different conditions of Al flow and temperature. The intermetallic compounds formed by exposing the ferrous to liquid Al were characterized using the Energy Dispersive X-ray Spectroscopy (EDS) and Electron Back Scatter Diffraction (EBSD) techniques. The formation, growth and nature of reaction products were revealed to establish a link to the liquid Al corrosion resistance.

A relationship between the chemical composition and liquid Al corrosion resistance of cast irons could not established in the past. In the present work, the corrosion rate was found to depend upon the graphite morphology and fraction of each Fe-C phase of cast iron matrix, which can be controlled by selecting the chemical composition. Moreover, present research suggested the guidelines for producing a cast iron with enhanced liquid

Al corrosion resistance. The presence of C-rich phases, graphite flakes and cementite was found to be effective in enhancing the liquid Al corrosion resistance of gray cast irons. Conversely, a higher Si content was found to enhance the susceptibility of cast irons to liquid Al corrosion.

The corrosion mechanisms for ferrous alloys in liquid Al are not fully understood. Thus the subsequent analysis of the dissolution data was supported by investigating the reaction products formed between Al and substrate materials. In addition to commonly existent η-Fe_2Al_5 and θ-$FeAl_3$ phases, the formation of Al_4C_3 and κ-Fe_3AlC compounds was confirmed for the first time in the intermetallic layers of ferrous alloys. The Fe_3Si phase in the intermetallic layers of high Si cast irons was found, which was believed to facilitate the high corrosion rates of high Si cast irons. Moreover, the mechanism by which C in Fe-substrates affects the liquid Al corrosion resistance can be better understood given the present work.

Furthermore, the analysis presented here gives an understanding of the nature, growth and dissolution of intermetallic compounds in several cast iron alloys. Higher Si additions to cast irons played an important role in molten metal corrosion by accelerating the material loss and changing the nature of intermetallic layers. The results of this study clearly indicated that the dissolution and the growth of intermetallic compounds are interrelated and the dissolution and/or spallation of the intermetallic layers may be the primary mode of liquid Al corrosion of ferrous alloys.

Table of Contents

Table of Figures

CHAPTER 1 : INTRODUCTION AND BACKGROUND

Since the earliest days of the development of the Al production process, there has been great concern over the materials compatible with the liquid metal environment. In order to reduce production costs - particularly maintenance costs - attention has focused on the equipment used for transferring and holding the liquid Al. With this consideration, the liquid Al corrosion characteristics of cast iron and steel alloys have been studied and this research was sponsored by New Zealand Aluminium Smelters (NZAS).

The Al production process is commonly known as the Hall-Héroult smelting process, named after its inventors. In Hall-Héroult smelting, Al is produced by the electrolytic dissociation of alumina (Al_2O_3) into Al and oxygen in smelting cells operating at high temperatures (940°C-970°C) [1]. At NZAS, each year around 360,000 tonnes of liquid Al are transferred from the smelting cells by using cast iron/steel pipes, which are commonly known as 'tapping pipes'. One end of the tapping pipe is periodically immersed in the liquid Al in the smelting cells and the liquid metal is transferred to refractory lined steel crucibles. Thus the tapping pipe surfaces are frequently exposed to a swift flow of liquid Al.

Tapping pipes fail through material loss and cracking. Material loss occurs because liquid Al is extremely active with ferrous materials [2]. The periodic flow of liquid Al causes steep thermal gradients leading to the cracking of pipes. Increasing the taping pipe lifetime is an opportunity to reduce replacement expenses and costly production downtime. Moreover, reducing the dissolution of pipe materials into Al is also a benefit in producing high purity Al.

Cast iron and steel represent two large groups of ferrous alloys, and these are possibly the most versatile of all engineering materials because they have several desirable properties such

as high strength, formability, structural rigidity, recyclability and low cost. Cast irons/steels are preferred for many engineering applications because of their high ratio of service life to component cost. These materials are commonly used in Al production and process industries for tooling and structural components, such as parts of furnaces, casting dies, spouts, crucibles and in the present case of tapping pipes.

Exposure of ferrous alloys to liquid Al can result in material degradation by chemical corrosion and physical erosion. Chemical corrosion provides a wider description when the exact nature of a metallurgical reaction is not known. Erosion can be defined as dissolution from chemical corrosion combined with mechanical erosion from the swift flow of melt relative to solid substrate [2]. Liquid metal corrosion can be classified in various categories such as intergranular penetration, dissolution, impurity and interstitial reactions, and alloying. In most cases, the four individual categories of corrosion are interrelated [3].

Intergranular corrosion is the localized attack at the grain boundaries upon exposure to liquid metal under certain impurity and microstructural conditions. This type of corrosion occurs when the grain boundaries have higher energy and/or become more anodic than the grains. In most cases, the alloy chemistry or the depletion of alloying elements makes the grains boundaries dissimilar to that of grains. An example is the corrosion of 316 stainless steel in nitrogen contaminated lithium [3].

Dissolution is the simplest type of corrosion that can occur in a liquid metal system. The amount of material loss from the solid depends upon the surface area of the solid exposed, the volume of the liquid metal, solid metal solubility in liquid metal and the kinetic properties of the rate controlling step in the dissolution reaction [3]. The terms corrosion and dissolution are used interchangeably in the present work.

Impurity or interstitial reactions are the interaction of light elements in the solid or liquid metal. In cases where the liquid metal has a low solid metal solubility, reactions involving light elements such as oxygen, nitrogen, and carbon may dominate the dissolution reaction. Decarburization of steel in lithium and the oxidation of steel in sodium occur by impurity or interstitial reactions [3].

Another type of corrosion that occurs between solid and liquid metals is alloying or alloy layer formation, for example, the present case of the Fe-liquid Al system. In this type of corrosion, stable products are formed from the reaction of atoms within the solid metal with those from the liquid metal. The product formed by this reaction may either be soluble or insoluble in the liquid metal. Assuming that chemical contact is maintained between the product layers, then at equilibrium, the growth of the intermetallic phase layers is controlled by volume diffusion [3].

The present research describes the assessment of liquid Al corrosion resistance of cast iron and steel alloys for tapping pipes and other similar applications. Moreover, the detailed analysis of corrosion kinetics was made which will be helpful to understand and predict the liquid Al corrosion behaviour of ferrous alloys.

The tapping pipes are frequently exposed to flowing liquid Al that causes temperature gradients across the pipe sections. Thermal gradients result in differential thermal expansion causing stresses across pipe sections. Repetitive thermal stresses can eventually cause progressive opening of the cracks during service. This type of component failure is known as thermal fatigue. From industrial point of view thermal fatigue is important; however, its academic importance is relatively small compared to the liquid Al corrosion of ferrous materials. Therefore, this thesis is based upon the investigations on the corrosion resistance

and mechanisms of liquid Al corrosion of ferrous alloys. Appendix A details the investigation of the thermal fatigue resistance of cast irons for tapping pipe applications.

1.1 Research Overview

Most metals dissolve quickly when immersed in liquid Al baths at typical industrial operating temperatures [2]. Thus the development of liquid Al corrosion resistant materials is of considerable importance not only to the Al producers, but also to the industries involved in the processing of liquid Al.

Refractory coatings are commonly used to protect metallic materials against liquid Al corrosion. However, the coating efficiency strongly depends upon its adhesion to the substrate and its chemical inertness to liquid Al. Significant improvement in the protection effect through ceramic coatings has been achieved [4]. However, studies presented in [2] show that even the ceramics compatible with liquid Al such as SiC, AlN, Al_2O_3 and graphite have been found to react with liquid Al under certain conditions of temperature and time. Thus the main concern over ceramic coatings is whether the coating itself could survive for a satisfactory service life. Repeated thermal loading and erosion from liquid Al can eventually lead to cracking and exfoliation of the coatings. In addition, the costs of application of such coatings are high. Therefore, it is most desirable to improve the liquid Al corrosion resistance of ferrous substrates.

Numerous publications [5-9] have reported on the dissolution kinetics of pure iron, stainless steel and transition elements into liquid Al. However, experimental data on liquid Al corrosion resistance of steels and/or cast irons is limited [10-12]. For a particular service application, the intended mechanical and physical properties of cast irons and steels may be achieved by the controlled addition of suitable alloying elements [13]. In contrast, there are

no comprehensive reports that can be utilized in the selection of a ferrous alloy for a liquid Al environment.

Gray cast irons (GCIs) and ductile cast irons (DCIs) are more economical than cast steels (CSs); however, their relative cost varies with the shape, size, and required mechanical and physical properties of the end product. On the other hand, steels possess better mechanical strength, higher toughness and better fracture toughness [14-15]. The scope of this research is therefore to investigate the performance of various cast irons and steels close to the industrial service conditions of liquid Al corrosion.

1.2 Research Objective

In this research project, the primary emphasis was upon enhancing the service life of tapping pipes. The optimum service life of tapping pipes requires a material with enhanced liquid Al corrosion resistance. Thus, current investigation utilized a series of experiments to determine the corrosion and associated substrate reaction mechanisms of steels, GCIs and DCIs in liquid Al baths at various temperatures.

Evaluation of liquid Al corrosion requires the experimental conditions to be as close as possible to the actual industrial service conditions. Previous research [10-11] tests were carried out in static melt conditions and it was found to be difficult to reveal the effect of the chemical composition of cast irons on liquid Al corrosion resistance. Thus in the present work, specialized experiments have been designed for testing the liquid Al corrosion at fixed temperatures under dynamic corrosion conditions.

Reports from the literature [10-11] compared the corrosion resistance of several cast irons. However, no detailed attempts have been made to understand the effect of microstructure on liquid Al corrosion resistance. In the present work, the liquid Al corrosion resistance of cast irons is analyzed with respect to the composition and microstructure. Exposure of ferrous

alloys to liquid Al results in the formation of intermetallic compounds, which have been suggested to control the corrosion rate [2]. Thus the nature of the intermetallic phases and their morphology are another subject of importance to the present study. Several ferrous alloys were exposed to static liquid Al so that the compound formation kinetics could be assessed against the liquid Al corrosion in static and forced flow melt conditions.

It is anticipated that enhanced comprehension of the liquid Al corrosion characteristics of ferrous alloys will enable improvements to service life of tapping pipes and related hardware. In addition to the significant industrial importance, the corrosion and intermetallic compound formation kinetics of cast irons and steels exposed to liquid Al will enrich the scientific literature.

1.3 Format of Thesis

This thesis comprises seven chapters and the contents of each chapter are described below:

- Chapter 1 (this chapter) briefly describes the overview and objectives of the present research program. The basics of the Al production process are described with an emphasis on understanding the service conditions of tapping pipes. Special focus is placed upon the degradation behaviour of tapping pipes by flowing liquid Al.

- Chapter 2 comprises the literature review pertinent to the present research, which is divided into three parts. The first section describes the role of the alloying elements in controlling the microstructure, and mechanical and physical properties of cast irons. The second section describes the formation and growth of the intermetallic compounds formed by Fe/Al interaction. The third section is based upon the dissolution test apparatuses and the previous studies on liquid Al corrosion resistance of ferrous alloys.

- Chapter 3 presents the compositions and microstructures of the materials used in the present investigation. This is followed by the description of microscopy techniques used to characterize the intermetallic compounds. Finally, the details of experimental apparatuses and methods used in the present investigation are described.

- Chapter 4 comprises the results derived from the present work. This chapter starts with the corrosion rates of several ferrous alloys under various conditions of temperature and flow of Al. Next is the description of the characterization of the various intermetallic compounds formed by the interaction between several ferrous alloys and liquid Al. This chapter also includes results of static immersion tests to reveal the characteristics of the intermetallic layers of several ferrous materials. Finally, the intermetallic layer morphologies of various ferrous alloys are discussed.

- Chapter 5 is the discussion section of the current investigation. This chapter starts with the analysis of the liquid Al corrosion resistance with respect to the chemical composition and microstructures of GCI, DCI and steel alloys. This is followed by the basic mechanisms of liquid Al corrosion of ferrous alloys and compound formation. Next the research is narrowed down to understand the underlying mechanisms of compound formation and liquid Al corrosion of GCIs, DCIs and CS. The intermetallic layer growth and dissolution of each type of alloy is discussed to provide a link between the two. The effect of Si on the liquid Al corrosion of cast irons also forms a part of this chapter.

- Chapter 6 presents the conclusions derived from the current work.

- Chapter 7 comprises the recommendations to industry and future work.

- Appendix A describes a brief literature review on thermal fatigue resistance of cast irons. The design and development of various thermal fatigue test set-ups are described, and the results obtained on the thermal fatigue resistance of cast irons are discussed.

- Appendix B describes the effect of surface condition on the liquid Al corrosion resistance of cast irons.

- Appendix C shows the material loss results obtained using the dynamic corrosion test apparatus.

- Appendix D describes the effect of boronizing surface treatment on the liquid Al corrosion resistance of steel and cast irons.

1.4 Background

This section focuses on the Al smelting process and the application of the tapping pipes in transferring the liquid Al from smelting cells, which is important in understanding the service conditions and failure of the tapping pipes. An analysis of the failure of after-service tapping pipes was carried out to determine the effect of service conditions on the degradation behaviour of pipe materials. In addition to the present study, analysis of service conditions and failure of the tapping pipes may also be useful for future research.

1.4.1 Al Smelting

Hall-Héroult process is a commercial process for producing Al by passing an electric current through a solution of alumina (Al_2O_3) dissolved in cryolite (Na_3AlF_6). In the Hall-Héroult process, Al_2O_3 is dissociated into Al metal and O by electrolytic reduction. It is a continuous process in which the alumina remains dissolved in a cryolite bath in the electrolytic cells called pots. Figure 1.1 shows a simplified diagram of a smelting cell and transfer of liquid Al using the tapping pipes.

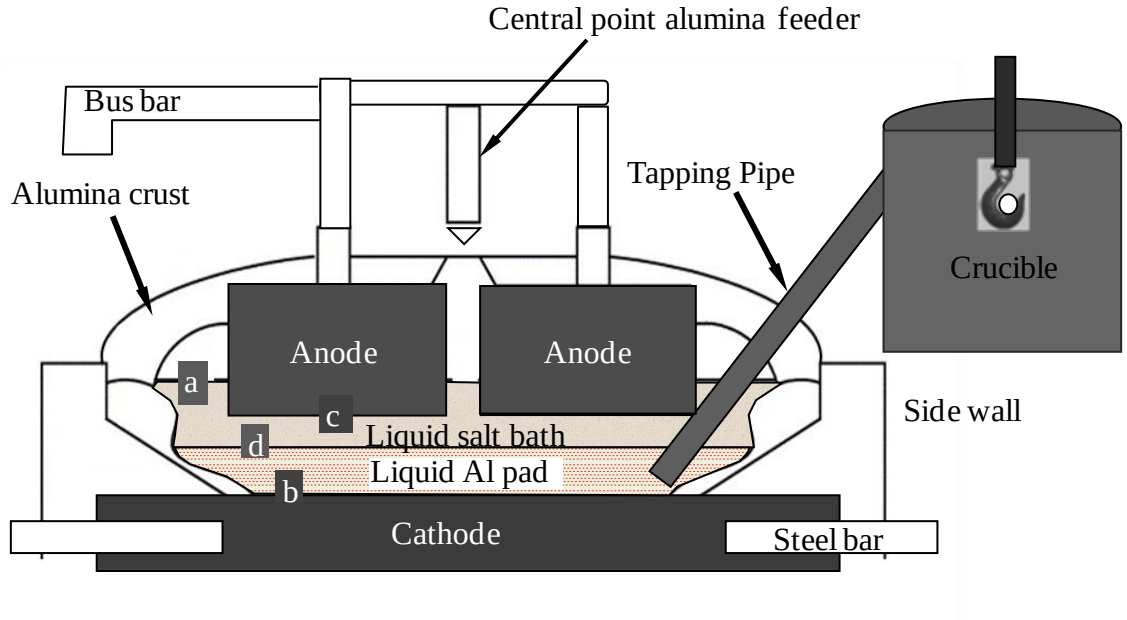

Figure 1.1 - A schematic of an Al smelting cell [16] and the application of tapping pipes in transferring the liquid metal.

As the electrolytic reaction proceeds - Al - which is slightly denser than the pot bath material - is continuously deposited in a metal pool on the bottom of the pot while oxygen reacts with the carbon material of the anodes to form oxides of carbon. A fraction of the Al collected at the bottom of the cell is removed using tapping pipes as shown in Figure 1.1. The liquid Al transfer operation is commonly known as ‘tapping’.

At NZAS, there are four reduction lines of smelting cells. Lines 1, 2 and 3 each contain 208 individual cells and Line 4 has 48 cells. Each cell in Lines 1-3 produces approximately 1450 kg and each cell in Line 4 produces approximately 1670 kg of molten Al every 24 hours. The molten Al is transported to the cast house for casting into billets.

1.4.2 Tapping Pipes and Service Conditions

1.4.2.1 Tapping Pipe Assembly

Figure 1.2 shows the tapping pipe assembly of Reduction Line 2 (representative of Lines 1-3), which consists of three pipe sections: the inner section, the top tapping pipe and the

bottom tapping pipe. These pipes are mounted over the lid of a refractory-lined steel crucible in which a vacuum is created to transfer the liquid Al.

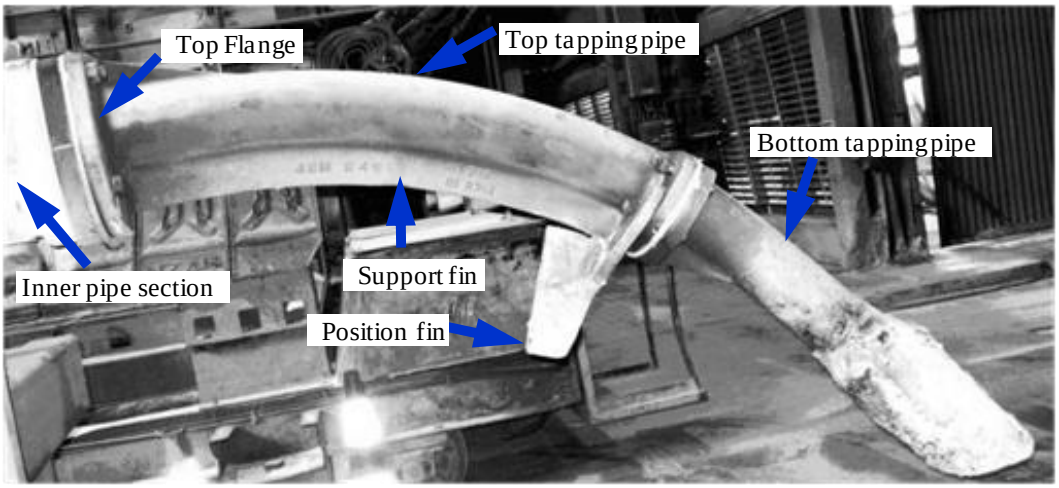

Figure 1.2 - The tapping pipe assembly (Lines 1-3).

1.4.2.2 Materials

The top tapping pipe material is cast steel, and the inner section and lower tapping pipes are GCI. The Line 4 tapping pipe assembly consists of a DCI top tapping pipe of a different design. The tapping pipe materials have been employed in service for several years, and owing to the lack of scientific background, the selection of these materials is likely to be based upon experience only.

1.4.2.3 Tapping Operation

Each year, at NZAS the tapping of Al from smelting cells occurs approximately 242,000 times. The preparation for a tapping operation starts with setting a lid - to which the tapping pipes are connected - over the steel crucible - followed by these steps:

a) Immersing the pipe inlet in the Al bath and connecting the compressed air supply to a large venturi mounted over the top of the crucible lid, which creates a vacuum inside the crucible.

b) Starting the tapping by placing a small glass lid over a hole in the crucible wall. The Al

flow velocity is adjusted by moving the glass lid, which controls the vacuum generated. The velocity of liquid Al must be within limits because a too high velocity draws the bath and increases cathode erosion [17].

c) Stopping tapping after withdrawal of approximately 1450 kg (Lines 1-3) of Al from a cell. Each tapping operation takes about three minutes. Tapping time between the cells varies between one to two minutes and depends on the location of the next cell for tapping.

d) One crucible can hold Al from three cells. Once full, the crucible full of metal is skimmed and subsequently transported to the cast house.

e) The crucible lid with tapping pipes assembly is fixed to the next crucible, and pipes are readied to tap the next cell. This process usually takes 15-20 minutes.

f) The liquid cryolite bath and Al solidify inside the tapping pipes during tapping and have to be removed periodically. The operation by which the tapping pipes are cleaned is known as ‘rattling’.

1.4.2.4 Thermal Gradients

A Land Cyclops Ti 814 thermal imaging camera was used to record the thermal gradients on the surface of the Line 2 tapping pipes during continuous tapping operations. The thermal images shown in Figure 1.3 (a) and (b) reveal that the temperature at the upper section of pipe was the highest. The presence of a support fin (Figure 1.2) at the lower pipe section helps to dissipate the heat and is the first possible cause of thermal gradients across the pipe circumference. The maximum temperature on the top tapping pipe surface showed a small increase (30-40°C) from the start to the end of an Al transfer operation. At this stage, the small temperature rise during tapping can be attributed to the solidification of the bath at the inner pipe surface. The thermal conductivity of cryolite salts is low (0.8-1.2 $Wm^{-1}k^{-1}$) [18], thus the solidified bath layer can act as a thermal insulator.

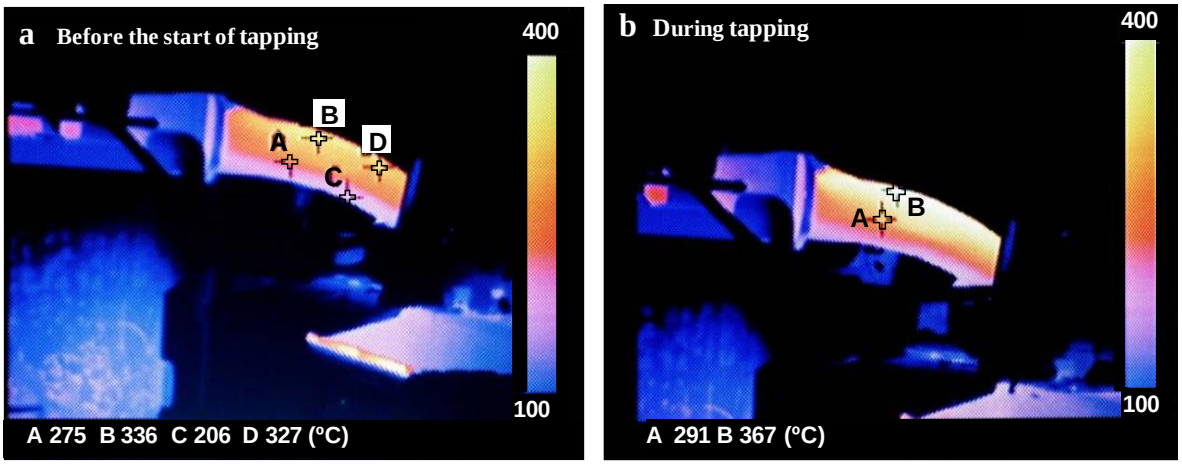

Figure 1.3 - Thermal gradients at the top tapping pipe surface, a) before the start of a tapping operation, b) during a tapping operation.

1.4.3 Failure of Tapping Pipes

Table 1.1 lists the number of pipe failures of various tapping pipe sections used in smelting Lines 1-3 in 2007 at NZAS.

Table 1.1- Number of failed tapping pipes in Lines 1-3 in 2007 at NZAS.

Inner Section	Top Tapping Pipe Section	Bottom Tapping Pipe Section
67	107	663

At NZAS the following types of failures have been reported in various tapping pipe sections:

a) Top tapping steel pipes (Lines 1-3) fail by means of holes through the wall thickness, Figure 1.4(a).

b) Over 95% of the failures of bottom tapping pipes (GCI) were found to occur through shortening of the pipe length the rest fail by cracking through the pipe thickness. A failed bottom tapping pipe section is shown in Figure 1.4(b).

c) The predominant mode of failure of DCI top tapping pipes (Line 4) is cracking occurring through the pipe wall. These pipes are reported to survive longer than the cast steel pipes; however, quantitative data is not available.

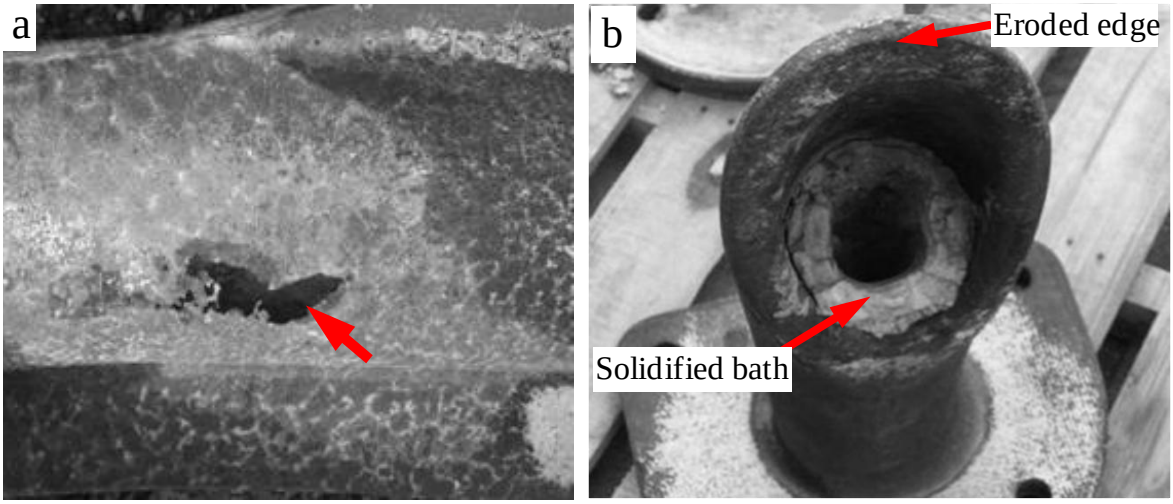

Figure 1.4 - a) A hole through the top tapping pipe wall, b) an after-service bottom tapping pipe section.

1.4.3.1 Top Tapping Pipe Failure Investigation

The failed after-service top tapping pipe (cast steel) section used in this investigation was supplied by NZAS. The main purpose of this analysis was to determine the failure mechanisms and the reasons underlying the failure that occurs by means of holes appearing through the pipe wall. In most of the cases, these holes appear at the top and sides of the circular pipe section and in a few cases near the downside of the top flange.

Owing to the high temperature and electrochemical effect of the flowing current in the smelting cells, the cryolite bath remains in liquid form. During the transfer of Al from cells, the entrapment of the cryolite bath in liquid Al is unavoidable, and its amount depends upon the skills of the operator and level of Al in the cell.

The contact angle of molten cryolite with steel is 0^{o} at 1050^{o}C [19], which signifies that liquid cryolite wets steel perfectly. Before the start of tapping, the tapping pipe surface remains at a lower temperature than the temperature of Al in the cell. When the liquid Al along with the bath starts to flow in the pipes, a fraction of the flowing bath solidifies at the pipe surface. At the same time, it is possible that there is an already existing layer of

solidified bath from the previous tapping operation. The solidified bath layer on the after-service pipe sections revealed 6-8 sub-layers, with each sub-layer possibly representing a tapping operation, Figure 1.5. On areas covered with solidified bath, liquid Al is unable to contact the pipe surface during subsequent tapping operations.

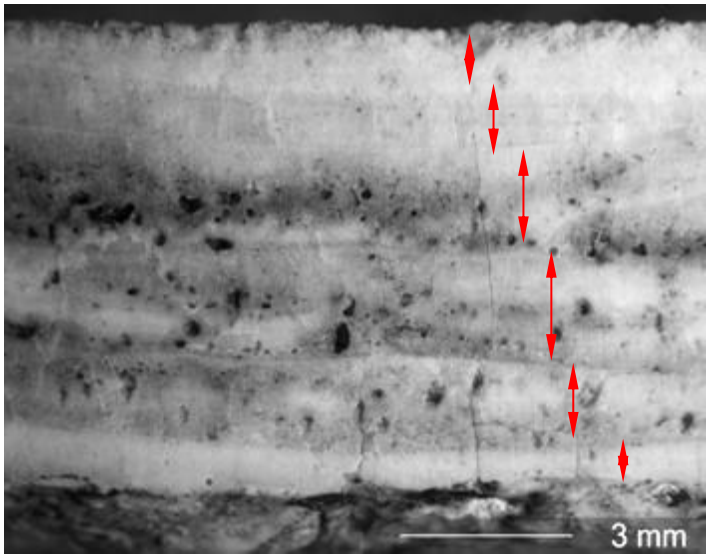

Figure 1.5 - Solidified bath layers on an ex-service top tapping pipe surface.

Previous flow visualization studies revealed that the flow of Al was highly turbulent (typically around R_e = 90,000) [17]. Therefore, it is also possible that at some pipe sections the bath is unable to solidify or the solidified bath becomes eroded with the flow. As a consequence, these pipe surfaces come into contact with flowing liquid Al and become intensely eroded.

The thickness of the solidified bath varied along the length and periphery of the top tapping pipe. The after-service top tapping pipe was sectioned into five pieces, which are arranged in order of increasing distance from the top flange in Figure 1.6. This pipe section failed due to a hole adjacent to the downside of the top flange. The solidified bath thickness decreased from inlet to outlet. At about 2/5 length from the inlet end, the bath thickness at the upper

cross-section was minimum, Figure 1.6(b), while it increased considerably near the outlet, Figure 1.6(a).

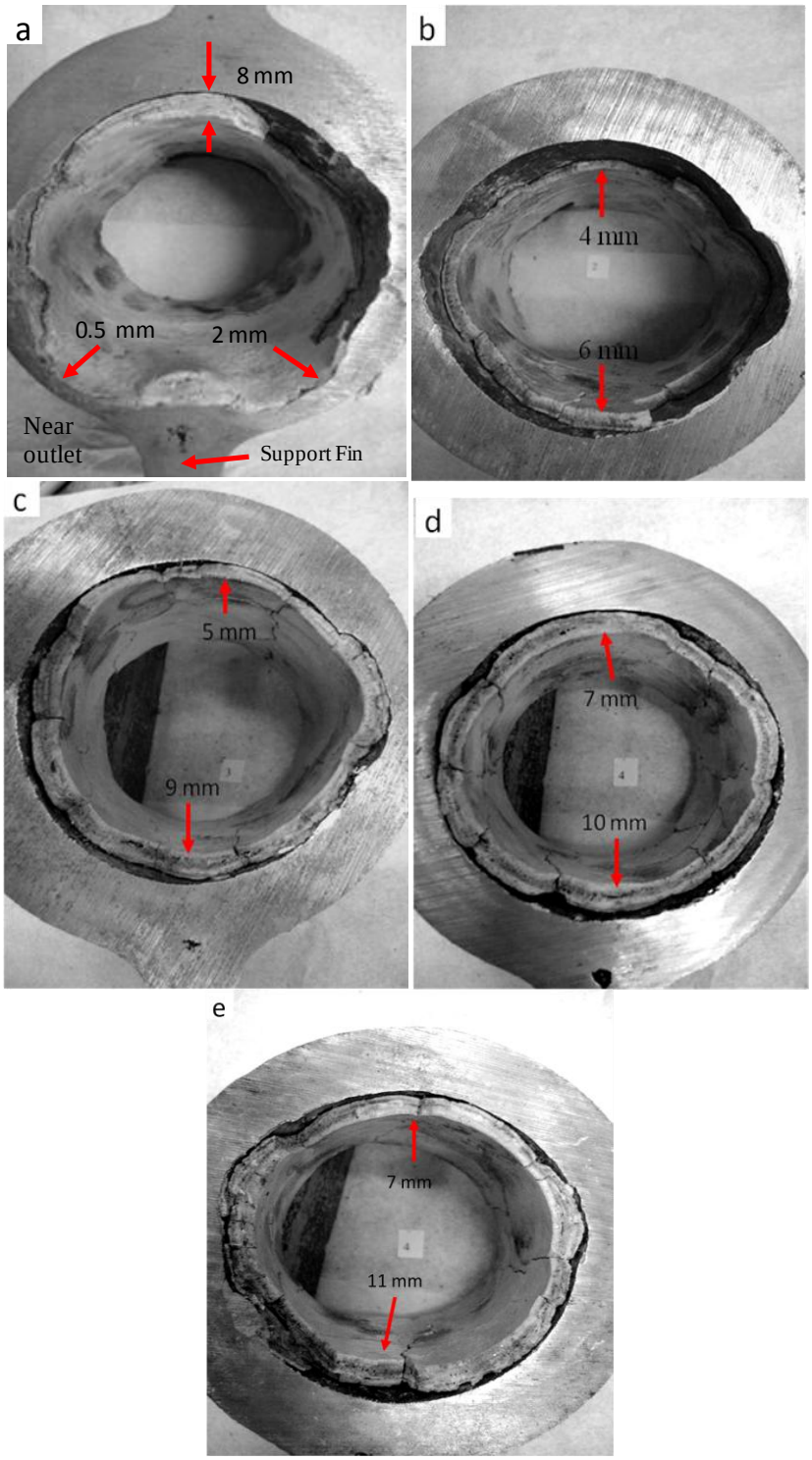

Figure 1.6 - Thickness of solidified-bath on top tapping pipe sections - arranged in order of increasing distance from the top end (outlet).

The thermal gradients in the infrared images (Figure 1.3) during a tapping operation may relate to the solidified bath thickness, because a smaller bath thickness should mean lesser resistance to the flow of heat thus a higher temperature at the outer surface. A very small thickness of bath layer can be seen in Figure 1.6(a), which was found near the hole through the pipe section, while the area just above the support fin is considerably less eroded compared to the sides. The different thicknesses of the solidified bath could depend upon temperature variation at the pipe surface and the density difference between cryolite salts and liquid Al. At the pipe surfaces where the temperature is lower the possibility of bath solidification is higher.

The tapping pipe is inclined at an angle of about 60° to the vertical at the end joined to the bottom tapping pipe and near the top end it is nearly horizontal (Figure 1.2). Thus the weight component of liquid Al at the lower pipe surface increases as it flows from inlet to outlet, which may have led to a greater amount of mechanical erosion at downside of the outlet section. Owing to the relatively lower temperature and the effect of bath solidification, the area over the support fin can be least vulnerable to failure by erosion. Thus the sides and upper portion of the pipe are more likely to contact flowing liquid Al and results in thinning of the pipe wall.

Visual observations of the transverse sections of the top tapping pipe revealed that in some areas the bath was solidified over the erosion zone, Figure 1.7. This type of layer solidification is most probable when there is a large time gap between subsequent tapping operations or the tapping pipe is put into operation after rattling. Thus the solidification of the bath over the previous erosion zone is able to stop further material loss by flowing Al. Conversely, the possibility of bath solidification is least in continuous tapping operations because the pipes remain at high temperature and Al could be present in the liquid state at the

erosion zones. This can prevent bath solidification due to the absence of pipe surface at a low temperature. Moreover, localized pipe wall thinning may cause a localized flow turbulence leading to a lower possibility of bath solidification.

After removing the solidified bath a top tapping pipe section was pickled in 5% (Dcon-90®) + 95% H_2O solution for 24 hours. Dcon-90® is the registered trademark of Zinsser Analytic GmbH, Germany. Figure 1.8 shows the pipe surface that was not corroded by liquid Al and the erosion pits, which identify the initiation of erosion at random locations on the pipe surface. Almost the entire pipe surface showed material loss by this type of pit patterns. This type of interaction is possible when the liquid Al contacts the entire pipe surface and is most likely to occur when a new pipe or existing tapping pipe is used for the first time after rattling operation. As mentioned previously, in subsequent tapping operations, further Fe-Al interaction could be stopped by the solidification of the bath over the reaction zone. Figure 1.9 shows a pickled pipe section near the failure zone; the pipe failure occurred through the creation of the holes near the downside of the top flange. Figure 1.6(a) shows the cross-sectional view of the pipe section close to the failure area.

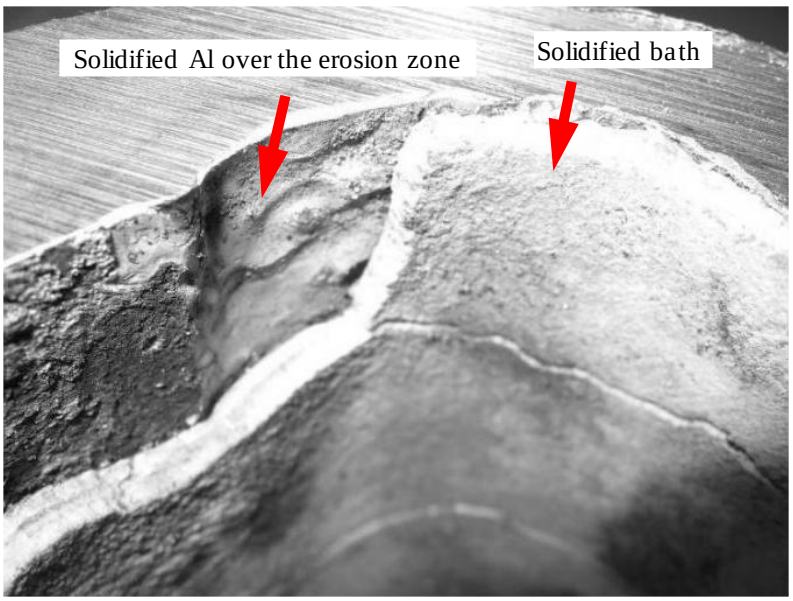

Figure 1.7 - Solidification of the bath over the erosion zone in the ex-service top tapping pipe.

Figure 1.10 is an image of a specimen cross-section that was obtained from the steel pipe adjacent to the failure zone. Liquid Al is known to be extremely active with ferrous alloys. Immediately after contact with ferrous substrates it forms Fe-Al intermetallic compounds. A continuous Fe-Al interaction layer was found on the surface of the after-service steel pipe.

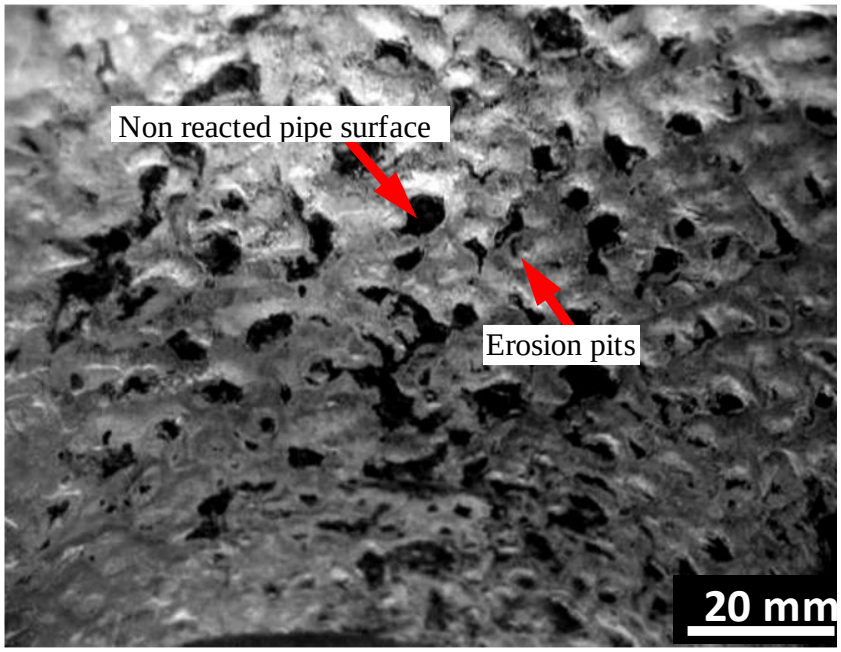

Figure 1.8 - An example of erosion patterns on the entire inner surface of an ex-service top tapping pipe.

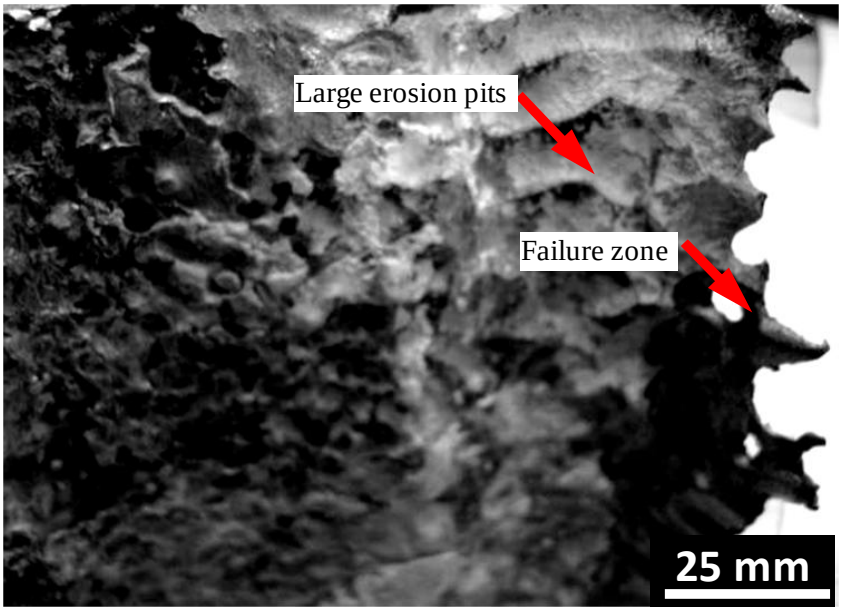

Figure 1.9 - Erosion pits formed by accelerated material loss at the place of failure in ex-service top tapping pipe.

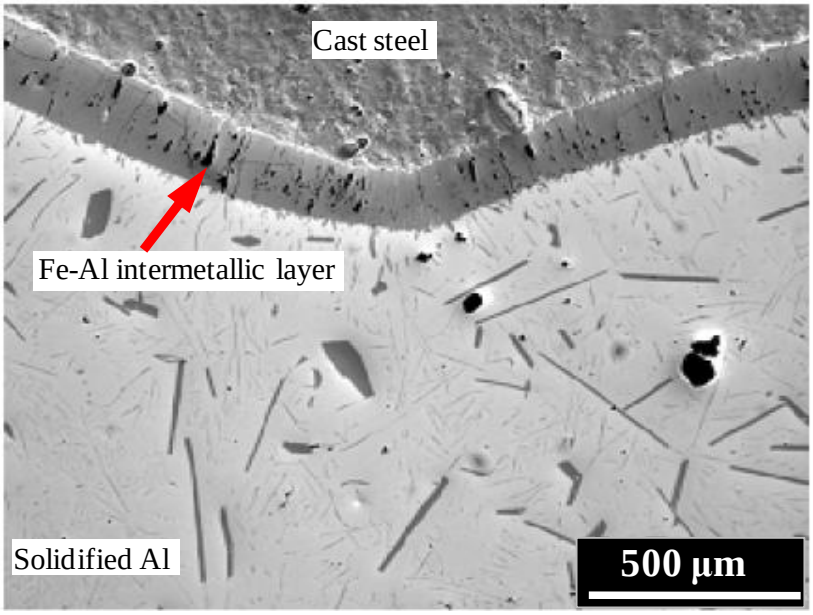

Figure 1.10 - Continuous intermetallic layer at the surface of an ex-service steel tapping pipe adjacent to the failure zone.

1.4.3.2 Bottom Tapping Pipe Failure Investigation

Three specimens of an ex-service bottom tapping pipe were sectioned adjacent to the eroded edge and prepared for metallographic analysis. A back scatter electron (BSE) image, Figure 1.11 shows the interfacial microstructure between the GCI and the Al bath.

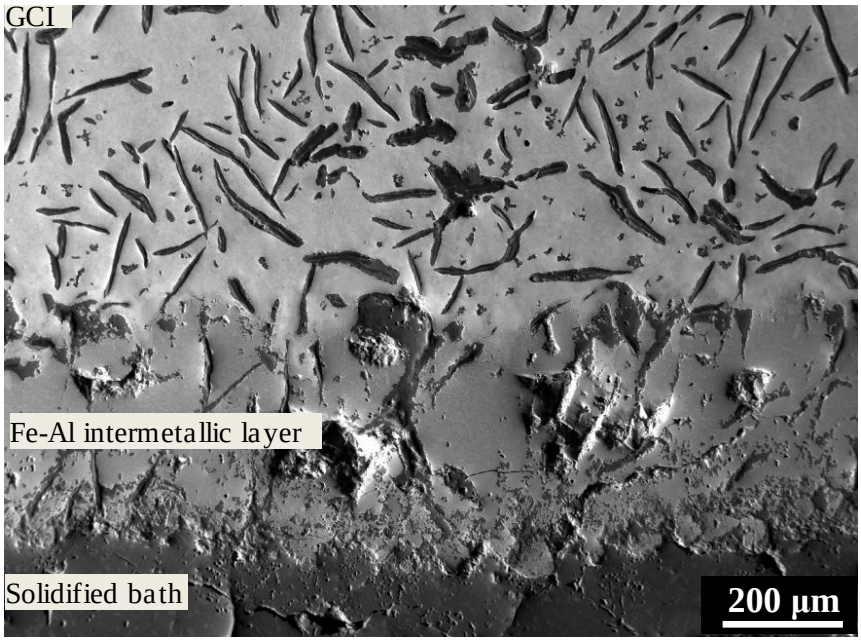

Figure 1.11 - A BSE image showing the bottom tapping pipe (GCI)/bath interface.

All specimens had a continuous Fe-Al intermetallic layer about 500 μm thick. This suggests that the corrosion of the bottom tapping pipe occurs through alloy layer formation. No cracks have been found in the GCI microstructure; however, a number of micro-cracks were found in the Fe-Al intermetallic layer.

Considering the possible corrosion protection provided by the bath solidification inside the top tapping pipes, the corrosion conditions for bottom tapping pipes are comparatively more severe. The lower end of the bottom tapping pipes, where the bath solidification is not possible, remains in contact with the flowing liquid Al during each tapping operation. This induces excessive material loss at the pipe inlet and renders the pipe useless by shortening the pipe length. The GCI substrate formed intermetallic compounds with Al, which are relatively brittle [20] and can easily exfoliate with the swift flow of liquid metal. These findings indicate that the principal mode of failure of bottom tapping pipes is also flow-assisted liquid Al corrosion.

1.4.4 Material Properties

Temperature of liquid Al in tapping pipes should be close to the bath temperature, 960°C. For tapping pipes, the thermal activation of corrosion is substantially higher owing to the very high liquid Al temperature and is further assisted by the turbulent flow of Al. Liquid Al corrosion of ferrous alloys was found to be a major factor causing the failure of tapping pipes. However, thermal fatigue resistance is an important factor when considering cast irons for replacing the existing steel and enhancing the service life of existing cast iron tapping pipes. Overall, the cost of the improved material must not outweigh the benefit of enhanced service life. Thus ceramics and other expensive coating options are not part of the present research. Moreover, the periodic removal of the solidified bath imposes a practical constraint

on the use of ceramic coatings because these coatings are always brittle and will spall during rattling operations.

Cast irons and steels are close competitors for tapping pipe applications because steels possess higher mechanical strength and better resistance to cracking under thermal loading [15], whereas cast irons are cheaper. It is surprising that there are very limited reports [10-11] available on enhancing the liquid Al corrosion resistance of cast irons and no correlation has been established between the corrosion resistance and chemical composition. Therefore, there is a need to address the liquid Al corrosion resistance of cast irons and steels close to the industrial service conditions of tapping pipes.

Chapter References

[1] ALCOA, available at : www.alcoa.com/global/en/about_alcoa/pdf/Smeltingpaper.pdf.

[2] M. Yan, Z. Fan, Journal of Materials Science, 36 (2001) 285-295.

[3] P.F. Tortorelli, J.H. Devan, Liquid Metal Corrosion Consideratios in Alloy Developement, Metals and Ceramics Division, Oak Ridge National Laboratory, Tennesee, USA.

[4] H. Mizuno, J. Kitamura, Journal of Thermal Spray Technology, 16 (2007) 404-413.

[5] M. Niinomi, Y. Ueda, M. Sano, Transactions of the Japan Institute of Metals, 23 (1982) 780-787.

[6] V. N. Eremenko, V. R. Ryabov, Materials Science, 4 (1968) 286-290.

[7] N. Tunca, G. Delamore, R. Smith, Metallurgical and Materials Transactions A, 21 (1990) 2919-2928.

[8] K. Barmak, V.I. Dybkov, Journal of Materials Science, 39 (2004) 4219-4230.

[9] M. Niinomi, Y. Suzuki, Y. Ueda, Transactions of the Japan Institute of Metals, 25 (1984) 429-439.

[10] F.A. Mountford, T.J. Glover, Foundry Trade Journal, 120 (1966) 849-852.

[11] D. Balloy, J.C. Tissier, M.L. Giorgi, M. Briant, Metallurgical and Materials Transactions A, 41 (2010) 2366-2376.

[12] S.H. Hwang, J.H. Song, Y.S. Kim, Materials Science and Engineering A, 390 (2005) 437-443.

[13] J.R. Davis, ASM Speciality Handbook-Cast Irons, ASM International, Materials Park, Ohio, 1996.

[14] M. Blair, T.L. Steven, Steel Castings Handbook, ASM International, Materials Park, Ohio, 1995.

[15] M.M. Shea, American Foundry Society Transactions, 04 (1978) 23-30.

[16] D.A. Weirauch Jr, Current Opinion in Solid State and Materials Science, 9 (2005) 230-240.

[17] M.L. Walker, Visualization of tapping flows, Light Metals, TMS Annual Meeting, Orlando, (1997) 215-219.

[18] V.A. Khokhlov, E.S. Filatov, A. Solheim, J. Thonstad, Thermal conductivity in cryolitic melts - new data and its influence on heat transfer in aluminum cells, TMS Annual Meeting, San Antonio, (1998) 501-506.

[19] I.E. Veneraki, A.D. Panasyuk, V.I. Deshko, Ukr Khim Zh, 42 (1976) 291-298.

[20] H.R. Shahverdi, M.R. Ghomashchi, S. Shabestari, J. Hejazi, Journal of Materials Processing Technology, 124 (2002) 345-352.

CHAPTER 2 : LITERATURE REVIEW

Introduction

The review of the literature pertaining to this thesis is divided into three sections. This chapter starts with an overview of cast irons by briefly discussing their mechanical properties and effect of alloying elements. Second part of this chapter introduces the formation and growth of various intermetallic compounds in Fe-Al interaction. In the third part, the basics of dissolution and the dissolution apparatuses used in the literature are discussed. Finally, the previous studies on liquid Al corrosion resistance of ferrous alloys are described.

2.1 Cast Irons

Cast irons consist of graphite inclusions of various shapes embedded in a Fe matrix and form a complex metallurgical system compared to steels. To optimize the liquid Al corrosion resistance of cast irons, it is crucial to understand the effect of compositional constituents on the microstructures of these alloys.

In general, the higher carbon content differentiates the cast irons from steels. Figure 2.1 shows the iron-iron carbide binary phase diagram, the Fe-C alloys up to 2 wt.% C are classified as steels, while the alloys with higher C contents are defined as cast irons. The amount of alloying elements present in most grades of steels is low; therefore, these can be considered as binary Fe-C alloys. However, cast irons contain appreciable amounts of Si in addition to higher C contents, so they must be considered as ternary Fe-C-Si alloys. When Fe is alloyed with Si and C in amounts of about 2 wt.%, the carbide in the Fe-C system becomes unstable. During solidification, Si causes the C to rapidly come out of the solution as graphite leaving a matrix of relatively soft Fe [1].

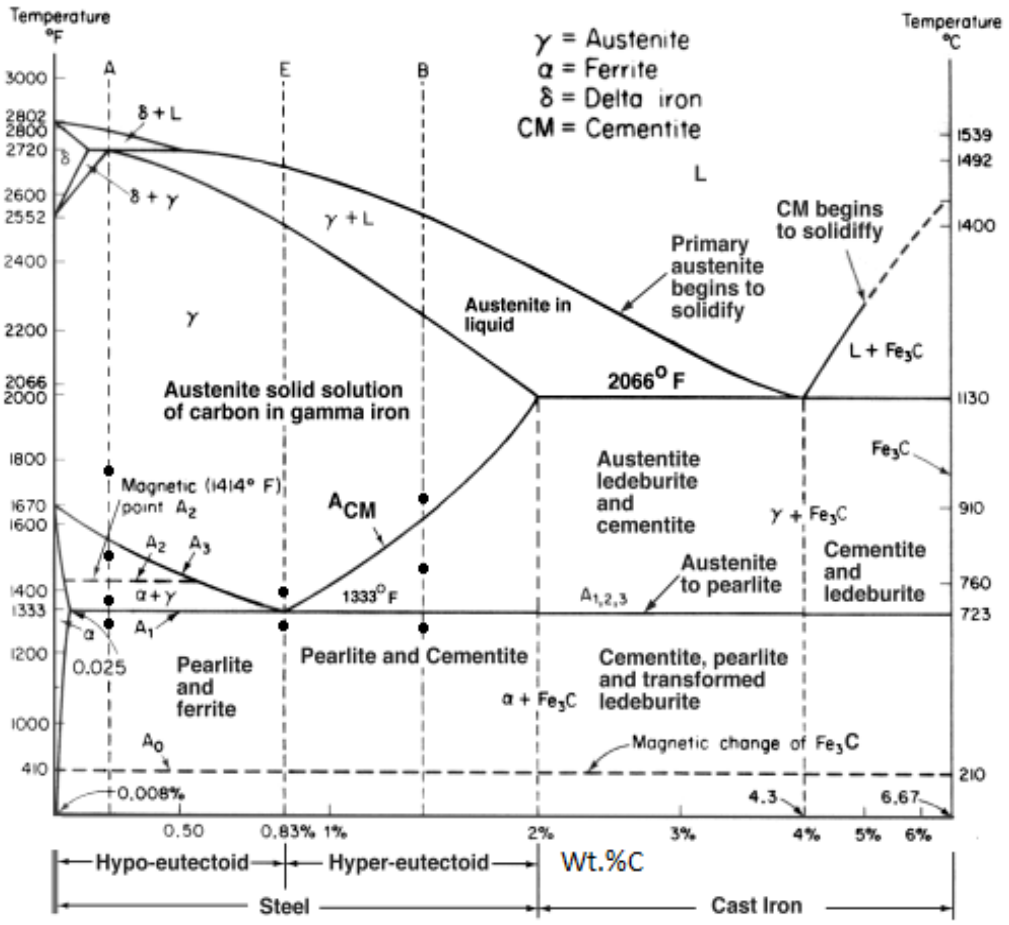

Figure 2.1- Iron-iron carbide binary phase diagram [1].

Variation in the amounts of C, Si and alloying elements strongly influence the microstructure and properties of cast irons. There are various types of cast irons such as GCIs, DCIs, white cast irons, compacted graphite irons and malleable cast irons [2]. Among these types of cast irons, GCIs and DCIs are most commonly used for industrial applications.

2.1.1 GCIs

GCIs are characterized by the presence of graphite in the form of long, thin flakes. During fracture these graphite flakes deflect the passing cracks and initiate countless new cracks resulting in a rough fracture surface that appears gray [2]. Of all the types of ferrous alloys, GCI is the most versatile foundry material. With a proper addition of C and Si, solidification occurs near the eutectic composition and results in low melting point, castable alloy.

The metallurgy of GCI is extremely complex because a variety of factors influence the solidification and solid state transformations. Much has been learned about the mechanisms of nucleation, solidification and solid state transformations of cast irons. However, only the important features of cast iron metallurgy, such as solidification and the effect of the alloying addition on microstructure and properties, are discussed here. Several good texts [2-3] are available for more detailed information.

Eutectic solidification of cast irons involves two types of transformation reactions; the stable graphite eutectic reaction and the metastable iron carbide reaction. The eutectic temperature of the graphite reaction is slightly higher than the iron carbide transformation. Figure 2.2 shows a typical cooling curve for a hypoeutectic GCI reflecting the sequence of events during the course of solidification. The austenite transformation starts from liquid cooling, which passes through the graphite eutectic, the sufficient undercooling at this stage causes graphite nucleation and the heat of fusion of the eutectic reaction increases the system temperature and subsequently the temperature decreases by continuous heat loss to the mould walls. If solidification ends above the iron carbide eutectic, Figure 2.2, the resulting structure will be a uniform dispersion of graphite particles with no carbides. Addition of alloying elements to cast irons can alter the iron-graphite eutectic temperature and iron-carbide eutectic temperatures. The elements which raise the iron-graphite eutectic temperature and decrease the iron-carbide eutectic temperature are known as graphite promoters (graphitizers). On the other hand, the elements which decrease the iron-graphite eutectic temperature and raise the iron-carbide eutectic temperature are known as carbide promoters [4].

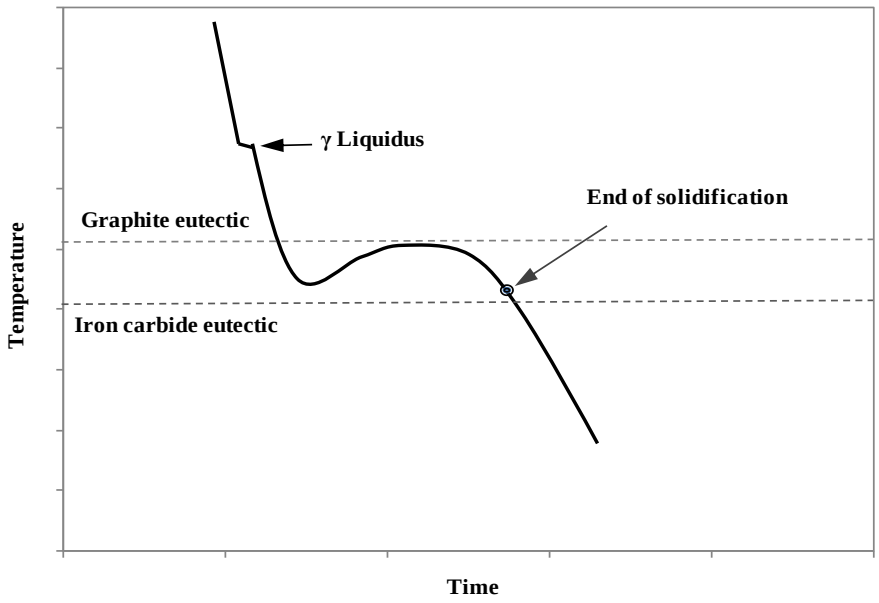

Figure 2.2 - Typical solidification cooling curve for a hypoeutectic GCI. [After [4]]

Solidification of cast irons begins with the precipitation and growth of austenite dendrites from the liquid. When the C content of the remaining liquid reaches 4.3 wt.%, eutectic solidification occurs. This consists of simultaneous and cooperative growth of austenite and graphite. Both the austenite and graphite phases are continuous within each eutectic cell. As the eutectic structure grows radially the graphite plates are subjected to twisting and branching. Therefore, the graphite flakes appear as discrete particles in 2-dimensional cross-sections instead of a continuous network. Figure 2.3 shows the graphite lamellae in deeply etched GCI. The increased amount of primary austenite dendrites strongly influences the strength of cast iron; however, these are difficult to identify. An increased fraction of primary austenite dendrites was found to be the main reason for the increase in strength of GCIs with decreasing C content [4]. On the other hand, the amount of eutectic graphite has a negative impact on the strength of GCI because a continuous graphite network can be viewed as a single graphite particle having the dimensions of a eutectic cell. Therefore, each graphite particle imparts a flaw that interrupts the continuity of the metallic matrix.

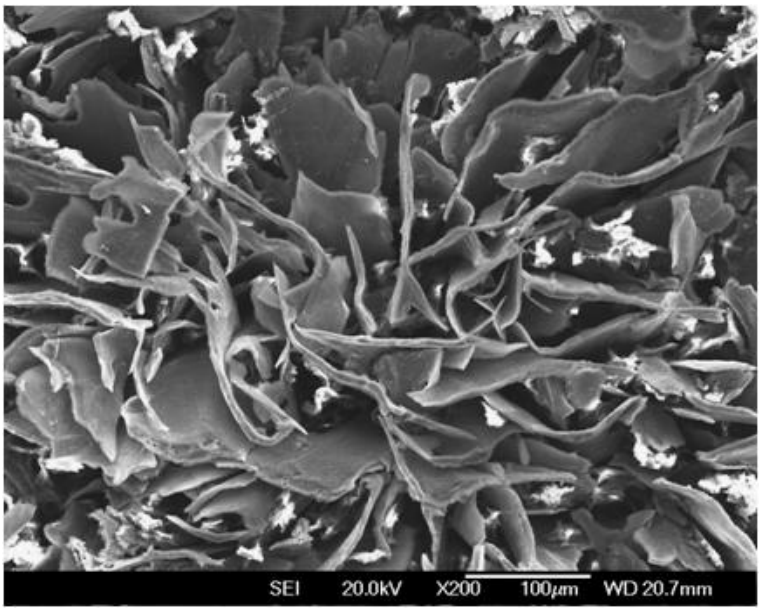

Figure 2.3 - Graphite flakes in GCI (deep-etched in 50% HNO_3).

Most of the alloying additions can change the eutectic C content thus changing the amounts of eutectic austenite and graphite. The type, size and distribution of graphite flakes are a function of solidification temperature and the rate at which solidification occurs, details are in [2]. Type A graphite is most desirable and is a random distribution of graphite flakes. This structure is normally obtained when the eutectic reaction begins and grows near the eutectic temperature. Both Si and P reduce the eutectic C content. The C equivalent (CE) with the addition of Si and phosphorus can be calculated by the relation:

$$CE = \%C + 1/3(\%Si + \%P) \quad (2.1)$$

This signifies that the Si and P are the substitutes for C. Therefore, addition of these elements imparts a similar effect as C. Since pearlite is stronger than ferrite, a higher strength GCI can be produced by increasing the pearlite content with the elimination of ferrite. Further, strengthening can be achieved by refining the pearlite, which is related to a lower pearlite reaction temperature that can be achieved by the following:

a) Rapid cooling that forces the transformations to occur at lower temperatures producing a finer pearlitic structure.

b) Alloying additions that delay the initiation and growth of the pearlitic reaction [4].

2.1.1.1 Alloying Elements and GCI Microstructure

The desired mechanical properties for a particular service application can be achieved by the addition of suitable alloying elements to cast irons. Some alloying elements segregate into the liquid phase and lower the solidification temperature, which helps to retard the eutectic cell growth. Elements such as V, Cr, Mo, P and Bi are known to increase the eutectic cell count. Some alloying elements are very effective in imparting the finer pearlitic microstructure, but have detrimental effects on the solidification process resulting in chill or carbides. Chill means the undercooling of the melt to the temperatures below the iron-carbide eutectic temperature, under such conditions C precipitates as carbide rather than graphite. Iron-carbide raises hardness and drastically reduces the machinability and decreases the impact strength of cast irons. These factors place foundry metallurgists in a quandary. For instance, Cr is very effective in imparting pearlitic structures in thick sections. However, it may cause carbides in thinner sections. Si can be added to balance the effect of chill and carbides. Nevertheless, it reduces the strength of the casting by promoting ferrite in thick sections [4]. The effect of various compositional constituents that were used in the current work is discussed in the following section.

2.1.1.1.1 Si

Si addition reduces carbides; on the other hand, it reduces the strength of GCI because in addition to raising CE, it promotes ferrite. It is also believed that Si has a negative effect on pearlite strengthening because it raises A1 (eutectoid) temperature and temperature of pearlite formation thus promoting coarse pearlite. Si depletes C from the cast iron matrix by ferrite formation and this C adds to the graphite volume, which results in inferior mechanical strength [4].

2.1.1.1.2 Mn

Mn reduces the amount of ferrite and moderately refines pearlite. It is required in excess to combine with the sulphur present in the raw materials for producing GCI. Mn strongly promotes pearlite because it stabilizes austenite by increasing the C solubility in austenite. Large additions of Mn can alter the state of nucleation resulting in lower eutectic cell count and coarse or undercooled graphite [4].

2.1.1.1.3 Cu

Cu is of dual character, it promotes the pearlite and also increases the amount of graphite. The dispersity and stability of eutectoid pearlite can also be improved by the addition of Cu. It also acts as a hardenability agent and the micro hardness of Cu alloyed pearlite can reach 600-700 H_V or higher, though the mechanism by which it increases the hardenability is still not known [5]. Cu weakly refines pearlite, nevertheless, in conjunction with other alloying elements (such as Mo) Cu has a greater hardenability effect [4]. The maximum effect of Cu on the degree of pearlitization of the structure occurs when it is contained in an amount of 1 wt.%. When the Cu concentration is high, it forms an insoluble phase. In copper bearing pearlite, thin layers (about 3 nm) of a Cu-rich phase lie between the cementite and ferrite lamellae. The thin layers of the Cu-rich phase were believed to play an important role in the stabilization of pearlite due to low diffusivity of C atoms in this phase even at high temperatures. For this reason, the Cu bearing pearlite is quite stable at high temperatures and its decomposition by graphitization occurs very slowly [5]. Because of the graphitization character of Cu, it can be used in partial substitution for Si to offset the chilling tendency without promoting free ferrite [4].

2.1.1.1.4 Cr

Cr promotes pearlite because it increases the C solubility in austenite and inhibits the nucleation of ferrite. It also promotes carbides and chill during solidification. While Si and

inoculation are effective in reducing chill caused by Cr, these are not effective in reducing the interdendritic carbides [4].

2.1.1.1.5 Mo

Mo behaves in an unusual manner because it has a powerful retarding effect on the pearlitic transformation, but a minimal effect on the ferrite formation. Mo additions delay the pearlite reaction and allow more time for C diffusion leading to ferrite formation. Consequently, adding Mo to an unalloyed iron may increase the ferrite in heavier sections. Therefore, Mo is generally used in conjunction with pearlite promoting elements [4].

2.1.2 DCIs

In DCIs, the eutectic graphite separates from the molten iron during solidification in a similar manner to GCIs. However, because of the addition of Mg or Ce (known as nodulizing treatment) the graphite grows as spheres rather than flakes in GCIs [2]. Figure 2.4 shows the dispersion of spheroidal or nodular graphite particles in a DCI matrix.

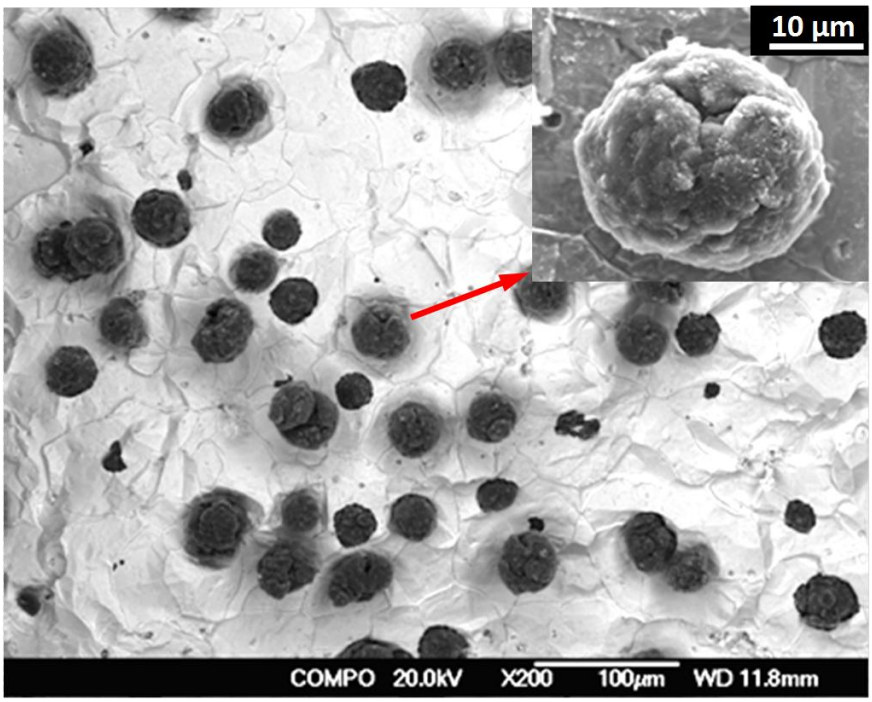

Figure 2.4 - Dispersion of graphite spheroids in a ferritic DCI (deep-etched with 50% HNO_3).

Spheroidal graphite cast iron does not impart discontinuities in the metallic matrix as lamellar graphite does. Therefore, the relatively high strength and toughness of DCI give an advantage over GCI in several structural applications. On the other hand, the raw materials used for DCIs must be of high purity. The presence of impurity elements such as sulphur must be below specified limits to impart an effective nodulizing treatment. Moreover, DCI castings need relatively large risers because of their increased tendency for shrinkage compared to GCIs. These factors lead to the increased cost of DCI castings compared to GCI. The mechanical properties of the DCIs with perfect spheroidal shape were found to be superior to the shapes intermediate between true nodular form and flake form. The size and uniformity of the distribution of graphite nodules also influence the properties, but to a lesser degree than the shape. Small and numerous nodules usually give higher tensile properties and tend to reduce the formation of chills in thin sections or edges [2].

2.1.2.1 Effect of Alloying in DCIs

The basic metallurgy of DCIs is similar to GCIs. However, as mentioned before, greater metallurgical and process control is required in the production of DCIs. Mg imparts the nodular shape to graphite, Mn and Cu serves the same purpose as in GCIs. A brief summary of the effects of C and Si is as follows:

2.1.2.1.1 C

C influences the fluidity of molten iron and shrinkage characteristics during solidification. An excess C in suspension instead of solution reduces fluidity. The volume of spheroidal graphite is approximately 3.5 times the volume of iron. As DCI solidifies, excess C in solution precipitates out and causes the expansion, which can offset the shrinkage of the DCIs to some extent. Excess C can lead to a decrease of tensile strength and fatigue resistance of DCIs. The size and number of graphite nodules formed are also influenced by the amount of C [2].

2.1.2.1.2 Si

Si is a strong graphite promoter for both GCIs and DCIs. In addition to promoting ferrite, increasing Si content contributes to solution strengthening and hardness of ferrite. High Si DCIs have proved to be best suited for elevated temperature service [4].

2.1.3 Elevated Temperature Properties of Gray and Ductile Cast Irons

Scientifically, the maximum service temperatures of unalloyed or low alloy GCIs should be in the 500-600°C range because, at higher temperatures, microstructural transformations can lead to deterioration of mechanical properties [2]. DCIs are suitable for higher temperatures because they possess higher strength and greater oxidation resistance than GCIs. Since GCIs and DCIs are cheaper than steels, they are commonly employed in the temperature range of 700-1000°C [6]. Typical examples of high temperature applications are brake drums, hot mill rollers, moulds for Al, Cu and pig iron casting, and tapping pipes.

The selection of cast irons for high temperature applications is difficult because it depends upon balancing a number of material properties such as, dimensional stability, resistance to oxidation, creep resistance and high temperature strength. Moreover, there is a lack of data on the elevated temperature properties of cast irons, especially for service conditions involving temperatures higher than 600°C [2].

The selection process is further complicated when the service conditions involve frequent temperature variations because the material performance under such conditions depends upon several factors such as thermal conductivity, elastic modulus, high temperature strength and creep resistance. The repeated heating and cooling induces thermal fatigue. Higher elastic modulus induces stresses of higher magnitude for the same temperature difference. Higher thermal conductivity helps to distribute heat within the material more uniformly reducing the temperature gradients within a component. Compared to DCIs, GCIs have inferior

mechanical strength; however, they exhibit low elastic modulus and higher thermal conductivity. Thus all the required properties for the components under thermal fatigue cannot be satisfactorily met by a single class of cast irons [7]. More details on the thermal fatigue properties of cast irons are described in Appendix A. Elevated temperature properties of gray and DCIs are briefly discussed in the following sections and more information can be found in [2-3].

2.1.3.1 Growth and Oxidation

When cast irons are subjected to elevated temperatures of a continuous or interrupted heating and cooling service, they have a tendency to grow in size (swell) and exhibit oxidation at the surface. This may occur from one or more of the following factors [2]:

a) Decomposition of carbides.
b) The structural breakdown of the pearlite to ferrite, which is accompanied by the increased volume of graphite particles.
c) Internal cracking owing to cyclic heating. Formation of these fine cracks accelerates the oxidation. This internal oxidation contributes to the growth of GCI [7].

Growth in GCIs occurs more rapidly than DCIs. Growth was found to be more rapid in GCIs with higher C contents. The resistance to growth can be enhanced by either producing a ferritic matrix with no pearlite to decompose at elevated temperatures or stabilizing the carbides so that their breakdown into ferrite or graphite can be prevented [2]. The most effective growth reduction in GCIs can be achieved with strong carbide stabilizers such as Cr and Mn. Moderate alloying additions of Cr, Cr+Mo and Cr+Mo+Ni decrease the amount of growth in GCIs up to 500°C. The Cr+Mo combination was found to induce a dramatic effect in reducing the growth of GCIs [2].

Unlike GCIs that experience growth by both graphitization and oxidation, the growth in DCIs occurs from graphitization only. Annealed ferritic DCIs are free from growth up to 815°C, while pearlitic cast irons begin to grow above 538°C owing to the decomposition of pearlite to ferrite. Both ferritic and pearlitic DCIs show larger amounts of growth above 815°C, with pearlitic irons growing more than the ferritic grades. Higher addition of Si alone or combined with Mo stabilizes the ferritic matrix, and a Si-rich oxide layer at the surface inhibits further oxidation [2].

2.1.3.2 Elevated Temperature Strength

In terms of elevated temperature strength, GCIs were found to be inferior to DCIs. However, the strength of both types of cast irons can be enhanced by the addition of suitable alloying elements. Increasing C content in GCIs adversely affects the high temperature strength. Unalloyed GCIs exhibit small changes up to 400°C, while above this temperature the tensile strength decreases quite rapidly. The Mo alloyed cast irons show greater resistance to plastic deformation at temperatures above 400°C [8].

Turnbull and Wallace [9] also studied the elevated temperature strength of GCIs alloyed with Mo and Cr in the temperature range of 427°C-650°C. The tensile strength was found to increase with increasing the Mo content from 1.4-1.9 wt.% in both plain and Cr alloyed GCIs. The tensile strength of unalloyed pearlitic DCIs decreases continuously with increasing temperature. At about 400°C, it retains about two thirds of its room temperature strength, whereas ferritic DCIs retain approximately 75% [2].

2.1.3.3 Creep Properties

A number of researchers studied the influence of alloying elements on the creep and stress rupture properties of GCIs. Turnbull and Wallace [9] demonstrated the beneficial effects of Cr and Mo additions on the stress rupture properties of GCIs in the temperature range of

400°C-650°C. The addition of Mo up to 2 wt.% to an unalloyed GCI continuously raised the stress to rupture at all the temperatures. Additions of both Cr and Mo showed a substantial increase in the creep and stress rupture properties of GCIs. Similarly, Gundlach [10] found that the Cr and Mo additions improved the creep properties at 540°C, while the combined addition of these alloying elements imparted synergetic effects to enhance the creep properties.

The creep resistance of ferritic DCI is comparable to that of annealed low C steel up to 650°C and improvement in creep strength can be achieved by alloying with Mo or Cu. The addition of Mo up to 2 wt.% to high Si (4 wt.%) DCIs raises the rupture strength [2].

2.2 Formation and Growth Kinetics of Fe-Al Intermetallics

Liquid Al is extremely reactive to ferrous alloys. Fe-Al intermetallic compounds form instantly on the surface of ferrous alloys when these are immersed in liquid Al [11-13] and simultaneously the Fe substrate starts to dissolve into the melt. It is crucial to understand the dissolution process of ferrous alloys in order to enhance their resistance against liquid Al corrosion, which further requires an investigation of the chemical composition and growth of the Fe-Al intermetallic compounds. A major portion of the present research is dedicated to the characterization and determination of the growth kinetics of the intermetallic compounds formed during the interaction between cast irons and liquid Al. Therefore, a review of the previous investigations and the basics of Fe-Al interaction are presented in this section.

2.2.1 Fe-Al Binary System

The Fe-Al binary system can be described as an Fe based solid solution and six intermediate non-stoichiometric intermetallic compounds, β_1-Fe_3Al, β_2-FeAl, ζ-$FeAl_2$, ε-Fe_2Al_3, η-Fe_2Al_5 and θ-$FeAl_3$. Figure 2.5 shows the Fe-Al binary phase diagram. Table 2.1 summarizes the crystal structures and compositional stability ranges of the Fe-Al intermetallic compounds,

and a summary of phase transformations of the Fe-Al system is given in Table 2.2. In fact, the Fe-Al binary system is a complex system and because of the lack of reliable experimental evidence, it has various fields of uncertainty, such as α + ε and α + ζ fields [14]. In addition, the disordered (α-Fe) to ordered (β_2-FeAl) transformation is still under investigation [15], and the boundary between α and α + ε relies solely on thermal results [14]. In the Fe-Al phase diagram [16], instead of a liquidus maximum at 1161ºC (θ-$FeAl_3$) and a eutectic $FeAl_3$ (θ) - Fe_2Al_5 (η) at 1159ºC (74 at.% Al), studies [17] suggested a peritectic reaction, η-Fe_2Al_5 + L = θ-$FeAl_3$. The thermal data and microstructural investigations of the alloys with 72.8 at.% Al and 73.7 at.% Al showed peritectic rather than the eutectic structures, which are in favour of the generally accepted version of Fe-Al phase diagram, Figure 2.5 [14, 17-18].

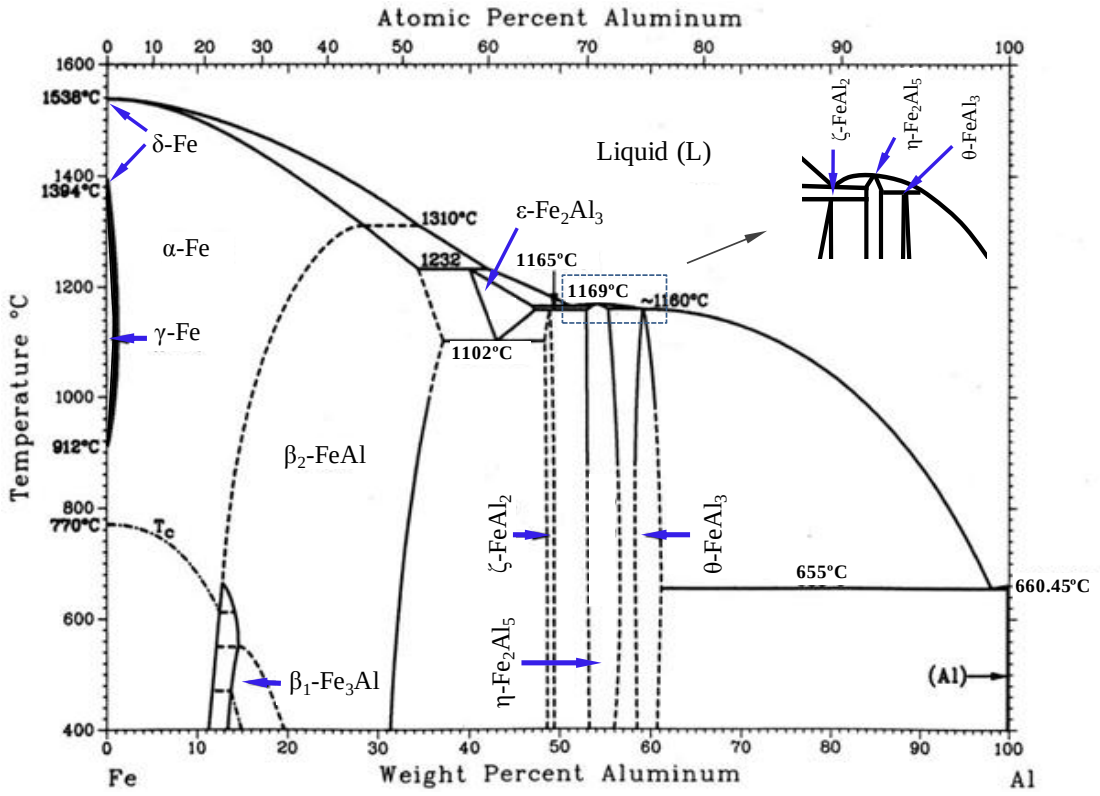

Figure 2.5 - Fe-Al binary phase diagram. [After [16]]

The formation of various Fe-Al compounds is discussed in the following sections.

The maximum solubility of Al in γ-Fe is reported to be in the 2.0-2.4 at.% Al range [19-20]. The existence of γ / (γ+α) and α / (α+γ) boundaries extend up to about 1.2 at.% Al and 2.0

at.% Al respectively, at about 1150°C [21]. In the 0-34 at.% Al range, three solid solution phases; α-Fe, β_2-FeAl and β_1-Fe_3Al were found to exist. Much uncertainty exists as to the equilibrium stability of these phases, despite numerous investigations [14-15, 17-20]. Up to about 18.5 at.% Al, the random atomic distribution of Fe/Al in the BCC lattice α-Fe was found to be independent of the cooling rate [22].

The Fe-Al alloys in the 18.5 to 25 at.% Al range showed a random atomic arrangement after quenching from the temperatures of 600ºC or higher, while slow cooling led to increased ordering of the structure, reaching to 92% at 25 at.% Al. The $D0_3$ lattice of Fe_3Al with twice the lattice constant of α-Fe was found to emerge gradually from the random arrangement of α-Fe. The structural transformation from β_1-Fe_3Al to β_2-FeAl starts between 25-34 at.% Al. Above 34 at.% Al, the structure was found to be β_2-FeAl. It was found that the β_1-Fe_3Al lattice was formed below 600ºC, while the β_2-FeAl remained stable up to 700ºC. No regions of both β_1-Fe_3Al + β_2-FeAl and α-Fe + β_1-Fe_3Al could be found. Therefore, it was concluded that the transition from one type of structure to another occurs in a continuous fashion [23].

Table 2.1 - Crystal structures of intermetallic phases of Fe-Al system [16].

Phase	Crystal structure	Stability range (at.% Al)
γ- Fe	FCC	0-1.3
β_1-Fe_3Al	$D0_3$	23-34
α-Fe	BCC	0 – 28
β_2-FeAl	B2	23-55
ε-Fe_2Al_3	Cubic (complex)	58-65
ζ-$FeAl_2$	Triclinic	66-66.9
η-Fe_2Al_5	Orthorhombic	70-73
θ-$FeAl_3$	Monoclinic	74.5-76.5

Table 2.2- Phase transformation reactions in Fe-Al phase diagram [24].

Phase transformation/reaction type	At.% Al	Temperature, °C
Melting $L \longleftrightarrow \delta\text{-Fe}$	0	1538
Allotropic $\delta\text{-Fe} \longleftrightarrow \gamma\text{-Fe}$	0	1394
Allotropic $\gamma\text{-Fe} \longleftrightarrow \alpha\text{-Fe}$	0	912
Tricritical $\alpha\text{-Fe} \longleftrightarrow \beta_2\text{-FeAl}$	23.9	662
Critical $\beta_2\text{-FeAl} \longleftrightarrow \beta_1\text{-Fe}_3\text{Al}$	26.5	552
Critical $\alpha\text{-Fe} \longleftrightarrow \beta_2\text{-FeAl}$	45	1310
Peritectic $L + \beta_2\text{-FeAl} \longleftrightarrow \varepsilon\text{-Fe}_2\text{Al}_3$	52	1232
Eutectoid $\varepsilon\text{-Fe}_2\text{Al}_3 \longleftrightarrow \beta_2\text{-FeAl} + \zeta\text{-FeAl}_2$	55	1102
Peritectoid $\varepsilon\text{-Fe}_2\text{Al}_3 + \eta\text{-Fe}_2\text{Al}_5 \longleftrightarrow \zeta\text{-FeAl}_2$	66.5	1156
Eutectic $L \longleftrightarrow \varepsilon\text{-Fe}_2\text{Al}_3 + \eta\text{-Fe}_2\text{Al}_5$	70.5	1165
Congruent melting $L \longleftrightarrow \eta\text{-Fe}_2\text{Al}_5$	71	1169
Unknown $L \longleftrightarrow \eta\text{-Fe}_2\text{Al}_5 + \theta\text{-FeAl}_3$	72	1160
Peritectic $L + \eta\text{-Fe}_2\text{Al}_5 \longleftrightarrow \theta\text{-FeAl}_3$	76.6	1159
Eutectic $L \longleftrightarrow FeAl_6$ (metastable) + Al	85.7	653
Eutectic $L \longleftrightarrow \theta\text{-FeAl}_3 + Al$	99.1	655
Melting $L \longleftrightarrow Al$	100	660

Based upon a transition temperature study, the short-range ordered structure of $Fe_{13}Al_3$ (18.75 at.% Al) was also claimed to exist in the 10-24 at.% Al range, and co-exists with β_1-Fe_3Al in Fe-Al alloys with composition greater than 21.4 at.% Al [25].

In the composition range of 54-100 At.% Al, the existence of four distinct Fe-Al intermetallic compounds, ε-Fe_2Al_3, ζ-$FeAl_2$, η-Fe_2Al_5 and θ-$FeAl_3$ is in common agreement. Among these phases the ε-Fe_2Al_3 forms peritectically around 1230ºC and decomposes by eutectoid transformation around 1100º C [14, 18-19]. At 1158ºC, another phase was believed to form

by peritectoid transformation in the composition range of 65-70 at.% Al [14]. This phase was named as ζ, and shown to be formed by $\varepsilon + \eta \rightarrow \zeta$ peritectoid transformation reaction. Owing to the rapid cooling and insufficient annealing, no single phase alloy could be obtained in this range. Later the ζ phase was shown to contain about 65 at.% Al and was consistent with ζ-$FeAl_2$ [24]. The η-Fe_2Al_5 phase forms by congruent melting reaction at about 1169°C and 71 at.% Al. At about 1159°C and 76.6 at.% Al, a peritectic reaction between the melt and η-Fe_2Al_5 produces θ-$FeAl_3$ [14, 17-18].

The existence of θ-$FeAl_3$ as a stable intermetallic compound is widely accepted; however, X-ray studies [18] indicated the decomposition of θ-$FeAl_3$ into η-Fe_2Al_5 and Fe_2Al_7 below 600ºC. The stability range of Fe_2Al_7 was found to be 77.5 to 78.6 at.% Al. The X-ray diffraction (XRD) pattern of Fe_2Al_7 differed only slightly from that of θ-$FeAl_3$. In another investigation [26], there was no difference in the XRD patterns of the alloys containing 76.4-76.8 at.% Al, quenched from 900ºC or subjected to long term anneal at 470ºC. Therefore, it was suggested that the θ-$FeAl_3$ does not decompose into η-Fe_2Al_5 and /or Fe_2Al_7. Additional work may be required to clarify these and other findings. There is also agreement on the existence of the $FeAl_6$ phase [16] (which is known to be metastable) and the ε-Fe_2Al_3 phase exists above 1092°C. These phases are not relevant to the corrosion studies in Al melts. Therefore, the formation of only the five phases, β_1-Fe_3Al, β_2-FeAl, ζ-$FeAl_2$, η-Fe_2Al_5 and θ-$FeAl_3$, is of interest to the present study.

2.2.2 Intermetallic Compounds of Fe-Al Interaction

Several researchers have reported the formation of intermetallic compounds formed by liquid Al interacting with pure Fe and steels [11-13, 27-34]. The formation of all the possible intermetallic compounds shown by the Fe-Al equilibrium phase diagram, Figure 2.5, has been discovered in Fe-liquid/solid Al interaction. However, these studies do not necessarily

agree with one another with regard to the constitution of the intermetallic layers formed. The formation of Fe-Al intermetallic compounds has been studied by two routes:

a) The solid Fe-liquid Al interaction has been studied. In this category, most researchers have found the existence of the two intermetallic compounds, η-Fe_2Al_5 and θ-$FeAl_3$ [11, 27-28, 33, 35].
b) Fe-Al solid state diffusion couples have been studied. The solid Al layer over the steel/Fe is first formed by dipping into liquid Al, then the bi-metal is subjected to annealing. In this type of interaction, in addition to η-Fe_2Al_5 and θ-$FeAl_3$, the formation of β_2-FeAl or Al rich α-Fe has been commonly reported. A few workers have reported finding β_1-Fe_3Al and/or ζ-$FeAl_2$ as well [29, 32].

The η-Fe_2Al_5 compound forms the major portion of the reaction layer, and it is widely accepted that its formation and growth depend on both diffusion and reaction kinetics [36-37], details are in Section 2.2.3.1. The literature on intermetallic compound formation in solid-liquid and solid state Fe-Al couples is described in following sections.

2.2.2.1 Formation of Intermetallics by Solid Fe-Liquid Al Interaction

The phase constitution of the Fe-Al system suggests that, a series of phases with increasing Al contents (α-Fe, β_2-FeAl, ζ-$FeAl_2$, η-Fe_2Al_5 and θ-$FeAl_3$) should form between the Fe substrate and the melt. Nevertheless, as previously mentioned - the existence of only two phases - η-Fe_2Al_5 and θ-$FeAl_3$ - is in common agreement. Figure 2.6 shows an example of the intermetallic layer formed on a DCI specimen after withdrawal from the Al melt. The η-Fe_2Al_5 phase formed the major portion of the intermetallic layer whereas the θ-$FeAl_3$ appears as the minor phase towards the solidified Al. More details on the characterization of the intermetallic compounds can be found in Chapter 4. The predominance of the η-Fe_2Al_5 has been attributed to kinetic factors arising from the defect crystallography of this phase. The

existence of a large fraction (about 30%) of Al vacancies along the c-axis of the orthorhombic unit cells permits high diffusion rates of the reactant species along this axis [38].

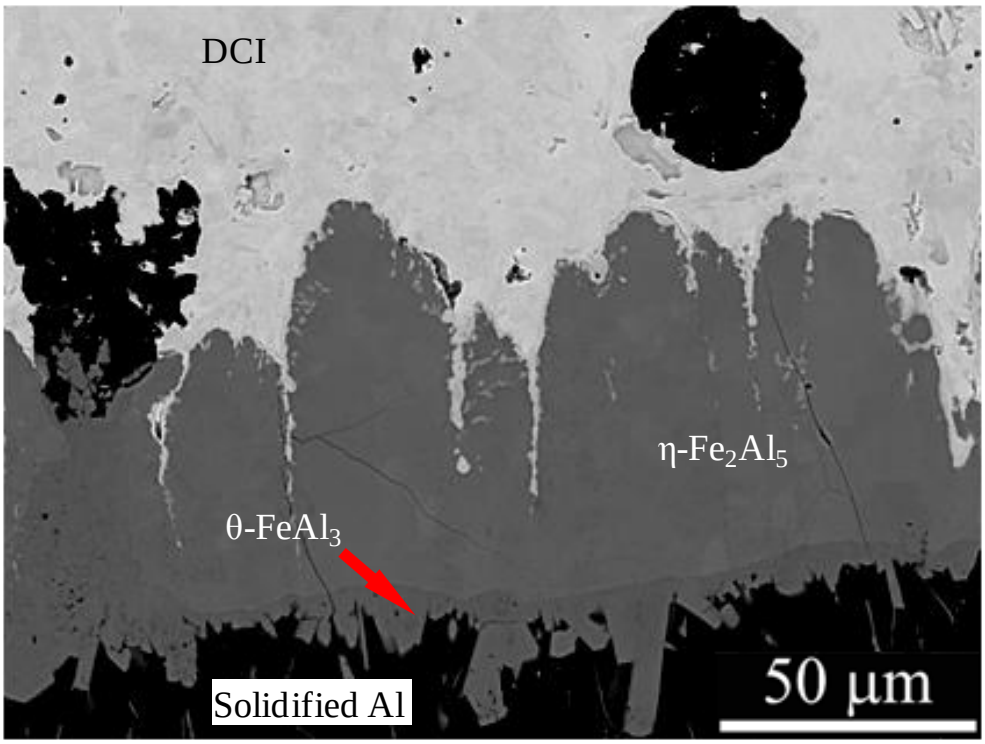

Figure 2.6 - A high contrast BSE image showing the formed η-Fe_2Al_5 and θ-$FeAl_3$ compounds on a DCI substrate.

The θ-$FeAl_3$ phase is always found as a minor phase [11, 13, 27-28] of the intermetallic layer. This suggests that η-Fe_2Al_5 may grow at a greater rate than θ-$FeAl_3$. The limited growth of θ-$FeAl_3$ is particularly surprising on thermodynamic grounds, since it appears the most energetically favoured of all the intermetallic compounds of the Fe-Al system because the Gibbs free energy of formation (ΔG_f) of this compound is more negative than the other Fe-Al compounds at 850°C, Table 2.3. Thus there is a possibility that θ-$FeAl_3$ may be growing at a higher rate but, simultaneously, it may be dissolving and/or spalling into the melt.

Table 2.3 Gibbs free energy of the formation of various Fe-Al compounds at 850°C [39].

Phase	Free energy of formation $\Delta G_{850°C}$ (J mol^{-1})
β_1-Fe_3Al	34269
β_2-FeAl	- 48747
ζ-$FeAl_2$	- 69108
η-Fe_2Al_5	- 95707
θ-$FeAl_3$	- 102980

Jones and Denner [40] suggested that the formation of θ-$FeAl_3$ as a reaction product at the η-Fe_2Al_5 surface is difficult to establish. This conclusion was put forward because Al dissolves about 2.5 at.% Fe at 700°C. Cooling to 655ºC (eutectic) initiates the separation of θ-$FeAl_3$ at approximately at 1 at.% Fe, then it may grow on the η-Fe_2Al_5 surface or within the melt solidifying at the outer surface of the intermetallic layer. Furthermore, a mechanism to account for the absence or limited growth of the θ-$FeAl_3$ phase was proposed, which involves the stresses generated from the growth of this phase. These growth stresses within the layer prevent further compound formation and then the formation and spallation of θ-$FeAl_3$ repeatedly occurs. The same authors [41] also observed the θ-$FeAl_3$ layer for interaction times of less than 15s and revealed inclusions of θ-$FeAl_3$ particles within the η-Fe_2Al_5 phase layer. So there is a basis for hypothesizing that these two intermetallics can form and grow simultaneously. The absence of the θ-$FeAl_3$ layer at longer immersion times was reported and attributed to its dissolution and rapid conversion to η-Fe_2Al_5 [41]. These authors described the both type of possibilities of formation of θ-$FeAl_3$. However, it remains unclear that these particles grow during ongoing Fe-liquid Al interaction and/or during solidification of Al around the sample.

In the literature, there is uncertainty as to the identification of the particles found in the outer solidified Al. Some studies [42-43] claimed θ-$FeAl_3$, while another [27] suggested these

phases were of several compositions such as η-Fe_2Al_5, ζ-$FeAl_2$ and θ-$FeAl_3$. It is to be noted that these particles were identified on the basis of EDS, no precise characterization was made.

In 1994, Richards *et al.* [13] published an extensive review on the metallurgy of hot dip aluminizing that included a number of previous reports on the formation of intermetallic compounds by Fe-Al interaction. Therefore, only a few of the latest investigations are discussed here.

Bouche *et al.* [28] studied the interaction between Armco Fe (99.78 wt.%) and high purity liquid Al in the temperature range of 700°C-800°C. EDS analysis indicated the presence of η-Fe_2Al_5 (adjacent to Fe) and θ-$FeAl_3$ adjacent to Al. XRD patterns were consistently indexed as orthorhombic structure of η-Fe_2Al_5 (a = 0.7675 nm, b = 0.6403 nm, c = 0.4203 nm) and a monoclinic structure of θ-$FeAl_3$ (a = 1.5489 nm, b = 0.8083 nm, c = 1.2476 nm). To evaluate the Fe/Al interdiffusion coefficients, these authors [28] assumed that that θ-$FeAl_3$ layer adjacent to η-Fe_2Al_5 grows during ongoing liquid Al corrosion and the θ-$FeAl_3$ particles grow during solidification. However, it is difficult to consider and analyse the θ-$FeAl_3$ intermetallic layer separately to the θ-$FeAl_3$ particles, Figure 2.6 shows an example.

Bouayad *et al.* [27] also found the existence of only two intermetallic compounds (η-Fe_2Al_5 and θ-$FeAl_3$) formed during the interaction of solid Fe and liquid Al in the temperature range of 700°C-800°C. The origin of the columnar morphology of η-Fe_2Al_5, similar to that shown in, Figure 2.6 remains unexplained, although, the anisotropic diffusion owing to the high vacancy concentration along the c-axis of the η-Fe_2Al_5 structure [38] could be a possible explanation.

Shahverdi *et al.* [11] studied the interaction between pure Fe and liquid Al maintained at 800°C. Rectangular coupons, 60 mm x 20 mm x 17 mm, were ground and polished using 0.5 μm diamond paste and immersed into liquid Al for 90-3000s. By using EDS and XRD, the

intermetallic compounds were identified as η-Fe_2Al_5 (about 200 μm thick) and θ-$FeAl_3$ with the latter being the minor phase (10 μm thick). The microhardness (H_v) of η-Fe_2Al_5 was found to be in the range of 700-800, whereas θ-$FeAl_3$ exhibited relatively higher hardness with a value of 900-1000 H_v. The solidified Al layer was found to contain needle shaped particles, which were not identified and it was suggested that these may have resulted from the mixing of Fe within the melt. Furthermore, owing to the higher hardness of the θ-$FeAl_3$ phase it was suggested that cracking of this layer is easier than the η-Fe_2Al_5 owing to the stresses generated during the intermetallic reaction. It was further suggested that it is possible to miss the existence of θ-$FeAl_3$ because of the following:

a) The small quantity of θ-$FeAl_3$ owing to its slower growth than the η-Fe_2Al_5
b) the similarity between the XRD patterns of η-Fe_2Al_5 and θ-$FeAl_3$
c) the spalling, subsequent remelting and dissolution of θ-$FeAl_3$.

Shih and Tu [34] performed hot dipping experiments using 1020 (0.2 wt.% C) and 1040 (0.4 wt.% C) steel bars (d = 16 mm and l = 50 mm) that were immersed into commercial purity Al and Al-7 wt.% Si alloy melts at 700°C for time periods varying between 3-60 minutes. They apparently found only the η-Fe_2Al_5 phase because nothing was mentioned about the θ-$FeAl_3$ phase. The η-Fe_2Al_5 intermetallic layer morphology of 1040 steel was found to grow over time from a columnar structure to a planner interlayer and finally become ragged following the increased dipping time in pure Al melt. The columnar morphology was found to be much more apparent for the 1020 steel than for the 1040 steel.

In comparison with the pure Al melt, the reactive layer in Al-7 wt.% Si alloy melt was found to be thinner, which was attributed to the presence of Si in the reaction layer leading to the slower interdiffusion rates of Fe and Al atoms. However, the dissolution of the intermetallic layer was not considered. C diffusion to the ferrite boundaries and to the interface between

the steel surface and the intermetallic phase was also reported, which suggested the enrichment of C along the growing projections of η-Fe_2Al_5. Moreover, the C entrapped in the η-Fe_2Al_5 layer in the form of so-called "white spots" was believed to contain aluminium carbide (Al_4C_3) particles [34]. Before the report of [34], in high carbon steels a thin C enrichment zone has also been suggested to form ahead of the η-Fe_2Al_5 projections [44]. However, owing to the lack of experimental verification, Richards *et al.* [13] disregarded the formation of such a zone and suggested this as the α-Fe solid solution. Research needs to address the confirmation of such a zone if it forms under some specific material and liquid Al exposure conditions.

Shih and Tu [34] also suggested an oxide film based mechanism to account for the columnar structure of η-Fe_2Al_5. When a ferrous alloy comes into contact with liquid Al, the air trapped in the surface notches would react with liquid Al to form Al_2O_3, then the oxide particles form and/or the oxide film fractures, which provide specific sites for nucleation and subsequent growth of η-Fe_2Al_5. The columnar (η-Fe_2Al_5) growth proceeds preferentially in a direction perpendicular to the steel substrate and also towards the parallel sides, afterwards the side growth stops due to the impingement of side walls of growing columns [34].

Niinomi and Ueda [12] published the results of their study on several ferrous alloys including pure Fe, Fe-C, Fe-Si, Fe-Mn, Fe-Ni, Fe-Cu and Fe-Cr, the alloying contents in these materials were 2 wt.% and 3 wt.%. These alloys were dipped into liquid Al at 700°C, 750°C and 800°C for various time periods. Irrespective of the chemical composition of the alloys under investigation, only the two phases, η-Fe_2Al_5 and θ-$FeAl_3$ were found in the reaction layers. Cementite was found to remain in the intermetallic layer of Fe-3 wt.% C alloy formed at 700°C; however, it was not observed at 750°C and 850°C. The presence of cementite was not observed on Fe-2 wt.% C alloy intermetallic layer at any temperature. In Fe-3 wt.% Si alloy,

the Si enrichment at the interface of the substrate/intermetallic layer was found; however, the existence of any Fe-Al-Si compound was not clarified. Moreover, an Al-rich α-Fe was found to exist between the Fe-substrate and projections of η-Fe_2Al_5 phase in most of the ferrous alloys except the Fe-C and Fe-Cu combinations. These alloying elements are commonly (Si, C, Mn, Cu, Cr and Mo) added to cast irons, it would be interesting to know their effect on compound formation and liquid Al corrosion mechanisms.

In a recent (2010) publication, Balloy *et al.* [45] presented the results of a study on intermetallic compound formation by the interaction of GCIs and steel with saturated (4 wt.% Fe) liquid Al melt. Two GCIs, one ferritic (3.5 wt.% C, 4.50 wt.% Si, 0.22 wt.% Mn), the other pearlitic (3.7 wt.% C, 1.76 wt.% Si, 0.68 wt.% Mn, 1.1 wt.% Cr, 1.9 wt.% Al, 0.37 wt.% P) and AISI 1030 steel (0.37 wt.% C) were immersed into Al melt at 690°C for time periods of 2, 8 and 72 hours. After 72 hours of interaction, in addition to η-Fe_2Al_5 and θ-$FeAl_3$, the steel substrate was found to form a solid solution with Al (α-Fe) and a layer composed of ζ-$FeAl_2$. These results were based upon the EDS analysis of the intermetallic layers, no precise confirmation was made. In addition, the precipitation of needle shape particles (a few microns long) was also found towards the steel substrate. These particles were not characterized but were suggested to be graphite or Al_4C_3. In cast irons specimens, Si enrichment was found between the cast iron substrate and η-Fe_2Al_5 projections. However, no ζ-$FeAl_2$ phase layer was detected in the case of cast irons.

Komatsu *et al.*[30] studied the effect of Si on the intermetallic layer composition by subjecting various alloys to pure Al and Al-Fe-Si alloy melts in the 700°C-770°C temperature range. When Si was added to Fe or liquid Al, two intermetallic layers were always present in the reaction zone: The one closest to the Fe matrix was composed of η-Fe_2Al_5 and the other

closest to Al was composed of a mixture of θ-$FeAl_3$ and Al. The solubility of Si in the columnar layer (η-Fe_2Al_5) was determined to be 2-3 wt.% by EDS.

2.2.2.2 Intermetallic Compounds in Solid Fe-Al Couples Subjected to Annealing

Cheng *et al.* [46] investigated the intermetallic compounds formed on commercial steel with composition 0.14 C, 0.48 Si, 0.34 Mn, 5.25 Cr and 0.55 Mo (in wt.%). Rectangular specimens of the dimensions 20 mm x 8 mm x 1 mm were aluminized in a molten Al bath at 700°C for 180s. After the hot dip treatment, the specimens were exposed to a temperature of 750°C for times varying between 8 minutes to 72 hours. After 15 minutes of diffusion treatment, the θ-$FeAl_3$ phase and solidified Al layer disappeared and only the single phase η-Fe_2Al_5 was found. After 1 hour interaction, two new phases, ζ-$FeAl_2$ and β_2-FeAl were found between η-Fe_2Al_5 and the steel substrate. Only the β_2-FeAl and ζ-$FeAl_2$ phases were found after 72 hours of diffusion. It was found difficult to clearly characterize the β_2-FeAl phase with EBSD because of the similar body centred structures of β_2-FeAl and α-Fe. However, EDS revealed a uniform layer of similar composition of β_2-FeAl phase. From the Fe-Al binary phase diagram, at 750ºC the solubility of Fe in Al and Al in Fe is about 2 at.% and 24 at.%, respectively. On the basis of this fact, it was suggested that the precipitation of Fe-Al intermetallic compounds is easier on the Al-rich side than the Fe-rich side [46].

Kobayashi and Yakou [29] published their research on aluminized specimens of structural steel (0.44 C, 0.21 Si and 0.82 Mn, in wt.%). The steel specimens were aluminized in commercial grade Al (99.7 wt.% Al) maintained at 700°C-900°C. Afterwards, the aluminized specimens were subjected to diffusion treatments at the temperatures of 600°C, 800°C, 1000°C and 1100°C for 20-60 minutes. The reaction products were analyzed using XRD. The coating layers of all the aluminized specimens exhibited only the two phases, η-Fe_2Al_5 and θ-$FeAl_3$. For diffusion temperatures lower than 1000°C, a single phase (η-Fe_2Al_5) intermetallic

layer was found, while the Fe rich intermetallic compounds β_2-FeAl and β_1-Fe_3Al were found to evolve at temperatures higher than 1000°C.

Murakami *et al.* [32] developed a new method of aluminizing the surface of iron and steel utilizing a powder liquid coating method. Discs of high purity Fe (99.9 wt.%) were used as specimens. A paste of Al and Ti powders mixed with ethylene glycol was applied to the specimens. Subsequently these were dried at 200°C for 1 hour. Afterwards, the specimens were annealed at 900°C and 1000°C under a vacuum of 1.3×10^{-3} Pa. XRD, EDS and Auger electron spectrometry (AES) were used to characterize the intermetallic compounds. Two types of heat treatments were applied. In both type of heat treatments, the specimens were heated at a rate of 1.33°C/s. In the first type, immediately after attaining the set temperature the specimens were quenched in nitrogen gas flow. In the second type, before quenching, the specimens were isothermally annealed at a fixed temperature for predetermined times. In the specimens of first type of treatment, η-Fe_2Al_5 was found to be the major phase of the intermetallic layer. No clear ζ-$FeAl_2$ layer was formed in the specimen quenched from 900°C, whereas a 10 μm thick layer of ζ-$FeAl_2$ was observed by EDS in the specimens quenched from 1000°C. In the isothermally annealed specimens at 1000°C for 1080s, the η-Fe_2Al_5 and ζ-$FeAl_2$ compound layers were no longer apparent, and the entire layer consisted of α-Fe. This phase was suggested as α-Fe instead of β_2-FeAl, which was attributed to the broad solid solubility of Al in α-Fe, therefore, all the Al at the surface can be involved in the α-Fe phase.

From these studies it is clear that that when there is not enough Al to form η-Fe_2Al_5 or θ-$FeAl_3$, the formation of Fe-rich phases overrides the strong growth kinetics of the former phases. In other words, the Fe rich phases grow at a slower rate than η-Fe_2Al_5. As a general consideration, with the ongoing interaction of Fe-Al, the Al in the outer layer gets consumed with time and in the shortage of Al the Fe-rich Fe-Al compounds tend to grow.

Maitra and Gupta [31] studied the pure Fe and a high purity Al-Si melt interaction in the temperature range of 600°C-900°C. η-Fe_2Al_5 was the only intermetallic phase at 600°C, but the β_2-FeAl and η-Fe_2Al_5 phases were observed at 800°C. The solubility of Si was found to be small in the 1-7 at.% range in θ-$FeAl_3$, η-Fe_2Al_5 and θ-$FeAl_3$, but relatively high (17 at.%) in the β_2-FeAl phase.

2.2.3 Growth Kinetics of Fe-Al Intermetallic Compounds

The growth of intermetallic compound layers that initially evolve by subjecting the ferrous alloys to liquid Al depends upon several factors, such as melt temperature and composition, time of interaction, and constitution of the Fe substrate [27-28, 33, 47]. The control of intermetallic layers is considered important in many manufacturing processes such as diffusion bonding, hot dip aluminizing and Fe-Al composites. Therefore, the growth kinetics of intermetallic compounds in Fe-Al systems has been extensively studied for improving the interfacial strength between ferrous substrates and Al [13, 32, 48]. The intermetallic layer growth kinetics are also important to understand the process of dissolution of ferrous alloys into liquid Al melts [37]. However, there are very few systematic studies that considered the dissolution while investigating the Fe-Al intermetallic layer growth kinetics. The literature presented in this section will provide some insight into the kinetics of intermetallic layer growth in solid Fe-liquid Al systems.

2.2.3.1 Reaction-Diffusion Mechanism of Compound Formation

When ferrous substrates are subjected to liquid Al, the alloy layer formation occurs by a mechanism known as reaction-diffusion. As the name implies, it is a mechanism of compound formation governed principally by a combination of reaction and diffusion within the solid product or intermetallic compound. Many excellent textbooks are available detailing the theory of diffusion. Nevertheless, there are only a few theoretical descriptions [36-37] of solid-solid and solid-liquid interaction phenomena, especially where the formation of

intermetallic compounds is involved. In bi-metal systems, the term reaction-diffusion [36] implies that the intermetallic compound formation progresses by the two processes:

a) Diffusion of the atoms of the two components in opposite directions across the intermetallic compound.

b) Chemical reaction taking place at the compound/substrate interfaces with the involvement of the diffusing atoms of one component and the surface atoms of the other component.

Figure 2.7 shows a schematic of the compound formation between two pure solids A and B.

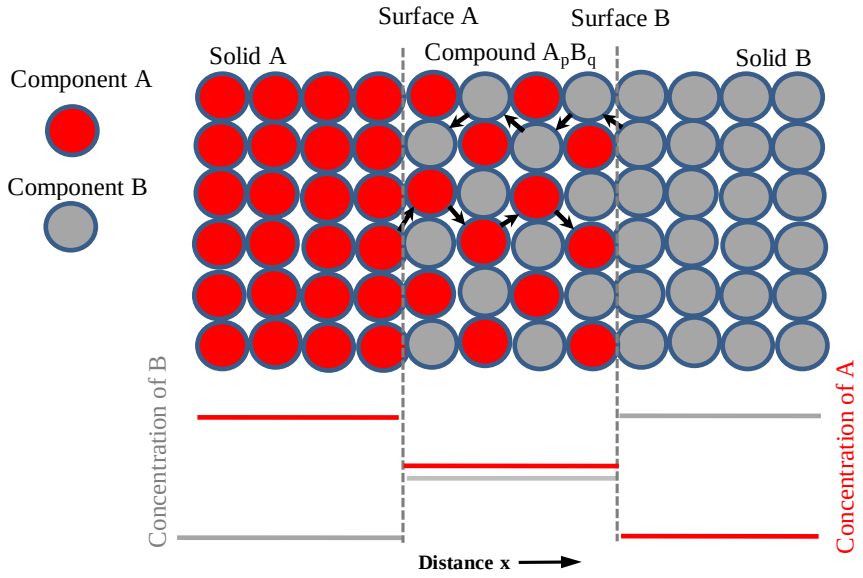

Figure 2.7 - A schematic of the reaction-diffusion mechanism of compound formation between two solids. [After [36]]

In the initial period of interaction between two substances, when there is no compound layer, the two substances can react directly at a common interface. This stage includes the nucleation of the compound A_pB_q at the A-B interface. In Fe-liquid Al systems, the initial layer thickness was found to be small, and it forms in less than a minute - a small fraction of the total interaction time. However, in this time period the growth kinetics were found to be fast as compared to the subsequent time period of interaction [36]. In the initial time period the supply of A and B atoms at the respective surfaces Surface-B and Surface-A is almost

instantaneous because of the short diffusion paths. This regime is known as a kinetic regime in which the compound grows at the highest possible rate under the given conditions, also known as reaction controlled growth.

At longer interaction times, the compound growth is diffusion controlled; indeed the growing layer continuously complicates the supply of atoms at the respective surfaces. Therefore, with the passage of time, the total rate of formation of the intermetallic layer becomes more and more dependent on diffusion, whereas the effect of the rate of chemical transformations gradually decreases and becomes insignificant. Considering the compound layer formation due to the diffusion of atoms of solid A and solid B, a generalized relationship was derived by [36]:

$$x^2 = 2\, k_1 t \qquad (2.2)$$

where k_1 is the diffusional constant of A and B atoms in A_pB_q

More commonly [13, 29, 33] diffusion controlled growth is represented by a parabolic rate equation of the form:

$$x^2 = k\, t \qquad (2.3)$$

where k is the growth rate constant having units m^2s^{-1}.

or

$$x = k' t^{1/2} \qquad (2.4)$$

where $k' = k^{1/2}$.

In solid bi-metal couples, the applicability of the parabolic growth is well established [29, 36]. However, in solid-liquid systems [33, 47], intermetallic layer growth showed deviations from the parabolic law of compound growth.

2.2.3.2 Intermetallic Layer Growth in Fe-Liquid Al Systems

Sasaki *et al.*[33] performed immersion tests on three types of steels, C05 (0.05 wt.% C), C45 (0.45 wt.% C) and C88 (0.88 wt.% C). Rectangular specimens measuring 50 mm x 25 mm x 2 mm were immersed in liquid Al maintained at 700°C, 750°C, 800°C and 850°C for various times. Figure 2.8 shows the intermetallic layer thickness versus square root of time plots.

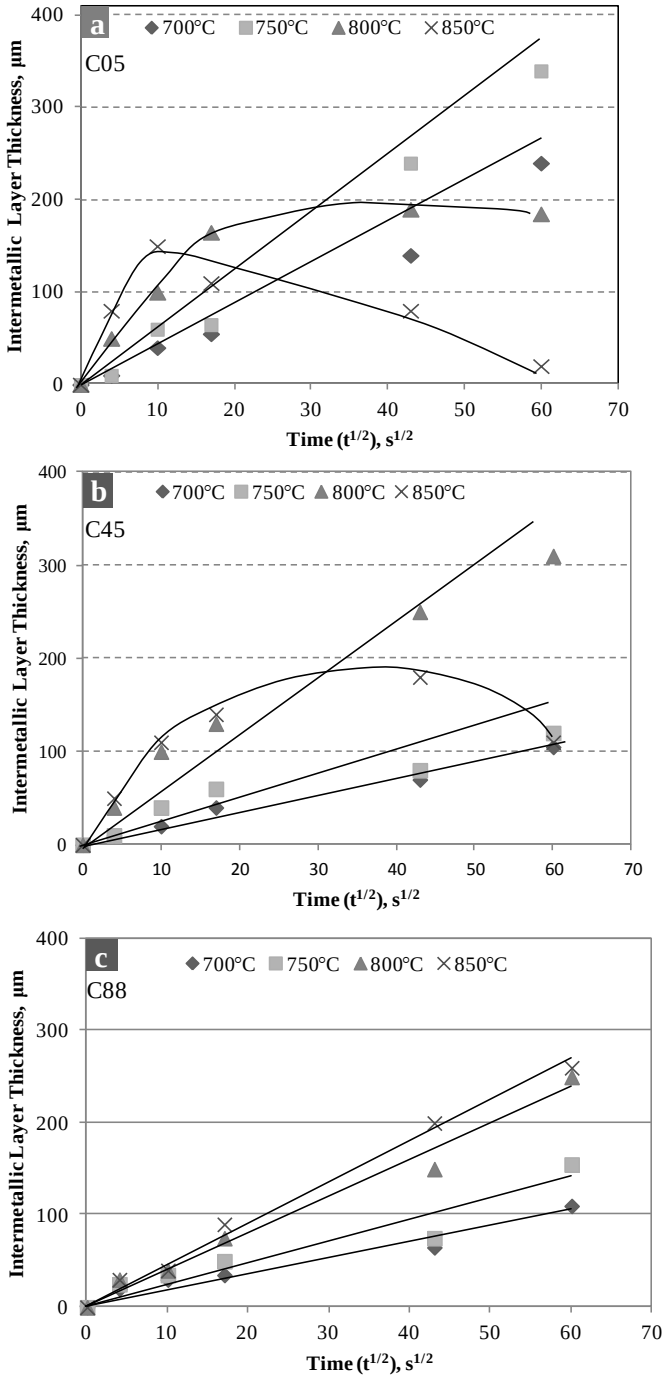

Figure 2.8 - Intermetallic layer thickness versus square root of immersion time at 700°C, 750°C, 800°C and 850°C, a) C05 steel, b) C45 steel, c) C88 steel. [After [33]]

In the case of the C05 steel, the alloy layer thickness at temperatures lower than 800°C increased linearly with increasing time ($t^{1/2}$). However, at temperatures of 800°C or higher the intermetallic layer thickness showed a maxima and then decreased with increasing $t^{1/2}$. This tendency, wherein intermetallic layer thickness decreases, was most remarkable at 850°C. The C88 steel, behaved differently from the steels with lower carbon contents: at all the temperatures the intermetallic growth followed a parabolic relationship. It was conjectured that the dissolution of all the steels occurs at a higher rate when the temperature is raised, which could lead to the thinning of the intermetallic layer; however, no dissolution analysis was made. The reasons behind the consistent increase in intermetallic thickness with the rise in temperature of the high carbon steel (C88) were not analyzed in Sasaki *et al.*'s work.

Bouche *et al.* [28] investigated the growth kinetics of intermetallic layers on pure Fe specimens immersed into the liquid Al at 700°C, 800°C and 900°C. The electrolytically polished rectangular specimens, 35 mm x 5 mm x 3 mm, were immersed into liquid Al for various time periods between 30s to 45 minutes. The growth of intermetallic layers was measured from the initial solid (Fe-substrate)-liquid boundary. Depending upon the immersion time, different behaviours of intermetallic growth were observed. For 30s, the solid-liquid boundary moved towards liquid at all temperatures. For longer immersion time (900s), there was an increase in thickness at 700°C and loss of thickness at higher temperatures (800°C and 900°C). In the case of movement of solid-liquid boundary towards solid, Bouche *et al.* [28] concluded that dissolution has mainly taken place and on the contrary a growth towards liquid shows the predominance of the growth. Based upon these observations, it was suggested that more than one mechanism was involved during the solid-liquid interaction. However, no further details were found on the effect of dissolution on the intermetallic layer growth.

Shahverdi *et al.* [47] performed a series of experiments to investigate the kinetics of intermetallic layer growth in solid Fe and liquid Al couple. Rectangular, 60 mm x 20 mm x 1.7 mm, Fe coupons (0.1 wt.% C, 0.34 wt.% Mn, 0.1 wt.% Si) were immersed into liquid Al at 700°C, 800°C and 900°C for various time periods. At 700°C and 800°C, the thickness of the intermetallic layer increased monotonically with immersion time. However, in the case of 900°C the thickness of the intermetallic layer reached a maximum at about 400s and decreased afterwards.

After dipping tests, the total dimensions of each specimen were also noted; it was found that for 700°C and 800°C specimen thickness including the intermetallic layer increased up to 1500s and 750s, respectively. At 900°C, the initial thickness of the Fe coupon decreased continuously from 185s and at 3000s, the Fe specimen was completely dissolved into liquid Al. They [47] suggested that the dissolution of Fe specimens was started at about 1500s, 750s and 185s for 700, 800 and 950°C respectively. To demonstrate the effect of dissolution on the parabolic growth, two types of trend lines showing the intermetallic layer growth were plotted; Figure 2.9 shows an example at 800°C.

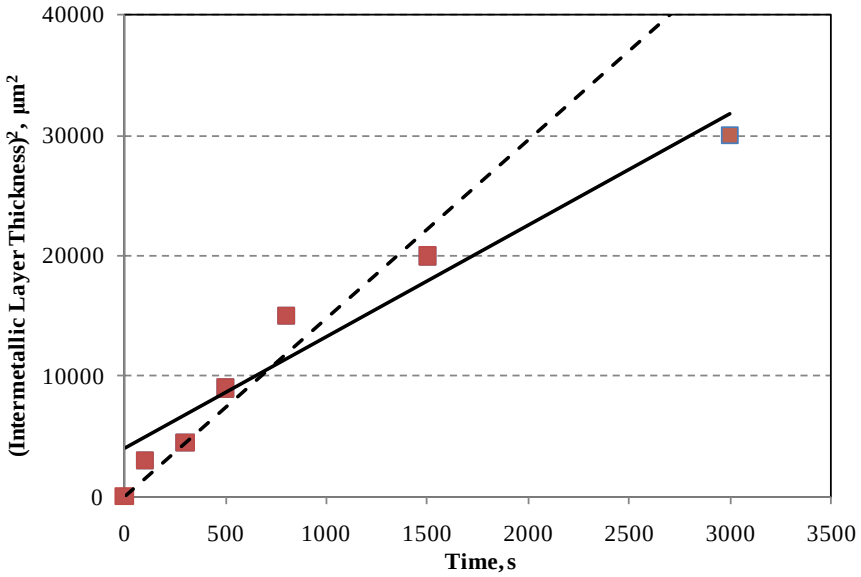

Figure 2.9 - Square of intermetallic thickness plotted against time for 800ºC. [After [47]]

The solid line (Figure 2.9) presents the intermetallic layer growth without passing through the origin and broken lines were drawn through the origin in order to identify dominance of growth and dissolution with increasing interaction time. In agreement with Bouche *et al.* [28], dissolution of the intermetallic layer was suggested [47] to be responsible for the negative deviations from the parabolic growth. Moreover, it was postulated that with increasing time, the sequence of the processes controlling the intermetallic layer thickness can be summarized as:

Reaction ⟶ Diffusion ⟶ Diffusion + Dissolution ⟶ Dissolution

In the literature described in this section, the negative deviations to the parabolic growth of intermetallic layer were frequently attributed to the dissolution. However, no detailed dissolution analyses were made to quantify the amount of dissolution occurring at each stage of the reaction. As dissolution can be a combination of spallation and/or dissolution of the intermetallic layer, and the direct diffusion of Fe to the melt owing to the existence of a concentration gradient between the intermetallic layer and liquid Al. Thus it is not clear what causes the negative deviations in the growth of intermetallic layer with time. Moreover, when the formation of η-Fe_2Al_5 occurs, the Fe atoms are displaced by Al diffusion and Fe diffuses towards the melt. Since η-Fe_2Al_5 has significantly lower density (4100 Kg/m^3) than Fe-substrates (about 7800 Kg/m^3), due to the increase in volume by the formation of η-Fe_2Al_5, this compound should grow in both directions. However, the simultaneous dissolution/spallation of η-Fe_2Al_5 may limit its growth towards the melt. Even if the specimens showed an increase in size (including the intermetallic layer) after interaction, it does not necessarily mean that the dissolution and/or spalling of the intermetallic layer into liquid Al had not occurred.

2.2.3.3 Effect of Alloying Elements on the Growth of the Intermetallic Layer

The present research is focused upon the minimization of liquid Al corrosion by modifying the substrate composition of cast iron and steel alloys. Si and C are the major constituents of the cast irons. Therefore, it is crucial to understand the effect of these alloying elements on the properties of the intermetallic layer. Moreover, the other alloying additions such as Mn, Cu, Cr and Mo could also influence the formed intermetallic layer. However, there are very limited reports on the intermetallic layer growth that focused on the mechanism or the effect of adding Si (or other alloying elements) to Fe substrates. These investigations are discussed in the following sections.

The presence of alloying elements in liquid Al and substrate materials was found to affect the growth of the intermetallic layer. Most of the studies are related to the addition of alloying elements to liquid Al because of their potential application in hot dip aluminizing. In aluminizing, an efficient control of the intermetallic layer thickness is required, since a very thick intermetallic layer leads to cracking and delamination of the Al coating upon subsequent fabrication [13]. An extensive review of the effect of liquid Al alloying additions on the intermetallic layer thickness has been described in [42]. Of various alloying elements, Si is the most important element added to liquid Al because it strongly reduces the intermetallic layer thickness. However, little is known about the mechanism by which Si reduces the intermetallic layer thickness, and the available literature contains controversial reports.

Komatsu *et al.* [30] performed a series of experiments to determine the effect of Si present in the ferrous substrate and in the Al melts. Various ferrous alloys having different Si and C contents were immersed in pure liquid Al and Al-12.4 wt.% Si alloy melt in the 700°C-770°C range. Table 2.4 shows the chemical compositions of the ferrous alloys.

Table 2.4 - Chemical compositions of the ferrous alloys [30].

Ferrous alloys	C	Si	Mn	*
Low carbon steel (S15C)	0.16	0.24	0.48	
Medium carbon steel (S40C)	0.39	0.25	--	
High carbon steel (SK3)	1.09	0.35	0.38	
GCI	3.47	2.23	0.54	
Fe-1%Si alloy	--	0.95	--	
Fe-3%Si alloy	--	2.94	--	
Fe-5%Si alloy	--	4.84	--	
Fe-8%Si alloy	--	8.10	--	

*Balance Fe

When the Fe-Si alloys were tested in pure liquid Al at 770°C for 2 hours, the intermetallic layer thickness exhibited a sharp decrease from 1-3 wt.% Si. Material loss was increased by approximately 15 percent for 1 and 3 wt.% Si additions. The cast iron specimens were immersed into pure liquid Al and Al-12.4 wt.% Si alloy melts for 4 hours at 770°C. The presence of Si (12.4 wt.%) in the Al melt decreased the intermetallic layer thickness, concurrently, the dissolution of the cast iron substrate was found to increase significantly. The carbon steels also showed similar trends to those of the GCI. On the basis of these results, Komatsu *et al.* suggested that Si in liquid Al did not inhibit the growth of a reaction layer, but accelerated its dissolution into liquid Al [30].

Eggeler *et al.* [49] also investigated the effect of Si addition to Al melts. A low alloyed steel (0.16 wt.% C, 0.34 wt.% Si, 0.51 wt.% Mn, 0.97 wt.% Cr, 0.45 wt.% Mo) was immersed into pure Al melt and Al-2 wt.% Si melt at 780°C and 792°C, respectively. The alloy layer growth was measured for immersion periods up to about 900s. Steel in pure Al melt exhibited parabolic growth, whereas in Al-2 wt.% Si melt intermetallic layer was significantly thinner than the former and showed no significant change with increasing exposure time.

The weight loss measurements were also made in both the cases of pure Al and Al-2 wt.% Si melt by determining the Fe concentration in the melt using a chemical titration method. It was

found that the Fe enrichment remained the same in both cases. From these results, it was suggested that the Si acts on the solid state side to reduce the alloy layer thickness. This supports the suggestion of Nicholls [50] that Si changes the diffusion conditions by occupying the structural vacancies of the η-Fe_2Al_5 phase resulting in a slower growth rate. Eggeler *et al.* [49] dismissed the conclusion of Komatsu and co-workers [30]] that Si accelerates the rate of Fe enrichment in Al melt. However, Komatsu and co-workers [30] measured the weight loss and intermetallic layer thickness for longer times (2-8 hours), whereas Eggeler *et al.* studied them for only 15 minutes considering the practical aluminizing conditions accompanied by the indirect measurement of weight loss of the steel substrate. Moreover, the Si content in the melt used by Komatsu *et al.* was substantially higher than that used by Eggeler and co-workers. The effects of Si may be dissimilar for different Si concentrations and exposure times. Thus it remains controversial that how Si affects the intermetallic layer thickness and dissolution. These authors [30, 49] suggested two types of possible effects of Si. However, the mechanisms explaining the effects of Si on the intermetallic layer growth and/or dissolution of Fe-substrates remain unclear.

Niinomi and Ueda [12] studied the alloy layer growth of several ferrous alloys including pure Fe, Fe-C, Fe-Si, Fe-Mn, Fe-Ni, Fe-Cu and Fe-Cr, with alloying element contents in these materials varying from 2 wt.% and 3 wt.%. The alloys were dipped into liquid Al at 700°C, 750°C and 800°C for various times. The addition of each alloying element (C, Si, Cu, Ni, Mn and Cr) to Fe substrate was found to reduce the thickness of the intermetallic layers compared to pure Fe. Si, Ni and Cu had the greatest effect. However, the mechanism by which these alloying elements affect the thickness of intermetallic layer remains unexplained.

Hwang *et al.* [51] studied the corrosion kinetics of three steels designated as SM20C, SM45C and STC3 (Table 2.5). Pure Al and an Al alloy containing 9.08 wt.% Si and 0.98 wt.% Fe

were used as corrosion media, and the melt temperatures were maintained at 660ºC. Disc shaped specimens were immersed into the Al-Fe-Si alloy melt and subsequently rotated at either 16 or 26 rpm.

The material loss and intermetallic layer thickness were found to decrease with the increase in C content in the steel substrate, which suggests that dissolution and the growth of the compound layer are interdependent. The interface between the compound layer and steel substrate was found to become smoother with increasing C content of the steel.

Table 2.5 - Chemical compositions of steels compared for dissolution and intermetallic layer growth in liquid Al [51].

Steel type	C	Si	Mn	P	S	*
SM20C	0.2021	0.21	0.53	0.17	0.026	
SM45C	0.456	0.22	0.73	0.013	0.049	
STC3	1.103	0.16	0.36	0.008	0.002	

*Balance Fe

As described before, the Si addition to the Al melt is well known to retard the growth of the intermetallic layer. To clarify the effect of C alone, the hot dipping experiments in a molten commercially pure Al were also carried out. For all steels, the intermetallic layer in the case of pure liquid Al was found to be much thicker than that of the Al-Fe-Si melt. Since Si present in the melt reduces the intermetallic layer thickness, C present in the steel was also postulated to have a similar effect. Unfortunately, Hwang and co-workers were unable to clarify the mechanism by which the C or Si reduces the intermetallic layer thickness.

2.3 Dissolution of Ferrous Alloys in Al Melts

The flow of molten metal in industrial applications has a strong accelerating effect on the corrosion of metals into metallic melts. Therefore, the dissolution of solid metals into metallic melts has been extensively studied. In the literature, numerous solid-liquid systems

including ferrous materials and liquid Al have been studied in static as well as forced flow melt conditions. Most of the research has been dedicated to establishing the relationships between the dissolution kinetics and hydrodynamic flow conditions. Nevertheless, there is a lack of literature on comparing or enhancing the corrosion resistance against liquid Al by modifying the substrate composition. This section starts with a brief overview of the hydrodynamics involved in the dissolution of solids into liquids that were studied at the initial stage of this project for the development of experimental methodologies. Finally, the available literature on the dissolution of cast irons and steels into liquid Al is discussed.

2.3.1 Dissolution and Hydrodynamics

The dissolution studies of solids into liquids are most common in the pharmaceutical literature because dissolution plays an important role in drug release from tablets. At the initial stages of research, the dissolution of solids in liquids was generally described using a stagnant diffusion layer model. With the passage of time, various modifications to dissolution theories were made and several dissolution test devices were studied to relate the dissolution of solids to the hydrodynamic flow conditions [52-53].

According to the theories of Shchukarev in 1891 and Nernst in 1905, it was assumed that under steady state conditions a thin layer of liquid at the surface of the dissolving surface exists where the liquid velocity is zero. Figure 2.10 shows a schematic of dissolution of a solid into liquid. The mass transfer through this layer was suggested to be a diffusion process occurring due to a concentration gradient that remains constant over the whole layer. Under such postulation the relationship, Equation 2.5, known as the Nernst-Shchukarev equation, can be used to determine the dissolution rate [53].

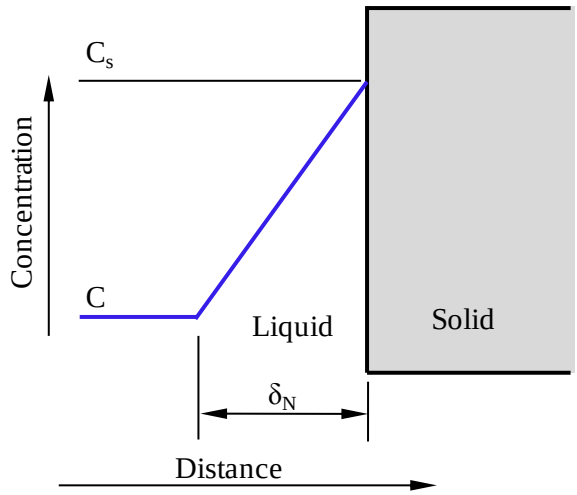

Figure 2.10 - A schematic of dissolution of solid into liquid by Nernst-Shchukarev concept.

$$\frac{dC}{dt} = \frac{DS}{\delta_N V}(C_s - C) \tag{2.5}$$

where C is the concentration of the solute in the bulk of solvent at time t, C_s is the saturation concentration, D is the diffusion coefficient, S is the surface area of the dissolving solid, δ_N is the Nernst diffusion layer thickness and V is the solvent volume.

Diffusion from a dissolving surface into a static liquid was generally considered to be very slow owing to the low values of diffusion coefficients. The driving force for diffusional mass transport is only the concentration gradient, which decreases continuously during a mass transfer process. When a fluid flows along a solid surface, the velocity of liquid in the vicinity of the surface is reduced by friction and a thin boundary layer exists at the surface in which fluid velocity varies gradually. The flow velocity approaches zero at the surface and becomes nearly equal to the bulk velocity at its outer border. This thin zone of changing velocity in the vicinity of the surface is called the hydrodynamic boundary layer. Therefore, the entire zone of liquid motion near the substrate can be roughly divided into two regions: (i) the bulk where transport of dissolved material mainly takes place by macroscopic fluid flow, (ii) the boundary layer region near the dissolving surface. Compared to the bulk flow, there is

slower removal of dissolved matter by convection in the boundary zone. Thus near the surface, a higher concentration of solute exists than in the bulk. This causes a net diffusion in the perpendicular direction to the dissolving surface. Diffusion of dissolved solute through the boundary layer into the bulk remains a process of short duration, since at a short distance from the dissolved surface, convection dominates the mass transport by diffusion. Therefore, in most of the solid-liquid systems, mass transport is not controlled by molecular diffusion alone, but convective mass transfer also plays an important role. The contribution of each mechanism to overall mass transfer depends upon the distance of the mainstream from the dissolving surface and the hydrodynamic flow conditions [53-54].

It thus follows that the Nernst-Shchukarev dissolution model does not capture ordinary mixing conditions where no stagnant layer exists as there is a change in velocity through the hydrodynamic boundary layer [53].

Levich [54] modified the Nernst-Shchukarev equation by introducing the concept of effective boundary layer δ based upon the actual hydrodynamics at the dissolving surface. The diffusion coefficients of the liquids are so small that even at low flow velocities ($Re \leq 10$), the mass transport in the bulk of the solution was found to be totally convective. On the other hand, in the immediate vicinity of the dissolving surface where the liquid motion is almost absent, a region of rapidly changing concentration exists, where the diffusion must be taken into account. The effective boundary layer model included both diffusion and convective mass transfer. Levich determined the hydrodynamic boundary layer thickness (d_h) at a semi infinite plate surface as:

$$d_h = 5.2 \left(\frac{\nu X}{U_b} \right)^{1/2} \tag{2.6}$$

where ν is the kinematic viscosity, X is the distance from the leading edge parallel to the flow direction and U_b is the bulk velocity parallel to the plate surface.

The following equation can be used to calculate the thickness of an effective diffusion boundary layer for a semi-infinite plate in laminar flow [54]:

$$\delta = K_1\left(\frac{D}{\nu}\right)^{1/3} d_h \tag{2.7}$$

K_1 is found to be around 0.6, and

$$\delta = 3\left(\frac{D}{\nu}\right)^{1/3}\left(\frac{\nu X}{U_b}\right)^{1/2} \tag{2.8}$$

Using the effective diffusion boundary layer the Nernst-Shchukarev equation can be rewritten as.

$$\frac{dC}{dt} = \frac{DS}{\delta V}\left(C_s - C\right) \tag{2.9}$$

or

$$\frac{dC}{dt} = K\frac{S}{V}\left(C_s - C\right) \tag{2.10}$$

where, $K = \frac{D}{\delta}$

K is known as the dissolution rate constant. In other words the D and δ vary in such a manner that their ratio remains constant for the dissolution of pure solid into liquid [54], and the modified Nernst-Shchukarev equation can be integrated to find c(t):

$$\ln\frac{C_s - C_o}{C_s - C} = K\frac{St}{V} \tag{2.11}$$

where C_o is the solute concentration at t = 0.

2.3.2 Dissolution Test Apparatuses

For the development of the experimental test method, the characteristics of established dissolution test apparatuses were studied. Several dissolution devices were invented with two main aims: (i) to relate the dissolution with hydrodynamic flow conditions, (ii) good

reproducibility of the results. The best known devices in each of these categories are described in the following sections.

2.3.2.1 Rotating Disc Method

Levich [54] investigated the hydrodynamics of the boundary layer at the surface of a dissolving disc. Figure 2.11 shows a schematic diagram of the rotating disc method; in this method a small disc (10-15 mm in diameter) was rotated into the solvent. With the rotation of the disc, it was observed that the fluid flows in both radial and tangential directions and to balance these components the fluid flows in the axial direction too. In the case of the rotating disc, Levich defined the hydrodynamic boundary layer as the distance from the disc surface where the tangential velocity decreases to 0.05 times its magnitude at the disc surface. The thickness of hydrodynamic boundary layer (d_h) at the disc surface was given by:

$$d_h \cong 3.6\left(\frac{\nu}{\omega}\right)^{1/2} \tag{2.12}$$

where ω is the angular velocity of the disc.

Another worker Riddiford [55] defined d_h in a similar way, but of relatively smaller thickness:

$$d_h \cong 2.8\left(\frac{\nu}{\omega}\right)^{1/2} \tag{2.13}$$

It is to be noted that these equations can be applied only to laminar flows up to $Re \leq 10^4$. Also at very low speeds of rotation, natural convection may cause deviations from the theory because at low velocities, the thickness of the hydrodynamic boundary layer becomes comparable to the radius of the disc [53]. Levich [54] derived the following equations for the diffusion boundary layer (δ) and dissolution rate (R) (kg/s) for the rotating disc method.

$$\delta \cong 0.5\left(\frac{D}{\nu}\right)^{1/3} d_h \tag{2.14}$$

$$R = 1.9\, D^{2/3} \nu^{-1/6} \omega^{1/2} (\Delta C) r^2 \qquad (2.15)$$

where $\Delta C = C_s - C$ and r is the radius of disc.

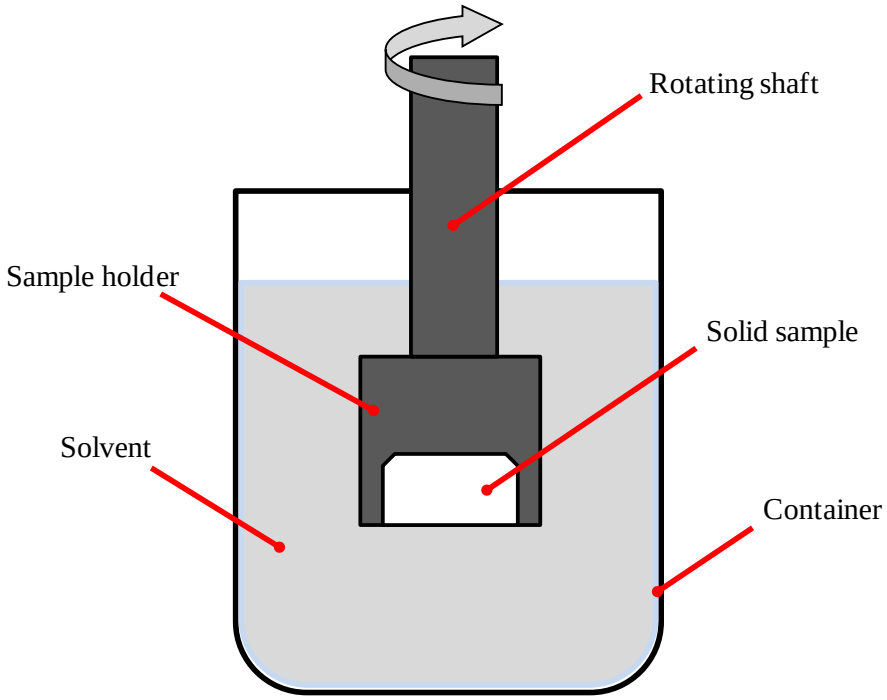

Figure 2.11 - A schematic of the rotating disc method.

The hydrodynamic boundary layer thickness is constant over the whole surface of the disc. As a result the diffusion layer thickness is also constant at the disc surface, which is a very interesting feature of the rotating disc system. The rotating disc method is known as the best available method to relate the dissolution rate to the hydrodynamic conditions under laminar flow ($Re \leq 10^4$).

2.3.2.2 USP-II Apparatus

The USP-II (The United States Pharmacopoeial Convention) apparatus, shown in Figure 2.12(a), is most widely used in pharmaceutical research [52]. This apparatus consists of a rotating impeller inside a solution and the tablet for dissolution studies is fixed at the bottom

of the container. For the USP-II apparatus, the material dissolution was found to increase linearly with increasing time. Figure 2.12(b) shows the dissolution versus time relationship for the USP-II apparatus.

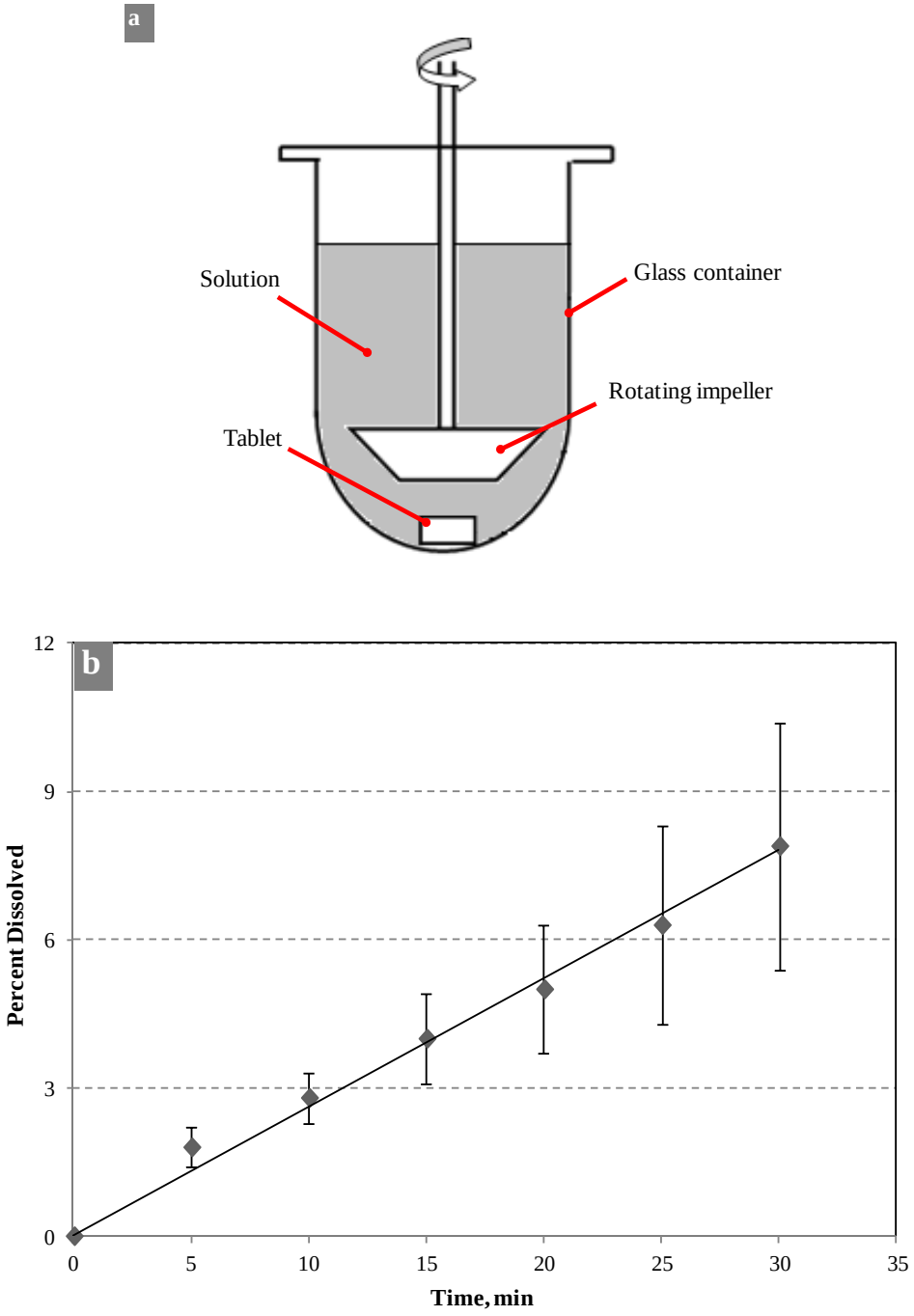

Figure 2.12 - a) The USP-II apparatus for studying the dissolution of tablets under forced convection, b) dissolution versus time for USP salicyclic acid calibrator tablets in a water-sodium hydroxide solution at 100 rpm. [After [52]]

Withey and Bowker [56] investigated the flow patterns and dissolution of six devices including the rotating disc system. As far as the reproducibility of the dissolution rate and the uniformity of mixing are concerned, the USP-II dissolution apparatus was suggested as the most suitable device. As a quantitative hydrodynamic analysis of dissolution rate is almost impossible in this case, the only purpose is a good reproducibility [56]. The USP-II apparatus is difficult to apply to the metallic systems owing to the practical difficulties of its operation such as erosion of the rotor and increased oxidation of the melt (e.g. Al) by stirring action.

2.3.3 Rotating Disc Method for Fe-Liquid Al Systems

The rotating disc system can be used to measure dissolution in metallic systems. The Nernst-Shchukarev relationship, Equation 2.11, can be used to find the dissolution constant (K). Most of the investigations [37, 51, 57] have demonstrated the applicability of the Nernst-Shchukarev equation to the dissolution of solid metals in liquid metals using the rotating disc method.

Eremenko and Natanzon [58] were the first researchers to design the rotating disc apparatus with the facilities of vacuum and remote sampling of the melt during the test. The vacuum in the melt chamber was used to prevent oxide formation in Al melts because the use of a protective flux over the liquid metal surface was known to contaminate the melt.

In their two successive publications [59-60], Eremenko *et al.* have shown experimentally that the dissolution of pure Fe (Armco Fe) in pure Al and Al-3 wt.% Si alloy does not follow the Nernst-Shchukarev equation owing to the protective properties of the Fe-Al intermetallic layer in the initial stages. The K for pure Fe in Al was found to decrease with increasing time and then started to increase as shown in Figure 2.13.

Three types of relationships were proposed for the dissolution of Fe into liquid Al, in the first K is constant with time, in the second K increases with time and in the third K decreases as time increases. These behaviours were suggested to depend upon the protective properties of the intermetallic layer.

In 1981, Yeremenko *et al.* [37] published the results of their study in which they used the flux as a method of melt protection, and the dissolution of pure Fe in pure liquid Al was found to follow the Nernst-Shchukarev equation. Figure 2.14 shows that the K is constant. This finding suggested that maintaining the vacuum over the melt surface may not be a necessary condition. However, it was not possible to conclude the possible effect of rotation velocity and/or using flux on the evaluated dissolution rate constants.

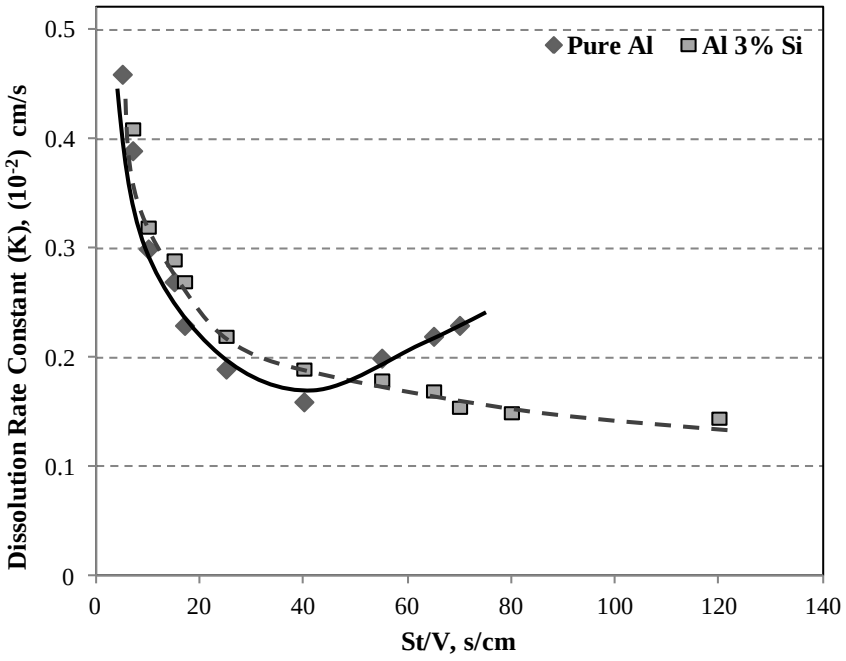

Figure 2.13 - Variation in dissolution constant (K) with time for pure Fe specimens rotated at 63.1 rpm in Al melts at 700° C under vacuum. [After [59]]

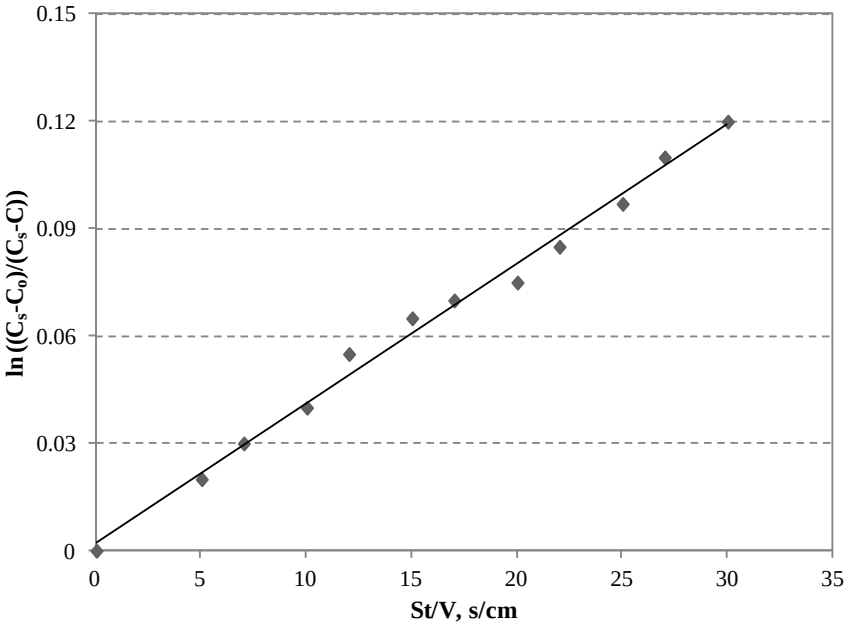

Figure 2.14 - ln (C_S-C_o/C_S-C) plotted against St/V for pure Fe in liquid Al at 700°C and at about 229 rpm, flux was used to protect the melt against oxidation. [After [37]]

Yeremenko *et al.* [37] also discussed two important observations about the rotating disc method. First was the deterioration of the results owing to the formation of an intermetallic layer if the weight loss of the solid specimen is used to evaluate the dissolution process and the duration of the experiment is short. In this case, the weight loss due to the dissolution and the increase in the specimen weight due to the interlayer formation become of the same order of magnitude. Using the specimen dimensions for dissolution measurement was also suggested to have similar drawbacks. This was suggested to be one of the reasons for the discrepancies in the results obtained before, for example [37]. Secondly, when the solute concentration (C) approaches the saturation concentration (C_s), owing to the small value of denominator (C_s-C) even a small error in the determination of the concentration could result in a large error in evaluation of the dissolution rate constant. Therefore, arbitrary limits on the solute concentrations for calculating K were suggested within $0.01 < C/C_s < 0.75$. It was further suggested that the evaluated K depends upon the accuracy with which the material loss is determined.

During the dissolution of Fe in liquid Al, the Fe concentration in the melt is non-uniform and can exceed the saturation limit in localized regions for a given temperature. This leads to the formation of primary intermetallic compounds. As they remain for long durations in the melt bulk, Fe containing intermetallic compounds grow in size and precipitate on the crucible bottom since their density (3.42-4.02 gm/cm^3) is almost double that of Al melt (2.1-2.4 gm/cm^3) [61]. Therefore, it can be ascertained that in the case of the rotating disc method, the collected melt samples for analysis may not represent the actual dissolution of Fe in Al. This may also be the reason that the method of collecting melt samples during testing was found to have poor reproducibility of results by [62].

Dybkov [57] conducted extensive experimentation on the dissolution of 18Cr-10Ni stainless steel in liquid Al at 700°C. While earlier studies [37] had verified the applicability of the Nernst-Shchukarev relationship for pure Fe, it was important to experimentally verify the dissolution kinetics of a relatively complex system such as stainless steel. The experimental results defined for the first time the interdependence of dissolution and alloying elements of a high alloy content ferrous material. The saturation concentration of Fe (as in pure liquid melt) was found to be the rate controlling factor and the other two elements were present in the melt in the same ratios as in the substrate material.

Also Barmak and Dybkov [63], and Hwang *et al.* [51] verified the Nernst-Shchukarev equation for the dissolution of stainless steels (10% Cr and 25% Cr), and carbon steels in liquid Al, respectively. The values of the dissolution rate constants (K) obtained by various researchers for different alloys are listed in Table 2.6.

Table 2.6 - Dissolution rate constants for various ferrous alloys by the rotating disc method.

Type of ferrous alloy/ Composition (wt.%)	Dissolution rate constant (K), m/s (10^{-5})	Test conditions
Stainless steel (72%Fe, 18%Cr, 10% Ni)	4.6	700ºC, pure Al, 229 rpm [57]
Stainless steel (90%Fe, 10%Cr)	4.2	700ºC, pure Al, 229 rpm [57]
Stainless steel (75%Fe 25% Cr)	3.0	As above
Pure Fe	3.8	700ºC, commercial pure Al, 229 rpm [37]
Carbon Steel (0.25%C)	0.22	Al alloy (9.08Si + 0.98 Fe) 660ºC, 16 rpm [51]
Carbon steel (0.45 %C)	0.13	As above
Steel (1.1 %C)	0.12	As above

As mentioned in Section 2.3.1, the dissolution of solids into liquid metals generally takes place in two steps. In the first step, the atoms of solid pass into the melt and in the second the mass transport of the dissolved material into the volume of the melt takes place. These were more commonly referred to diffusion and kinetic regimes of the dissolution process. In a review paper Eremenko and Natanzon [62] asserted that the dominance of each of these processes depends upon the selection of the solid-liquid metal couple, and the dissolution under kinetic conditions is not the characteristics of metals because the majority of the metals were found to dissolve under diffusion conditions. The dissolution rate under diffusion conditions was suggested to be controlled by D, δ and C_s. The dependence of D and δ values ($D \approx 10^{-9}$ m^2/s, $\delta \approx 10^{-5}$ m) on the individual properties of metals was found to be small. Therefore, the C_s remained the main determinant of the dissolution rate under diffusion conditions, which was suggested to constitute the principal criteria for the choice of a metal compatible with any given melt [62].

2.3.4 Corrosion by Diffusion and Spallation of the Intermetallic Layers

In 1994, Richards *et al.* [13] suggested that the previous studies failed to clearly distinguish between dissolution by diffusion and dissolution by spalling of the intermetallic layer. Dissolution by the first process was expected to cease when the Al melt reaches the saturation concentration of Fe, while the second process continues during the entire time period of contact with the melt. Previous research [37, 49] suggested that Fe enrichment of the Fe saturated melts does not occur. On the other hand, in the view of Richards *et al.* [13], it is a conclusion directly contrary to industrial experience, where the Fe saturation of the bath does not prevent the continuous accumulation of significant amounts of dross in the melts. The dross has to be periodically removed to avoid inclusion in castings or to prevent degradation of the aluminized coatings. Moreover, it was argued that at longer immersion times the intermetallic layer growth diminishes in accordance with the parabolic kinetics; on the other hand, it may also result from the increased dissolution of the intermetallic layer into the melt [13].

Balloy *et al.* [45] published the results of their study on the corrosion rates of cast irons in liquid Al melts saturated with Fe. They [45] exposed the cast iron specimens to the Al melt at 690ºC for 8 hours and found that all materials showed the material loss. Thus in agreement in Richards *et al.*[13], the Fe saturation is unable to stop the corrosion of ferrous materials in Al melts. Theoretically, the Fe diffusion or dissolution of the intermetallic layer should stop when the melt saturates with Fe. On the other hand, it is possible that even after the melt saturates with Fe, Al can diffuse towards the Fe-substrate. Thus in saturated Al melts the intermetallic layers may grow at the expense of Al only. The formed intermetallic layers (η-Fe_2Al_5 and θ-$FeAl_3$) are suggested [11] to be brittle, which may spall owing to the presence of convection currents (natural or forced) in the melt. Moreover, the interaction of η-Fe_2Al_5 with liquid Al may form lath shaped θ-$FeAl_3$ particles extending towards the Al melt, which are

relatively easy so spall. Thus the formation and simultaneous spallation of η-Fe_2Al_5 and θ-$FeAl_3$ may continue at the expense of Al diffusion, leading to the material loss even in the melts saturated with Fe.

From this point of view, performing the dissolution tests in molten Al and measuring the melt concentration/mass loss over a time period does not provide a complete identification as to the mechanisms that produce the material loss in liquid Al melts. Therefore, more detailed analysis must be employed if a better understanding of the degradation progression of ferrous substrates in liquid Al melts is to be accomplished.

2.3.5 Comparing the Liquid Al Corrosion Resistance of Ferrous Alloys

There are limited studies comparing or modifying the ferrous substrates against the liquid Al corrosion. These are presented in the following sections.

In 1966, a publication [64] by Mountford and Glover cited the work done by the investigators of the British Cast Iron Research Association (BCIRA) and the British Non-Ferrous Research Association (BNFRA) in a joint program in the 1920s. Several compositions of GCIs including pure Fe, high Cr iron and an Fe-Al alloy (Cralfer) were tested at 800ºC and 900ºC for 6 hours. However, the detailed experimental conditions such as the specimen size, number of specimens and surface condition were not known. These alloys were tested in both as-cast and in annealed condition (6 days at 700ºC). The chemical compositions and comparative dissolution results are given in Table 2.7 and Figure 2.15, respectively.

Based upon these results, Mountford and Glover [64] suggested that the high-phosphorus GCI and Cralfer offered the best resistance to liquid Al corrosion. However, the presented results were slightly overlooked by [64] because unalloyed GCI-16 showed a slightly better performance than these two alloys. Moreover, the corrosion resistance of GCI-2 is also similar to Cralfer and high P cast irons.

Table 2.7 - Material compositions tested by BCIRA/BNFRA [64].

Cast Irons	C	Si	P	Mn	Ni	Cr	Other *
GCI-1	3.47	2.42	--	0.6	--	0.69	--
GCI-2	3.67	1.48	--	0.8	--	0.74	0.12Ti
Cralfer	3.0	0.98	--	0.7	--	0.73	7.4Al
GCI-3	3.73	1.47	0.55	0.8	--	--	--
GCI-4	3.47	1.55		0.8	---	---	---
GCI-5	3.48	1.24	1.0	0.7	--	--	--
GCI-6	3.5	2.45	--	0.8	--	--	--
GCI-7	2.41	1.8	--	0.63	13.7	3.37	6.41Cu
GCI-8	3.6	2.3	--	0.6	--	--	--
GCI-9	3.02	2.03	--	0.42	1.0	--	--
GCI-10	3.37	2.67	1.1	0.8	--	--	0.36Ti
GCI-11	3.61	1.48	--	0.8	--	0.74	--
GCI-12	3.26	2.42	--	0.6	--	0.69	--
GCI-13	2.42	4.75	--	0.85	--	--	--
High- chromium iron	0.88	--	--	0.12	0.26	30	--
GCI-14	2.11	4.91	--	0.9	19	2.31	--
GCI-15	3.63	1.48	--	0.8	--	--	--
Armco iron	--	--	--	--	--	--	--
GCI-16	3.67	1.44		0.82			
GCI-17	3.09	1.43	0.2	0.9	1.39	0.65	--

* Balance Fe

All the annealed cast irons showed an increase in dissolution compared to the as-cast condition. Even though a large number of alloys were tested, no clear correlation between the composition and liquid Al corrosion resistance could be established. Alloying additions such as Ni, Cu and Cr showed no beneficial effect.

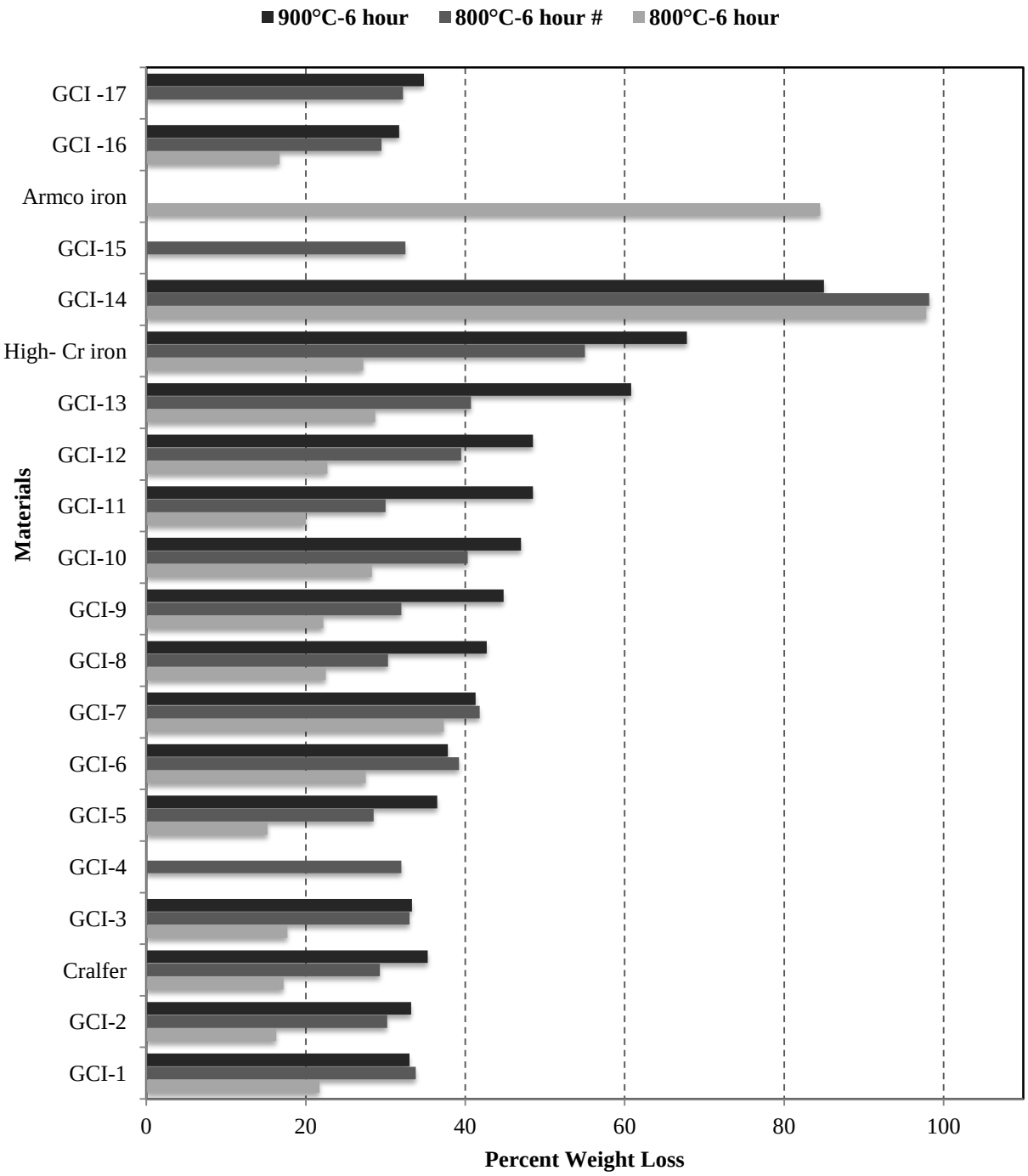

Figure 2.15 - Weight loss of specimens of several ferrous materials in liquid Al melts at 800ºC and 900ºC tested by BCIRA/BNFRA (# annealed condition). [After [64]]

Further investigation was carried out by Mountford and Glover [64] under industrial conditions. They used the downspouts of a continuous-casting machine as test specimens, which had a conical shape with a central hole. Four as-cast downspouts were fixed to the bottom of a large tray to which 280 pounds of liquid Al were poured in each cycle. After a

number of cycles, the downspouts were removed and the extent of corrosion was determined by measuring the depth of material loss at the downspout side-wall. The results were presented in terms of comparative corrosion resistance. The chemical compositions and comparative corrosion resistance of different cast irons alloys are given in Table 2.8 and Figure 2.16, respectively. One discrepancy was noted, the compositions of PDCI and FDCI were found to be the same. Apparently, they may have produced FDCI by heat treating PDCI or it was a misprint.

Table 2.8 - Cast iron compositions for field trials [64].

Cast Irons		C	Si	P	Mn	Cr	Al	Mg	*
High-phosphorus GCI	HPGCI	3.46	2.11	1.19	0.55	---	---	---	
Low-phosphorus GCI	LPGCI	3.61	2.09	0.14	0.54	---	---	---	
Pearlitic DCI	PDCI	3.7	2.1	---	0.42	---	---	0.068	
Ferritic DCI	FDCI	3.7	2.1	---	0.42	---	---	0.068	
Silal DCI	SADCI	2.07	6.56	---	0.47	---	---	0.050	
High Cr iron	HCI	1.32	1.09	---	0.45	35.8	---	---	
Low Al DCI	LADCI	3.34	1.93	---	---	---	6.00	0.057	
High Al DCI	HADCI	1.71	1.04	---	---	---	24.30	0.061	

*Balance Fe

High-P GCI outperformed all other alloys under investigation, and it was suggested to be the cheapest option to enhance the corrosion resistance of cast irons against liquid Al. Cr or Al additions to cast irons showed a significant decrease in corrosion resistance. Unfortunately, no detailed metallurgical analyses were made to relate the cast iron microstructure to the liquid Al corrosion resistance. Furthermore, it was suggested that even the presence of small amounts of porosity accelerated the liquid Al attack, and porosity-free high-phosphorus cast iron castings are difficult to produce. Moreover, the addition of P negatively affects the mechanical properties of cast irons [4]. Therefore, the high-P cast irons cannot be recommended for most structural applications.

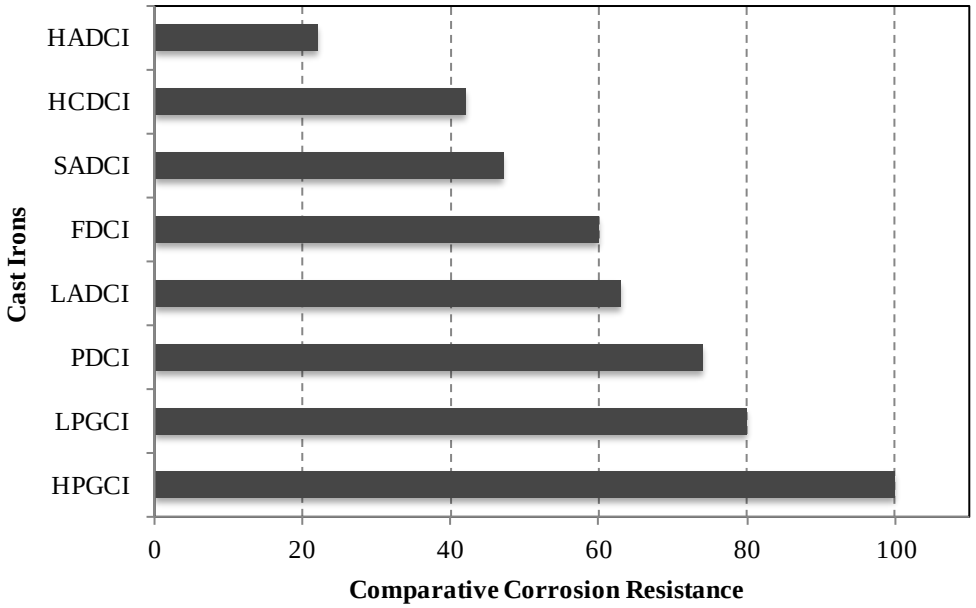

Figure 2.16 - Comparative corrosion resistance of downspouts subjected to flowing liquid Al at 800°C. [After [64]]

Hwang *et al.* [51] investigated the dissolution of three steels, SM20C (0.2 wt.% C), SM45C (0.45 wt.% C) and STC3 (1.1 wt.% C) in liquid Al melts using rotating disc method. Experimental details are described in Section 2.2.3.3. The dissolution of steels was found to decrease with a rise in C content. The decrease in dissolution of steels with increasing C was suggested to be due to the higher volume fraction of cementite [51].

Niinomi *et al.* [65] compared the dissolution of several ferrous alloys in molten Al at 700°C, 750°C and 800°C. The cylindrical specimens of these materials were immersed into the static melts for various time periods. Table 2.9 lists the chemical compositions of ferrous materials. The alloys under investigation were evaluated by determining the mass transfer coefficient (k) from the experimental data, by using the following relationship:

$$-(dw/dt)/L = kA(C_s - C) \quad (2.16)$$

where w is the weight of specimen, L is the dipping length, t is the time, k is the mass transfer coefficient, A is the surface area, C_s is the saturated concentration of solute in liquid and C is

the concentration of solute in liquid after time t. Figure 2.17 shows the mass transfer coefficients (k) of various ferrous alloys.

Table 2.9 - Chemical compositions of materials [65].

Material	C	Si	Mn	Cr	Cu	Ni	*
Fe-3C	2.94	0.24	0.23	--	0.05	--	
Fe-3Mn	--	0.01	3.16	0.06	--	0.01	
Fe-2Mn	--	2.85	2.36	--	--	--	
Fe-3Ni	--	0.09	0.12	0.06	--	3.00	
Fe-3Cu	--	0.11	0.19	0.15	2.97	0.02	
Fe-3Cr	0.009	0.15	0.18	2.94	--	0.02	
Fe-3Si	0.033	2.91	0.22	--	--	0.01	
Pure Fe	0.01	0.2	0.22	--	--	--	

* Balance Fe

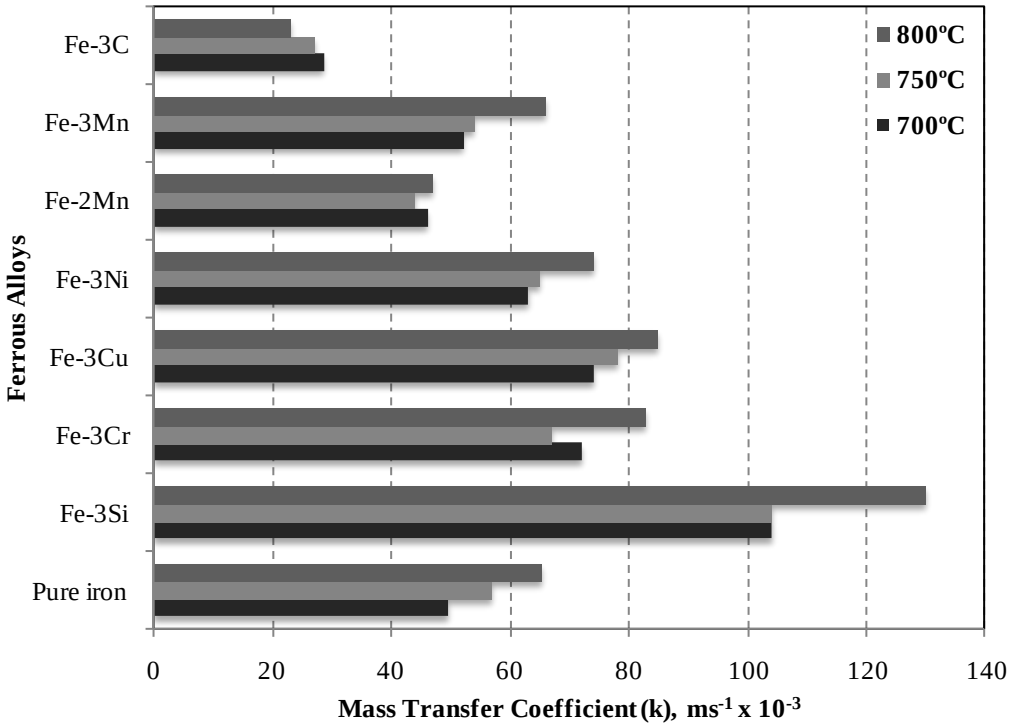

Figure 2.17 - Mass transfer coefficients (k) of various ferrous alloys subjected to static liquid Al. [After [65]]

The Fe-3C alloy was the most resistant to liquid Al corrosion whereas the Fe-3Si exhibited the highest dissolution rate. The addition of 2 wt.% Mn was found to slow down the corrosion; however, 3 wt.% Mn to pure Fe did not show improvement in the corrosion

resistance. The alloys with Cu, Cr and Ni dissolved at a faster rate than the pure Fe; however, all of these alloys exhibited similar mass transfer rates.

In a recent publication, Balloy *et al.* [45] cited a few rarely avialable studies on liquid Al corrosion of cast irons. Based upon these studies they [45] concluded that there is no corelation between cast iron composition and liquid Al corrosion resistance. They [45] investigated the corrosion of three ferrous alloys, plain carbon steel (C38), pearlitic gray cast iron (PCI) and ferritic gray cast iron (FCI). These materials were exposed to liquid Al (saturated with Fe) at 690°C for 8 hours. The chemical composition of these alloys is listed in Table 2.10.

Table 2.10 - The chemical compositions of cast irons and carbon steel [45].

Material	C	Si	Mn	Cr	Al	P	*
C38	0.37	0.25	0.8	0.043	0.03	0.02	
FCI	3.5	4.5	0.22	---	---	---	
PCI	3.71	1.76	0.68	1.14	1.93	0.37	

* Balance Fe

PCI with Al, Cr and P alloying elements showed three times less dissolution than C38 steel and eight times less than FCI. Presence of cementite particles in PCI was suggested to slow down the dissolution of PCI as cementite dissolved more slowly than pearlite and ferrite. Furthermore, it was concluded that the presence of the phosphorus-eutectic also helped to retard the material loss of PCI. The effect of Al and Si addition on liquid Al corrosion resistance was not analyzed in Balloy *et al.*'s work.

2.3.6 Boronizing Surface Treatment

Boronizing is a thermo-chemical process similar to carburizing or nitriding, which involves diffusion of boron into a base metal at a high temperature. Boronizing is commonly applied to steels. When boron atoms diffuse into the surface zone of a ferrous work piece, a

compound layer is formed that consists of either one iron boride (Fe_2B) or two iron borides ($FeB+Fe_2B$). The formed boride layers are very hard (1400-1700 HV), which can be used in wear-resistant applications. Boride layers were also found to be resistant against liquid Al corrosion. There is a large difference between the thermal expansion coefficients of the duplex phases (Fe_2B and FeB), which makes the FeB layer very likely to be exfoliated when the component is cooled from the treatment temperature. As a consequence, efforts are generally made to impart a single layer of Fe_2B, although Fe_2B is relatively lower in hardness than FeB [66].

Lou *et al.* [67] investigated liquid Al corrosion of 22Cr-5Ni duplex stainless steel (DSS), hot work tool steel (AISI H13), a DCI and a γ-TiAl intermetallic. Boronizing surface treatment was used as a method of protection against liquid Al corrosion. The chemical compositions of the ferrous materials are given in Table 2.11. γ-TiAl was used as reference material because it has a high liquid Al corrosion resistance. The DSS and tool steel were boronized at 1025°C, while the DCI specimens subjected to 850°C for 5 hours. The as-received and boronized rectangular coupons with dimensions 10 mm x 10 mm x 15 mm were immersed in molten 6080 Al alloy at 680°C for 4 hours.

Table 2.11 - Chemical compositions of the substrate materials [67].

Alloys	C	Si	Mn	Mo	Mg	Cr	V	Ni *
DSS	0.03	1.0	2.0	3.0	---	22	--	5.5
H13	0.38	1.0	0.4	13	0.02	5.3	0.9	0.05
DCI	4.0	3.0	0.13	---	---	---	---	---

*Balance Fe

The material loss of DSS was approximately half that of H13, while it is slightly more resistant than DCI to liquid Al attack. The boronizing surface treatment reduced the dissolution of DSS and DCI by a factor of 16 and 20 respectively. The corrosion rate of H13

steel was only reduced by a factor of 3, which was attributed to the porosity present in the boride layer on this alloy [67].

Tsipas *et al.* [68] published the degradation behaviour of boronized plain carbon steel in molten Al. Disc shaped specimens (40 mm diameter x 3 mm) were machined from plain carbon steel (0.2 wt.%). The specimens were boronized at 900°C for 4 hours. The boronized steel showed about 7 times lower weight loss compared to the as-received condition. A discrepancy was noted, the bath temperature of Al was stated to be 630°C, which indicates that they may have used an Al alloy since pure liquid Al melts at 660°C.

2.4 Concluding Remarks

- The prime consideration for a suitable material for tapping pipes is enhanced liquid Al corrosion resistance. Since the service application also involves temperature cycling, a material employed for tapping pipes should also possess good thermal fatigue resistance. Considering the benefits in achieving good elevated temperature properties, only Cr, Cu and Mo were considered as alloy additions to cast irons under the current investigation.

- Formation of all possible intermetallic compounds of the Fe-Al binary phase diagram have been found in solid Fe-Al couples at different conditions of liquid Al exposure. However, in Fe-liquid Al interaction only two phases, η-Fe_2Al_5 and θ-$FeAl_3$, phases were commonly found to exist. It was found that Fe-rich compounds such as β_2-FeAl and β_1-Fe_3Al form when Al is not abundantly available, as in solid state Fe-Al couples.

- With increasing immersion times of steel alloys into liquid Al, Fe-Al intermetallic layer growth showed negative deviations from the parabolic law of growth. In the literature, these deviations were frequently attributed to the dissolution of the intermetallic layer.

However, the dissolution behaviour with respect to intermetallic layer growth was not studied in sufficient detail. The dissolution can be considered to result from the spallation (and/or dissolution) of the intermetallic layer and the direct diffusion of Fe into the melt. Thus even comparing the time dependent intermetallic layer growth and dissolution of a single alloy would not be conclusive. To investigate this phenomenon various ferrous alloys need to be compared in terms of intermetallic layer growth and dissolution.

- The addition of Si to the ferrous alloy substrates and in the melt was found to reduce the intermetallic layer thickness; however, the mechanism by which it diminishes the intermetallic layer growth is not completely understood and remains controversial. Si and C are primary compositional constituents of cast irons thus it would be interesting to investigate the mechanisms by which these elements affect the corrosion rates and growth of the intermetallic compounds. Moreover, Si enrichment of the Fe-substrates has been reported in Fe-Si alloys and cast irons exposed to liquid Al. It is important to reveal the effect of Si on the corrosion resistance of cast irons and mechanisms of liquid Al corrosion.

- In the literature, the predominant appearance of η-Fe_2Al_5 was attributed to the high diffusion rate of Al along the c-axis of η-Fe_2Al_5 unit cell. On the other hand, θ-$FeAl_3$ formation was not studied in detail. Most studies proposed that θ-$FeAl_3$ grow during solidification of Al around the corroded specimen, on the other hand, a few studies suggested that it can grow during ongoing liquid Al corrosion. While others believed that θ-$FeAl_3$ in the form of layer grows during Fe/liquid Al interaction and θ-$FeAl_3$ particles grow after the solidification of Al. Moreover, the growth of θ-$FeAl_3$ in the form of lath shaped particles remains unclear. Thus to better understand the process of liquid Al corrosion, it is important to reveal the formation and growth characteristics of θ-$FeAl_3$.

- In the rotating disc method the saturation concentration was found to be the principal factor upon which the calculated dissolution rate constant depends and it must be known for each solid-liquid metal system under comparison. Moreover, the determined dissolution rate constant chiefly depends upon the accuracy by which the melt concentration or material loss is measured. Moreover, there is disagreement whether the dissolution of ferrous alloys stops when the Fe concentration in Al melt reaches saturation. When the melt saturates with Fe, the liquid Al corrosion may be occurring due to the diffusion of Al only. Therefore, comparing the dissolution rates with measures of melt chemistry may be problematic. Moreover, during flowing through of tapping pipes, the liquid Al never reaches the saturation concentration of Fe. Thus in the present work, the corrosion resistance of candidate materials should be compared in under saturated melts.

- In the literature, it was found difficult to establish a relationship between the chemical composition and liquid Al corrosion resistance of cast irons. It is to be noted that in the literature, the microstructures of cast irons were not considered while comparing the liquid Al corrosion resistance. As the microstructure of cast irons is strongly dependent upon chemical composition it is thus necessary to consider the microstructures while analysing the corrosion rates. Moreover, all of those investigations were carried out using static melts. Considering the service conditions of tapping pipes and to magnify the relative difference between the corrosion rates of different compositions of cast irons, a new apparatus is needed.

- Dissolution studies on cast irons showed that P addition enhances the corrosion resistance of GCIs. However, in industrial practice, the concentration of elements such as P and S is kept as low as possible due to their harmful effects on mechanical properties of cast irons.

Thus while preparing the alloys for the current work, these elements should be kept below the specified compositional limits.

- Increasing C content was found to enhance the corrosion resistance of steels, which was attributed to a higher amount of cementite. However, how cementite or high C in ferrous alloys raises the liquid Al corrosion resistance is not completely understood. Thus research needs to explore the mechanism by which C enhances the liquid Al corrosion resistance of ferrous alloys.

Chapter References

[1] H. Pollack, Material Science and Metallurgy, 4th Ed., Prentice-Hall, 1988.

[2] J.R. Davis, ASM Speciality Handbook-Cast Irons, ASM International, Materials Park, Ohio, 1996.

[3] H.T. Angus, Cast Irons-Physical and Engineering Properties, Buttersworth, 1976.

[4] J.F. Janowak, R.B. Gundlach, American Foundry Society Transactions, 90 (1982) 847-863.

[5] G. Silman, V. Kamynin, V. Goncharov, Metal Science and Heat Treatment, 49 (2007) 387-393.

[6] J.M. Chou, J.L. Lee, Y.C. Ko, Journal of Materials Science, 25 (1990) 2971-2974.

[7] K. Roehrig, American Foundry Society Transactions, 86 (1978) 75-88.

[8] G.J.N. Gilbert, British Cast Iron Research Association Journal, 7 (1959) 478-566.

[9] G.K. Turnbull, J.F. Wallace, American Foundry Society Transactions, 67 (1959) 35-46.

[10] R.B. Gundlach, International Cast Metals Journal, 4 (1979) 11-20.

[11] H.R. Shahverdi, M.R. Ghomashchi, S. Shabestari, J. Hejazi, Journal of Materials Processing Technology, 124 (2002) 345-352.

[12] M. Niinomi, Y. Ueda, Transactions of the Japan Institute of Metals, 23 (1982) 709-717.

[13] R.W. Richards, R.D. Jones, P.D. Clements, H. Clarke, International Materials Reviews, 39 (1994) 191-212.

[14] A.C.G. Gwyer, H.W.L. Philips, in: M. Hansen (Ed.), Constitution of Binary Alloys, McGraw-Hill Book Company, New York, 1958.

[15] F. Stein, M. Palm, International Journal of Materials Research, 98 (2007) 580-588.

[16] H. Baker, ASM Handbook-Alloy Phase Diagrams, ASM International, Materials Park, Ohio, 1992.

[17] N.W. Ageew, O.I. Vher, in: M. Hansen (Ed.), Constitution of Binary Alloys, McGraw-Hill Book Company, New York, 1958.

[18] N.S. Kurnakow, G. Urasow, A. Grigorjew, in: M. Hansen (Ed.), Constitution of Binary Alloys, McGraw-Hill Book Company, New York, 1958.

[19] M. Isawa, T. Murakami, in: M. Hansen (Ed.), Constitution of Binary Alloys, McGraw-Hill Book Company, New York, 1958.

[20] F. Wever, A. Muller, in: M. Hansen (Ed.), Constitution of Binary Alloys, McGraw-Hill Book Company, New York, 1958.

[21] W. Olesen, in: M. Hansen (Ed.), Constitution of Binary Alloys, McGraw-Hill Book Company, New York, 1958.

[22] A.J. Bradley, A.H. Jay, in: M. Hansen (Ed.), Constitution of Binary Alloys, McGraw-Hill Book Company, New York, 1958.

[23] A.J. Bradley, A. Taylor, in: M. Hansen (Ed.), Constitution of Binary Alloys, McGraw-Hill Book Company, New York, 1958.

[24] Bulletin of Binary Phase Diagrams, ASM International, 1994.

[25] H. Saito, in: M. Hansen (Ed.), Constitution of Binary Alloys, McGraw-Hill Book Company, New York, 1958.

[26] G.V. Raynor, C.R. Faulkner, J.D. Noden, A.R. Harding, in: M. Hansen (Ed.), Constitution of Binary Alloys, McGraw-Hill Book Company, New York, 1958.

[27] A. Bouayad, C. Gerometta, A. Belkebir, A. Ambari, Materials Science Engineering A, A363 (2003) 53-61.

[28] K. Bouche, F. Barbier, A. Coulet, Materials Science and Engineering A, A249 (1998) 167-175.

[29] S. Kobayashi, T. Yakou, Materials Science and Engineering A, 338 (2002) 44-53.

[30] N. Komatsu, M. Nakamura, H. Fujita, Journal of Japan Institute of Metals, 18 (1968) 474-482.

[31] T. Maitra, S.P. Gupta, Materials Characterization, 49 (2003) 293-311.

[32] K. Murakami, N. Nishida, K. Osamura, Y. Tomota, T. Suzuki, Acta Materialia, 52 (2004) 2173-2184.

[33] T. Sasaki, T. Yakou, K. Mochiduki, K. Ichinose, The Iron and Steel Institute of Japan International, 45 (2005) 1887-1892.

[34] T.S. Shih, S.H. Tu, Materials Science Engineering A, 454-455 (2007) 349-356.

[35] M. Niinomi, Y. Suzuki, Y. Ueda, Transactions of the Japan Institute of Metals, 25 (1984) 429-439.

[36] V.I. Dybkov, Reaction Diffusion and Solid State Chemical Kinetics, The IPMS Publications, Kyiv, 2002.

[37] V.N. Yeremenko, Y.V. Natanzon, V.I. Dybkov, Journal of Materials Science, 16 (1981) 1748-1756.

[38] T. Heumann, S. Dittrich, Zeitschrift Fuer Metallkunde, 50 (1959) 617-625.

[39] E.G. Ivanov, Metal Science and Heat Treatment, 21 (1979) 449-452.

[40] R.D. Jones, S.G. Denner, 10th World Congress on Metal Finishing, Matel Finishing Society of Japan, Tokyo, (1980) 371-375.

[41] S.G. Denner, R.D. Jones, Metals Technology, 4 (3) (1977) 167-174.

[42] S.G. Denner, R.D. Jones, R.J. Thomas, Iron and Steel International, 48 (1975) 241-252.

[43] D.R. Gabe, Reviews on High Temperature Materials, 1 (2) (1972) 157-163.

[44] N.W. Ageew, O.I. Vher, Institute of Metals - Advance Papers, Institute of Metals Meeting, London, 44 (2) (1930) 83-95.

[45] D. Balloy, J.C. Tissier, M.L. Giorgi, M. Briant, Metallurgical and Materials Transactions A, 41 (2010) 2366-2376.

[46] W.J. Cheng, Y.Y. Chang, C.J. Wang, Surface & Coatings Technology, 203 (2008) 401-406.

[47] H.R. Shahverdi, M.R. Ghomashchi, S. Shabestari, J. Hejazi, Journal of Materials Science, 37 (2002) 1061-1066.

[48] S. Shankar, D. Apelian, Metallurgical and Materials Transactions B, 33 (2002) 465-476.

[49] G. Eggeler, W. Auer, H. Kaesche, Journal of Materials Science, 21 (1986) 3348-3350.

[50] J.E. Nicholls, Corrosion Technology, 11 (1964) 16-21.

[51] S.H. Hwang, J.H. Song, Y.S. Kim, Materials Science and Engineering A, 390 (2005) 437-443.

[52] J. Mauger, J. Ballard, R. Brockson, Dissolution Technologies, 8 (2003) 6-14.

[53] H. Grijseels, D. Crommelin, C. Blaey, Pharmaceutisch Weekblad Scientific Edition, 3 (1981) 1005-1020.

[54] V.G. Levich, Physiocochemical Hydrodynamics, Prentice-Hall, New Jersey, 1962.

[55] A.C. Riddiford, in: P. Delahay (Ed.), Advances in Electrochemistry and Electrochemical Engineering, Interscience, New York, 1966.

[56] R.J. Withey, A.J. Bowker, Jounal of Pharmacy and Pharmacology, 24 (1972) 345-351.

[57] V.I. Dybkov, Journal of Materials Science, 25 (1990) 3615-3633.

[58] V.N. Eremenko, Y.V. Natanzon, Soviet Materials Science, 2 (5) (1968) 411-413.

[59] V.N. Eremenko, Y.V. Natanzon, V.R. Ryabov, Soviet Materials Science, 4 (6) (1972) 486-490.

[60] V.N. Eremenko, Y.V. Natanzon, V.R. Ryabov, Soviet Materials Science, 4 (3) (1968) 209-212.

[61] V. Sharshin, S. Skitovich, V. Kechin, D. Subbotin, Russian Journal of Non-Ferrous Metals, 48 (2007) 341-346.

[62] V.N. Eremenko, Y.V. Natanzon, Powder Metallurgy and Metal Ceramics, 9 (1970) 645-658.

[63] K. Barmak, V.I. Dybkov, Journal of Materials Science, 39 (2004) 4219-4230.

[64] F.A. Mountford, T.J. Glover, Foundry Trade Journal, 120 (1966) 849-852.

[65] M. Niinomi, Y. Ueda, M. Sano, Transactions of the Japan Institute of Metals, 23 (1982) 780-787.

[66] S. Sen, U. Sen, C. Bindal, Vacuum, 77 (2005) 195-202.

[67] D. Lou, O.M. Akselsen, M.I. Onsien, J.K. Solberg, J. Berget, Surface and Coatings Technology, 200 (2006) 5282-5288.

[68] D.N. Tsipas, G.K. Triantafyllidis, J.K. Kiplagat, P. Psillaki, Materials Letters, 37 (1998) 128-131.

CHAPTER 3 : EXPERIMENTAL METHODS AND MATERIALS

Introduction

Determining the comparative liquid Al corrosion resistance and characteristics of Fe-Al intermetallic compounds of several ferrous materials are two major parts of the present investigation. To study these characteristics, two types of apparatuses were used. Firstly, a test apparatus was designed and fabricated to compare the corrosion rates of ferrous materials under static and flow assisted liquid Al corrosion conditions. Secondly, another apparatus was set up to expose specimens of various types of ferrous alloys to similar conditions of static liquid Al in a relatively small melt volume. Afterwards, the exposed specimens were utilized for determining the formation and growth characteristics of Fe-Al intermetallic compounds. This chapter starts with the lists of chemical compositions and microstructures of the materials used in the present work followed by the experimental details. Boronizing surface treatment was also applied to selected ferrous alloys in order to evaluate their performance under dynamic corrosion conditions of liquid Al.

3.1 Materials

3.1.1 Material Selection

Failure investigations described in Section 1.4.3 showed that the liquid Al corrosion is the primary factor that decides the service life of tapping pipes. Moreover, the melt contamination by the dissolution of tapping pipe materials is a crucial concern in producing high purity Al. Cast irons and steels are close competitors for tapping pipe applications because cast irons are significantly cheaper to manufacture than steels while steels generally possess better resistance to thermal fatigue cracking [1] and higher strength [2, 3]. Thus the primary aim of the current work is to select the tapping pipe materials with enhanced corrosion resistance under the constraints of cost and thermal fatigue resistance. The high

temperature properties of ferrous materials can be improved by alloy additions (Section 2.1.3); on the other hand, there are no comprehensive reports (Section 2.3.5) that can be utilized to improve their liquid Al corrosion resistance. Thus there is a need to determine the comparative liquid Al corrosion resistance of various alloys of GCIs, DCIs and steels.

It is well established that the controlled addition of Cr, Cu and Mo improves the elevated temperature properties of cast irons (Section 2.1.3). Thus besides C, Si and Mn - the cast irons were alloyed with only Cr, Cu and Mo to maintain the high temperature properties. The pipe alloys currently employed in service were selected as benchmarks for comparison with the candidate alloys. There were two sets of ferrous materials that were tested to determine their liquid Al corrosion resistance. The preliminary test materials were designated Series-I and the second Series-II materials. Chemical compositions of the Series-II materials were determined from the results of the corrosion resistance investigation on Series-I materials.

To investigate the effect of fractions of different phases (ferrite, pearlite, cementite and graphite) on corrosion resistance, Series-I GCIs were cast with different C and Si contents. DCIs were cast with high Si contents because Si enhances the high temperature properties of DCIs [2]. Moreover, it was considered important to reveal the effect of varying Si content on liquid Al corrosion and thermal fatigue resistance of DCIs.

Series-II GCIs were designed aiming at the material replacement for bottom tapping pipes, and in this case, a high corrosion resistance is of prime importance. The existing steel pipes fail by liquid Al corrosion while the predominant mode of failure of DCI pipes is by the occurrence of thermal fatigue cracks. Thus a steel alloy with enhanced liquid Al corrosion resistance could be a potential material to replace the existing steel and DCI alloys because the literature [1] suggested that steels generally possess a higher thermal fatigue resistance

than cast irons. For this reason, two steel alloys were selected for comparing their liquid Al corrosion resistance with the existing steel and DCI alloys.

3.1.2 Compositions and Microstructures

Several compositions of GCIs and DCIs were prepared in a 200 kg induction furnace by The Casting Shop and cast in sand moulds. Optical Emission Spectroscopy (OES) was used to determine the chemical compositions of ferrous alloys.

3.1.2.1 Specimen Preparation for Optical Microscopy

Rectangular specimen blocks of 20 mm x 20 mm x 15 mm were sectioned from the as-cast blocks (45 mm x 45 mm x 160 mm) of cast irons using an Buehler Delta® Abrasimet abrasive cutter. First, the rectangular as-cast blocks were cut into two halves then the rectangular specimen blocks of about 20 mm x 20 mm x 15 mm were removed leaving 15-20 mm from the as-cast surfaces. The specimens were polished manually using a LECO AP-60® polisher, including the following grinding and polishing steps:

a) Successive grinding steps of 240 and 600 grit SiC papers were performed using water as the lubricant at a wheel rotation speed of 220 rpm. During grinding and polishing, the specimens were rotated in the opposite direction to the wheel rotation. The usual time for each step was 2-5 minutes. This was primarily determined by the substrate material and the surface condition.
b) Sequential polishing was carried out using Buehler MetaDi 9 μm diamond polishing compound on Buehler Trident® cloth, followed by the final polishing step using Buehler MasterMet® 0.06 μm colloidal silica suspension. A turntable speed of 100 rpm was used for both of the polishing operations.

Ferrous alloy specimens were etched with 2% Nital (2 ml HNO_3 + 98 ml ethanol). Optical microscopy was used to reveal the microstructures of cast irons and steels. Leica DM-Inverted Research Microscope was used to capture the images.

3.1.2.2 Determining Phase Fraction

LECO M-400-HI Microhardness Tester was used to differentiate between ferrite and cementite phases present in the cast iron microstructures, since cementite has higher hardness (500-600 H_v) compared to ferrite (200-300 H_v). Etching by alkaline sodium picrate (25 gm sodium hydroxide, 2 gm picric acid and 100 ml water, 60s at 60°C) was also performed to confirm the ferrite and cementite phases. After etching the cementite present in cast iron microstructure appears dark brown when viewed under the optical microscope. Figure 3.1 shows an example of the etched microstructure of GCI-S. For each alloy the average graphite fraction was determined from two optical images at 100x using Image-J analysis software. The average fraction of ferrite, pearlite and cementite was evaluated from two optical images at 200x magnification.

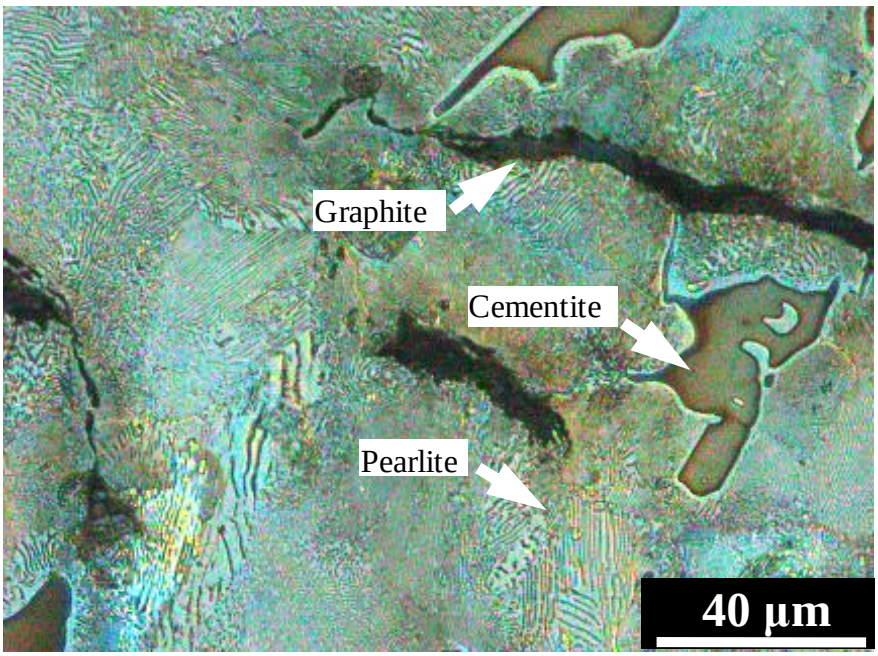

Figure 3.1 - Optical image of GCI-S etched with alkaline sodium picrate, cementite appears brown.

3.1.2.3 Series-I Materials

The chemical compositions of Series-I ferrous alloys, are listed in Table 3.1. DCI-T composition is currently employed as a top tapping pipe material. The cast steel (CS) specimens were an after-service material obtained from a back spout, all other materials were used in as-cast condition. Same material composition (CS) is employed as top tapping pipe material. The optical images in Figure 3.2 show the as-cast microstructures of Series-I cast irons and CS. Figure 3.3 summarizes the measured fraction of each phase in Series-I alloys.

Table 3.1- Chemical compositions of Series-I ferrous alloys for dissolution and intermetallic layer growth comparison.

Ferrous alloys		C	Si	Mn	Cr	Cu	Mo	S	P	Mg	*
GCIs	GCI-A	3.75	1.90	0.40	0.37	0.98	0.00	0.03	0.02	0.00	
	GCI-B	2.93	2.64	0.44	0.45	0.71	0.94	0.09	0.04	0.00	
	GCI-S	3.06	1.73	0.91	0.54	0.00	0.57	0.01	0.02	0.00	
DCIs	DCI-C	3.58	3.16	0.27	0.02	0.02	0.03	0.00	0.02	0.06	
	DCI-D	3.54	3.35	0.21	0.18	0.87	0.03	0.00	0.04	0.06	
	DCI-T	3.29	2.19	0.29	0.01	0.26	0.03	0.00	0.01	0.04	
Cast steel	CS (AS 2074)	0.20	0.21	0.06	2.39	--	0.95	0.03	0.027	--	

*Balance Fe

The GCIs were found to have graphite flakes distributed in a pearlitic matrix. GCI-A has the highest C content among these GCIs, which is reflected by the largest flake volume. No cementite was found in GCI-A matrix, while a dispersion of free cementite particles can be seen in the GCI-B and GCI-S microstructures. Compared to GCI-B, relatively lower C and Si contents - combined with Cr addition - led to higher cementite content in GCI-S. This is because the lower CE (%C + 1/3 %Si) of GCI-S, and Cr addition raises the cementite-eutectic temperature and decreases the iron-graphite eutectic temperature promoting the formation of cementite [4]. The DCIs comprise graphite spheroids distributed in pearlitic-ferritic matrixes. All DCIs have similar C contents, while the amount of Si is lowest in DCI-T

followed by DCI-C and DCI-D, in that order. The presence of pearlite promoters (Cr and Cu) in DCI-D led to a higher pearlite volume compared to unalloyed DCI-C. The CS specimens are mainly ferritic with some bainite.

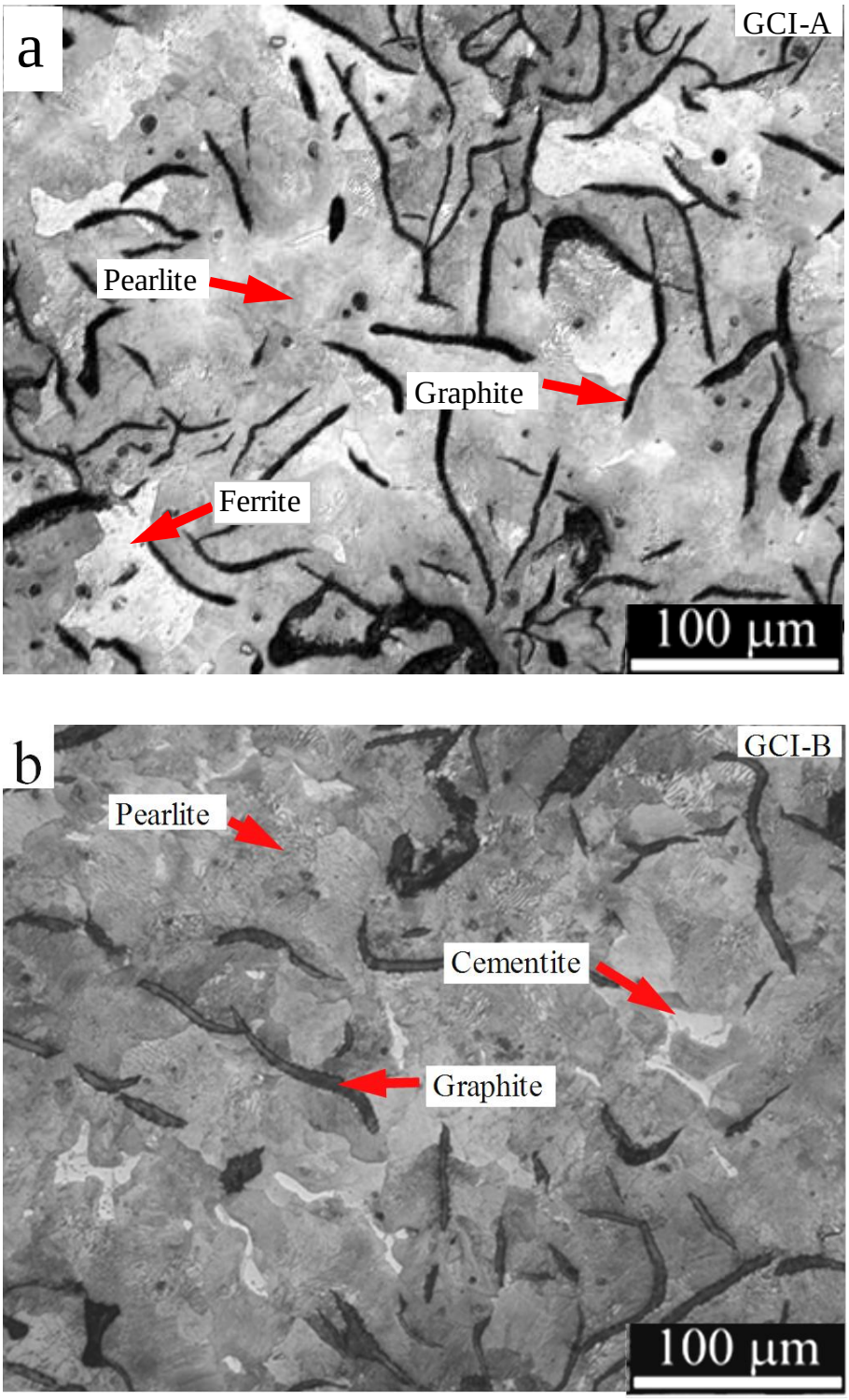

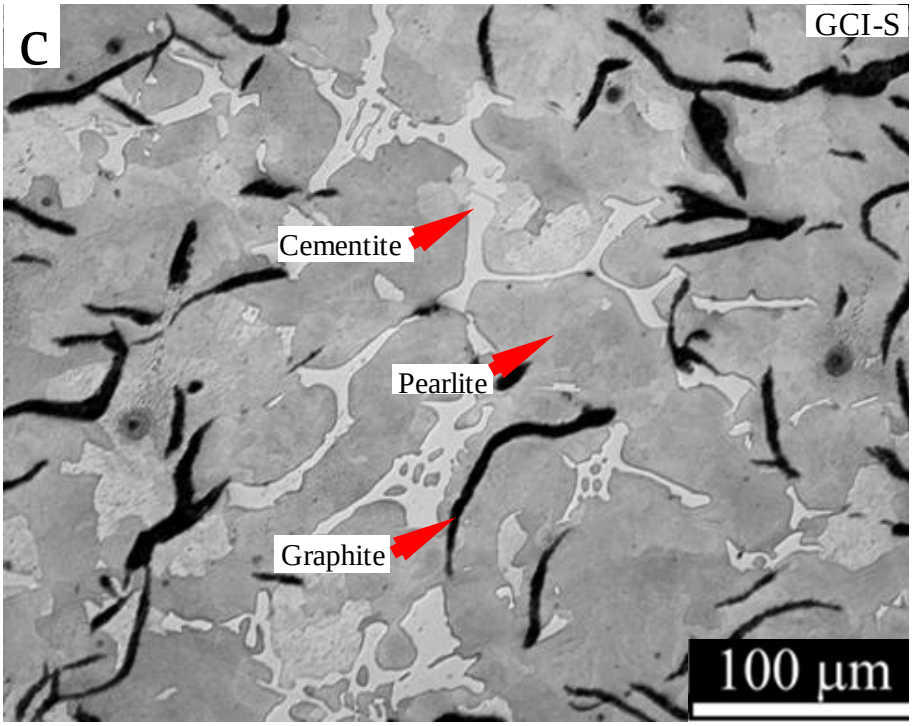
c
GCI-S
Cementite
Pearlite
Graphite
100 µm

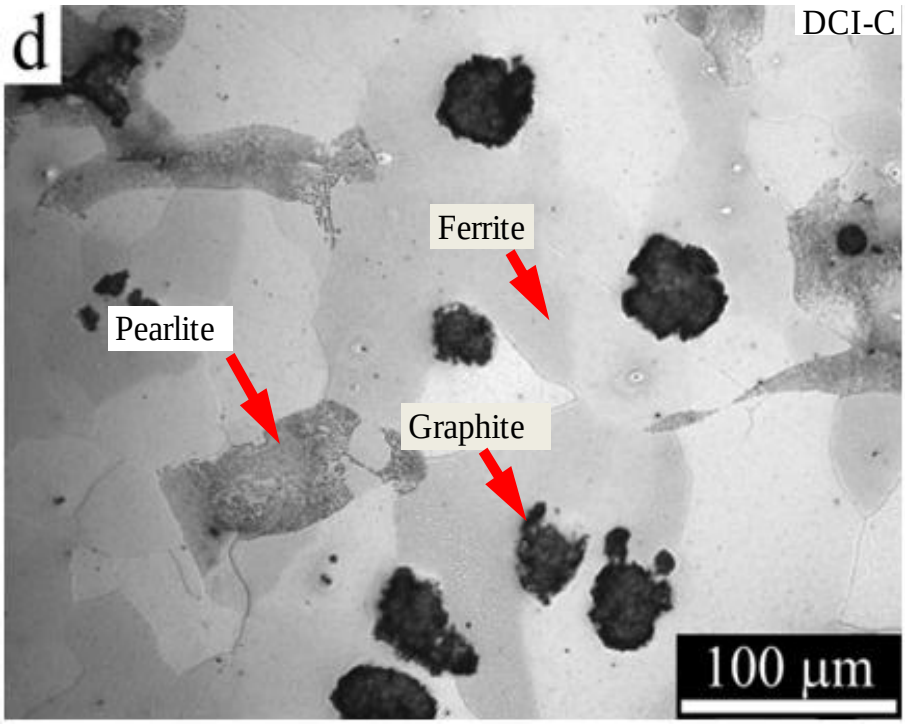
d
DCI-C
Ferrite
Pearlite
Graphite
100 µm

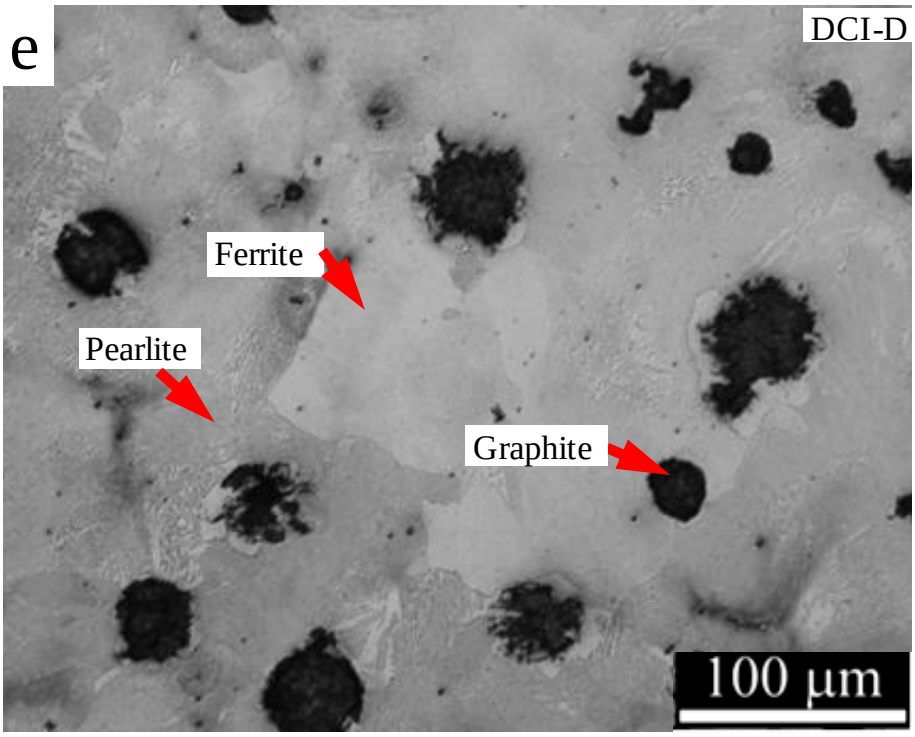
e
DCI-D
Ferrite
Pearlite
Graphite
100 µm

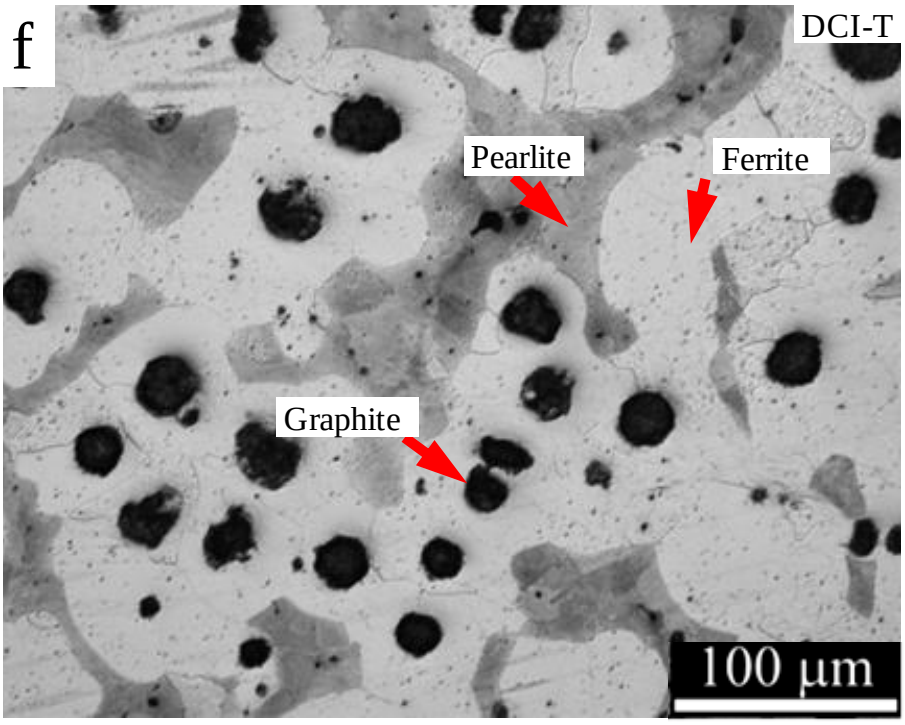
f
DCI-T
Pearlite
Ferrite
Graphite
100 µm

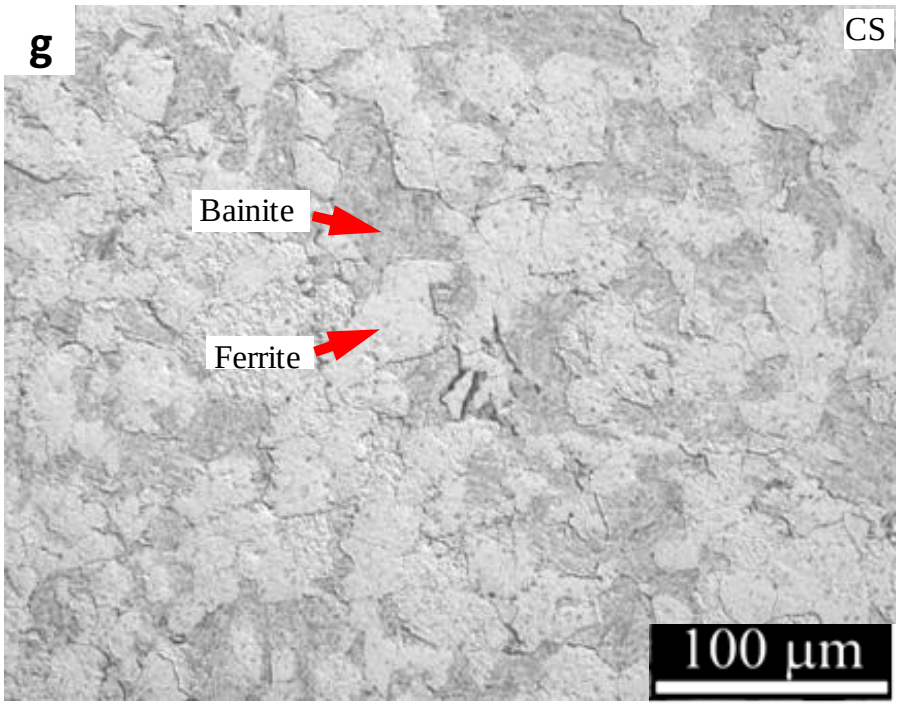

Figure 3.2 - Optical images of Series-I cast irons, a) GCI-A, b) GCI-B, c) GCI-S, d) DCI-C, e) DCI-D, f) DCI-T. B) CS (etched with 2% Nital).

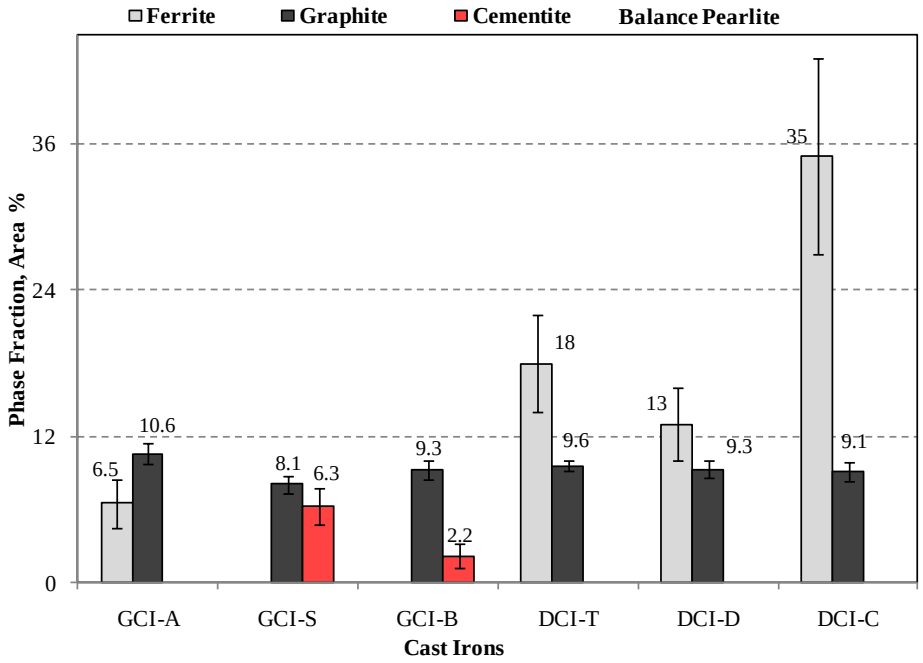

Figure 3.3 - Phase fractions of ferrite, cementite, graphite in Series-I cast iron alloys.

3.1.2.4 Series-II Materials

After analyzing the liquid Al corrosion characteristics of Series-I alloys, Series-II alloys were designed to obtain alloys with improved liquid Al corrosion resistance. Table 3.2 contains the list of Series-II cast iron compositions including two steel alloys.

Table 3.2 - Chemical compositions of Series-II GCIs and steels.

Ferrous alloys		C	Si	Mn	Cr	Cu	Mo	S	P	*
GCIs	GCI-E	3.62	1.37	0.94	1.16	--	0.60	0.01	0.03	
	GCI-F	3.63	1.46	1.02	1.29	1.00	--	0.01	0.03	
	GCI-BT	3.60	1.52	0.71	0.52	1.00	--	--	--	
	GCI-L	3.66	1.38	0.83	0.79	1.21	--	0.00	0.01	
Steels	AISI 4140	0.40	--	0.80	0.95	--	0.25	--	--	
	AISI W1	1.1	0.4	0.36	0.43	--	--	--	--	

* Balance Fe

The GCI-E is alloyed with Cr+Mo and the GCI-F alloy contains the Cr+Cu combination; both of these alloys have a similar base composition. The Cr+Mo combination is well established in improving the high temperature properties of GCIs; such as: tensile strength and oxidation and creep resistance. Compared to Cr+Mo, additions of Cu+Cr to GCI are known to enhance the oxidation resistance by a similar extent [5]; however, Cu+Cr addition was found to result in a slightly inferior thermal fatigue resistance [6-7]. Nevertheless, Mo is about five times costlier than Cu [8]. Thus selecting an alloy combination, Cr+Mo or Cr+Cu, for tapping pipes and other similar applications would largely depend upon the comparative liquid Al corrosion resistance and the cost of alloying.

Figure 3.4 shows the microstructures of Series-II alloys. Dispersion of cementite and graphite flakes can be seen in pearlitic matrixes of GCIs. No free ferrite was found in any of the GCI microstructures. Figure 3.5 summarizes the average fraction of cementite and graphite present in the Series-II GCIs.

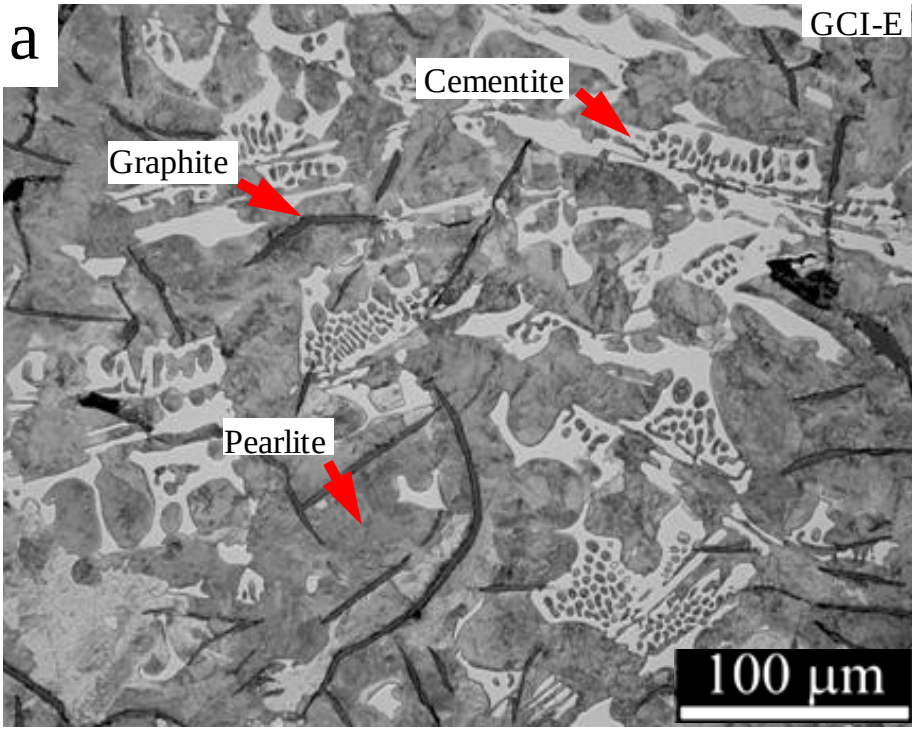
a
GCI-E
Cementite
Graphite
Pearlite
100 µm

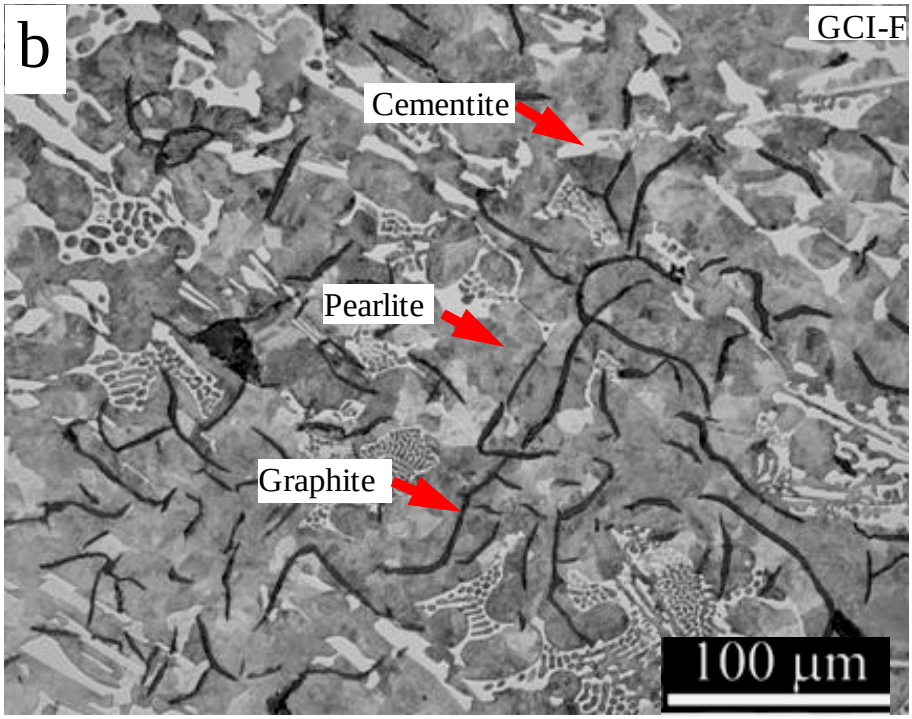
b
GCI-F
Cementite
Pearlite
Graphite
100 µm

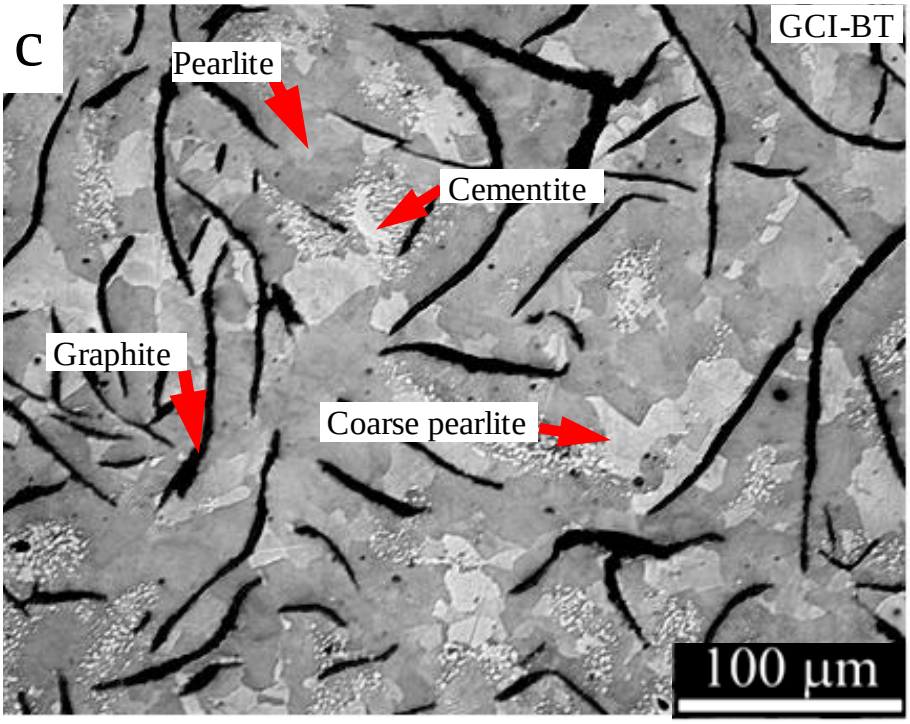
c
GCI-BT
Pearlite
Cementite
Graphite
Coarse pearlite
100 µm

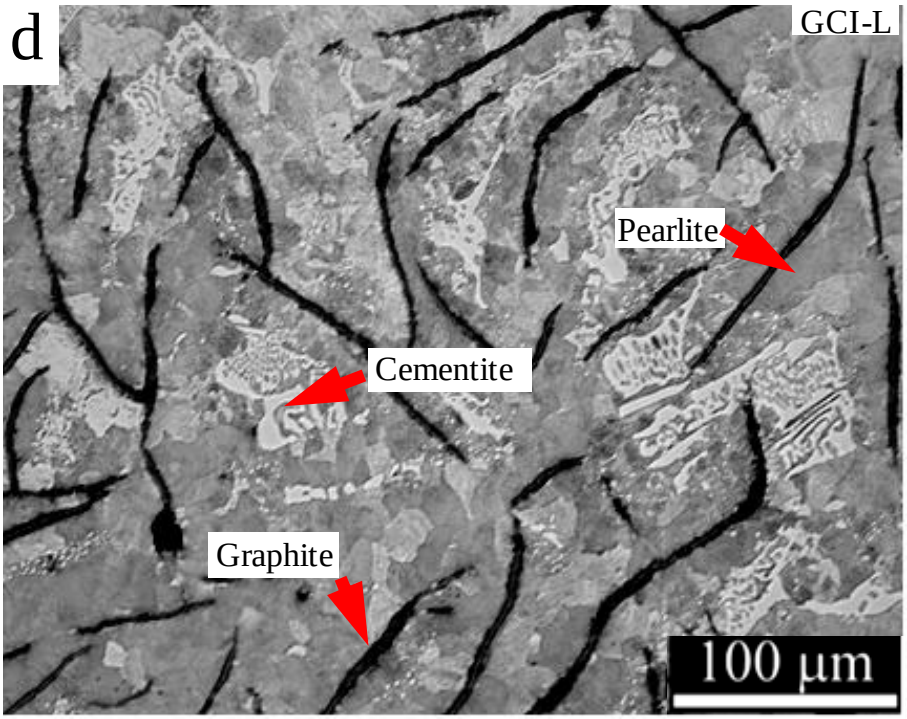
d
GCI-L
Pearlite
Cementite
Graphite
100 µm

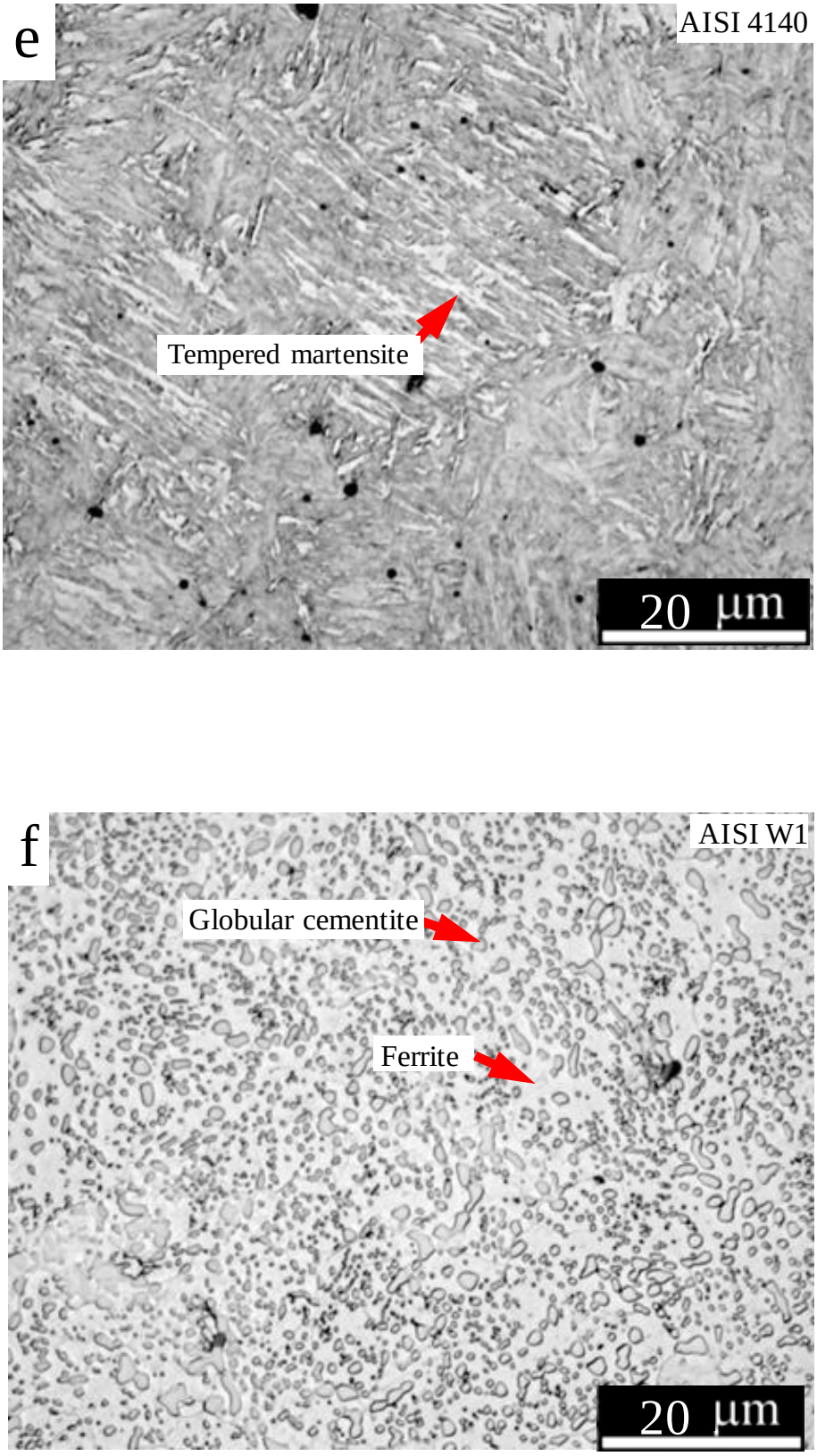

Figure 3.4 - Light optical micrographs of Series-II alloys, a) GCI-E, b) GCI-F, c) GCI-BT, d) GCI- L e) AISI 4140, f) AISI W1 (etched with 2% Nital).

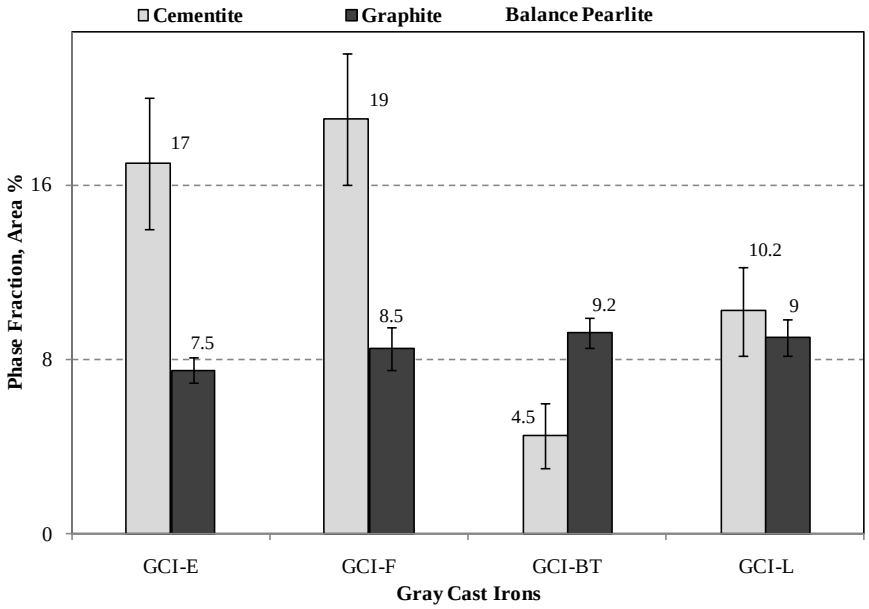

Figure 3.5 - Fractions of cementite and graphite in Series-II GCIs.

Both GCI-E and GCI-F contains about 1.2 wt.% Cr and 1 wt.% Mn, this resulted in a large fraction of cementite in their microstructures while the graphite fraction is reduced. GCI-BT composition is currently being used for bottom tapping pipes. Compared to GCI-BT, GCI-L composition is slightly higher in C, Mn, Cr and Cu and slightly lower amount of Si. The graphite fraction in GCI-L is slightly lower whereas cementite fraction is about two times greater than GCI-BT.

The as-received AISI 4140 steel specimens showed a typical structure of tempered martensite. This class of steels commonly goes through hardening and tempering heat treatment to achieve a higher strength. The as-received AISI W1 steel specimens were found to consist of globular cementite particles distributed in a ferritic matrix. This globular form of cementite is desirable for better machinability of high carbon steels.

3.2 Experimental Methods

3.2.1 Dynamic Corrosion Test Apparatus (Method-I)

The rotating disc method [9] is known to be the best available method to relate the hydrodynamic conditions to the dissolution rate under laminar flows. In this method, a solid disc shape specimen rotates into the melt and the solute concentration in the melt or mass loss is measured to determine the dissolution. However, this method was found to have a few limitations as described in Section 2.3.3.

Mountford and Glover [10] published the results of mass loss of 17 alloys of GCIs that were subjected to static Al melt at 800°C and 900°C. A link between the chemical composition and the liquid Al corrosion resistance of GCIs could be established, and no microstructural analyses were carried out [10]. Present research also involves a number of cast iron alloys to be compared for liquid Al corrosion resistance. Using the rotating disc method, it was anticipated that there could be difficulties in ranking the corrosion resistance of cast iron alloys. Moreover, the liquid Al in industrial application never reaches the saturation concentration (of Fe) thus the laboratory tests should be conducted in well undersaturated melts. Therefore, a new apparatus was needed. Figure 3.6 shows a schematic of the corrosion test apparatus that was designed to subject specimens of candidate materials to forced flow conditions of Al melt. The present apparatus has the following distinguishable features:

a) Highly dynamic forced flow conditions to compare the ferrous alloys for tapping pipe applications.
b) Parallelization of experiments as six specimens can be tested at a time.
c) Bulk liquid composition and temperature remains same for all specimens.

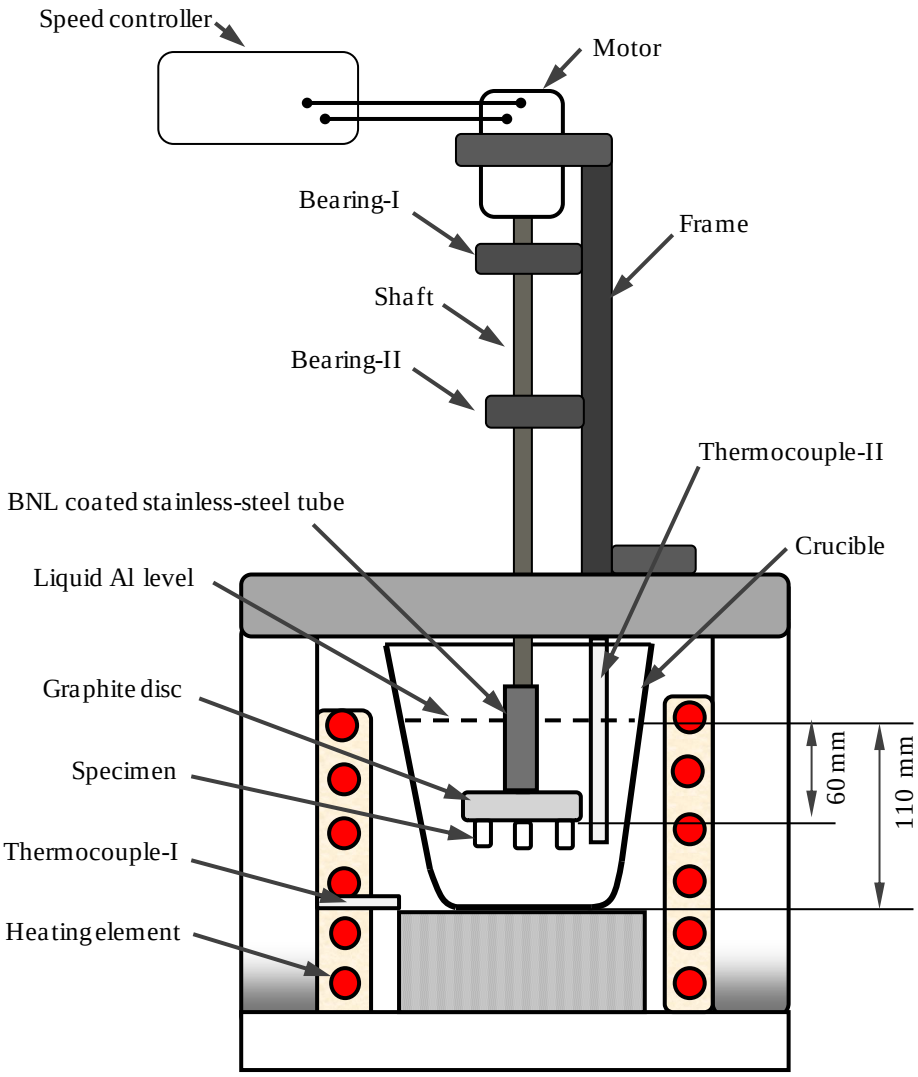

Figure 3.6 - A schematic of test apparatus for determining the corrosion resistance of ferrous alloys under forced flow.

A graphite disc (dimensions d = 100 mm, t = 20 mm) was used to hold specimens, so that they could be immersed and rotated within the Al melt at the required speed. The rotation speed of specimens was controlled within ± 0.02 m/s of the required speed. An electric resistance furnace of 5.5 kW capacity was used for melting and holding the Al at required temperature. A clay-graphite crucible was used to contain the liquid Al. Two K-type thermocouples were used: thermocouple-I for controlling the furnace temperature and thermocouple-II to indicate the actual melt temperature. The shaft connecting the motor and

disc was safeguarded against molten Al by a sacrificial Boron Nitride Lubricoat® (ZYP Coatings, USA) coated stainless steel tube, which was recoated before each test.

A large quantity (4 kg) of commercially pure (99.97%) Al was used for each test so that the concentration of Fe remains well below its saturation concentration. The cylindrical test specimens were threaded so they could be screwed to the lower surface of the graphite disc. Figure 3.7 shows a photograph of the cylindrical test specimens. The cylindrical (d = 11 mm, h = 15 mm) test specimens were machined from the as-cast blocks (45 mm x 45 mm x 160 mm) of cast irons. CS specimens were machined from approximately 40 mm x 50 mm x 200 mm section of an after-service back spout, while for AISI 4140 and AISI W1 steels, 14 mm diameter rods were used. At the initial stage of dissolution testing, the as-machined specimens with one circular face in as-cast condition were utilized. However, owing to the difficulties in ranking the corrosion resistance of cast irons (Appendix B), specimens with all finished surfaces were used for subsequent testing.

Figure 3.7 - Photograph of cast iron specimens for corrosion testing under forced flow.

The experimental procedure for the dissolution testing included the following steps.

a) The specimens were finished with 220 grit and 600 grit SiC papers and ultrasonically cleaned in ethanol. Two specimens of each alloy were compared at each set of time and

temperature. Before testing, the mass of each specimen was measured using an electronic weighing balance with a standard accuracy of ± 0.0001 g.

b) 25 kg Al billets obtained from NZAS were cut into small pieces (60 mm x 80 mm x 80 mm approx.) using a band saw. Al pieces were melted and maintained at the required temperature.

c) For each test, the graphite disc with six specimens screwed at a fixed radius (38 mm) was preheated to 110°C and subsequently immersed into liquid Al. Attack of liquid Al on specimen collars was found to cause difficulties in unscrewing the specimens after test. Therefore, the successive coatings of FIBERFRAX® (UNIFRAX, USA) and Boron Nitride Lubricoat® were applied to protect the specimen collars.

d) The test temperatures were kept at 850 ± 5°C and 950 ± 5°C, and the total exposure time varied between 1200s and 4500s. The melt was superheated by 20-25°C above the test temperature and the mass loss during the temperature stabilization period was excluded from the total mass lost. For evaluating the mass loss during the temperature stabilization period, separate dissolution tests were performed for a period of 600s. In dynamic corrosion tests the speed of rotation was kept at 0.48 m/s because at this speed oxide formation at the melt surface was equivalent to the static melt conditions. The amount of oxide was determined from the amount of Al recovered after each test.

e) The loose solidified Al from the specimens was first removed mechanically (by pulling apart). Afterwards, the specimens were immersed in 10 % NaOH solution for at least 3 hours and this step was repeated a few times to ensure the complete removal of Al.

f) The specimens were ultrasonically cleaned in acetone and dried. The mass of each specimen was measured.

In order to achieve similar melt conditions for cast irons, it was considered important to test these simultaneously, thus one specimen of each alloy was tested at a time. Two specimens of each alloy were utilized for each set of time and temperature. Wherever required the dummy specimens of cast irons were used because the experimental set up takes six specimens at a time.

Considering the available literature [11], relating the dissolution rate to the hydrodynamic parameters is difficult in this case. The expected outcome therefore was the ranking of cast iron and steel alloys according to their corrosion resistance.

3.2.2 Method for Characterizing Formation and Growth of Intermetallic Compounds (Method-II)

In order to investigate the Fe-Al intermetallic compound growth and dissolution characteristics, cast iron and steel alloys were subjected to static Al melts. In addition to recording the intermetallic layer thickness, dissolution in-terms of specimen dimensions was also noted.

To determine the intermetallic layer growth kinetics of several ferrous alloys at various temperatures, a large number of specimens were required. In consideration of the dissolution test apparatus (Method-I), machining a large number of cylindrical specimens of cast irons with threaded ends was not convenient. Moreover, a large quantity (4 kg) of Al was required for each test, which involves a considerable amount of time in cutting the Al billets into small pieces.

Furthermore, there may be a correlation between the intermetallic layer growth in a small melt volume and the dissolution in a large melt volume comprising the dynamic corrosion conditions. Such a link would be useful to predict the relative liquid Al corrosion

resistance of ferrous alloys from their intermetallic layer growth characteristics in a confined melt volume that is more convenient to use in a laboratory environment.

An immersion test apparatus (Figure 3.8) was devised to subject various ferrous alloy specimens to similar Al melt conditions. A 1.5 kW electric resistance furnace was used to maintain the liquid Al at temperature. Two K-type thermocouples were used; thermocouple-I was used to control the furnace temperature and thermocouple-II was used to indicate the melt temperature.

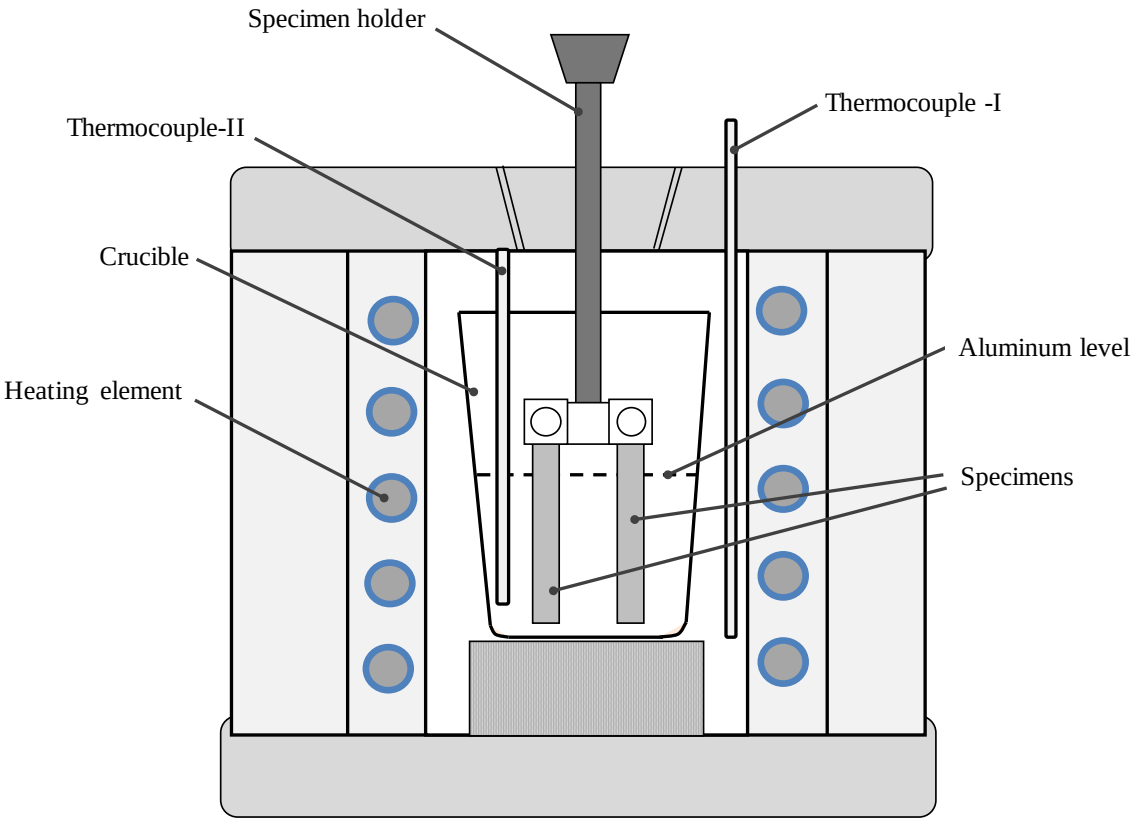

Figure 3.8 - A schematic of static immersion test apparatus for determining the intermetallic layer growth characteristics.

Figure 3.9 shows the photograph of a test specimen coupon (6 mm x 6 mm x 45 mm). For each test, four ferrous alloy specimens were mounted in a suitably designed fixture that was used to immerse the specimens into liquid Al.

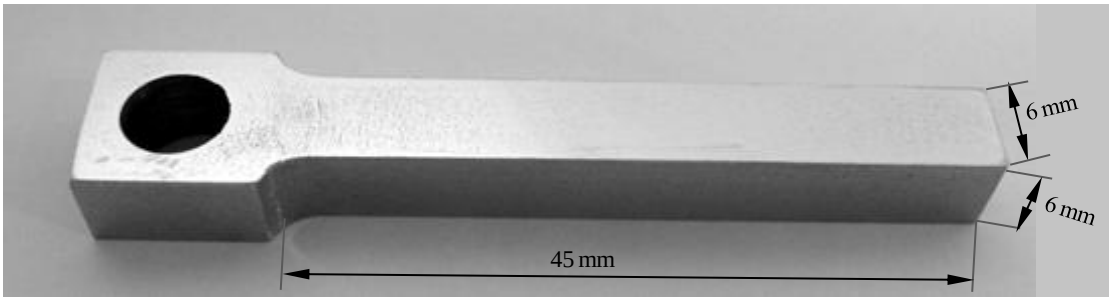

Figure 3.9 - Photograph of the specimen for the formation and growth analysis of the intermetallic compounds.

The test procedure included the following steps.

a) For each test, 0.25 kg of commercially pure Al obtained from NZAS was melted in a Boron Nitride Lubricoat® coated clay-graphite crucible. Prior to melting, the oxide layer on the Al pieces was removed by dipping in 10 % NaOH solution for 1200s, followed by washing in a detergent and ethanol rinse.

b) All lateral surfaces of the machined specimens were finished with 600 grit SiC paper and subsequently ultrasonically cleaned in ethanol. The specimens were preheated to 110°C before immersion. Before immersing the specimens into melt, the Al oxide layer from the melt surface was skimmed off.

c) To compensate for the heat lost during immersion, the melt was superheated by 30°C, 40°C and 55°C for the respective test temperatures of 750°C, 850°C and 950°C. The temperature was controlled within ± 5°C except the initial immersion time (0-180s); immediately after immersing the specimens into the melt - the temperature was recorded at 5-12°C lower than the test temperatures.

d) Generally, the test time varied between 60s and 2400s; for specific tests, the specimens were also tested for 7200s. After each test, the specimens were slowly removed from the melt and allowed to air cool.

3.2.2.1 Specimen Preparation and Electron Microscopy Techniques

After the immersion test, specimens were cut perpendicular to their longitudinal axis 10 mm from the lower end to examine the intermetallic compounds. The cutting plane was maintained perpendicular to the longitudinal axis of specimen. The 10 mm sections of the test specimens were mounted in Buehler Probemet® conductive mounting compound and polished using LECO AP-60® automatic polisher following the steps described in Section 3.1.2.1. The specimens were further polished with 50 nm and 20 nm size colloidal silica suspension (MasterMet®) using a Buehler Minimet-II® automatic polisher.

The polished immersion test specimens were examined by optical and scanning electron microscopy techniques. A JEOL JSM 6100 SEM and a JEOL 7000F field emission SEM were used for the identification and growth analysis of intermetallic compounds. The JEOL EX-2300 BU Energy Dispersive X-ray Analyzer fitted on JEOL 7000F SEM was used for the compositional analysis of the formed intermetallic layers. For enhanced phase contrast, the BSE mode was used to capture the images of the intermetallic layers. Afterwards, these photomicrographs were used to record the growth of intermetallic compounds. A magnification of 200x was used for evaluating the intermetallic layer thickness of η-Fe_2Al_5.

The crystal structures of the intermetallic compounds were characterized using the HKL Technology Nordlys II EBSD system mounted on a JEOL - 6100 SEM. The specimen holder was tilted at 70° with respect to the incident beam. An accelerating voltage of 20 kV and working distance of 30 mm was used. The BSE (Back Scattered Electrons) from the crystallographic planes of specimen surface cast a unique crystallographic diffraction pattern known as “Kikuchi pattern”, which indicates the phase present and the crystallographic orientation. The obtained electron back scatter patterns were compared with the possible intermetallic compounds entered and stored in HKL Technology’s Flamenco software. In

addition to the characterization of the intermetallic compounds, EBSD was also utilized to reveal the crystallographic growth direction of η-Fe_2Al_5 and θ-$FeAl_3$.

The specimen dimensions before and after the test were measured using the digital micrometer on LECO M-400-HI Microhardness Tester with a cumulative measurement accuracy of ± 5 μm.

3.3 Boronizing

To address the feasibility of a boronizing treatment for tapping pipe applications, selected ferrous alloys (DCI-T, GCI-S and CS) were boronized for comparing their corrosion rates under flow assisted liquid Al corrosion.

Three cylindrical specimens of each alloy were boronized: two for corrosion resistance comparison and the third for determining the morphology of Fe-B intermetallic layers. A layer of Ekabor® (BorTec GmbH, Germany) boronizing paste of 4-6 mm thickness was applied to the cylindrical specimens with finished surfaces. The pasted specimens were dried in hot air and then placed in a cylindrical steel container that was filled with sand to minimize the possible oxidation during heat treating. The steel container containing the specimens was heat treated at 950°C for 4 hours. The formed boride layers are discussed in Appendix D.

Chapter References

[1] M.M. Shea, American Foundry Society Transactions, 04 (1978) 23-30.

[2] J. Janowak, J.D. Crawford, K. Roehrig, Casting Engineering, 14 (1982) 31-41.

[3] M. Blair, T.L. Steven, Steel Castings Handbook, ASM International, Materials Park, Ohio, 1995.

[4] J.F. Janowak, R.B. Gundlach, American Foundry Society Transactions, 90 (1982) 847-863.

[5] J.R. Davis, ASM Speciality Handbook-Cast Irons, ASM International, Materials Park, Ohio, 1996.

[6] M.C. Rukadikar, G.P. Reddy, International Journal of Fatigue, 9 (1987) 25-34.

[7] K. Roehrig, American Foundry Society Transactions, 86 (1978) 75-88.

[8] www.internationalpbx.com/pdfs/PBX-Brochure.pdf.

[9] V.N. Eremenko, Y.V. Natanzon, Materials Science, 2 (1968) 411-413.

[10] F.A. Mountford, T.J. Glover, Foundry Trade Journal, 120 (1966) 849-852.

[11] H. Grijseels, D. Crommelin, C. Blaey, Pharmaceutisch Weekblad Scientific Edition, 3 (1981) 1005-1020.

CHAPTER 4 : RESULTS

Introduction

This chapter starts with a comparison of the performance of cast iron and steel alloys under static and flow assisted liquid Al corrosion. When a cast iron is exposed to liquid Al, the Fe-Al reaction phases form and grow, and simultaneously, the Fe-substrate starts to dissolve into the melt. The liquid Al corrosion rate of ferrous alloys was believed to depend upon the advance of intermetallic layer towards the substrate, and its dissolution and/or spallation into the melt. To understand these two types of phenomenon, the substrate/intermetallic layer interfaces of various ferrous alloys were investigated and growth of the intermetallic layers was compared with the corrosion rates.

4.1 Characteristics of the Dynamic Corrosion Test Apparatus

The newly designed dynamic corrosion test apparatus (Section 3.2.1) was successfully used to compare the corrosion rates of various ferrous alloys. From the initial test runs, it was clear that all seven ferrous alloys were corroded aggressively by liquid Al. Two methods were employed to determine the dissolution-time relationship of ferrous alloys using the dynamic corrosion test apparatus: i) mass dissolution and, ii) semi-instantaneous dissolution.

Mass dissolution was determined by mass lost per unit time. Semi-instantaneous dissolution considered the decreasing area of specimen to calculate volume loss per unit time and per unit area. For details see Appendix C. In both types of analysis, at 850°C, the dissolution and time relationship was found to be linear. However, at 950°C, the initial corrosion rates (at 600s) of the majority of alloys were found to be significantly higher than the subsequent periods of exposure. These results identified that the new apparatus with dynamic corrosion conditions can be used to obtain a linear rate constant from a set of dissolution-time data obtained after an initial exposure time (600s). Relatively lower corrosion rate after the initial

time period may be related to factors such as changing hydrodynamic conditions, phase transformations in the substrate materials and formation of Al oxide within the melt. These effects were not investigated in the current work.

The feature of providing dynamic corrosion conditions depicted a clear picture of the corrosion resistance of various alloys of GCI, DCI and steel. Under flow assisted corrosion conditions, material loss occurred at an enhanced rate, which magnified the relative differences between the dissolution rates of cast irons. Moreover, this apparatus provided the increased uniformity in bulk melt composition and temperature for the alloys under comparison.

4.2 Comparative Liquid Al Corrosion Resistance

The dynamic corrosion test apparatus was used to compare the corrosion rates of ferrous alloys under static and forced flow conditions of liquid Al. As mentioned in Section 4.1, with respect to the exposure time, two different regimes of material loss were identified. To simplify the data analysis, the comparative corrosion resistance of ferrous alloys was determined in terms of the mass dissolution rate over a single time period. Static tests were also performed on Series-I alloys. Two samples of each material were used for each set of conditions. The mass dissolution rate (R′) can be given by:

$$R' = \frac{m'}{t'} \tag{4.1}$$

where m′ is the mass dissolution over a single test period (t′). Table 4.1 lists t′ for different conditions of flow and temperature.

Table 4.1 - Test times (t′) for calculating R′ of ferrous alloys.

Test	850°C-static	850°C-0.48 m/s	950°C-static	950°C-0.48 m/s
t′(s)	2400	3900	2400	3000*

*For Steels t′ = 600s

4.2.1 GCIs

The corrosion resistance of Series-I GCIs was investigated under different conditions of temperature and liquid Al flow, Figure 4.1 shows the obtained R′ of GCIs. It is clear that GCI-A has a higher corrosion resistance than GCI-S, and GCI-B showed the highest material loss at each set of conditions. Under static melt conditions at 850°C, GCI-B and GCI-S dissolved more slowly than GCI-A. Also, a large difference in the dissolution rates of two specimens for each alloy is apparent in this case - shown by error bars. Under static melt conditions, this difference was within ±10 to ±26 % of the mean value while under forced flow it varied between ±2 to ±6 %.

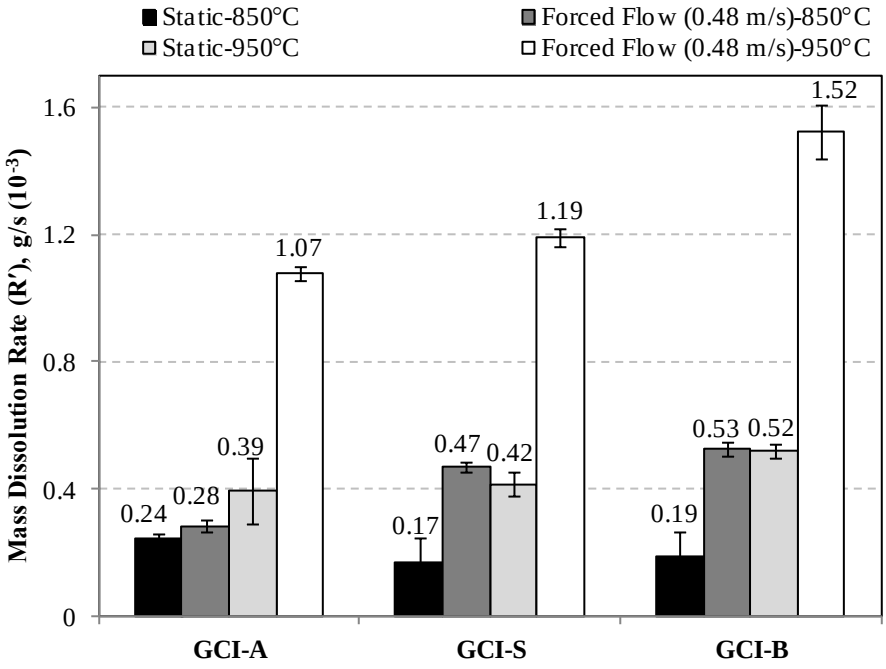

Figure 4.1 - Mass dissolution rate (R′) of Series-I GCIs under static and forced flow (0.48 m/s) melt conditions at 850°C and 950°C.

At 850°C, with the change in melt condition from static to forced, a slightly increased dissolution rate of GCI-A is apparent, while GCI-S and GCI-B dissolved at a higher (> 2.5 times) rate. As expected, the dissolution of all materials was more rapid at 950°C than at 850°C. Under static and forced flow conditions at 950°C, GCI-S dissolved at a rate

approximately 1.1 times higher than GCI-A. However, under forced flow at 850°C, this ratio was 1.7. Under forced flow conditions at 850°C, GCI-B dissolved approximately 2 times faster than GCI-A. While under forced flow at 950°C, this ratio was decreased to 1.4.

From the analysis of corrosion rates of Series-I alloys, Series-II alloys were prepared to further investigate the effect of composition and microstructure on liquid Al corrosion. Figure 4.2 shows a comparison of R′ of Series-I and Series-II GCI alloys. Series-II alloys dissolved more slowly than Series-I alloys. The dissolution rate of GCI-BT was about 17% slower than that of GCI-A. GCI-BT composition is currently used for bottom tapping pipes. GCI-E and GCI-F were corroded at similar rates (differed only by 4%). GCI-F exhibited about approximately 12 % higher dissolution rate than GCI-BT. Alloy GCI-L outperformed all the GCIs under investigation, which showed a dissolution rate of approximately 20 % lower than GCI-BT.

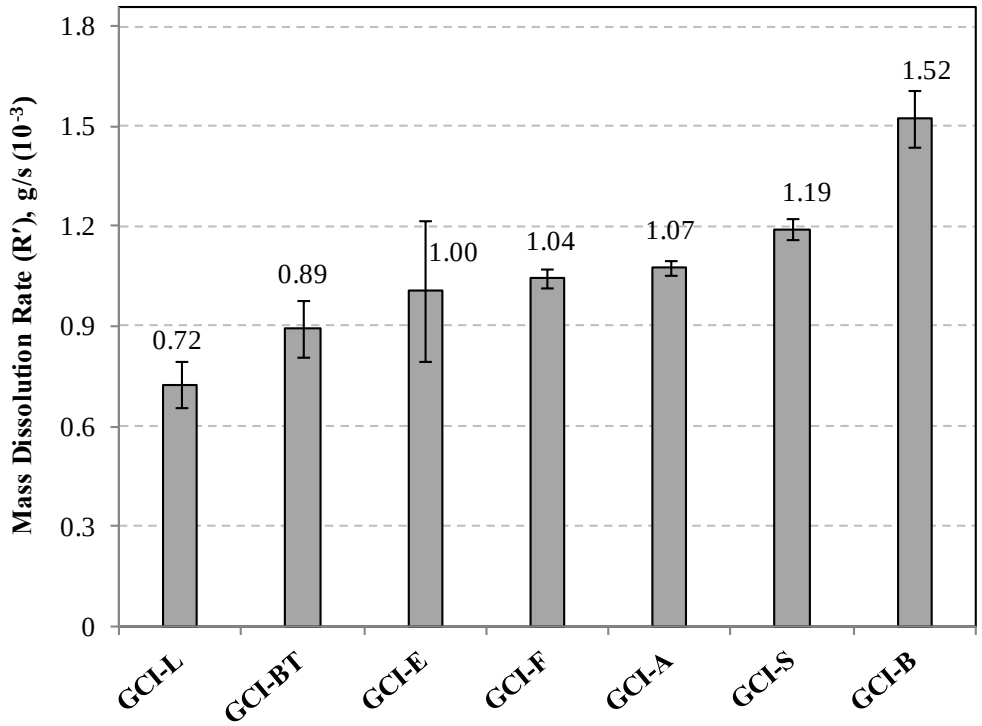

Figure 4.2 - Mass dissolution rates (R′) of Series-I and Series-II GCIs under forced flow (0.48m/s) at 950°C.

4.2.2 DCIs

Figure 4.3 shows R′ of DCIs under various test conditions. DCI-C showed the highest dissolution rate at both test temperatures. The corrosion resistance of DCI-D was found to be inferior than DCI-T. However, DCI-D was found to possess significantly superior corrosion resistance compared to DCI-C. At both the temperatures, DCI-C was largely affected by the change in melt conditions from static to forced flow. It was surprising that under forced flow conditions DCI-C exhibited higher dissolution at 850°C compared to 950°C. At each set of conditions, DCI-D dissolved approximately 1.2-1.3 times faster than DCI-T. Under static conditions, DCI-C dissolved 2 and 1.3 times faster than DCI-T for the respective temperatures of 850°C and 950°C. At 850°C under forced flow, corrosion rate of DCI-C was about 5 times greater than DCI-T.

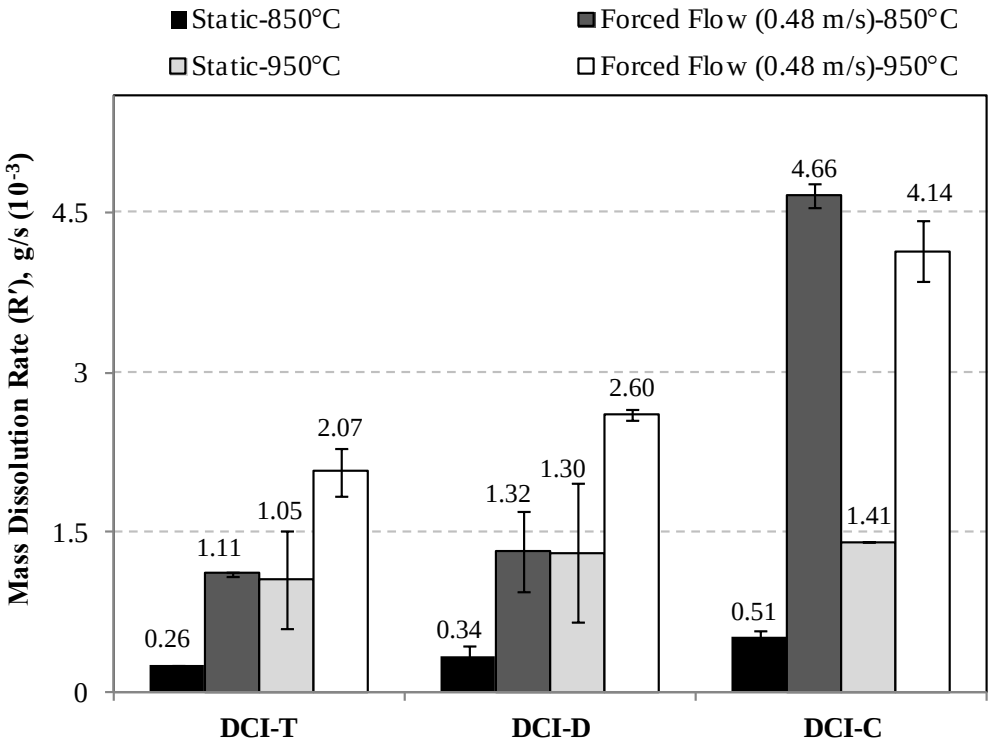

Figure 4.3 - Mass dissolution rate (R′) of Series-I DCIs under static and forced flow (0.48 m/s) melt conditions at 850°C and 950°C.

4.2.3 Steels

Corrosion rates of CS were investigated at various conditions of flow and temperature. Figure 4.4 shows the R′ of CS under various exposure conditions. At 850°C, with a change in melt conditions from static to forced, the corrosion rate of CS was increased about 12 times. Under static melt conditions, CS dissolved about 6 times faster at 950°C than 850°C. Under the forced flow at 950°C, CS samples dissolved completely thus their actual rate is expected to be higher than the recorded value.

Series-II steels were tested at 950°C-0.48 m/s, Figure 4.5 shows the calculated R′ of CS, AISI 4140 and AISI W1 steels. The steels with higher C contents (AISI 4140 and AISI W1) performed exceptionally well compared to the low C (CS). A significant decrease of corrosion rate (~12 times) was found with increase in C content from 0.2 (CS) to 0.4 wt.% (AISI 4140). However, a further increase to 1.1 wt.% C (AISI W1) exhibited a slight decrease in the corrosion rate.

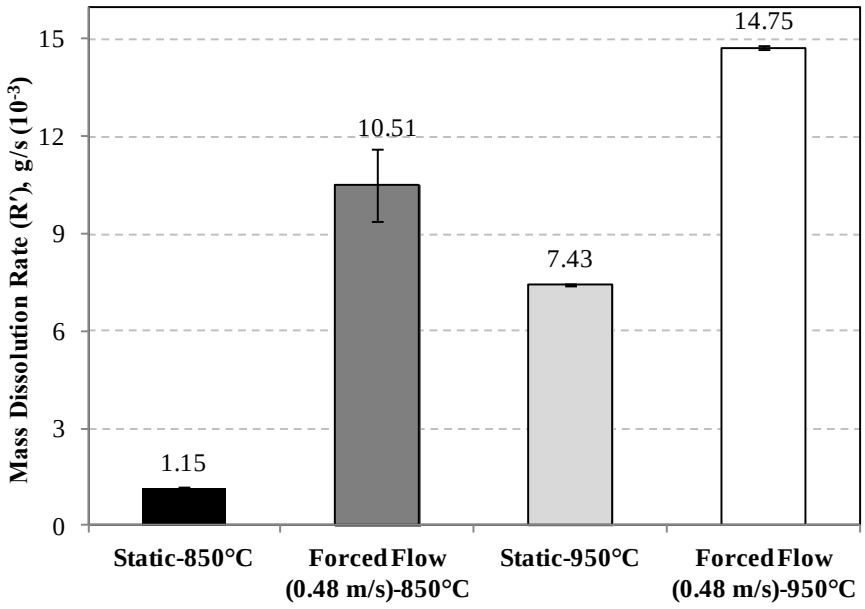

Figure 4.4 - Mass dissolution rate (R′) of CS under static and forced flow (0.48 m/s) melt conditions at 850°C and 950°C.

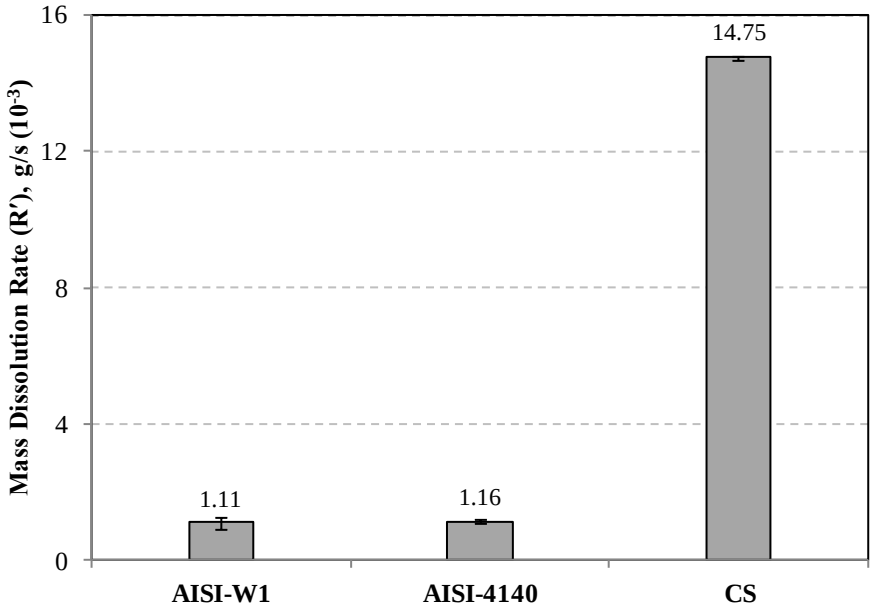

Figure 4.5 - Mass dissolution rates (R′) of steel alloys at 950°C under forced flow (0.48 m/s).

4.2.3.1 Comparing GCIs, DCIs and Steels

Data presented in Figure 4.1, Figure 4.2, Figure 4.3 and Figure 4.5 clearly illustrate that, regardless of the test conditions, the GCIs generally possess greater liquid Al corrosion resistance than DCIs and steels. However, AISI 4140 and AISI W1 steels showed significantly better corrosion resistance than GCI-B. DCI-T showed the lowest corrosion rate among the Series-I DCIs, and AISI 4140 steel exhibited approximately 1.7 times lower dissolution rate than DCI-T.

4.3 Identification of Intermetallic Phases

Intermetallic compounds formation at the substrate/liquid Al interfaces of several alloys of cast irons and steels were investigated to explore the mechanisms of corrosion. Moreover, to compare the liquid Al corrosion behaviour of cast irons and steels under industrial environment and laboratory conditions, materials from both types of exposure conditions were examined for the intermetallic compound formation.

4.3.1 Laboratory Materials

A series of experiments were undertaken to investigate the intermetallic compounds formed by exposing several compositions of GCIs, DCIs and steels to static liquid Al melts. The experimental method used for this purpose is described in Section 3.2.2. In the present work, various new phases were found to form from the exposure of cast iron and steel alloys to liquid Al, which are discussed after the description of common characteristics of compound formation in these materials.

4.3.1.1 Common Characteristics

4.3.1.1.1 η-Fe_2Al_5 and θ-Fe_3Al

The results of EBSD and EDS analysis of the intermetallic layers showed that irrespective of the different chemical compositions, all ferrous alloys exhibited a thick layer of η-Fe_2Al_5, and a relatively thin (5-15 μm) stratum of θ-$FeAl_3$ was found towards the solidified Al. Figure 4.6 shows an example of the intermetallic layer. The morphologies and thicknesses of these intermetallic layers were found to depend upon the substrate composition and experimental conditions.

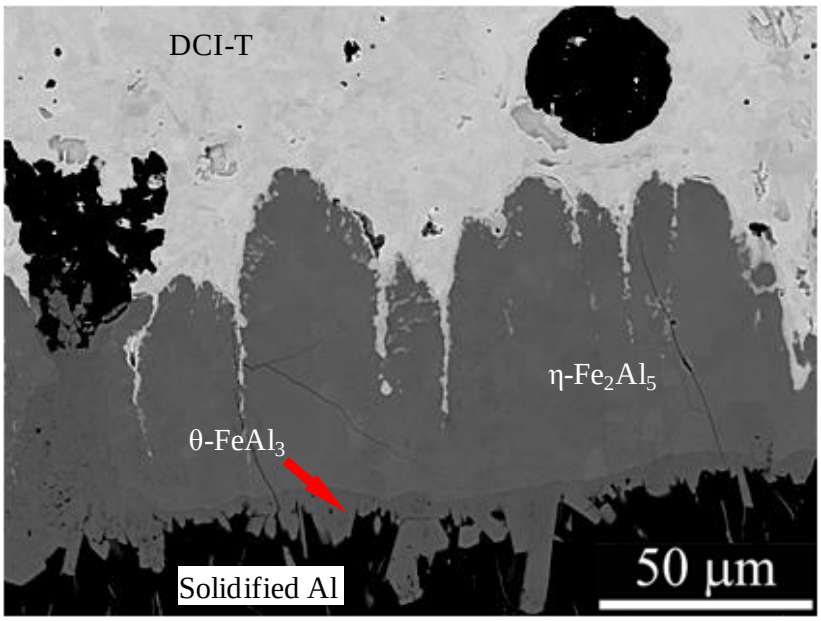

Figure 4.6 - An example of an intermetallic layer formed in laboratory samples.

Figure 4.7 shows an example of the dispersion of θ-Fe_3Al particles in solidified Al near the GCI-A substrate (950°C-2400s-static). However, in solidified Al no η-Fe_2Al_5 particles have been detected in any of the laboratory samples. This finding is in agreement with [1] and shows a discrepancy with [2], where the particles dispersed in solidified Al were suggested to be of various phases such as η-Fe_2Al_5, ζ-$FeAl_2$ and θ-$FeAl_3$.

Figure 4.7, shows the θ-$FeAl_3$ particles (typically 30-500 μm long) protruding from the η-Fe_2Al_5 of GCI-A specimen (950ºC-2400s-static) and relatively small size (typically 20-200 μm long) particles are seen dispersed in the solidified liquid Al. Figure 4.8 shows a magnified image of solidified Al at area 'A' in Figure 4.7 and the dispersion of needle-shaped particles can be seen. These are approximately 30-50 times smaller than the large θ-$FeAl_3$ particles, and found uniformly dispersed within the solidified Al. EDS detected Fe in these particles. However, owing to their small size conclusive identifications by EDS and EBSD could not be made. The formation the θ-$FeAl_3$ particles similar to GCI-A specimen (950ºC-2400s-static), was even found in the specimens of short durations (60s) of exposure. Figure 4.9 shows an example of CS specimen (950ºC-60s-static). Similar to GCI-A (950ºC-2400s-static), the typical direction of growth of θ-$FeAl_3$ was found to perpendicular to the specimen surface.

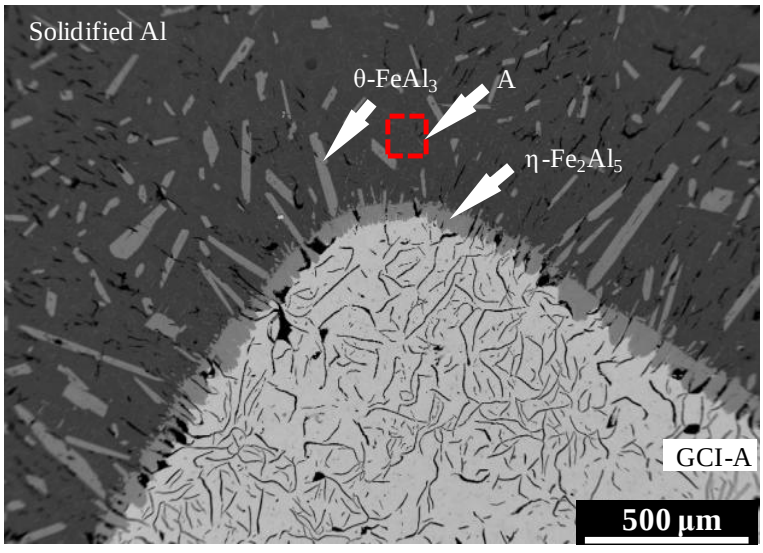

Figure 4.7 - θ-$FeAl_3$ particles at a GCI-A specimen (950°C-2400s-static).

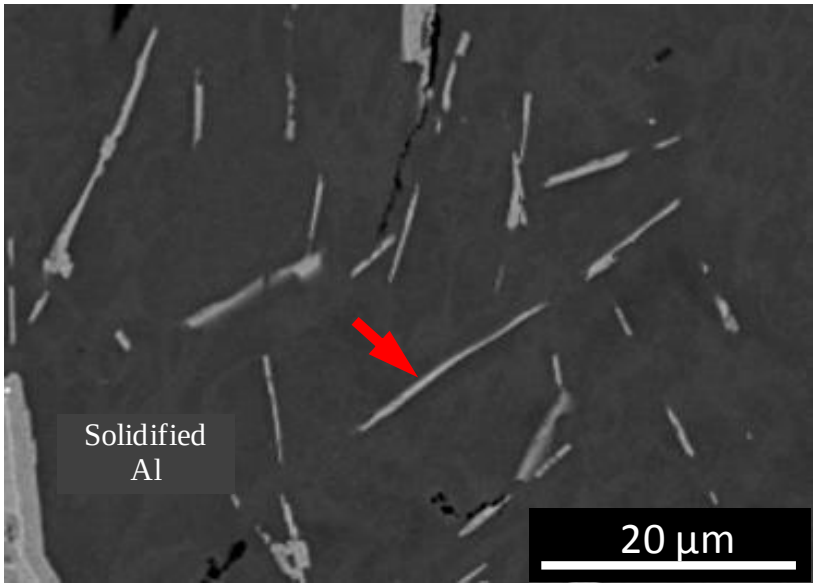

Figure 4.8 - Magnified image of area ‘A’ in Figure 4.7.

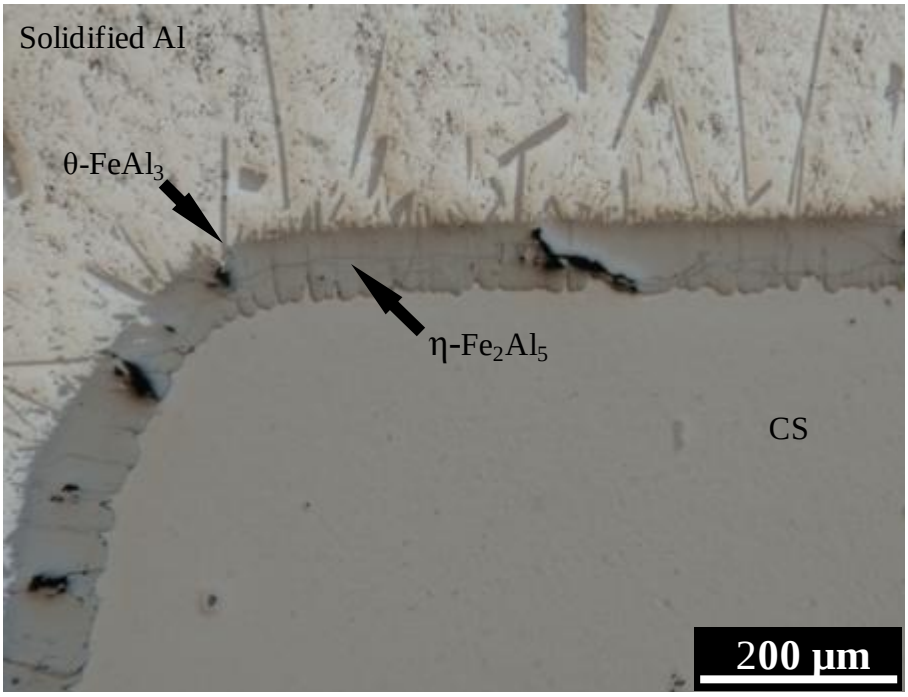

Figure 4.9 - θ-$FeAl_3$ particles at a CS specimen (950C-60s-static).

To reveal the growth characteristics of η-Fe_2Al_5 and θ-$FeAl_3$ phases, the intermetallic layers of specimens exposed to static liquid Al were examined using SEM and EBSD. Previous studies determined that η-Fe_2Al_5 preferentially grows along its c-axis [3-4]. However, to date there are no reports on the preferred growth direction of θ-$FeAl_3$.

Using EBSD the preferred crystal orientation of η-Fe_2Al_5 and θ-$FeAl_3$ with respect to the direction of their growth was determined. The EBSD analysis on CS, DCI-T and GCI-S specimens showed similar results; thus only the results on a CS (750ºC-1200s-static) specimen are presented here. In Figure 4.10 and Figure 4.12, SEM images show the η-Fe_2Al_5 intermetallic layer and θ-$FeAl_3$/η-Fe_2Al_5 interface on the CS specimen, respectively.

Figure 4.11 and Figure 4.13 show the respective EBSD maps and inverse pole figures for the preferred growth direction of η-Fe_2Al_5 and θ-$FeAl_3$ phases. EBSD analysis showed that each elongated crystallite of η-Fe_2Al_5 and θ-$FeAl_3$ is a single crystal. The θ-$FeAl_3$ layer that appears continuous in the SEM image is polycrystalline. Thus it is difficult to distinguish between the thin θ-$FeAl_3$ layer and θ-$FeAl_3$ particles. The entire layer can be the growing or remaining roots of the disintegrated of θ-$FeAl_3$ particles.

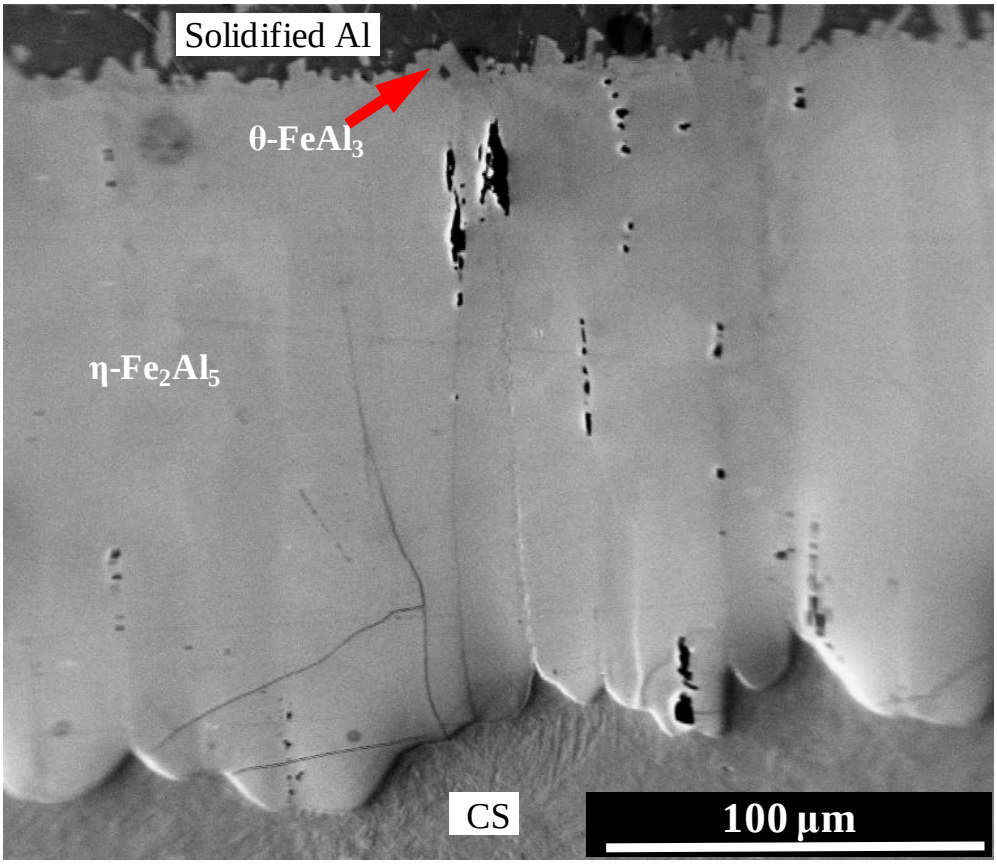

Figure 4.10 - SEM image showing the intermetallic layer at a CS specimen (750°C-1200s-static) for EBSD analysis.

The inverse pole figures were used to represent the relative alignment of the unit cells on the specimen surface with respect to a known axis. The Y0 axis in inverse pole figures represents the observed growth direction of η-Fe_2Al_5 and θ-$FeAl_3$, which is perpendicular to the specimen surface in contact with the liquid Al. In agreement with the literature, the orthorhombic crystals of η-Fe_2Al_5 were found to grow preferentially in the [001] direction, which is the shortest axis of the η-Fe_2Al_5 unit cell. Current work found for the first time that θ-$FeAl_3$ crystals preferentially grow in the [010] direction.

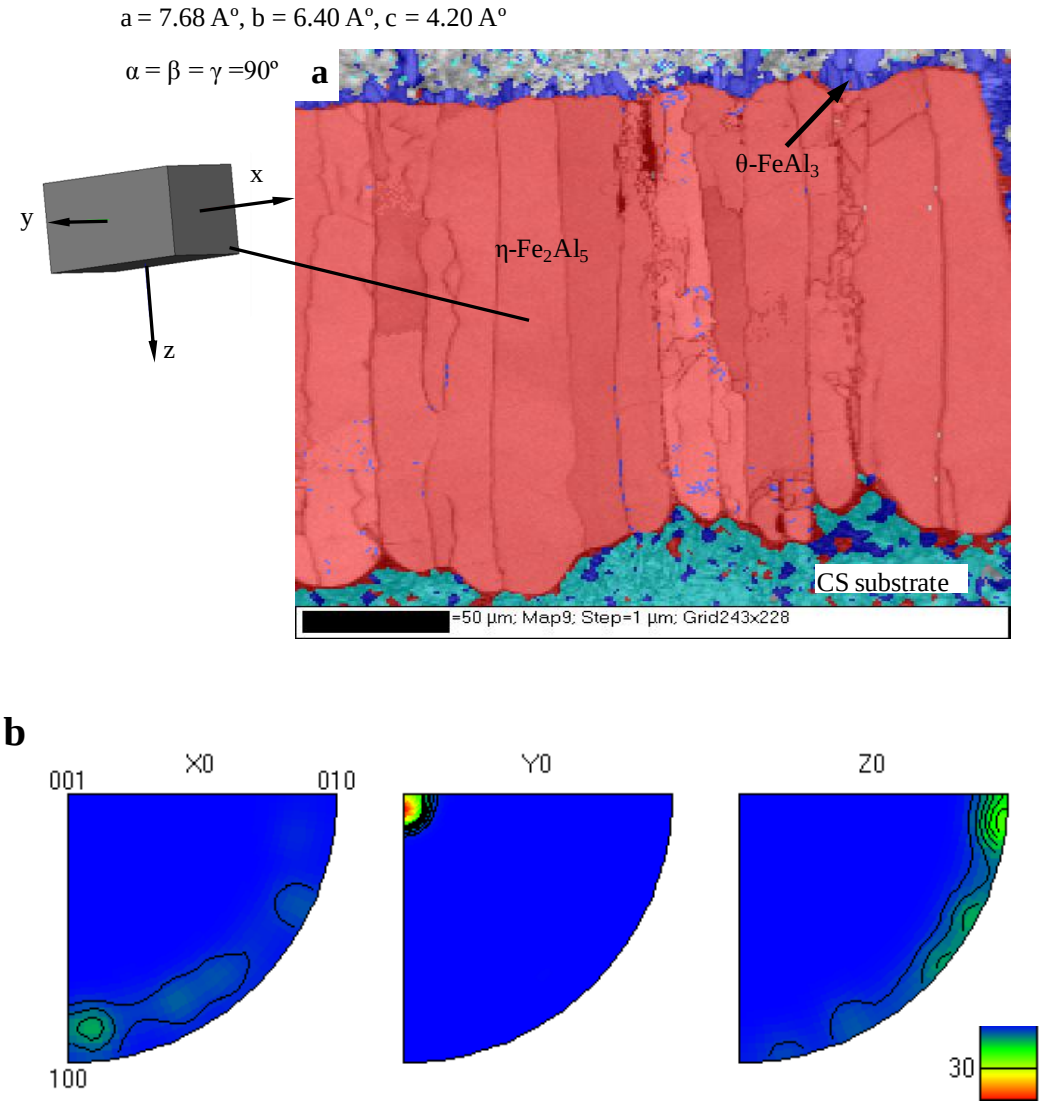

Figure 4.11 - CS specimen (750°C-1200s-static), a) EBSD map of η-Fe_2Al_5, b) inverse pole figures for η-Fe_2Al_5. Reference data source [5]

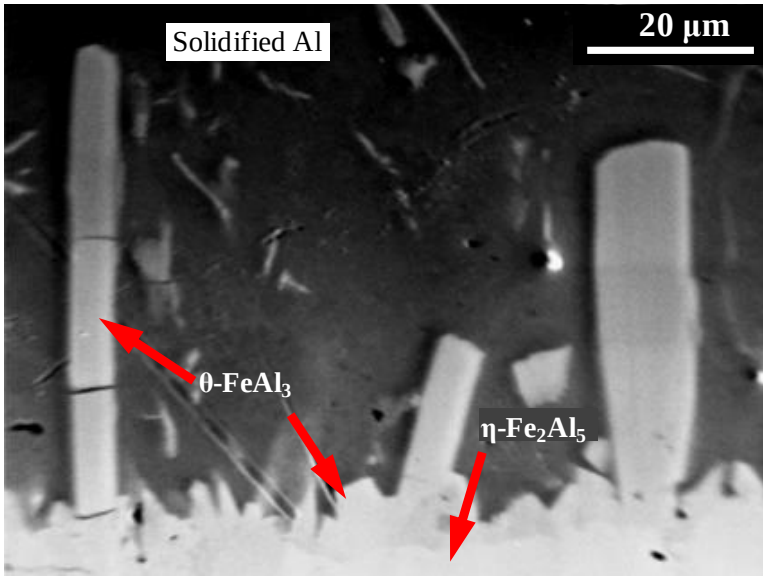

Figure 4.12 - θ-$FeAl_3$/η-Fe_2Al_5 interface on CS specimen (750°C-1200s-static).

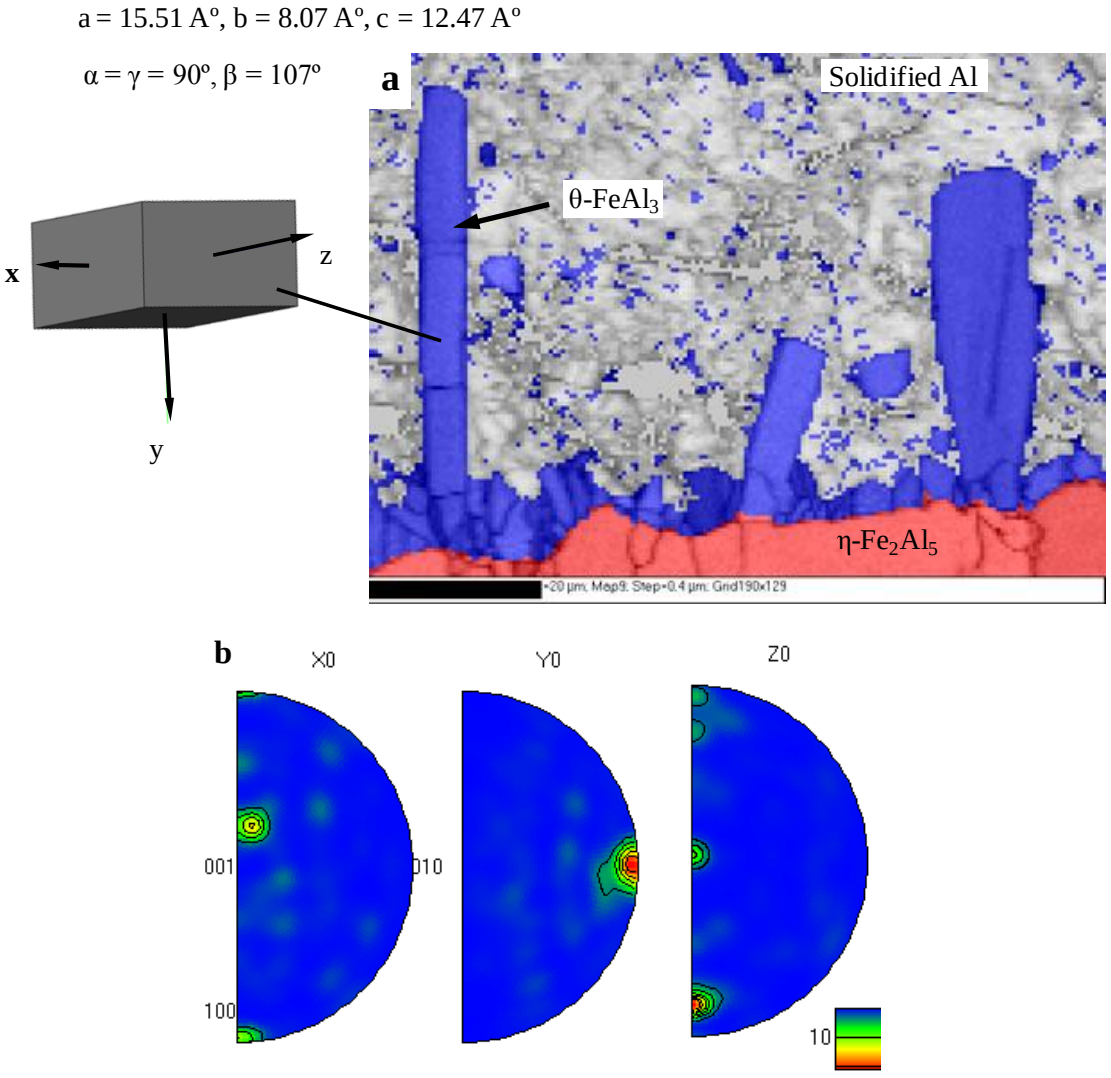

Figure 4.13 - CS specimen (750°C-1200s-static), a) EBSD map of η-Fe_2Al_5/θ-$FeAl_3$ interface, b) inverse pole figures for θ-$FeAl_3$. Reference data source [5]

4.3.1.1.2 Si-enrichment

Detailed EDS analysis of the intermetallic layers of several GCI and DCI alloys was carried out to discover the concentration of alloying elements across the intermetallic layer. The primary aim of this investigation was the identification of the alloying elements resistant to intermetallic layer growth, which could be helpful in designing an alloy with optimum resistance to liquid Al corrosion.

In all the investigated cast irons, Si was found in higher concentrations along the growing projections of the η-Fe_2Al_5 phase. Si K-α X-ray maps in Figure 4.14 and Figure 4.15, show the enrichment of Si (bright regions) on GCI and DCI specimens (850°C, 950°C-1200s-static), respectively. Apparently, Si enriches the cast iron substrate ahead of the advancing η-Fe_2Al_5 layer. The thickness and Si concentration of this Si enriched layer was varied from one alloy to other. For simplicity, the Si enriched layer was named as Si enriched phase (SEP). Compared to GCIs, the SEP was found to be thicker in DCIs. In general, the thickness and uniformity of SEP were found to increase with the rise in temperature from 850°C to 950°C. In addition to the SEP at the cast iron/η-Fe_2Al_5 interface, the Si-rich regions were also detected within the η-Fe_2Al_5 layer; however, exact identity of the $Fe_xAl_ySi_z$ phase could not be confirmed. These regions may be the SEP entrapped between adjacent η-Fe_2Al_5 columns or the projected regions of the SEP beneath the polished surface.

Figure 4.16 shows a plot between the Si concentration of cast iron substrates and typical Si concentration of SEP (950°C-1200s-static). The concentration of cast iron substrate was determined by OES, and EDS point analysis was performed at three locations within the SEP of each specimen to determine the Si concentration of SEP. Si concentration of SEP tends to increase with the increasing Si content in the cast iron substrate. Balloy *et al.* [6] reported the formation of a SEP on a high Si (4.5 wt.%) ferritic GCI, and it was suggested that the

diffusion of Si towards the Fe-substrate can be prevented by the graphite flakes present in the GCI matrix. In the present work, it is shown that Si enrichment primarily depends upon the Si content of the cast iron substrate. Within the bulk of the η-Fe_2Al_5 phase (excluding the visible SEP), the Si concentration for GCI-A, GCI-B, GCI-S and DCI-T varied typically between 1.2-2.1 wt.%, and 1.8-3.2 wt.% for DCI-C and DCI-D.

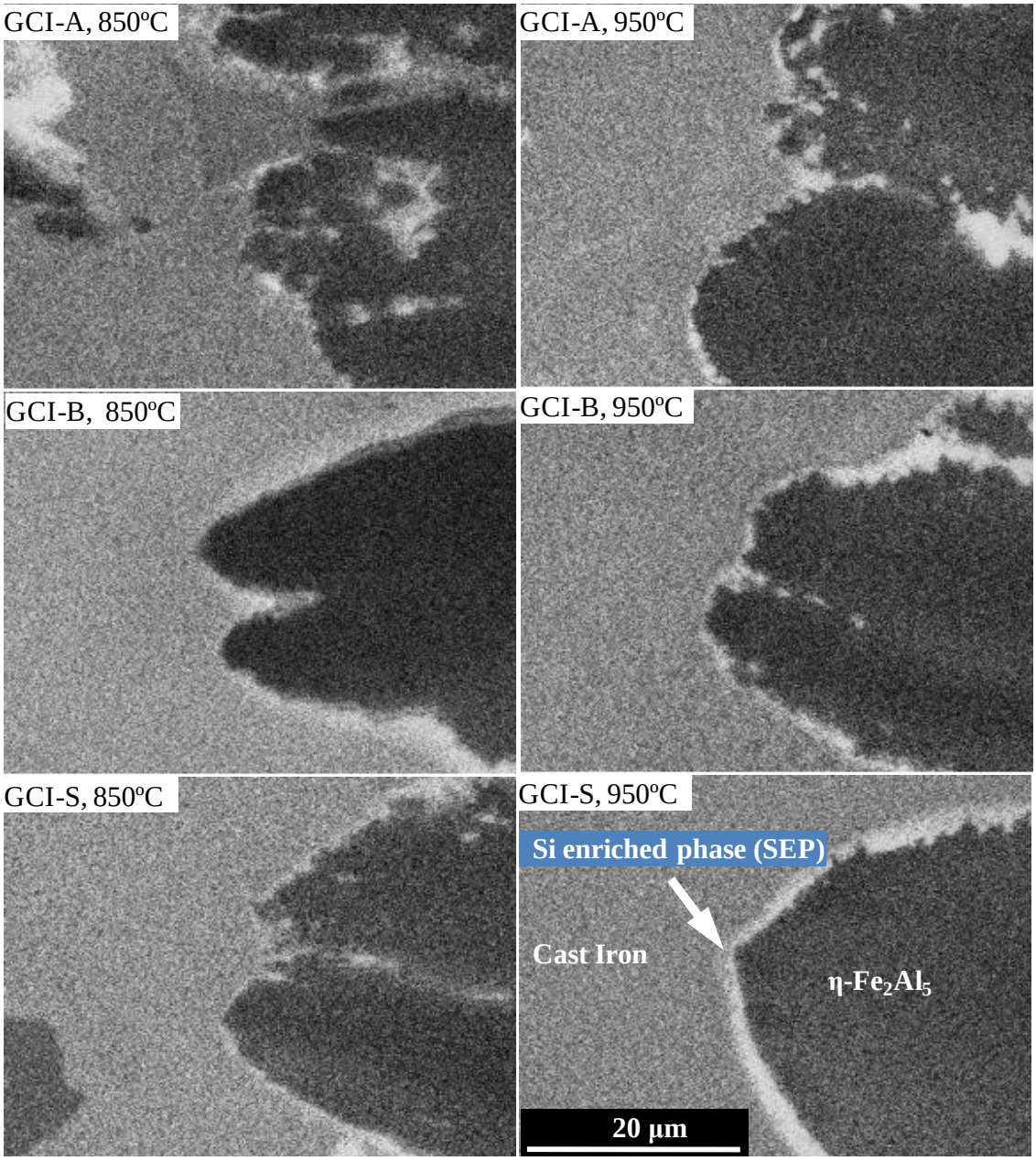

Figure 4.14 - Si K-α X-ray maps of GCIs specimens showing SEP (bright zones) at 850°C and 950°C (1200s-static).

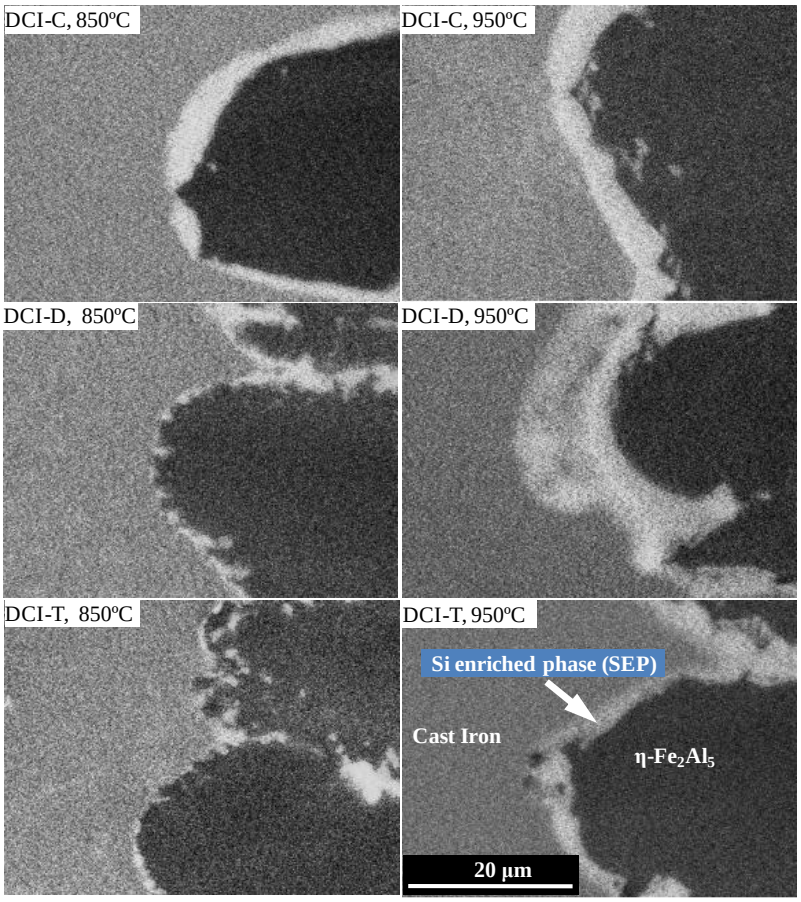

Figure 4.15 - Si K-α X-ray maps of DCIs showing SEP (bright zones) at 850°C and 950°C (1200s-static).

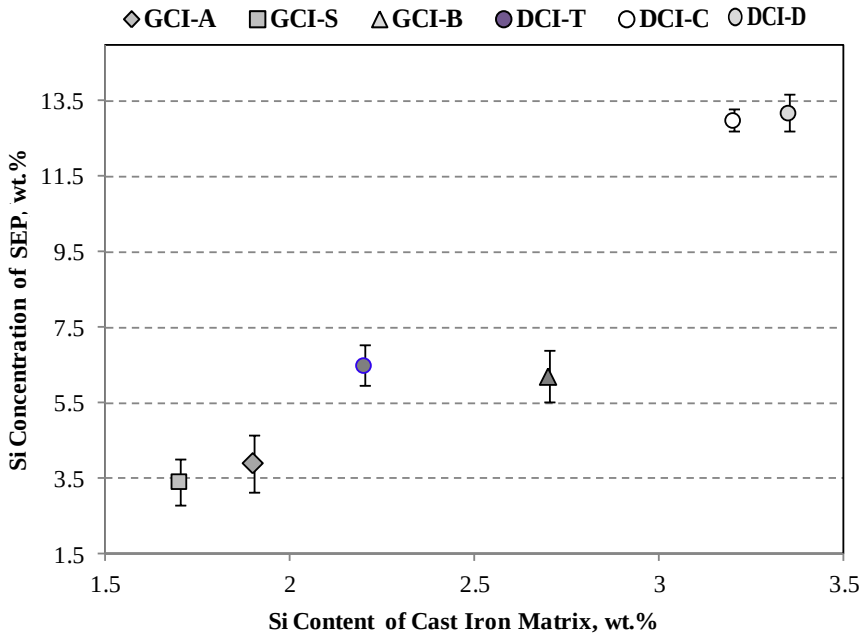

Figure 4.16 - Si content of the cast iron matrix versus Si concentration of the SEP (950°C-1200s-static).

4.3.1.1.3 Concentration Distribution of Alloying Elements

Figure 4.17 show an example of the variation in the concentration of alloying elements in the intermetallic layers of GCIs (GCI-S, 950°C-1200s-static). Unlike Si, no segregation of other alloying elements (Cr, Mo, Mn) was detected at the interface between the base alloy and the intermetallic layer. However, a decrease in the concentration of Cr, Mo and Mn is evident while moving from the cast iron substrate to the η-Fe_2Al_5 phase. K-α X-ray intensity maps, Figure 4.18, show the distribution of various elements across the DCI-C/η-Fe_2Al_5 interface. The other cast iron alloys also exhibited similar trends of variation in the concentration of alloying elements. The CS composition used in the present work has only two major alloying elements, Cr and Mo, which followed a similar trend of elemental concentration to cast irons; the concentration of Mo and Cr decreased while moving from substrate to η-Fe_2Al_5, Figure 4.19.

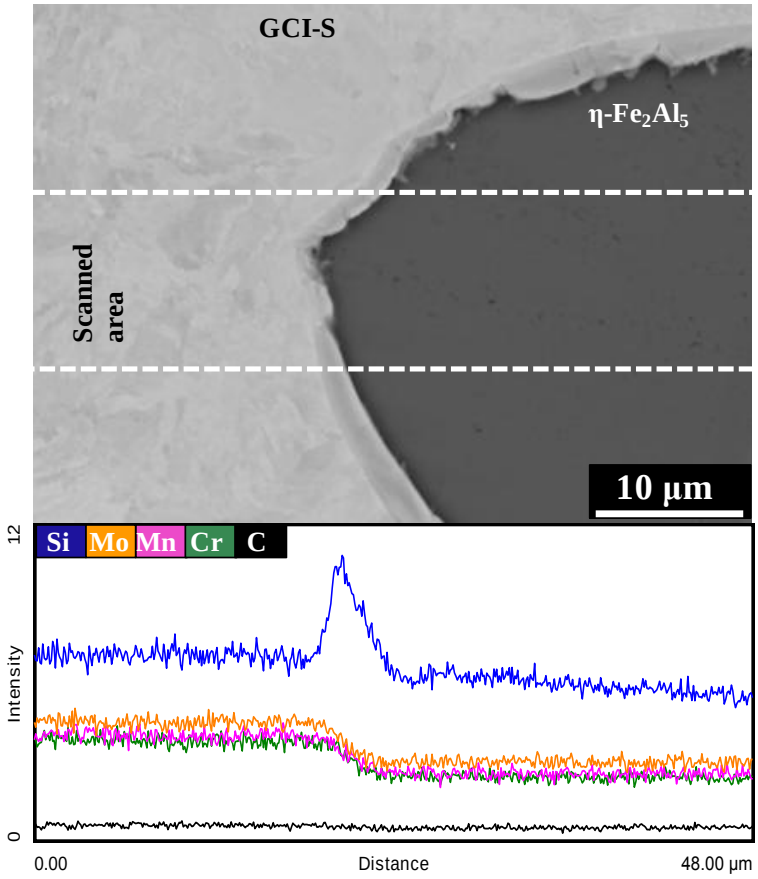

Figure 4.17 - EDS profiles of various alloying elements across the GCI-S/η-Fe_2Al_5 interface (950°C-1200s-static).

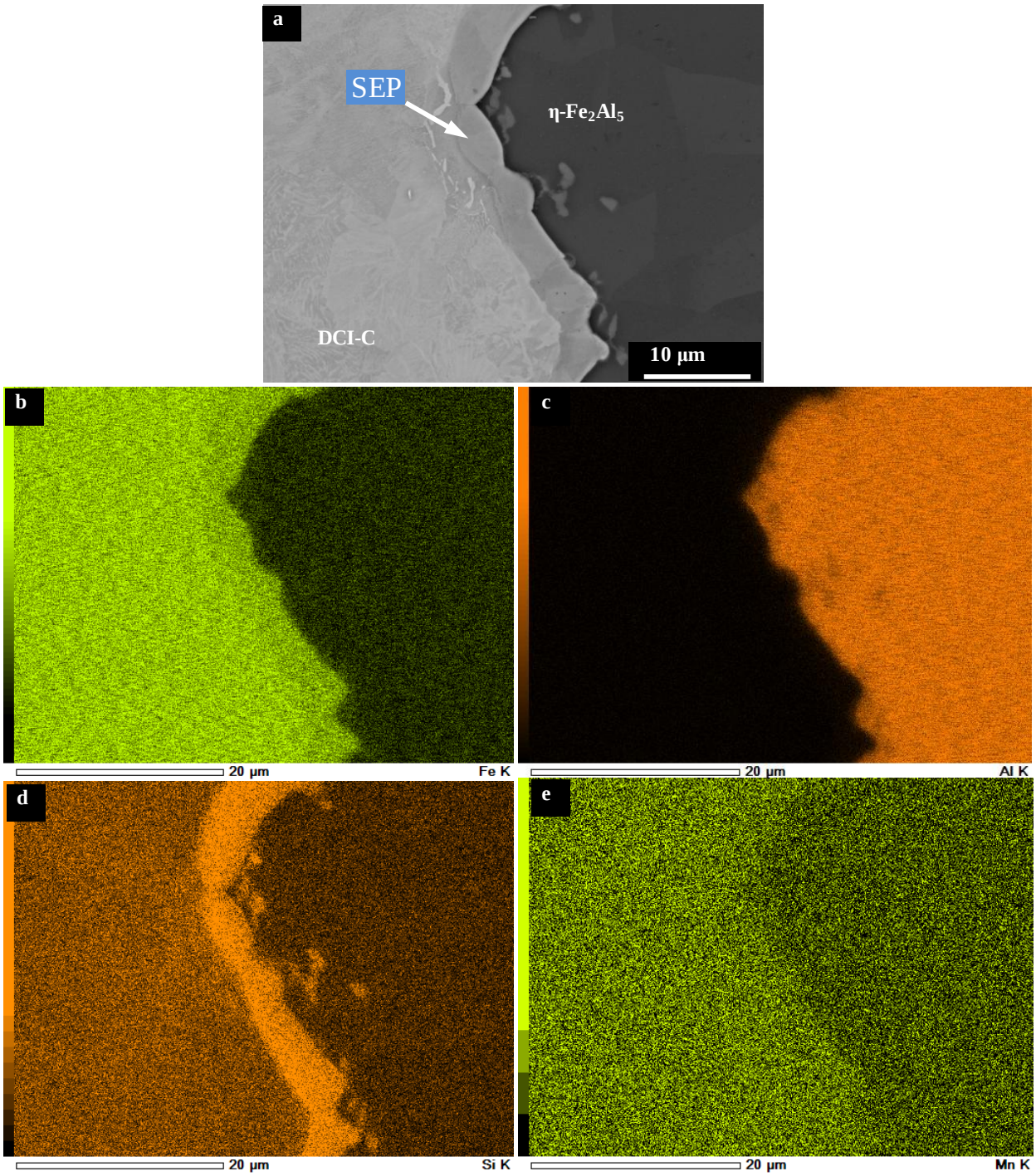

Figure 4.18 - K-α X-ray intensity maps of showing distribution of various elements across the DCI-C/η-Fe_2Al_5 interface (950°C-1200s-static), a) BSE image b) Fe, c) Al, d) Si, e) Mn. (Brighter the colour higher the concentration)

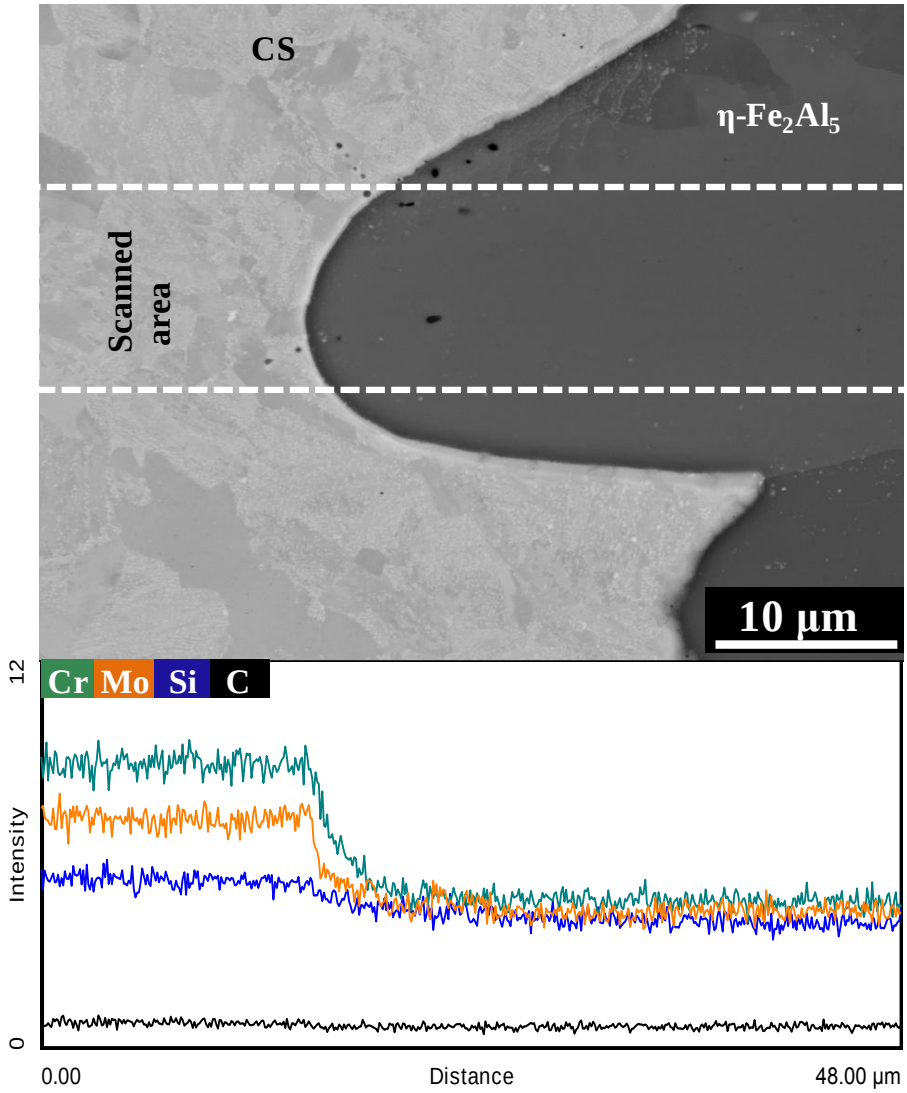

Figure 4.19 - EDS profiles of alloying elements across the CS/η-Fe_2Al_5 interface (850°C-1200-static).

4.3.1.2 GCIs

To investigate the effects of cementite, C and Si present in cast iron matrix, the GCI/η-Fe_2Al_5 interfaces were investigated for intermetallic compound formation. Characterization of various intermetallic compounds is discussed in the following sections.

4.3.1.2.1 Al_4C_3

A BSE image, Figure 4.20, shows the intermetallic layer formed on GCI-S specimen (950°C-1200s-static). Cementite particles in GCI-S may act as barriers to the advance of intermetallic layer towards substrate, and thus contribute in suppressing the liquid Al corrosion rate of cast

irons. Figure 4.21 also shows needle-shaped particles of a new phase extending from the cementite present in the GCI-S matrix, and also found dispersed within the η-Fe_2Al_5 phase.

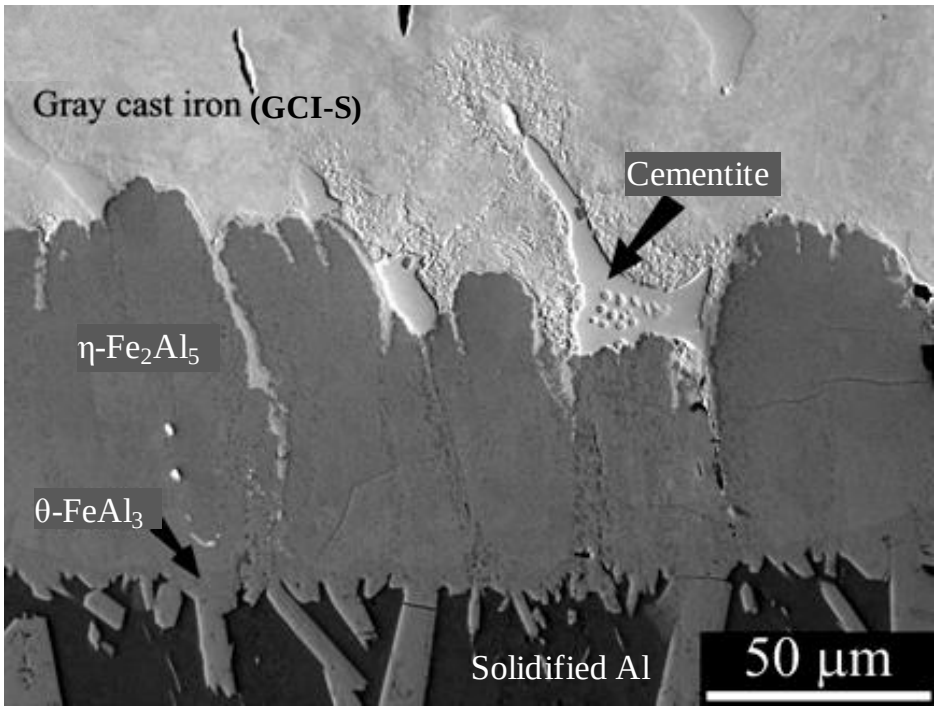

Figure 4.20 - BSE image of the intermetallic layer between GCI-S and Al (950°C-1200s-static).

In laboratory specimens of GCI-S, the formation this new phase was also found at 750°C and 850°C. EDS detected C and Al in these particles; however, conclusive identification using EDS or EBSD could not be made owing to their small size (1-5 μm long and 0.1-0.5 μm thick). The size of the needle-shaped particles was found to increase with increasing temperature and liquid Al exposure time. To obtain a sufficiently large particle size for phase identification using EBSD and EDS, the GCI specimens were exposed to static liquid Al at 950°C for 7200s. For this extended time period, there was a significant increase in the size of these particles, Figure 4.22. The EBSD patterns of these particles were consistently matched with Al_4C_3 (Figure 4.23), and the chemical composition detected by EDS was close to Al_4C_3 (Figure 4.24). In addition to Al_4C_3, other phases (labelled 'A', 'B' and 'C') in Figure 4.22 - were detected and characterization of these compounds is discussed in the next section.

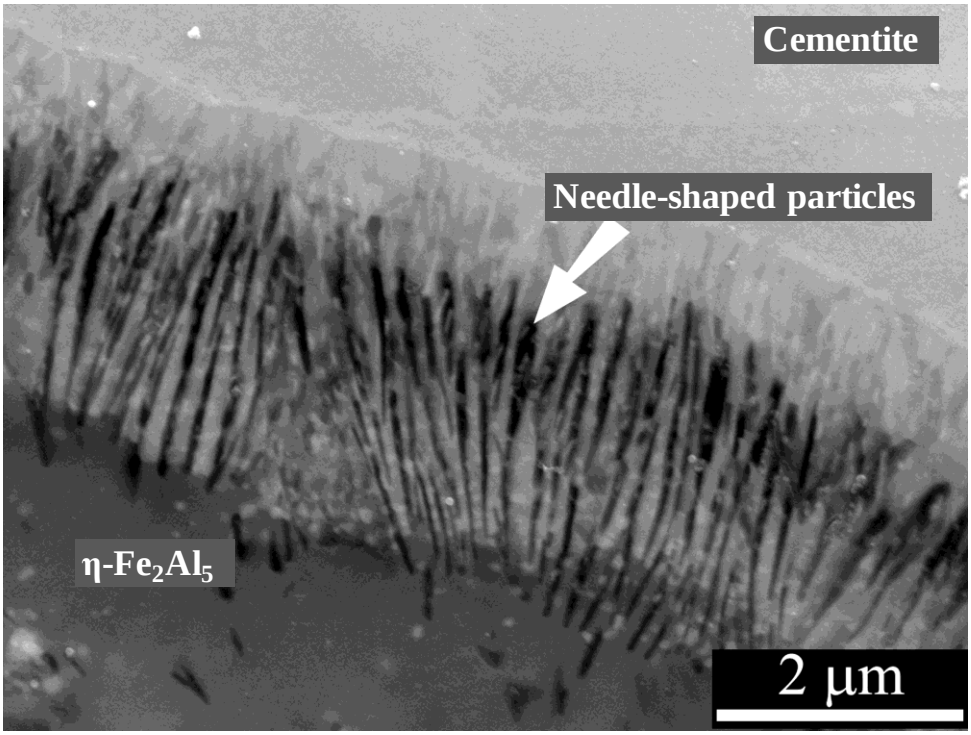

Figure 4.21 - An image of the cementite/η-Fe_2Al_5 interface in Figure 4.20 showing the needle-shaped particles (Al_4C_3).

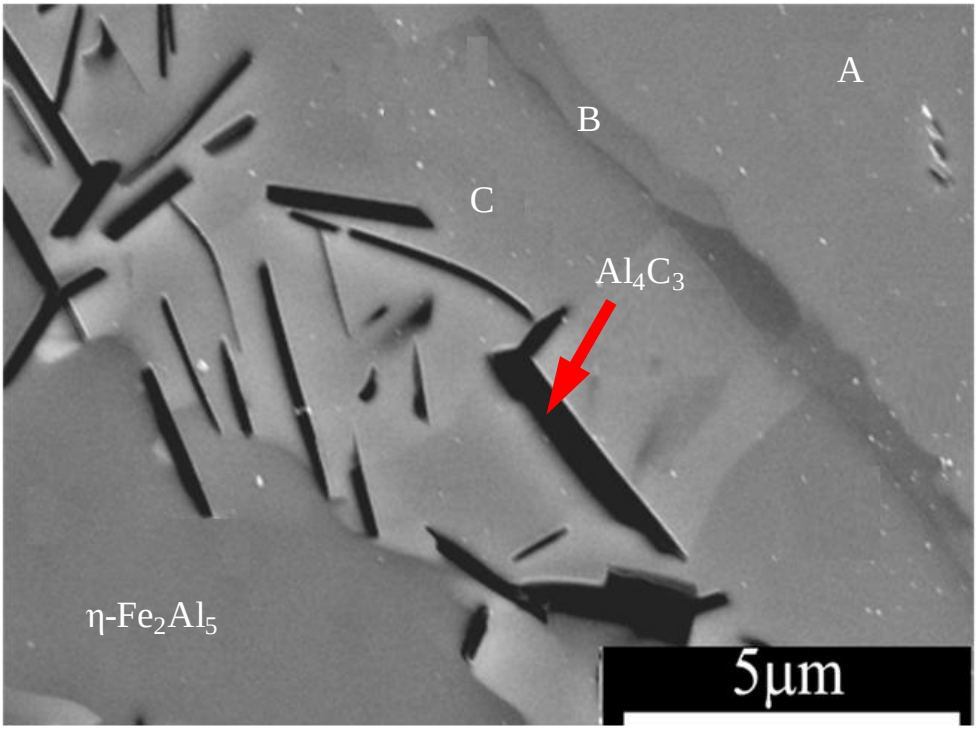

Figure 4.22 - Al_4C_3 particles in the GCI-S specimen (950°C-7200s-static).

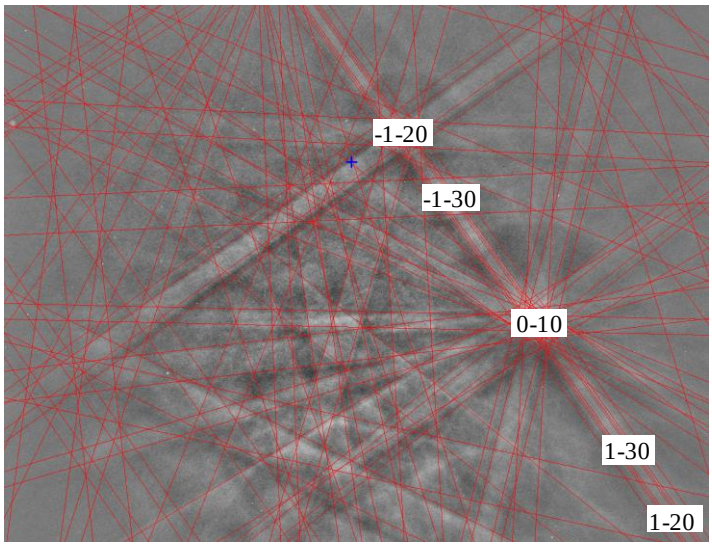

Figure 4.23 - EBSD pattern of the Al_4C_3 particle shown in Figure 4.22

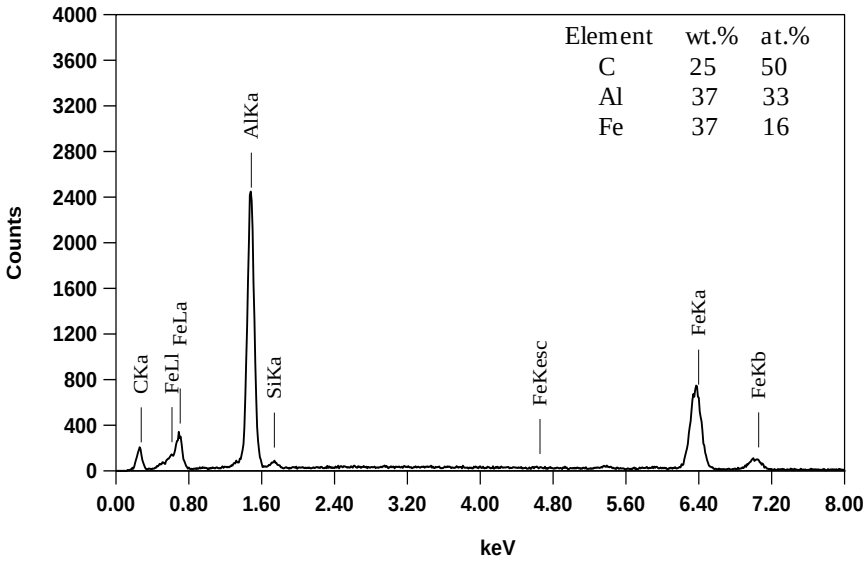

Figure 4.24 - EDS results of the Al_4C_3 particle shown in Figure 4.22.

4.3.1.2.2 α-Fe(Al, Si) solid solution, κ-Fe_3AlC and β_2-FeAl Phases

GCI specimens were exposed to liquid Al for 2400s and 7200s, Figure 4.25 shows the η-Fe_2Al_5/substrate interface cross-sections of GCI-S and GCI-A. For 2400s exposure, three layers (L1, L2, L3) were observed at the substrate/η-Fe_2Al_5 interface. Compared to GCI-A, GCI-S exhibited a thicker intermetallic layers (L1+L2+L3), and the thickness of these layers was found to increase with increasing exposure time. Table 4.2 shows the EDS results for

these layers. The Al-rich layer (L1) contained about 39 at.% Al. According to the Fe-Al binary phase diagram [7], L1 should be the β_2-FeAl phase.

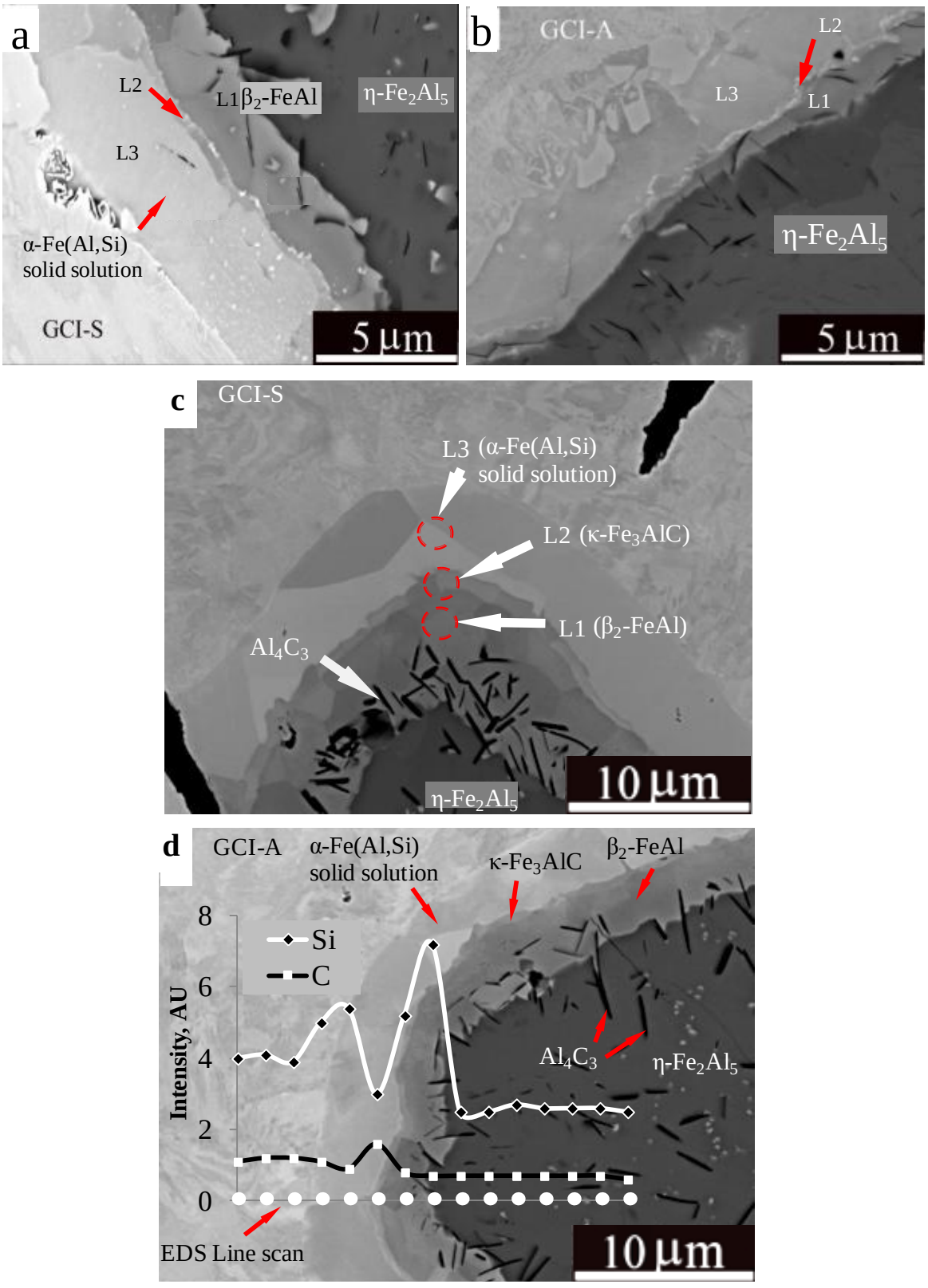

Figure 4.25 - Intermetallic layers at the GCI/η-Fe_2Al_5 interface (950°C-static), a) GCI-S, 2400s, b) GCI-A, 2400s, c) GCI-S, 7200s, d) GCI-A, 7200s.

Table 4.2 - EDS point analysis at various locations shown in Figure 4.25 (c).

Beam position	Fe Wt.(At.)%	Al Wt.(At.)%	Si Wt.(At.)%	C Wt(At.)%	Closest phase
L1	70(52)	25(39)	3.6(5.5)	0.8(2.8)	β_2-FeAl
L2	81(62)	12(19)	1.3(2)	3.5(12)	κ-Fe_3AlC
L3	91(84)	4.5(8.2)	3.3(6)	0.2(0.9)	α-Fe(Al, Si) solid solution

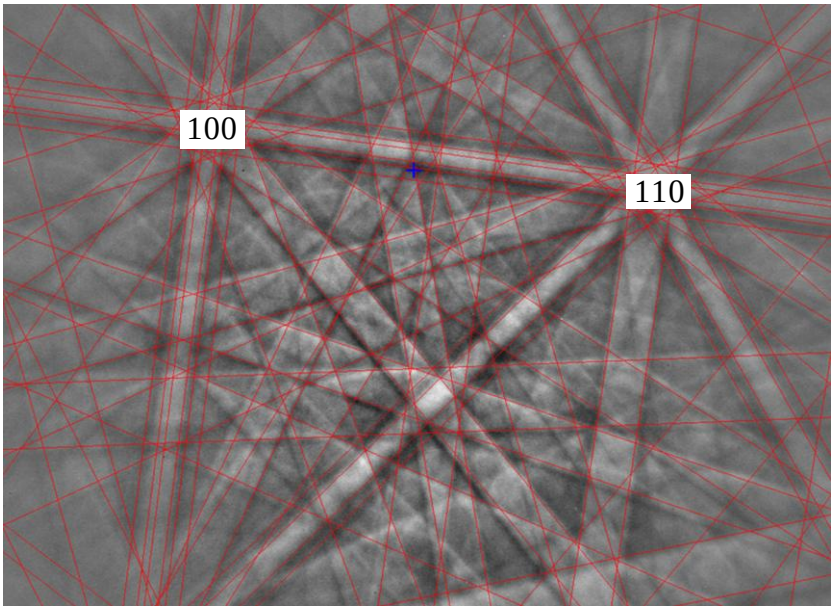

Figure 4.26 - EBSD pattern at location 'L2' in Figure 4.25(c), indexed as κ-Fe_3AlC.

The second (thin) stratum (L2) was found to contain more C (12 at.%), and EBSD patterns (Figure 4.26) were consistent with κ-Fe_3AlC. EBSD patterns of the third layer (L3) were matched to α-Fe thus this layer was identified as α-Fe(Al, Si) solid solution. Figure 4.25(d) shows the Si and C concentrations obtained from EDS line analysis across the diffusion interface of GCI-A, and various phases are labelled. Starting from the Al side, θ-$FeAl_3$, η-Fe_2Al_5, Al_4C_3, β_2-FeAl, κ-Fe_3AlC and α-Fe(Al, Si) solid solution were identified in the present study. In the present work, the Al_4C_3 and κ-Fe_3AlC phases were identified for the first time in Fe-substrate/liquid Al couples.

At the κ-Fe_3AlC zone, a large decrease in Si content is evident (Figure 4.25(d)), and in agreement with the findings of Maitra and Gupta [8], the β_2-FeAl compound was found to have higher Si content than the η-Fe_2Al_5 phase. A higher C concentration was detected in the substrate than in the α-Fe(Al, Si) solid solution, β_2-FeAl or η-Fe_2Al_5 phase layers.

Figure 4.27 (b) is a 3D representation of the Si K-α X-ray intensity distribution of an area of GCI-S specimen (950ºC-7200s-static) shown in Figure 4.27(a). Among all the phases of the intermetallic layer, the highest Si concentration can be seen in the β_2-FeAl phase, whereas the η-Fe_2Al_5 and κ -Fe_3AlC phases have lower amounts of Si.

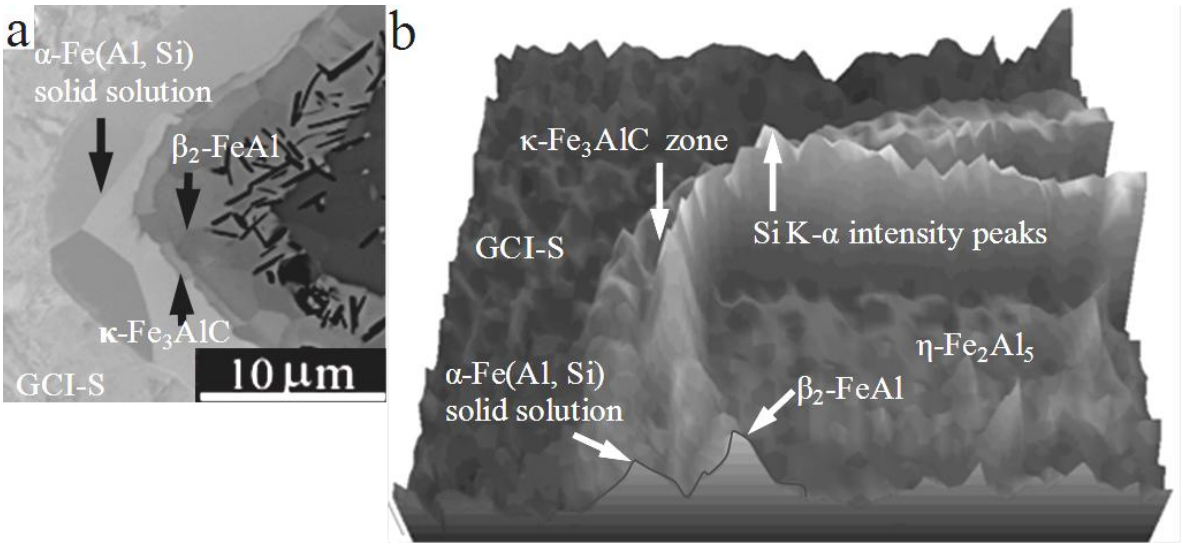

Figure 4.27 - a) BSE image of GCI-S specimen (950ºC-7200-static), b) 3D EDS map of Si K-α X-ray intensity distribution at an area of specimen in Figure 4.27 (a).

Black lath-shaped particles in Figure 4.27(a) were identified as Al_4C_3. The amount of Al_4C_3 was greater in GCI-S than GCI-A. For relatively short exposure times (< 2400s), the Al_4C_3 phase was found to extend from the cementite present in a GCI matrix. However, for extended immersion times at 950°C (Figure 4.25(c)), the Al_4C_3 particles were observed in the β_2-FeAl phase layer instead of extending from the cementite surface.

The GCI-B specimen (950°C-7200s-static) cross-section, Figure 4.28, shows the η-Fe_2Al_5/cast iron interface. Compared to GCI-S and GCI-A, only a single Si-rich layer at GCI-B substrate was found, and its composition (Table 4.3) was close to the Fe_3(Al, Si) phase.

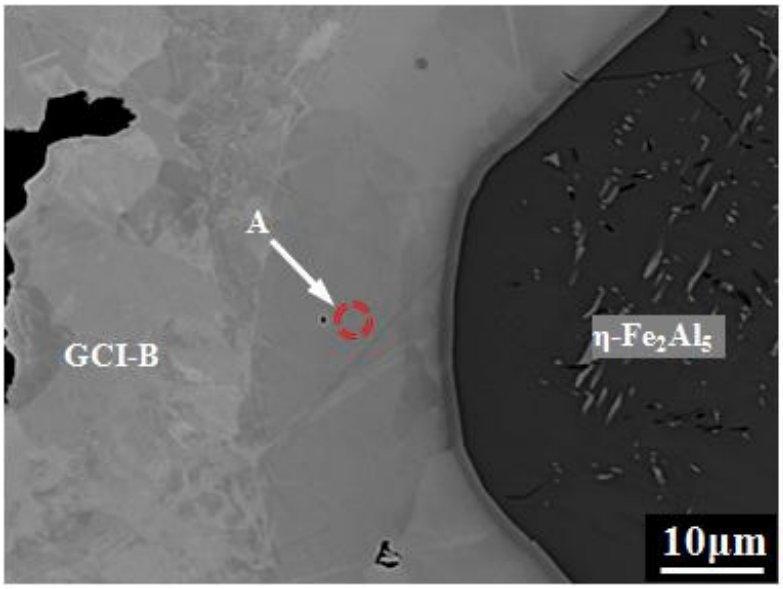

Figure 4.28 - Intermetallic layer at a GCI-B specimen (950°C-7200s-static).

Table 4.3 - EDS composition at the beam location 'A' in Figure 4.28.

Fe Wt.(At.) %	Al Wt.(At.)%	Si Wt.(At.)%	C Wt.(At.)%	Closest phase
86(74)	6(9)	7(13)	---	Fe_3(Al, Si)

Al_4C_3 phase fraction in GCIs was also determined in a 260 µm^2 rectangular area (Figure 4.29), one side of the rectangle kept outside to the tip of Al_4C_3 particle that appeared first towards the substrate side. The measured phase fractions of Al_4C_3 in GCI-S, GCI-A and GCI-B specimens (950°C-7200s-static) are given in Table 4.4. The amount of Al_4C_3 was also greater in GCI-S than GCI-A and GCI-B. The thickness of the κ-Fe_3AlC zone was greater in GCI-S than in GCI-A, and in GCI-B no such zone was detected.

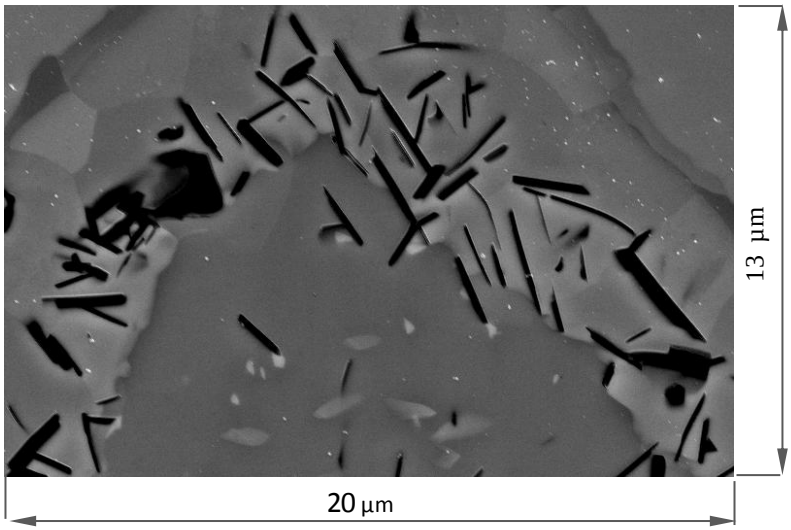

Figure 4.29 - Schematic of the area for determining the phase fraction of Al_4C_3.

Table 4.4 - Phase fraction of Al_4C_3 in GCI alloys (950°C-7200s-static).

GCIs	Al_4C_3 Fraction, Area %
GCI-S	12.7±2
GCI-A	8.2±1
GCI-B	1.3±0.3

4.3.1.3 Ductile Cast Irons

4.3.1.3.1 Fe-Al-Si and Fe_3Si Phases

BSE images of the Si-rich interfacial layers on DCI-C and DCI-T specimens (950°C, 1200s-static) are shown in Figure 4.30. Both DCIs exhibited Si-rich layers at the substrate/η-Fe_2Al_5 interface. Table 4.5 shows the EDS results in reference to Figure 4.30 (a) and (b). A negligible amount (0.35 at.%) of Al was detected in the SEP of high Si DCI (DCI-C). Balloy *et al*. [6] also found similar results on a high Si GCI and suggested the SEP was Si-rich α-Fe. In the present work, the composition of the DCI-C intermetallic layer was found to be consistent with Fe_3Si. However, the EBSD patterns for α-Fe and Fe_3Si structures were found to be similar and the precise identification could not be confirmed. The DCI-D alloy

exhibited similar results to DCI-C. Unlike GCIs, no C enrichment of DCI substrates was reported even after 7200s liquid Al exposure at 950°C.

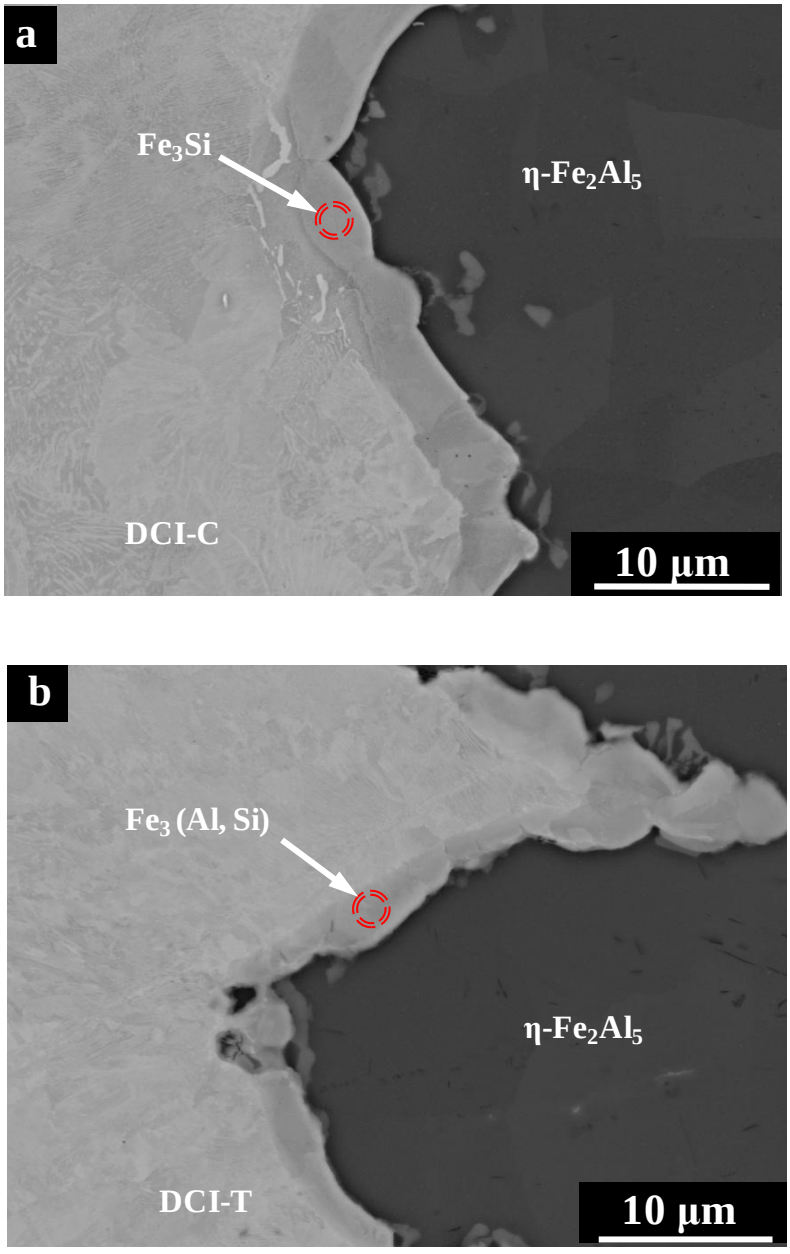

Figure 4.30 - BSE images of cast iron/η-Fe_2Al_5 interface (950°C-1200s-static), a) DCI-C, b) DCI-T.

Table 4.5 - Composition of Si-rich intermediate layers in Figure 4.30(a) and (b).

Substrate	Fe Wt.(At.) %	Al Wt.(At.)%	Si Wt.(At.)%	Closest phase
DCI-C	84(71)	0.2(0.35)	13.4(22.9)	Fe_3Si
DCI-T	87(74)	4.5(7.9)	6.5(11)	Fe_3(Al, Si)

4.3.1.3.2 Al_4C_3

Formation of Al_4C_3 in DCI specimens was found to be rare. Significantly smaller sized particles (< 1 μm in length), with similar morphology to Al_4C_3 (as found in GCIs), were found in the intermetallic layer of DCI-T. Figure 4.31(b) shows several tiny particles that may be Al_4C_3 near the DCI-T substrate (850°C-1200s-static).

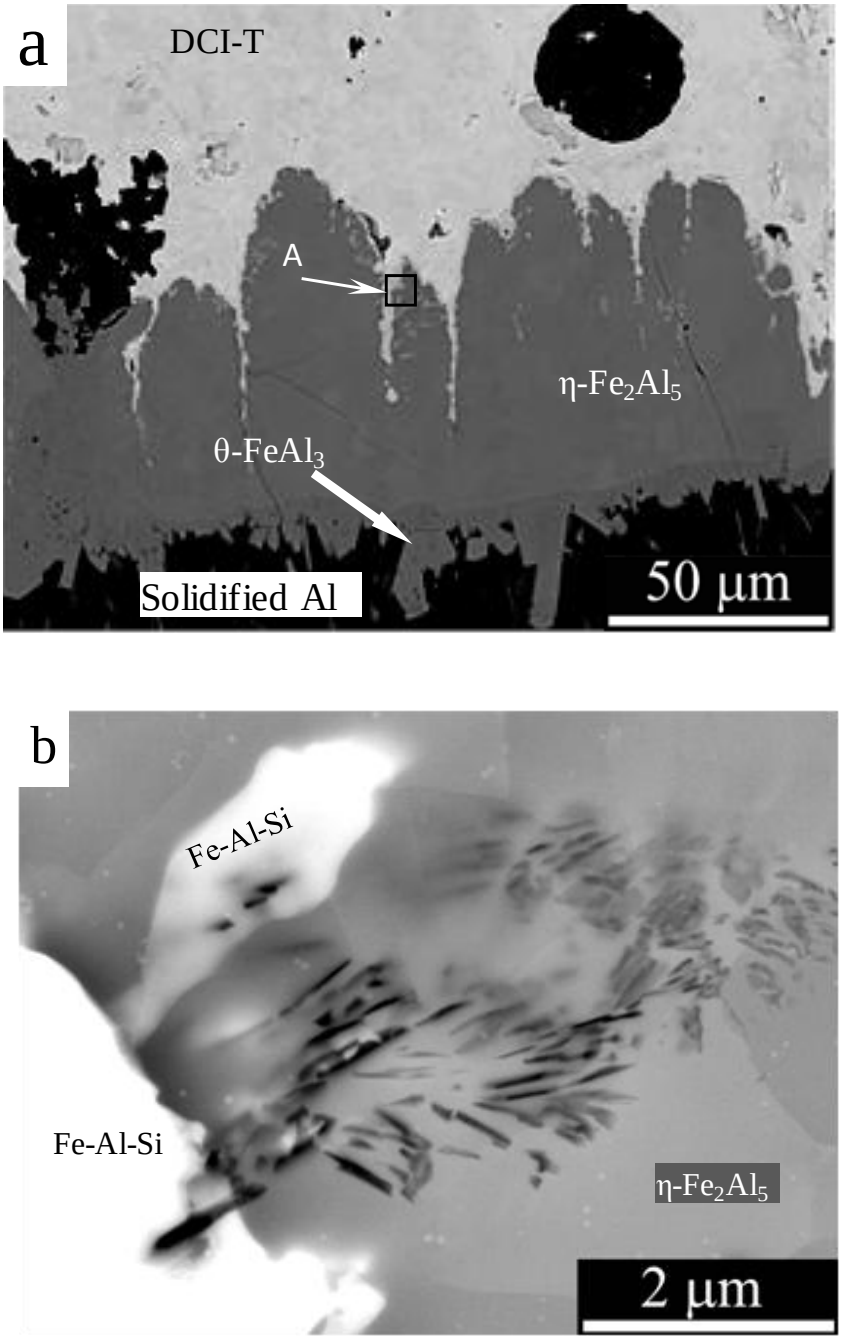

Figure 4.31 - (a) BSE image of intermetallic layer between DCI-T and Al (850ºC-1200s static), (b) particles (likely to be Al_4C_3) in the magnified area 'A' of Figure 4.31(a).

4.3.1.4 Steels

The substrate/η-Fe_2Al_5 interfaces of three steel alloys (CS, AISI 4140 and AISI W1) were investigated. Figure 4.32(a) shows a BSE image of the interfacial region of a CS specimen (950°C-2400s-static). Owing to the low Si (0.2 wt.%) content in CS, no Si-rich region was found in this case. However, a thin (< 5 μm) Fe-rich layer was observed ahead of the advancing η-Fe_2Al_5 serrations. EDS indicates that the composition of this stratum is consistent with the β_1-Fe_3Al phase, Figure 4.32(b).

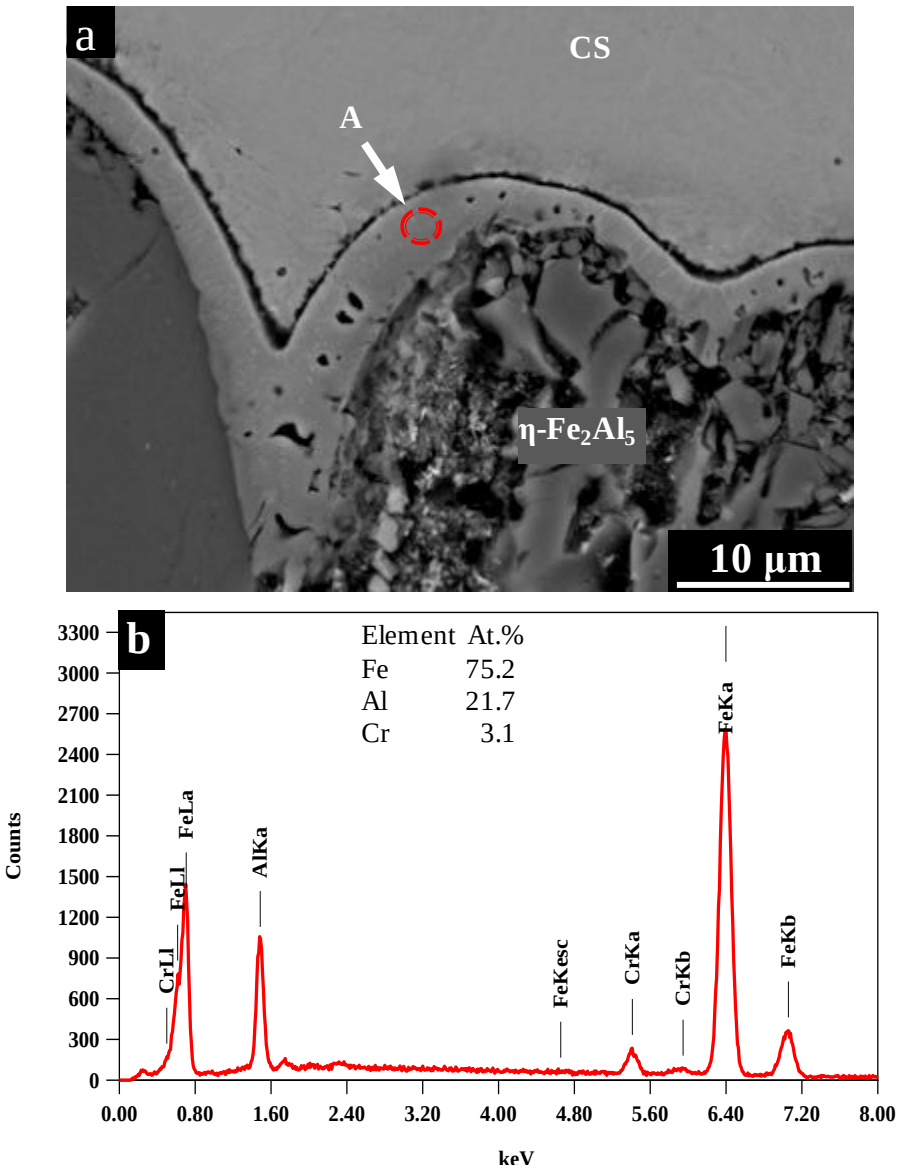

Figure 4.32 - a) BSE image of the CS intermetallic layer (950°C-2400s-static), b) EDS spectrum at beam location 'A' in Figure 4.32 (a).

However, precise confirmation of β_1-Fe_3Al was not possible owing to similar EBSD patterns of β_1-Fe_3Al and α-Fe. No distinguishable β_1-Fe_3Al layer was detected at 850°C and for shorter (< 2400s) interaction times at 950°C.

AISI 4140 and AISI W1 steels were exposed to static liquid Al at 950°C for longer durations. CS could not be tested greater than 2400s due to its high corrosion rate. Figure 4.33 and Figure 4.34 show the substrate/η-Fe_2Al_5 interfaces of AISI 4140 and AISI W1 steels at different exposure times, respectively. Similar to GCIs, both steels showed C enrichment ahead of the advancing η-Fe_2Al_5. However, the distinguishable triple layer zone (like GCIs) was only found in AISI W1-7200s-static specimen. Table 4.6 shows the composition of these layers (L1, L2 and L3) that was determined using EDS. The L1 layer was identified as β_2-FeAl. The composition of L2 layer was close to κ-Fe_3AlC. Since AISI W1 steel contains Si, a SEP was found in this case. The L3 layer was identified as α-Fe(Al, Si) solid solution.

The thickness of the triple layer zone in AISI W1 steel specimens was found to increase with increasing exposure time. Thus at short exposure times, the thickness of this zone may be too thin to detect. AISI 4140 has Cr as a main alloying element, and Cr concentration was found to decrease while moving from substrate to η-Fe_2Al_5, Figure 4.33. Moreover, the Al_4C_3 particles were found dispersed in the β_2-FeAl and η-Fe_2Al_5 layers of AISI W1. The size of these particles increased with increasing exposure time. The precise identification of Al_4C_3 and κ-Fe_3AlC phases was achieved for GCIs.

Black particles with identical morphology to Al_4C_3 were also found in η-Fe_2Al_5 near the substrate/η-Fe_2Al_5 interface of AISI 4140 specimens, Figure 4.35 shows an example of the particles dispersed in η-Fe_2Al_5 of AISI 4140-2400s-static specimen.

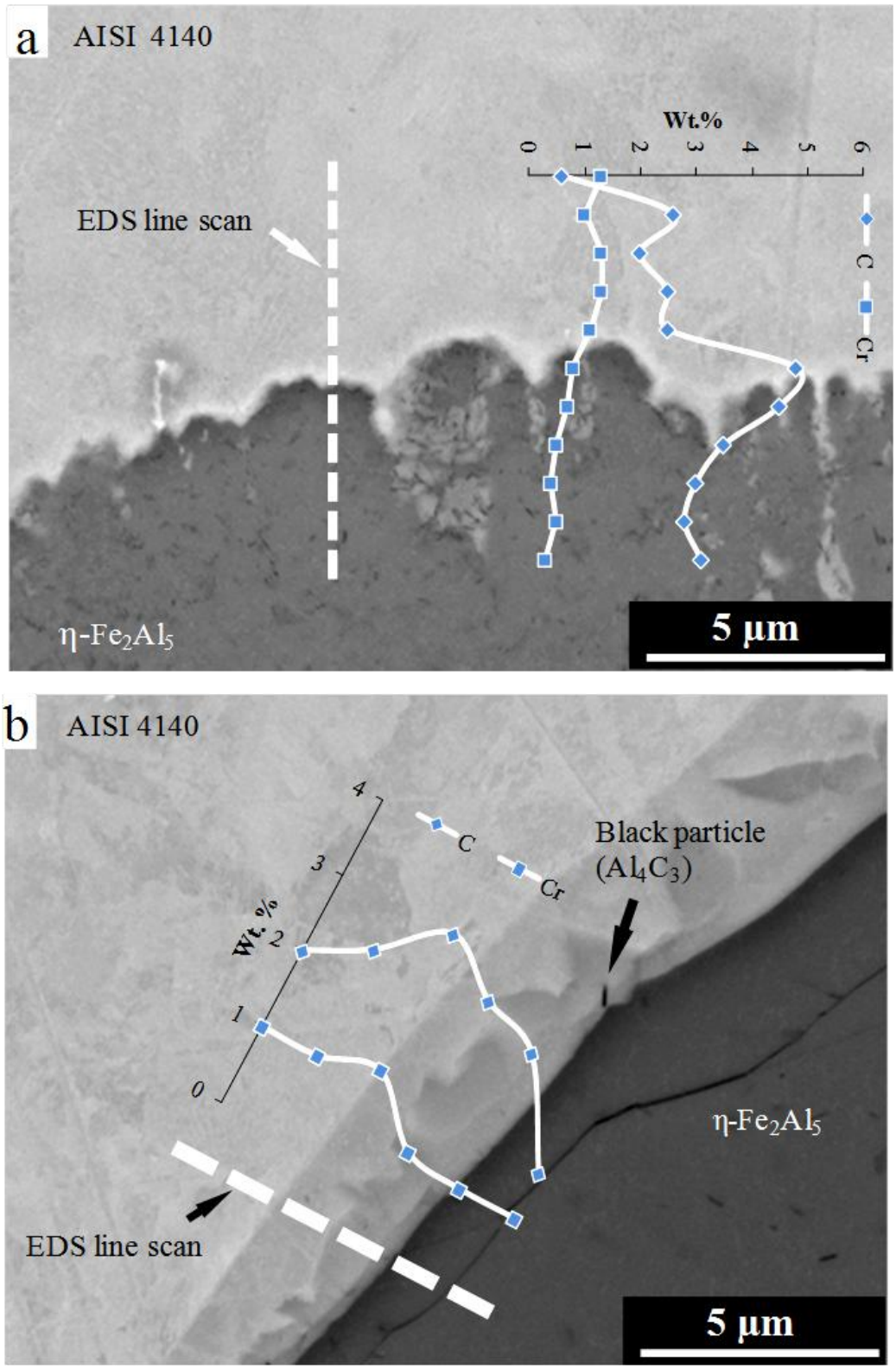

Figure 4.33 - BSE images showing EDS scan locations on substrate/η-Fe_2Al_5 interfaces of AISI-4140 specimens, a) 950°C-2400s-static and b) 950°C-7200s-static.

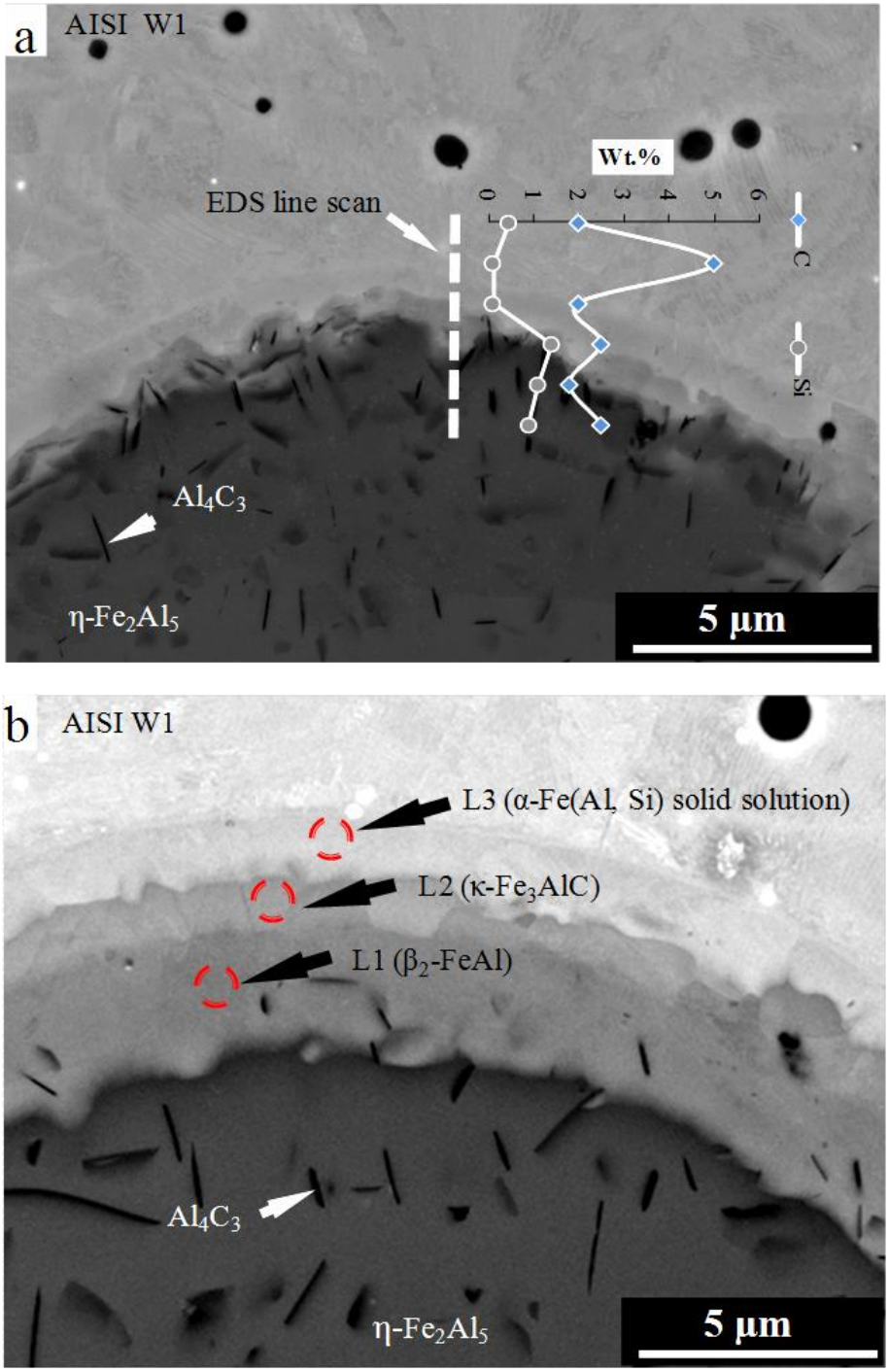

Figure 4.34 - BSE images showing EDS scan locations on substrate/η-Fe_2Al_5 interfaces of AISI-W1 specimens, a) 950°C-2400s-static and b) 950°C-7200s-static.

Table 4.6 - EDS point analysis at various locations as shown in Figure 4.34(b).

Beam position	Fe wt.(at.)%	Al wt.(at.)%	C wt(at.)%	Si wt.(at.%)	Closest phase
L1	67(47)	30(45)	2.3(7.7)	2.4(3.4)	β_2-FeAl
L2	79(60)	16(27)	4.6(16.2)	0.4(0.7)	κ-Fe_3AlC
L3	92.4(81)	4.5(8.1)	2.5(10.3)	2.1(3.5)	α-Fe(Al, Si) solid solution

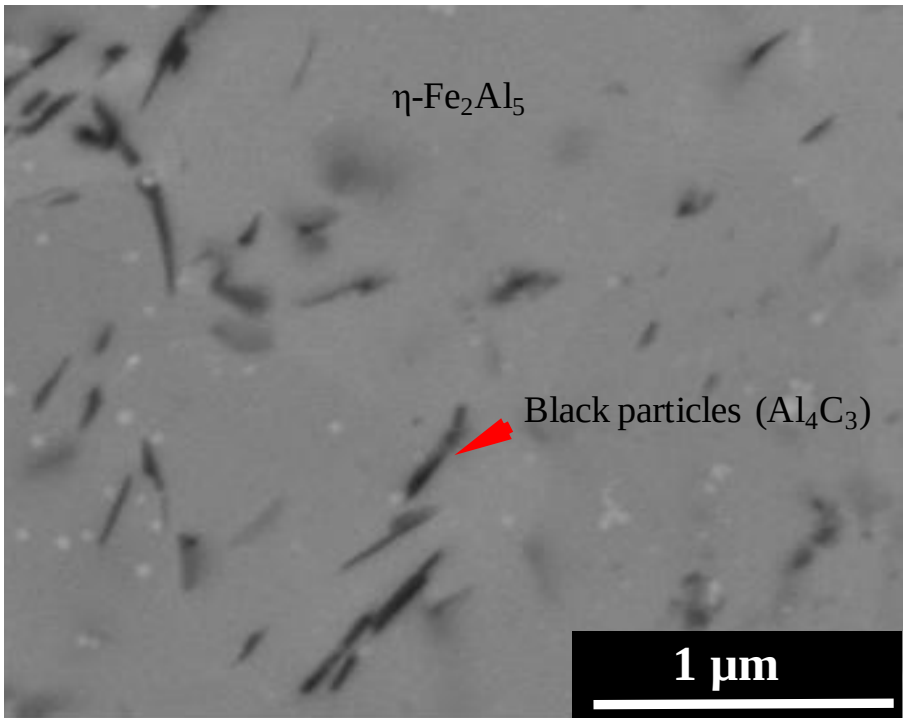

Figure 4.35 - An example of black particles (possibly Al_4C_3) dispersed in the η-Fe_2Al_5 layer adjacent to the AISI-4140 substrate (2400s-static).

4.3.2 After-service Materials

It is important to correlate after-service materials with laboratory test specimens to ensure that laboratory tests are pertinent or approach the actual service conditions. Metallographic specimens were prepared from the after-service tapping pipes supplied by NZAS. The tapping pipes experience liquid Al corrosion at the temperatures as high as 960°C (Chapter 1). Two types of after-service materials were investigated for compound formation. The first was a low carbon cast steel alloy (CS) currently employed as the top tapping pipe material Lines 1-3 at NZAS. The second was a gray cast iron (GCI-BT) employed as the bottom tapping pipe material on all lines.

4.3.2.1 CS

To analyze the Fe-Al reaction products a sample was sectioned near the point of failure. Figure 4.36 shows an Fe-Al intermetallic layer on the CS-substrate of the top tapping pipe.

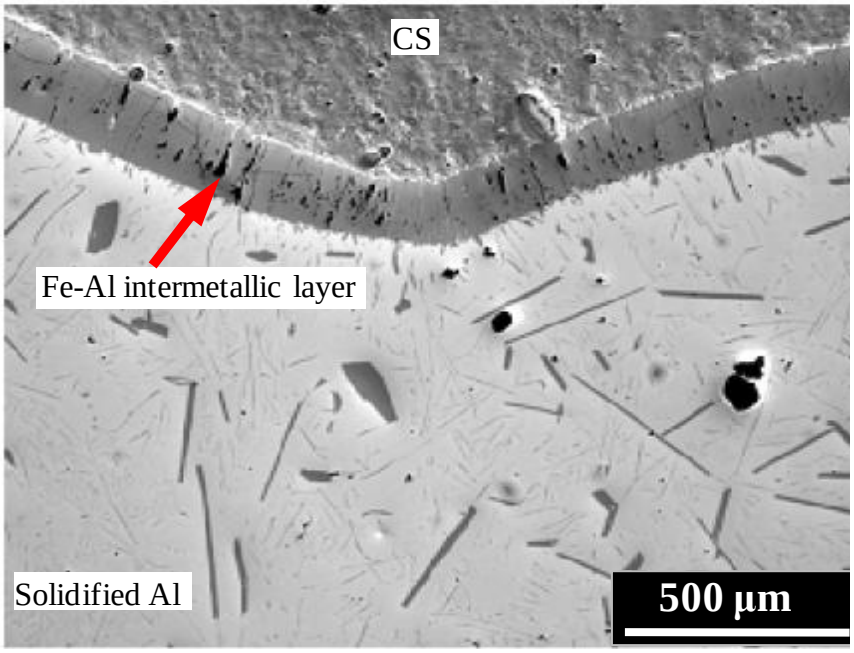

Figure 4.36 - An optical image of a CS sample cross-section obtained from an after-service top tapping pipe.

A dispersion of polyhedral particles of various sizes was observed in solidified Al over the Fe-Al interaction zone. Moreover, tiny shrinkage porosities and/or slag inclusions can be seen in the steel microstructure, which appear as discontinuities in the intermetallic layer. Owing to the brittle nature of Fe-Al phases [9], pores in the intermetallic layer can fall out during cutting and/or polishing operations, leading to large pits and cracking of the interphase layer. Moreover, the brittleness of the intermetallic layer may also be dependent upon the chemical composition and type of ferrous alloy and the exposure conditions of liquid Al. Figure 4.37 shows a high magnification image of the intermetallic layer adjacent to the steel substrate. The major phase was identified as η-Fe_2Al_5. Figure 4.38(a) shows the indexed EBSD pattern at the beam location shown in Figure 4.37, and Figure 4.38(b) shows the EDS spectrum of η-Fe_2Al_5. The minor phase of the intermetallic layer was found to be θ-$FeAl_3$ in the form of lath shape particles protruding towards the solidified Al. In Figure 4.39(a), the SEM image shows θ-$FeAl_3$ at the η-Fe_2Al_5 surface. Visually, the two phases can be distinguished by the relatively dark gray colour of θ-$FeAl_3$. Figure 4.39 (b) shows the SEM image of a particle in

the solidified Al. Figure 4.40(a) and (b) show the indexed EBSD pattern and EDS spectrum of θ-$FeAl_3$, respectively. Using EBSD the dispersed particles in the solidified Al were identified as θ-$FeAl_3$.

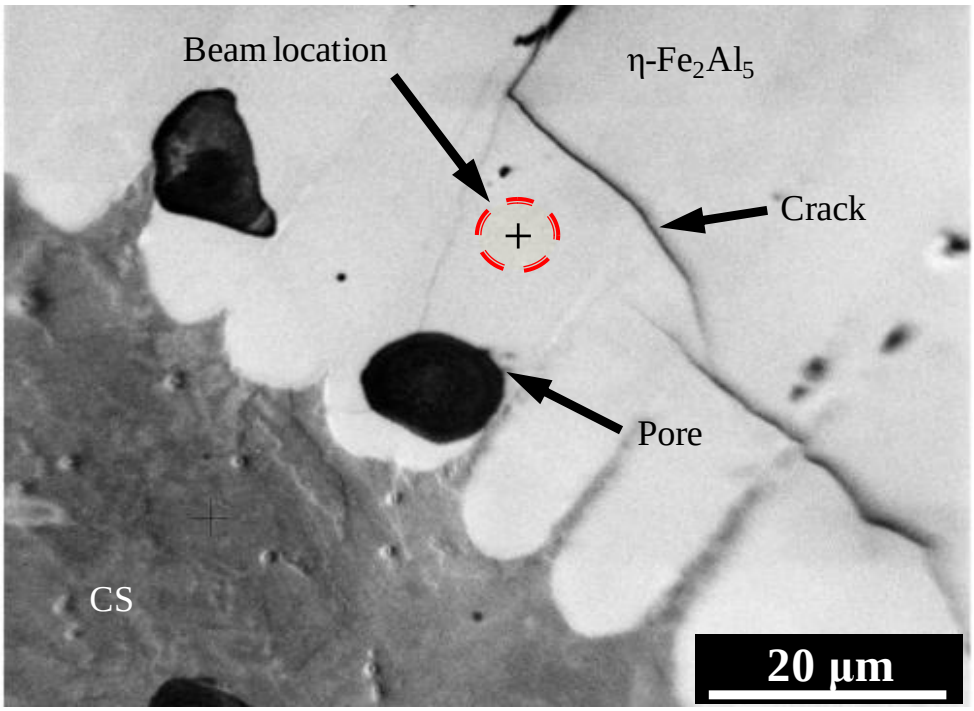

Figure 4.37 - A high magnification SEM image of the η-Fe_2Al_5/cast steel interface.

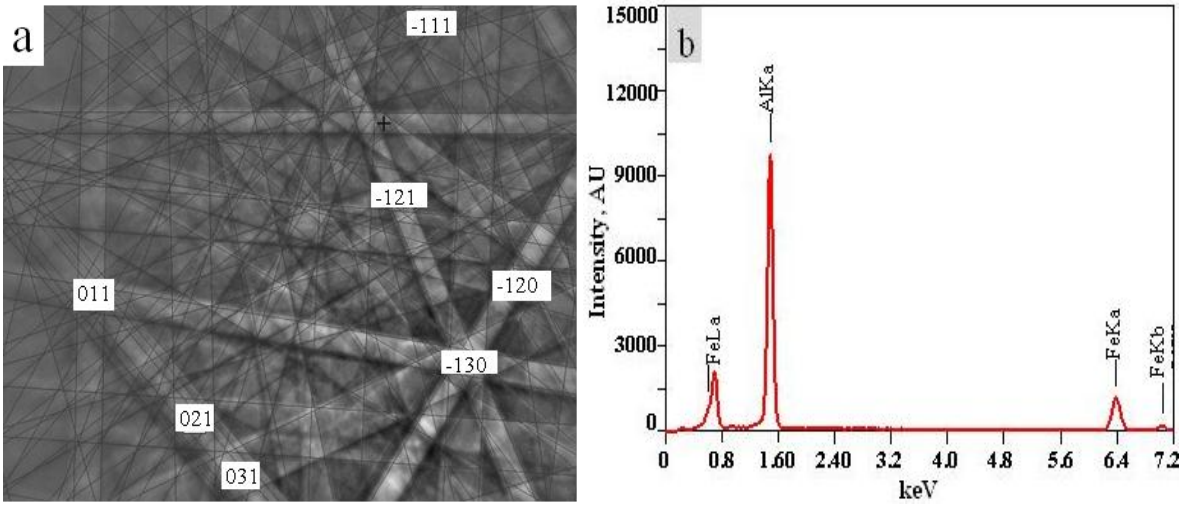

Figure 4.38 - a) EBSD pattern at the beam location shown in Figure 4.37 indexed as η-Fe_2Al_5, b) EDS spectrum of η-Fe_2Al_5.

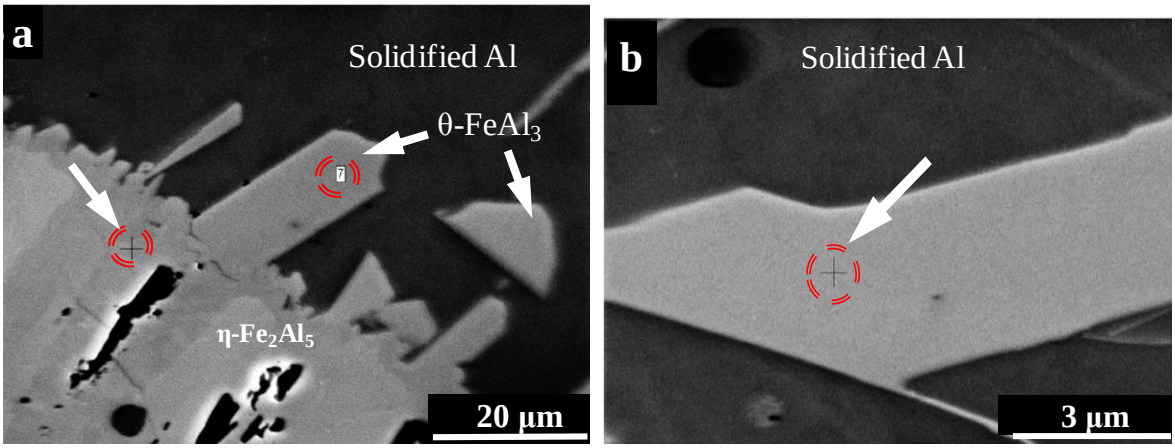

Figure 4.39 - a) SEM image of the η-Fe_2Al_5/Al interface showing θ-$FeAl_3$ particles protruding towards solidified Al, b) θ-$FeAl_3$ particle in solidified Al.

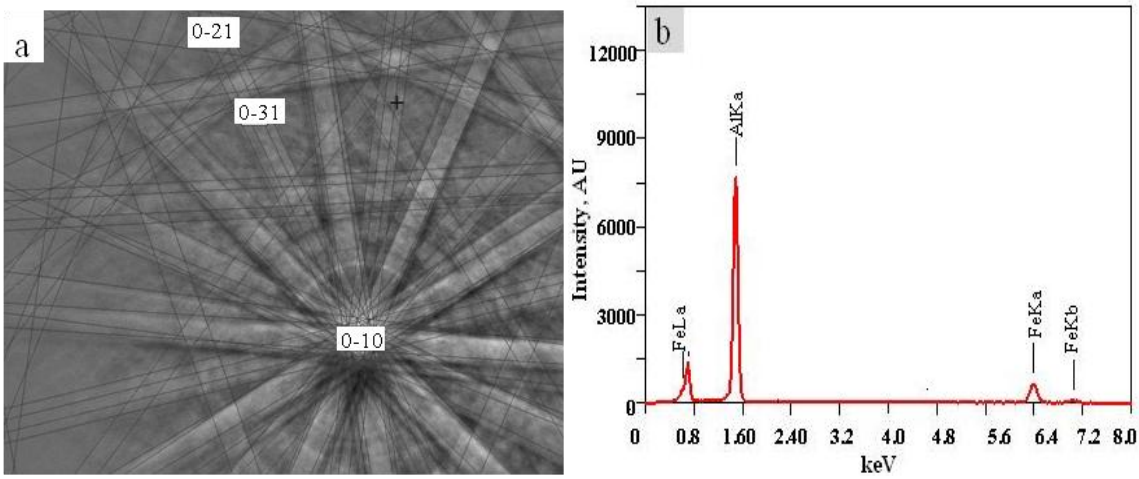

Figure 4.40 - a) An example of an EBSD pattern obtained from beam locations shown in Figure 4.39 that was indexed as θ-$FeAl_3$, b) EDS spectrum of θ-$FeAl_3$.

4.3.2.2 GCI

GCI bottom tapping pipes fail by liquid Al corrosion at the pipe inlet. To characterize the intermetallic compounds, samples were obtained from the corroded edge of a bottom tapping pipe and analyzed by EBSD and EDS. A BSE image, Figure 4.41, shows an intermetallic layer on the GCI-BT substrate. The entire intermetallic layer was composed of η-Fe_2Al_5 and no θ-$FeAl_3$ particles could be detected in the outer coating layer.

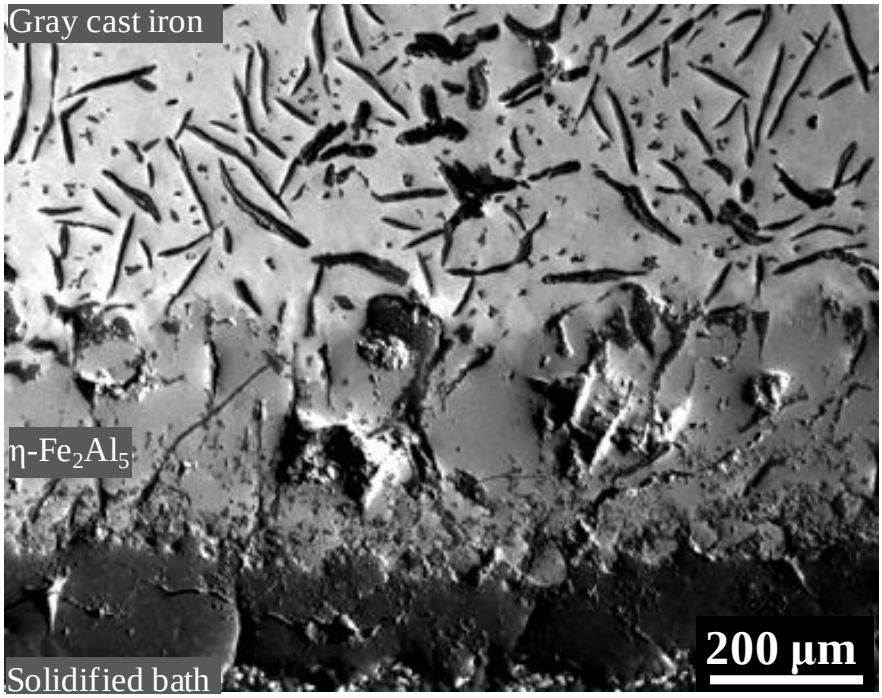

Figure 4.41 - BSE image of the region of interaction between GCI-BT and the liquid Al bath.

Figure 4.42(a) shows an optical image of the GCI-BT/η-Fe_2Al_5 interface. A distinguishable thin (approximately 8 µm) layer was found ahead of the η-Fe_2Al_5 columns. Tiny black lath-shaped particles were also found dispersed in this thin layer with maximum dimensions of 10 µm by 1.5 µm. EDS detected (Figure 4.43) about 40 at.% Al in the thin layer comprising the lath shape particles. According to the Fe-Al binary phase diagram [7], this phase should be the β_2-FeAl phase. The EBSD patterns of β_2-FeAl and α-Fe were found to be identical. Therefore, on the basis of compositional analysis this layer was characterized as β_2-FeAl. Small gray regions having composition close to β_2-FeAl were also found within the η-Fe_2Al_5 phase, Figure 4.42(a). The lath-shaped black particles in the β_2-FeAl layer were characterized by EBSD and EDS as Al_4C_3. Figure 4.42(b) shows the morphology of an Al_4C_3 particle and the EBSD and EDS results are given in Figure 4.44. The crystallographic data of Al_4C_3 for EBSD characterization was taken from [5].

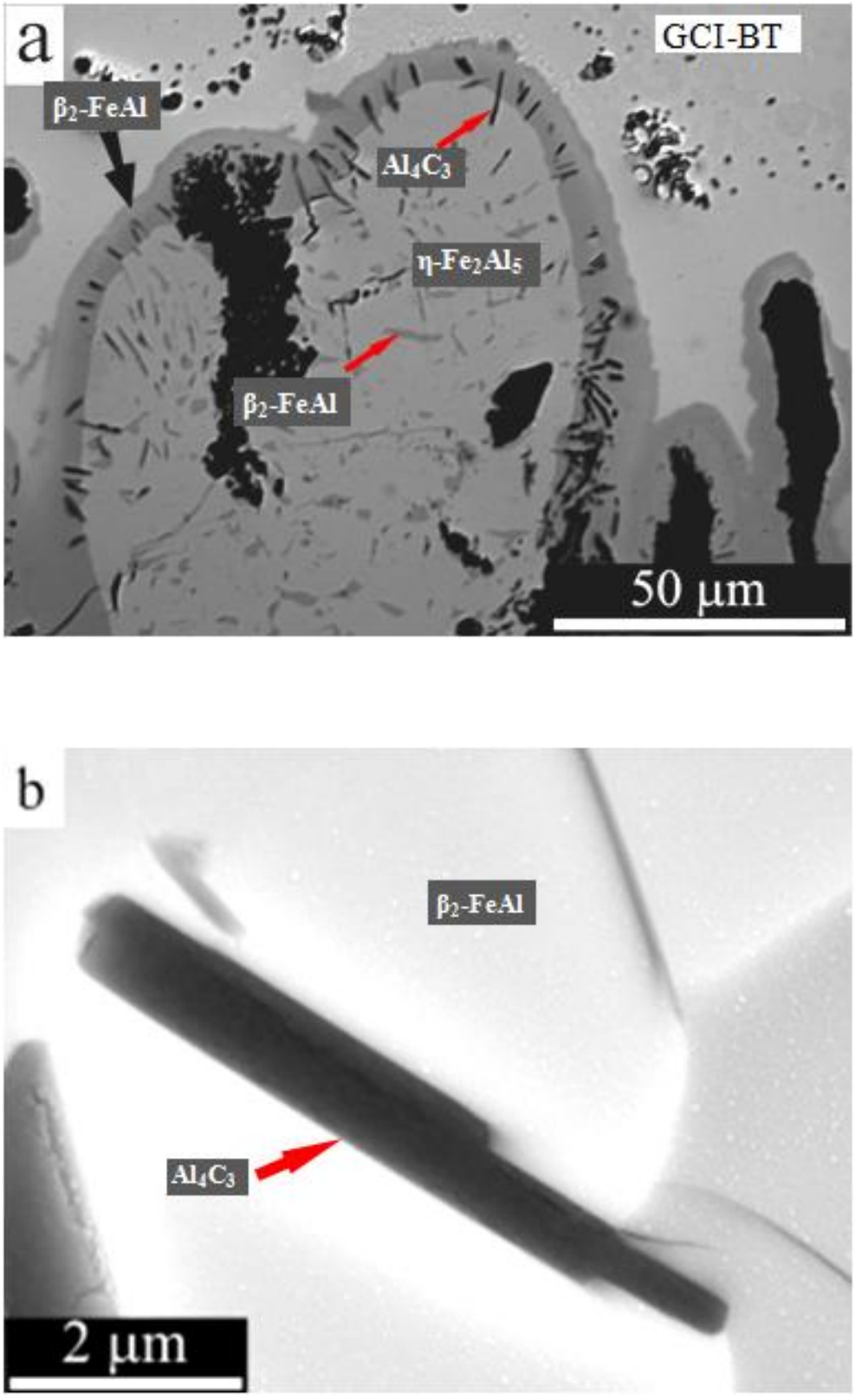

Figure 4.42 - a) An optical image of GCI-BT/η-Fe_2Al_5 interface, b) SEM image of a lath-shaped particle in a matrix of β_2-FeAl.

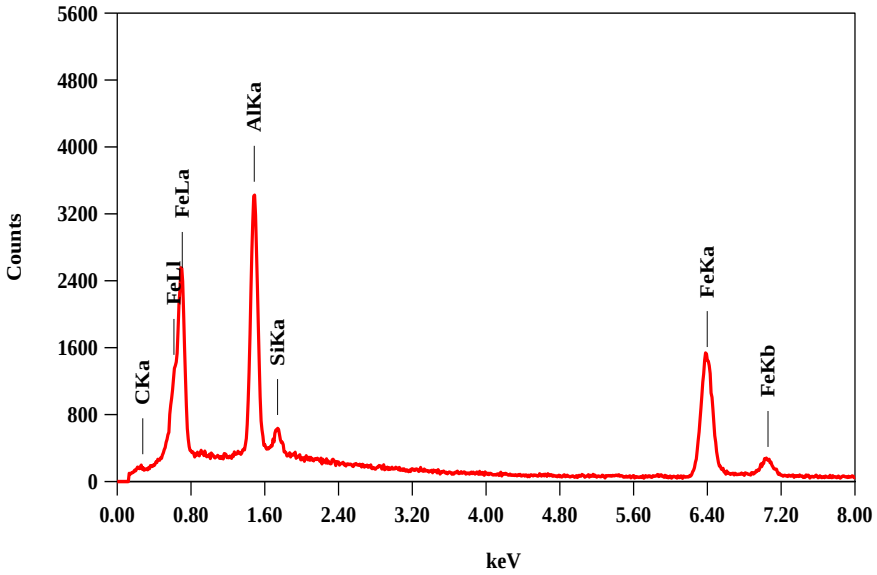

Figure 4.43 - An EDS spectrum of the β_2-FeAl phase layer in Figure 4.42(a).

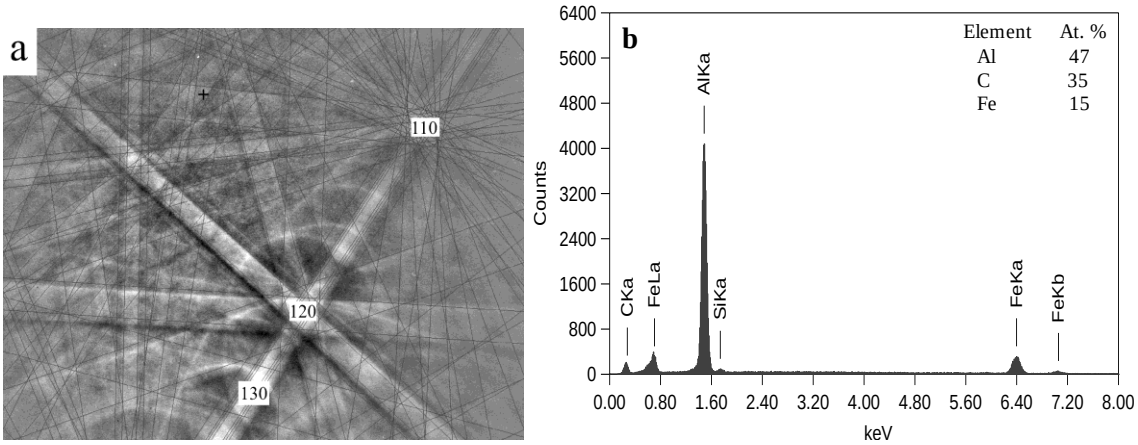

Figure 4.44 - (a) An example of the EBSD pattern of a lath-shaped particle, indexed as Al_4C_3, (b) EDS spectrum of the Al_4C_3 particle shown in β_2-FeAl phase in Figure 4.42 (b).

In addition to β_2-FeAl and Al_4C_3, formation of ζ-$FeAl_2$ has also been found in an ex-service GCI-BT sample. ζ-$FeAl_2$ was found at the interface between the η-Fe_2Al_5 and β_2-FeAl phases. Figure 4.45 shows the interface between η-Fe_2Al_5 and GCI-BT. Figure 4.46 and Figure 4.47 show the EBSD pattern and EDS spectrum of ζ-$FeAl_2$, respectively. This phase was detected only in the vicinity (4-5 μm) of the β_2-FeAl phase towards the η-Fe_2Al_5 phase. The ternary κ-Fe_3AlC phase was also detected between β_2-FeAl and GCI-BT substrate. Figure 4.48 and Figure 4.49 show the indexed EBSD pattern and EDS spectrum of κ-Fe_3AlC, respectively.

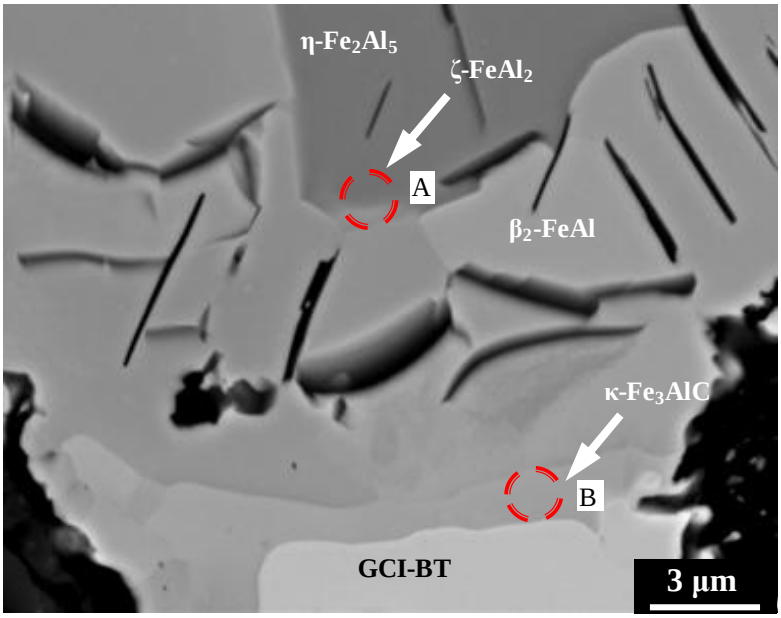

Figure 4.45 - GCI-BT/η-Fe_2Al_5 interface showing the beam locations for EBSD and EDS analysis.

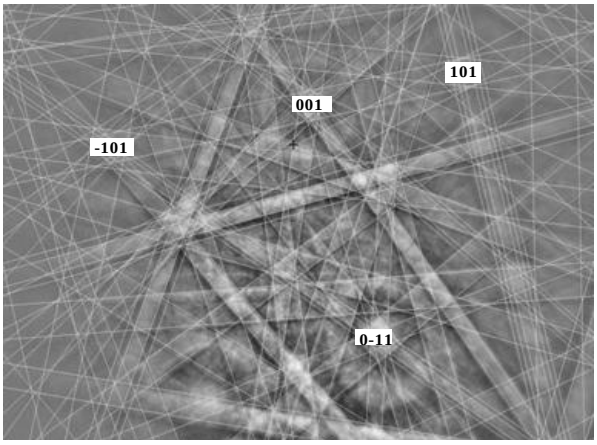

Figure 4.46 - EBSD pattern at the beam location 'A' shown in Figure 4.45, indexed as ζ-$FeAl_2$.

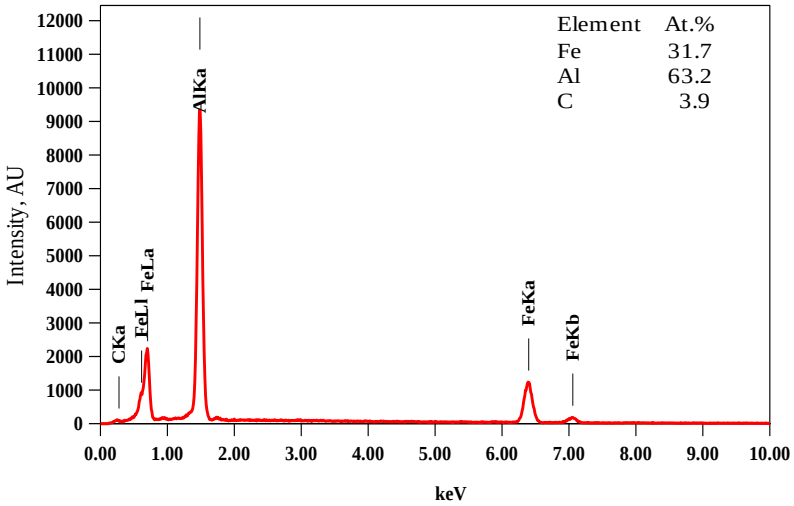

Figure 4.47 - EDS spectrum of ζ-$FeAl_2$ at beam location 'A' in Figure 4.45.

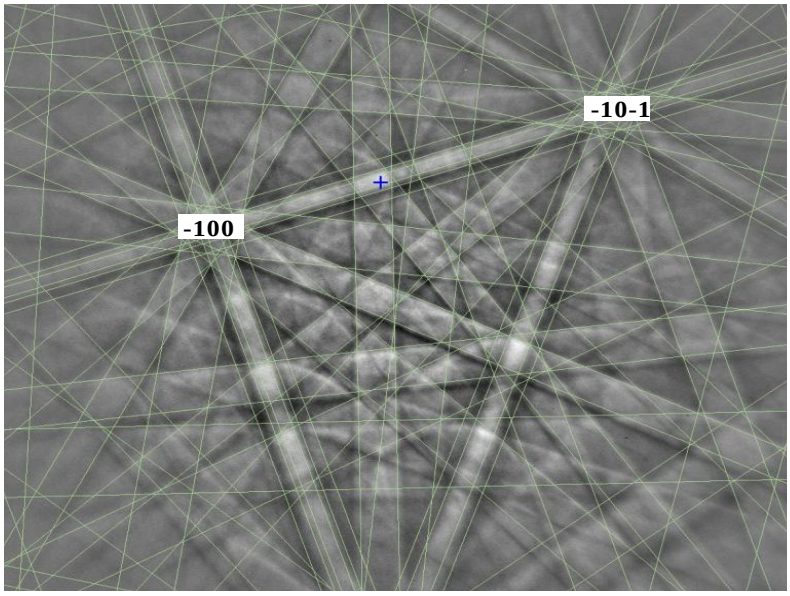

Figure 4.48 - EBSD pattern at beam location ‘B’ shown in Figure 4.45, indexed as κ-Fe_3AlC.

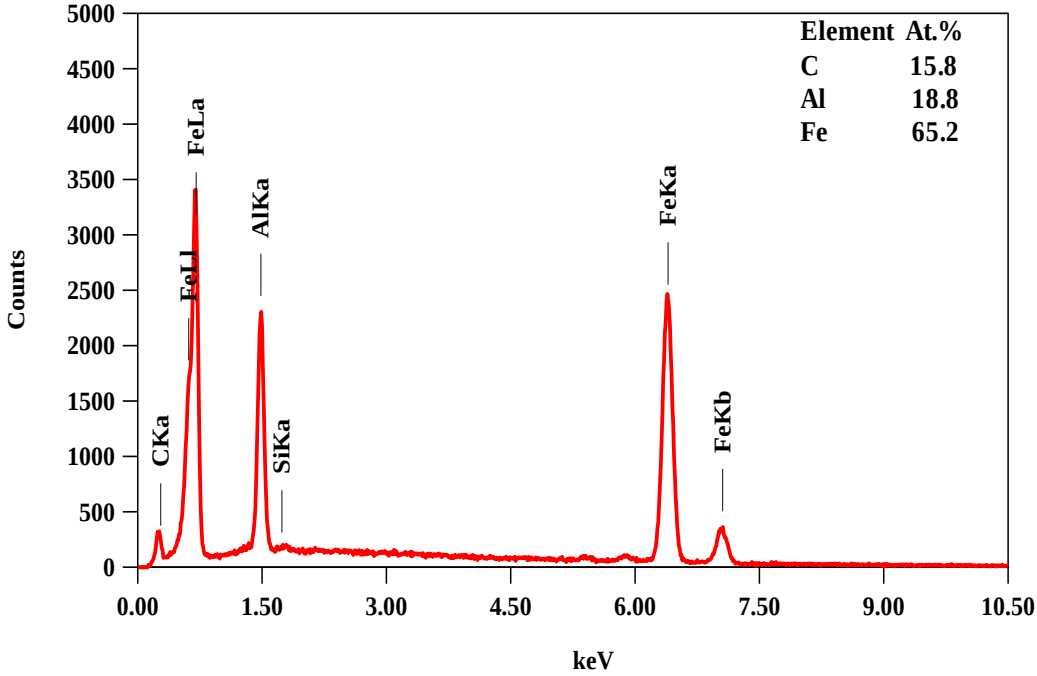

Figure 4.49 - EDS spectrum at beam location ‘B’ shown in Figure 4.45.

4.4 Intermetallic Layer Growth

This section describes the intermetallic layer growth characteristics of steel and cast iron alloys (Series-I) at three temperatures 750°C, 850°C and 950°C. Only the thickness of η-Fe_2Al_5 was considered for the intermetallic layer growth analysis. The θ-$FeAl_3$ layer

thickness of different alloys could not be compared because the size and number θ-$FeAl_3$ particles varied to a large extent from one specimen to other.

After the static immersion tests, the polished specimens were investigated under SEM. Before capturing the SEM images, the entire intermetallic layer was inspected in order to exclude the abnormally thin and thick regions, and then the images were captured at random locations. These regions may be occurring due to the inhomogeneous microstructures (ferrite, pearlite and cementite) of cast irons. BSE images in Figure 4.50, Figure 4.51 and Figure 4.52 show examples of the intermetallic layers of each alloy type: GCI-B, DCI-T and CS for time periods 300s-2400s at 750ºC, 850ºC and 950ºC.

4.4.1 Determining Mean Intermetallic Layer Thickness

The mean intermetallic layer (η-Fe_2Al_5) thickness of each alloy was evaluated from two BSE images at the magnification of 200x. Figure 4.53 shows a schematic for measuring the mean intermetallic layer thickness. The area of the η-Fe_2Al_5 phase - confined by the dotted line - is named ‘A’ and ‘b’ is the breadth of the intermetallic layer in a BSE image. The area of the η-Fe_2Al_5 phase was evaluated using image analysis software (Image J) and the mean thickness (x) of the intermetallic layer was calculated using the following relationship:

$$x = \frac{A}{b} \tag{4.2}$$

To compare the intermetallic layer thickness of each alloy type: GCI-B, DCI-T and CS - the x versus exposure time (t) plots of these alloys at 750°C, 850°C and 950°C are shown in Figure 4.54.

Alloy / Time	300s	600s	1200s	2400s
a) GCI-B				
b) DCI-T	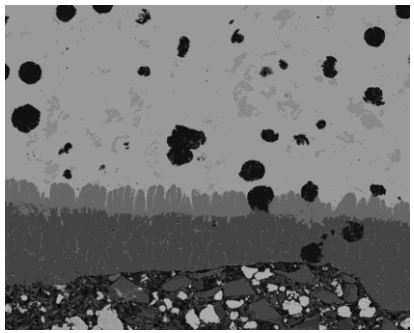	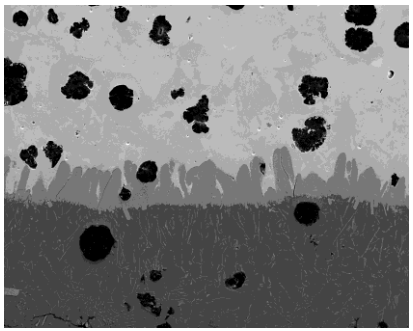		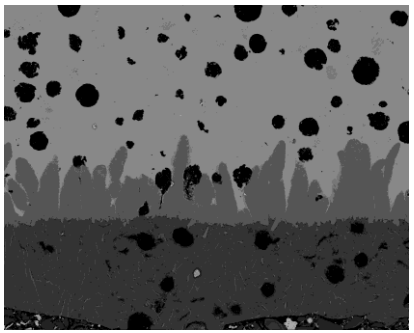
c) CS	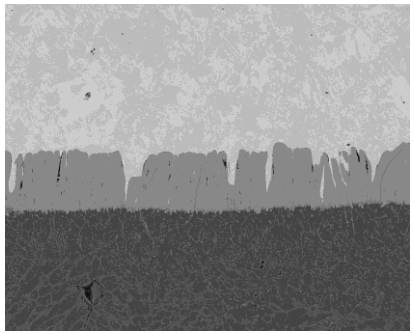	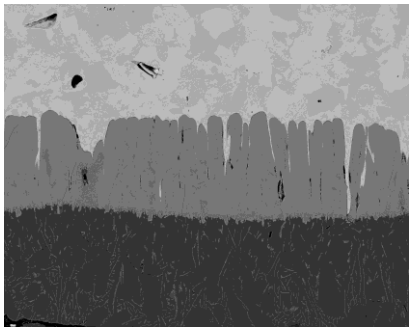	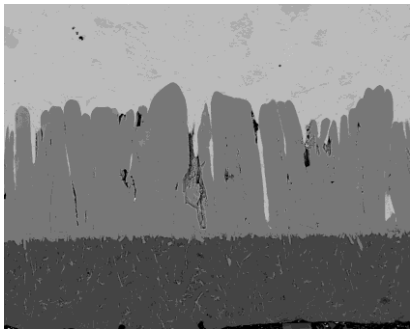	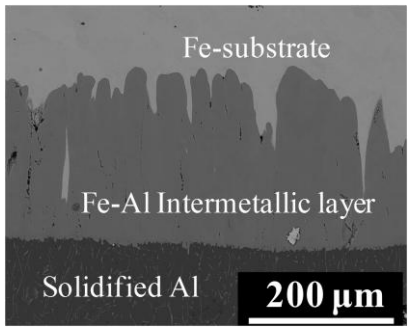

Figure 4.50 - BSE images of intermetallic layers, a) GCI-B, b) DCI-T, c) CS, obtained from 750°C-static specimens.

Alloy / Time	300s	600s	1200s	2400s
a) GCI-B	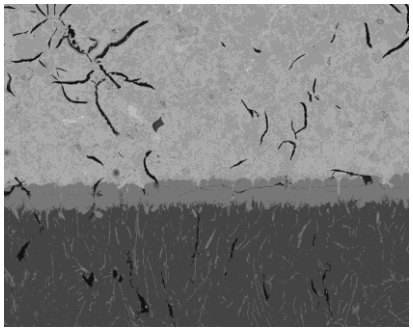			
b) DCI-T	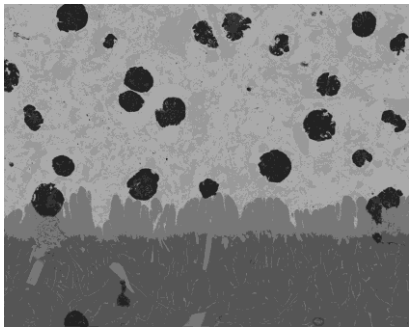		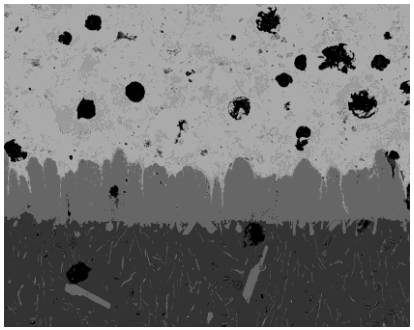	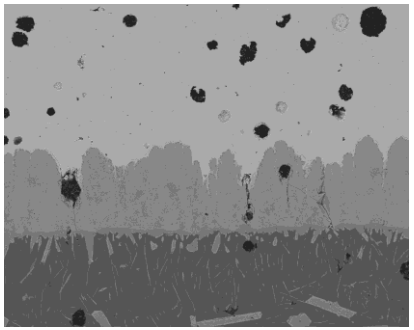
c) CS	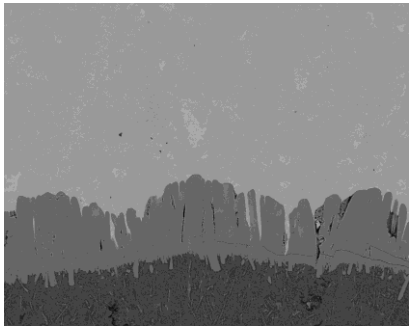		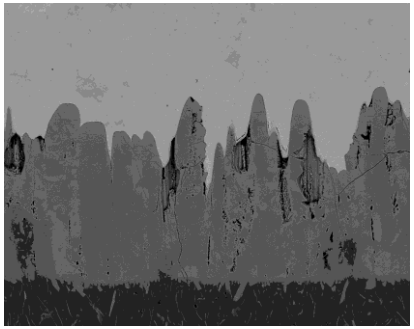	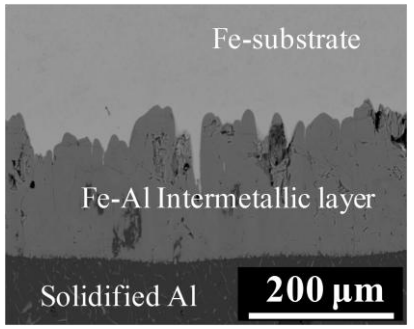

Figure 4.51 - BSE images of intermetallic layers, a) GCI-B, b) DCI-T, c) CS, obtained from 850°C-static specimens.

Alloy / Time	300s	600s	1200s	2400s
a) GCI-B			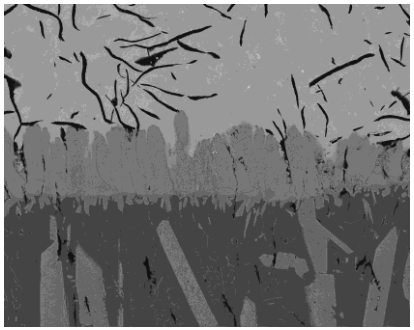	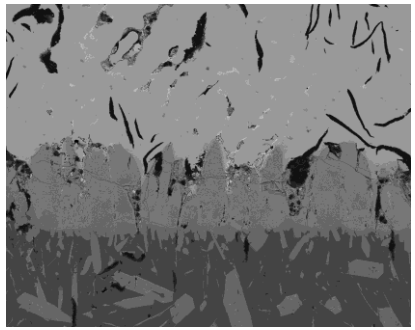
b) DCI-T	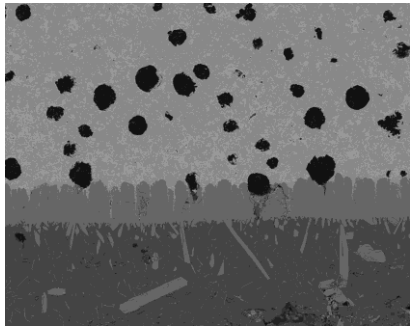		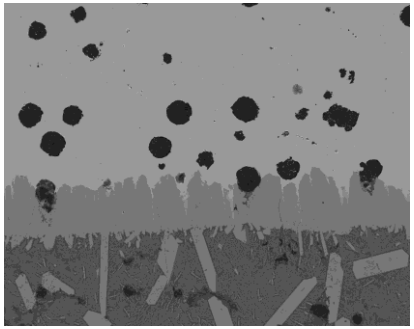	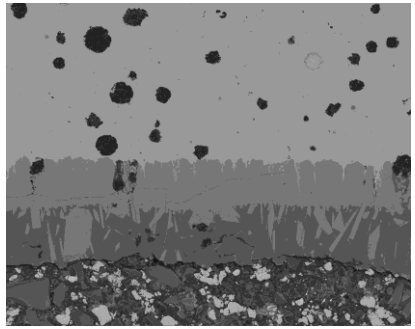
c) CS	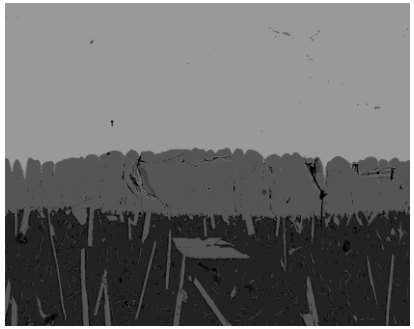	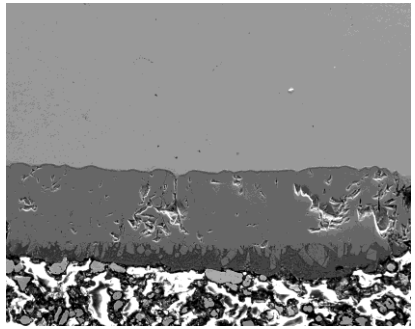	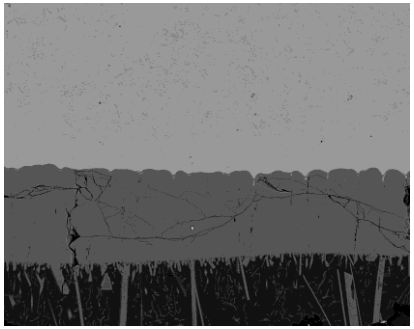	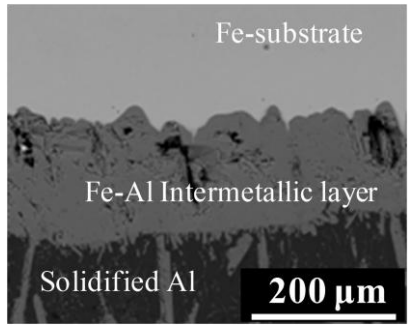

Figure 4.52 - BSE images of Intermetallic layers, a) GCI-B, b) DCI-T, c) CS, obtained from 950°C-static specimens.

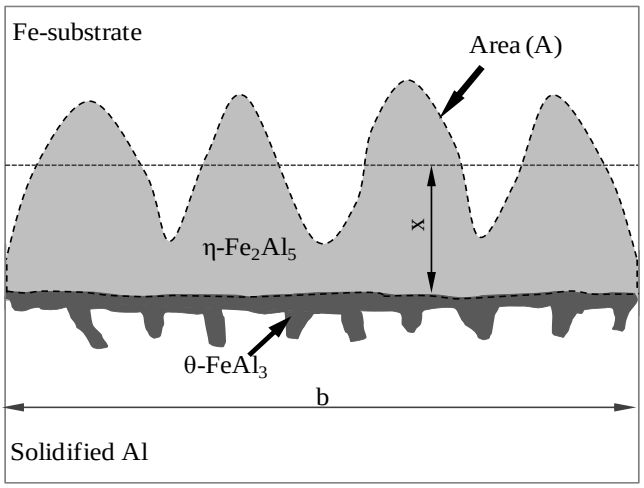

Figure 4.53 - A schematic for measuring the mean intermetallic layer (η-Fe_2Al_5) thickness.

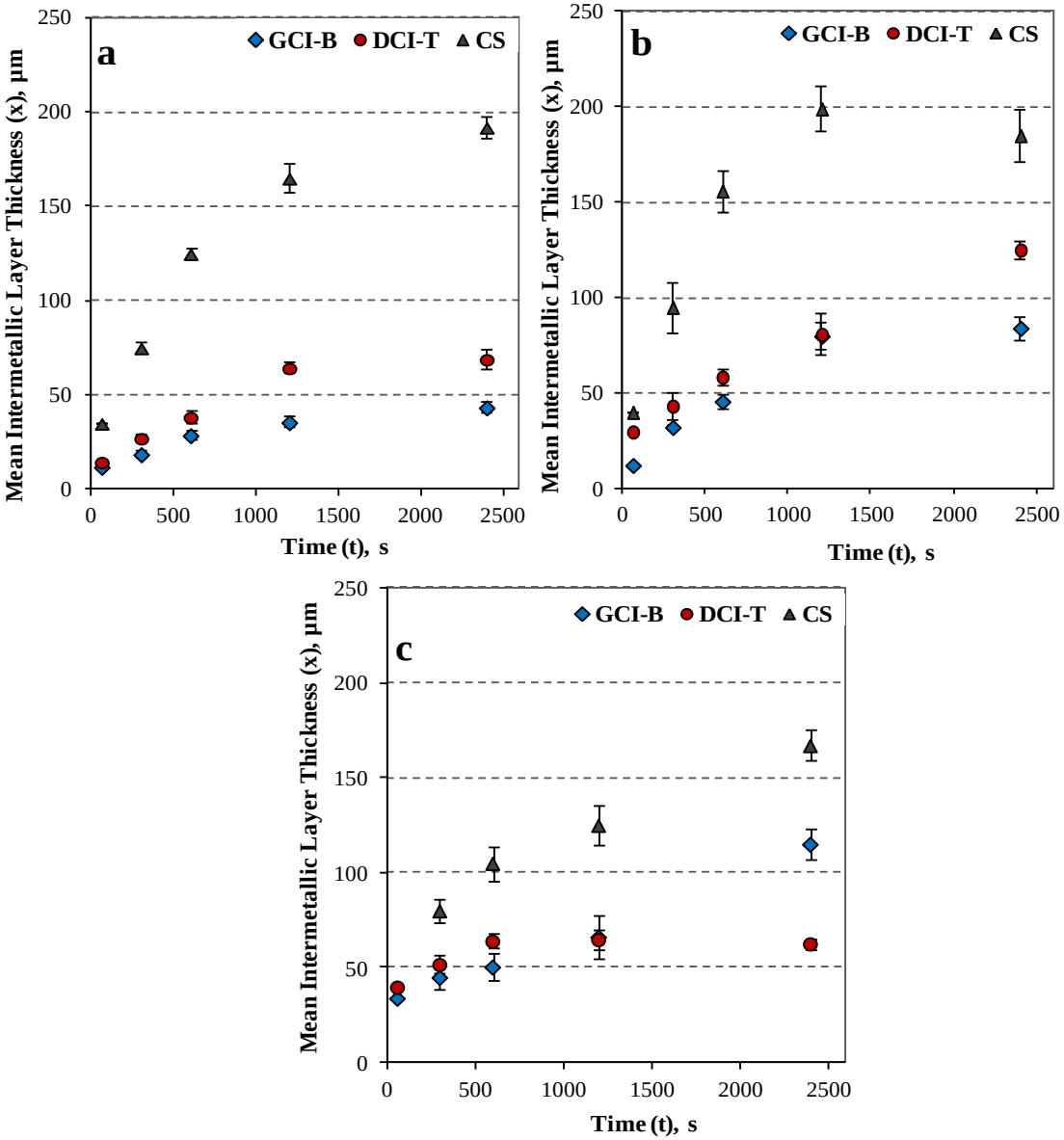

Figure 4.54 - Mean intermetallic layer (η-Fe_2Al_5) thickness v/s time plots of GCI-B, DCI-T and CS specimens exposed to static liquid Al, a) 750°C, b) 850°C, c) 950°C.

To show the effect of exposure temperature on the thickness of the η-Fe_2Al_5 intermetallic layer, x-t plots for each alloy at the three temperatures are given in Figure 4.55.

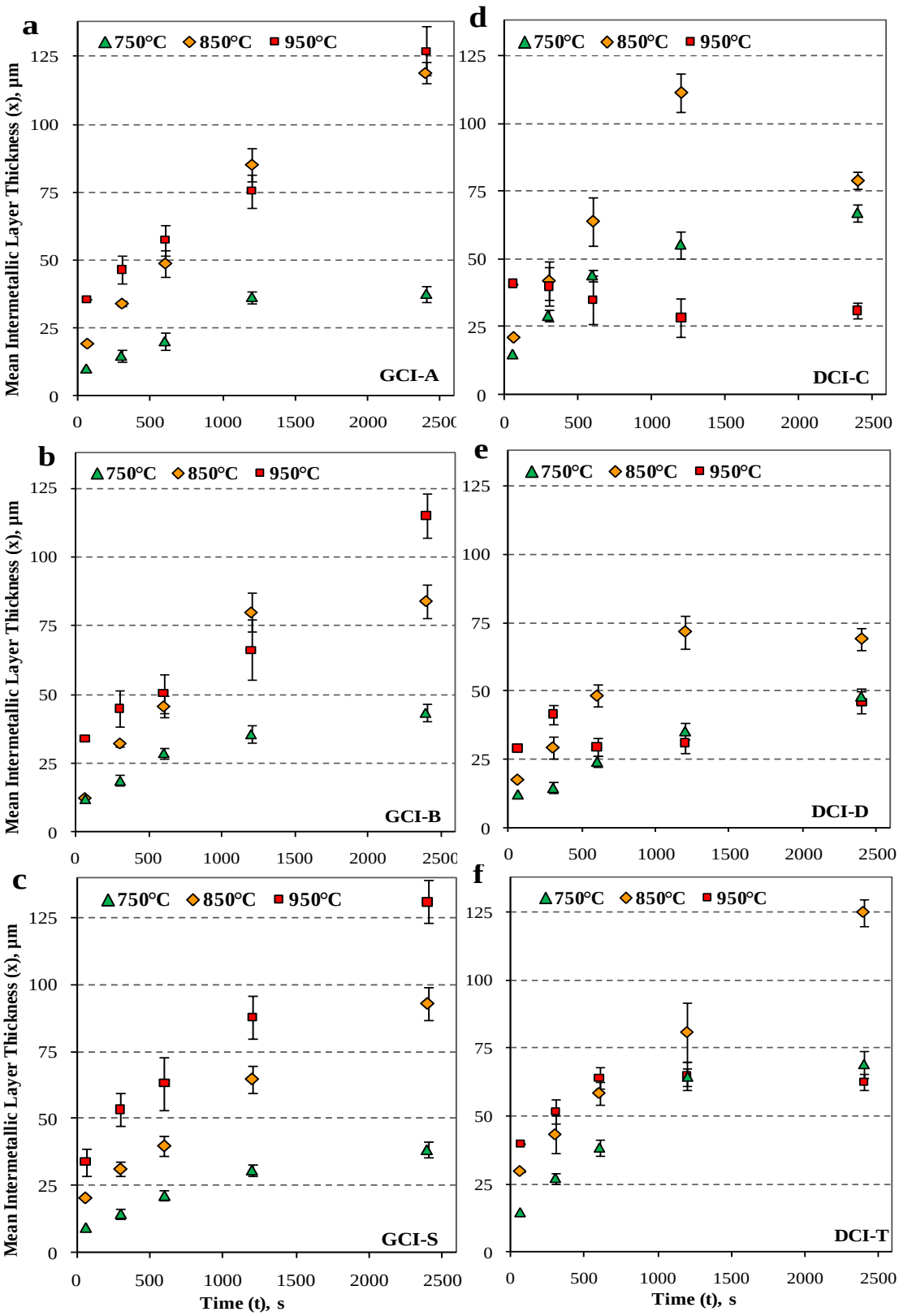

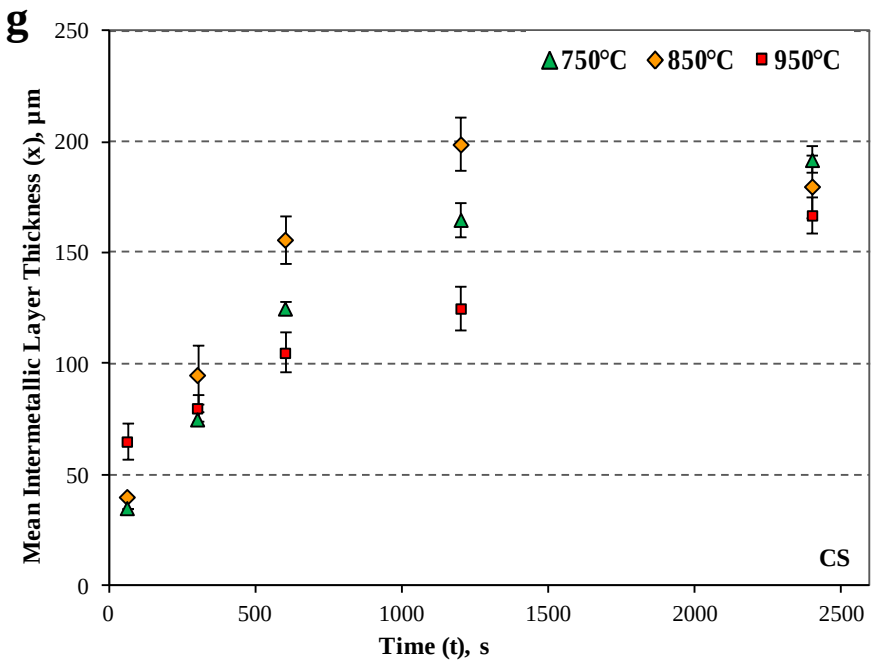

Figure 4.55 - Mean intermetallic layer (η-Fe_2Al_5) thickness of cast irons and steel at 750°C, 850°C and 950°C, a) GCI-A, b) GCI-B, c) GCI-S, d) DCI-C, e) DCI-D, f) DCI-T, g) CS.

4.4.2 Mean Intermetallic Layer Thickness and Time Relationship

In agreement with the previous studies [10] on Fe-Al interaction, at 950°C for initial exposure time (60s), the intermetallic layer growth for all alloys occurred at a considerably greater rate than the subsequent period. At the Fe-liquid Al interface, the processes of wetting, nucleation and reaction between the atoms of two metals occur in a short time (< 1s [11]), and the intermetallic layer growth in the initial period is reaction controlled. In this regime, the intermetallic layer is very thin and the diffusion paths are very short thus the supply of Fe/Al atoms was suggested to be almost instantaneous at the respective interfaces (Fe-Al, Al-Fe) and these react to their full extent [10].

The growth of the intermetallic layer between two solids follows the parabolic kinetics and can be given by the Equation 4.3 [4, 10], for details refer to Section 2.2.3.

$$x = (2k_1t)^{1/2} \quad (4.3)$$

where k_1 is intermetallic layer growth constant and t is the exposure time.

In Fe-liquid Al systems - previous reports reviewed in [4] showed that for pure iron and plain carbon steels in liquid Al at 800°C - the parabolic growth laws could not be deduced and the time exponents for the power growth law were found in the range of 0.27-0.38. For longer immersion times, the negative deviations to the parabolic growth law were frequently attributed to the dissolution and/or spalling of the intermetallic layer [4]. In present work, for t > 1200s, the DCIs and CS showed a decrease in mean intermetallic layer thickness. Thus for all alloys, x at 2400s was excluded from the analysis and the power law, Equation 4.4, was used to express the relationship between x and t.

$$x = K't^n \quad (4.4)$$

where K′ is the constant of intermetallic layer growth and n is the time exponent.

K′ and n were determined from the linear fitting of data points on Log(x) versus Log(t) plots as shown in Figure 4.56.

Table 4.7- K′ and n for power law growth of η-Fe_2Al_5 intermetallic layer of cast irons and steel at 750°C, 850°C, 950°C.

Materials	Time exponent (n)			Constant of intermetallic layer growth (K′), μms^{-n}			Goodness of linear fit (R^2)		
	750°C	850°C	950°C	750°C	850°C	950°C	750°C	850°C	950°C
GCI-A	0.39	0.47	0.24	1.83	2.50	12.58	0.896	0.960	0.953
GCI-B	0.37	0.54	0.21	2.50	1.50	13.86	0.973	0.985	0.957
GCI-S	0.39	0.36	0.30	1.71	4.27	09.35	0.965	0.941	0.983
DCI-C	0.44	0.54	- 0.11	2.37	2.14	68.86	0.993	0.976	0.731
DCI-D	0.34	0.46	0.01	2.61	2.43	30.47	0.853	0.964	0.006
DCI-T	0.48	0.32	0.17	1.89	7.38	19.50	0.975	0.966	0.956
CS	0.52	0.54	0.31	3.94	4.22	12.94	0.992	0.989	0.935

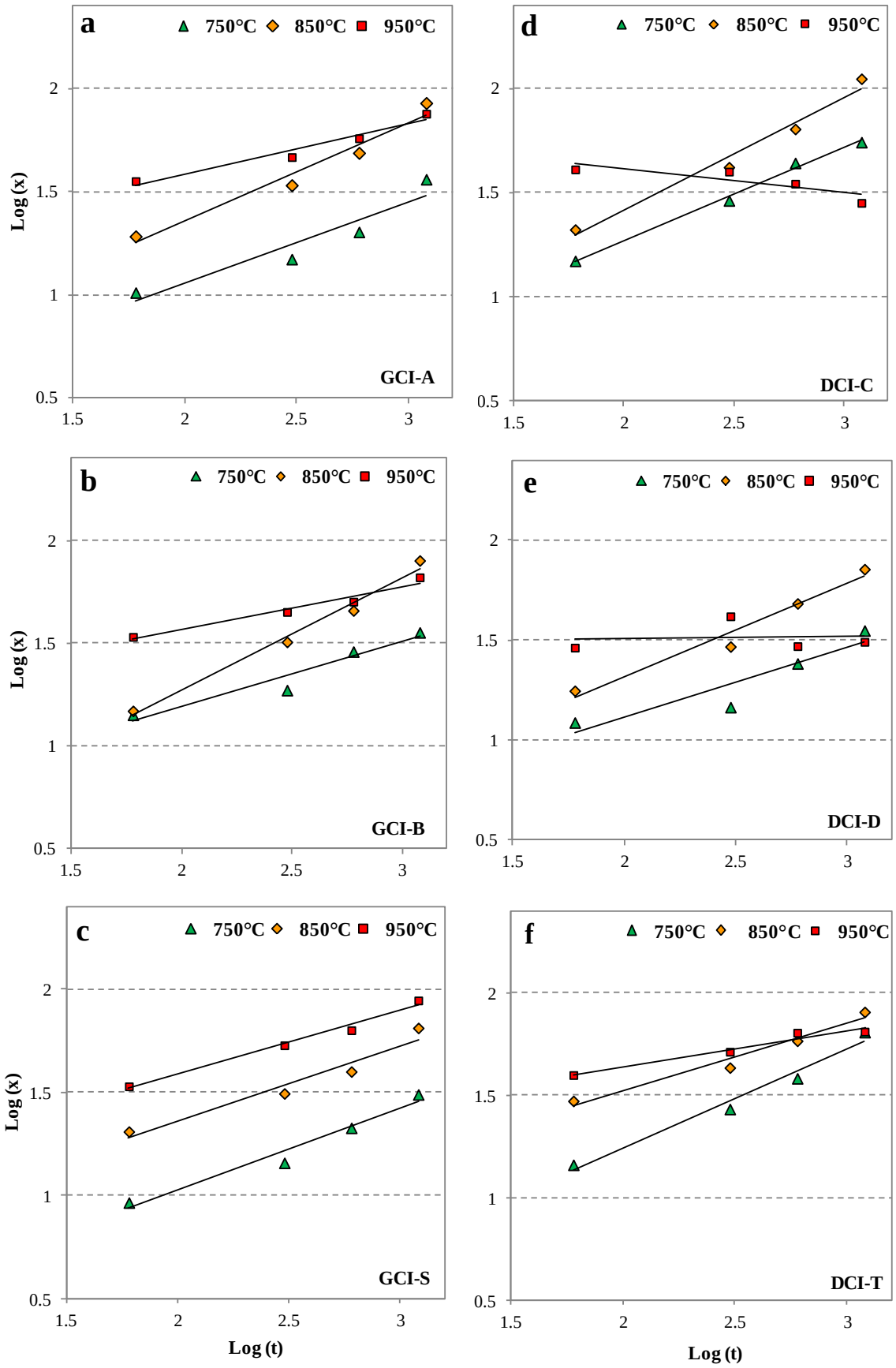
a
750°C 850°C 950°C
GCI-A
d
DCI-C
b
GCI-B
e
DCI-D
c
GCI-S
f
DCI-T
Log (x)
Log (t)
0.5
1
1.5
2
2.5
3

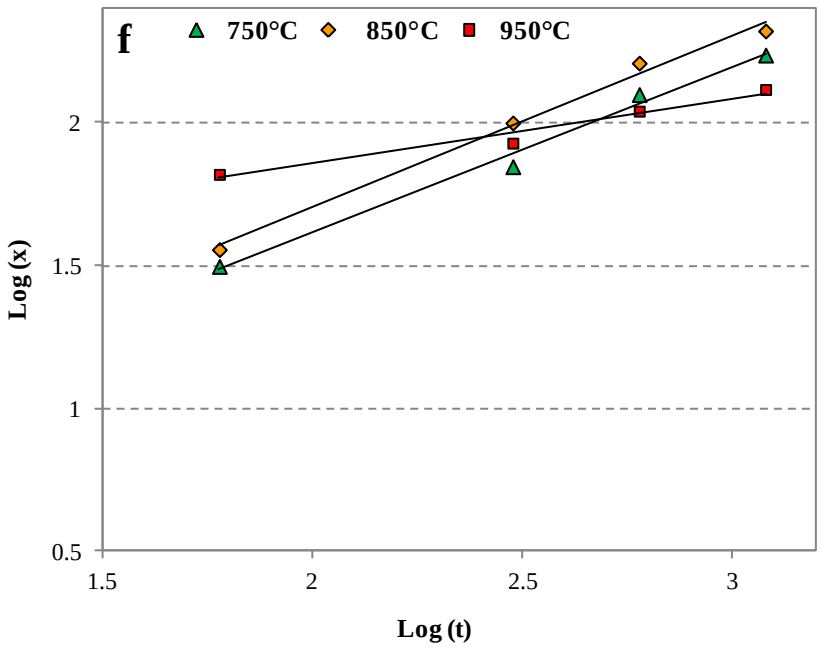

Figure 4.56 - Log(x) v/s Log(t) plots at 750°C, 850°C and 950°C, a) GCI-A, b) GCI-B, c) GCI-S, d) DCI-C, e) DCI-D, f) DCI-T, g) CS.

At 750°C and 850°C, the value of n varied between 0.32-0.54 and for CS and DCI-C the value of n was close to 0.5. In general, n increased with rise in temperature from 750°C to 850°C; however, with a further rise to 950°C, it decreased. Compared to GCIs and CS, the DCIs showed lower values of n at 950°C. At 950°C, DCI-C and DCI-D showed larger deviations from linearity than other alloys.

4.5 Dissolution and Intermetallic Layer Growth Kinetics

4.5.1.1 Determination of Dissolution

To determine the relationship between dissolution and growth of intermetallic layers of steel and cast iron alloys, the material loss of the static immersion specimens (Section 3.2.2) was measured in terms of the material thickness lost. Specimens from immersion tests of short durations (60s, 300s) showed an increase instead of a decrease in the dimensions by dissolution. Figure 4.57 shows a DCI-C specimen (850°C-300s-static) cross-section with the bi-directional growth of the intermetallic layer. The cast iron substrate at both sides of the interaction zone was protected using Boron Nitride Lubricoat® paste. At first, it appears that

no dissolution occurred. However, the increase in the specimen dimensions by the formation of η-Fe_2Al_5 is obvious because it has considerably lower density (about 4100 Kg/m^3 [12]) compared to the ferrous substrates (about 7800 Kg/m^3). Thus the formed intermetallic layer can grow towards the Al melt also.

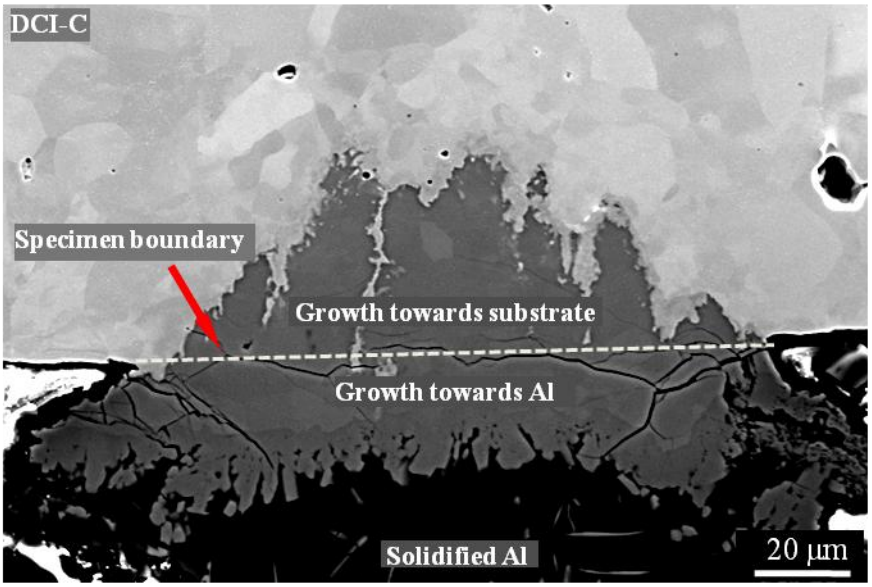

Figure 4.57 - Bi-directional growth of the intermetallic layer on a DCI-C specimen (850°C-300s-static).

When the dissolved thickness is measured for limited periods of immersion, the intermetallic layer growth may outweigh the dissolved thickness. Therefore, the question of including or excluding the interlayer thickness in the dissolution measurements was addressed by considering the Pilling Bedworth Ratio (PBR). PBR was established to determine the volume change caused by the formation of oxide during oxidation of metals [13]. Using PBR the dissolved thickness of Fe-substrate can be approximated. The PBR for the Fe-Fe_2Al_5 system can be calculated as:

$$PBR = \frac{V_{Fe2Al5}}{2V_{Fe}} \tag{4.5}$$

where V is the molar volume

$$V_{Fe_2Al_5} = \frac{W_{Fe2Al5}}{\rho_{Fe2Al5}} \quad (4.6)$$

and

$$V_{Fe} = \frac{W_{Fe}}{\rho_{substrate}} \quad (4.7)$$

where W is the molar weight and ρ is the density. Table 4.8 lists the used data and the calculated PBRs.

Table 4.8 - Property data and the calculated PBRs of cast iron and steel.

Molar weight, g/mol		Density (g/cm^3)			Calculated PBR	
W_{Fe2Al5}	W_{Fe}	ρ_{Fe2Al5}	ρ_{steel}	$\rho_{cast\ iron}$	Steel	Cast iron
246.58	55.84	4.1 [12]	7.8	7.225	4.32	3.89

The actual PBR of cast iron/ η-Fe_2Al_5 can differ from the calculated values considering the fact that graphite particles have significantly lower density than the Fe-matrix. Moreover, the alloying elements present in an alloy can also affect the density of the substrate and η-Fe_2Al_5. Thus the PBR here is simply used to signify the approximate amount of Fe present in the intermetallic layer, which has not been dissolved into the Al melt. Figure 4.58 shows a schematic for determining the dissolved thickness of substrate.

Plane A-A represents the initial specimen boundary, ζ is the total mean penetration depth of η-Fe_2Al_5 into the ferrous substrate. The mean intermetallic layer thickness (x) may be larger or smaller than ζ depending upon the growth and dissolution characteristics of the intermetallic layer. The volume dimensions perpendicular to the growth direction were assumed to be constant in the finite space under consideration. Therefore, the dimension of the intermetallic layer in the growth direction of the interlayer can be used to represent the volume change, and under such conditions, the dissolution in-terms of the thickness of Fe lost from the substrate (d_{Fe}) can be given by:

$$d_{Fe} = \zeta - \frac{x}{PBR} \quad (4.8)$$

and the amount of dissolution in terms of η-Fe_2Al_5 thickness ($d_{Fe_2Al_5}$) can be given by:

$$d_{Fe_2Al_5} = d_{Fe}(PBR) \quad (4.9)$$

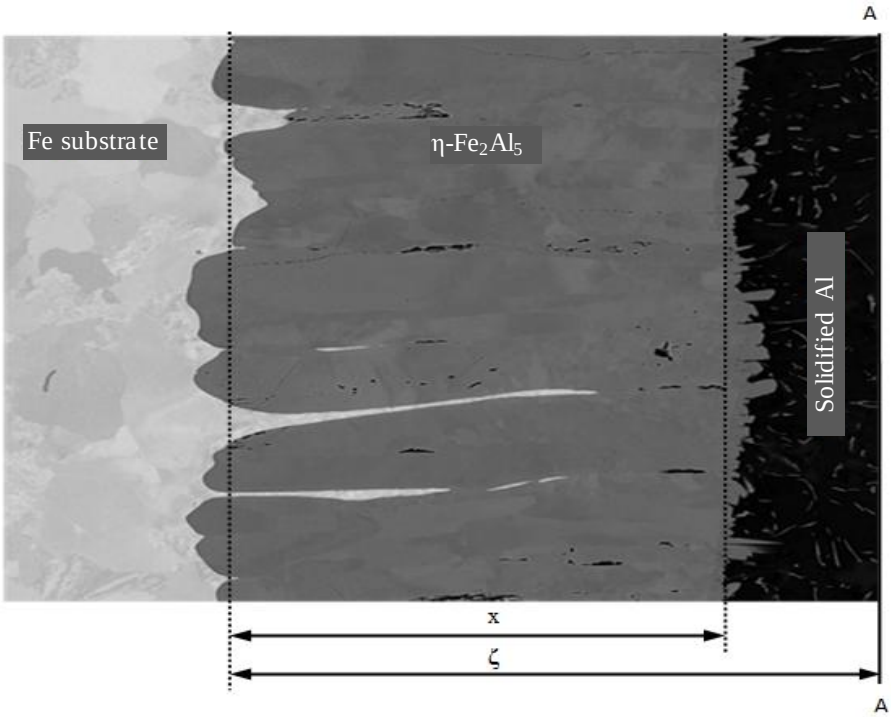

Figure 4.58 - A schematic for evaluating the dissolution of Fe-substrate in-terms of η-Fe_2Al_5 thickness.

It is to be noted that $d_{Fe_2Al_5}$ represents only a scale not how the dissolution has occurred. Dissolution of Fe-substrates can be a combination of dissolution and/or spallation of the intermetallic layer, and the direct diffusion of Fe atoms to liquid Al.

4.5.1.2 Comparing Intermetallic Layer Growth and Dissolution

GCIs, DCIs and CS showed dissimilar characteristics of intermetallic layer growth and dissolution. Figure 4.59 shows the x-t and $d_{Fe_2Al_5}$-t plots of cast iron alloys (950°C-static); $d_{Fe_2Al_5}$ is presented on the negative scale and x is plotted as positive.

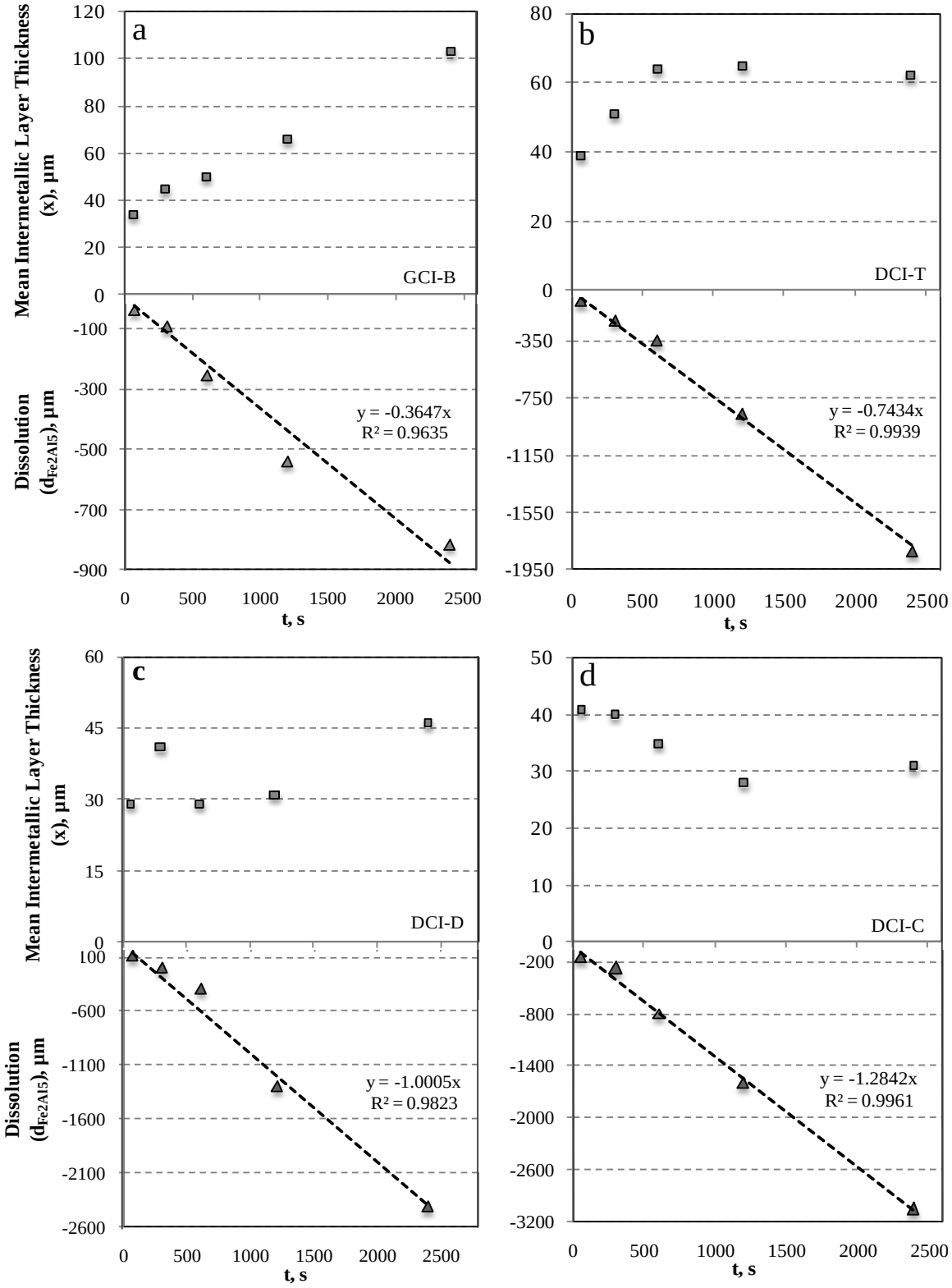

Figure 4.59 - Dependence of mean intermetallic layer thickness (x) and dissolution (d_{Fe2Al5}) upon time (950°C-static), a) GCI-B, b) DCI-T, c) DCI-D, d) DCI-C.

The $d_{Fe_2Al_5}$-t relationship was found to be linear for all alloys under investigation. GCIs showed considerably lower dissolution rate than DCIs. Among DCIs, DCI-T exhibited lowest dissolution rate followed by DCI-D and DCI-C, in that order. At 950°C, the growth of intermetallic layers of DCIs showed large negative deviations from the parabolic growth law ($x=K't^{0.5}$), Table 4.7, and decreasing trends in intermetallic layer thickness with increasing exposure time were commonly found. At 950°C, in GCIs, the negative deviations from the parabolic growth law were lower compared to DCIs, and thinning of the intermetallic layers of GCIs with increasing time or temperature was not observed. In contrast, DCIs commonly showed thinner intermetallic layers at 950°C compared to the lower temperatures.

4.6 Morphology of the Intermetallic Layers

The morphology of the intermetallic layer and corrosion rates were found to vary with the substrate composition and alloy type. In order to better understand the intermetallic compound structure, a deep-etching technique was also used to reveal the 3D morphology of the intermetallic layers of steel and cast irons. This analysis would be helpful to understand the effect of alloy composition on the structure of the intermetallic layer.

4.6.1 2D Morphology of the Intermetallic Layer

Figure 4.60 shows the examples of intermetallic layers of cast irons specimens for (850°C-600s-static) and (850°C-1200s-static). The intermetallic layer morphology of the DCI specimens was serrated and uneven. In contrast, the GCIs showed a uniform appearance. The morphology of intermetallic layers for these alloys was compared by evaluating the average maximum ($\overline{X}_{max}$) average minimum ($\overline{X}_{min}$) intermetallic layer thicknesses.

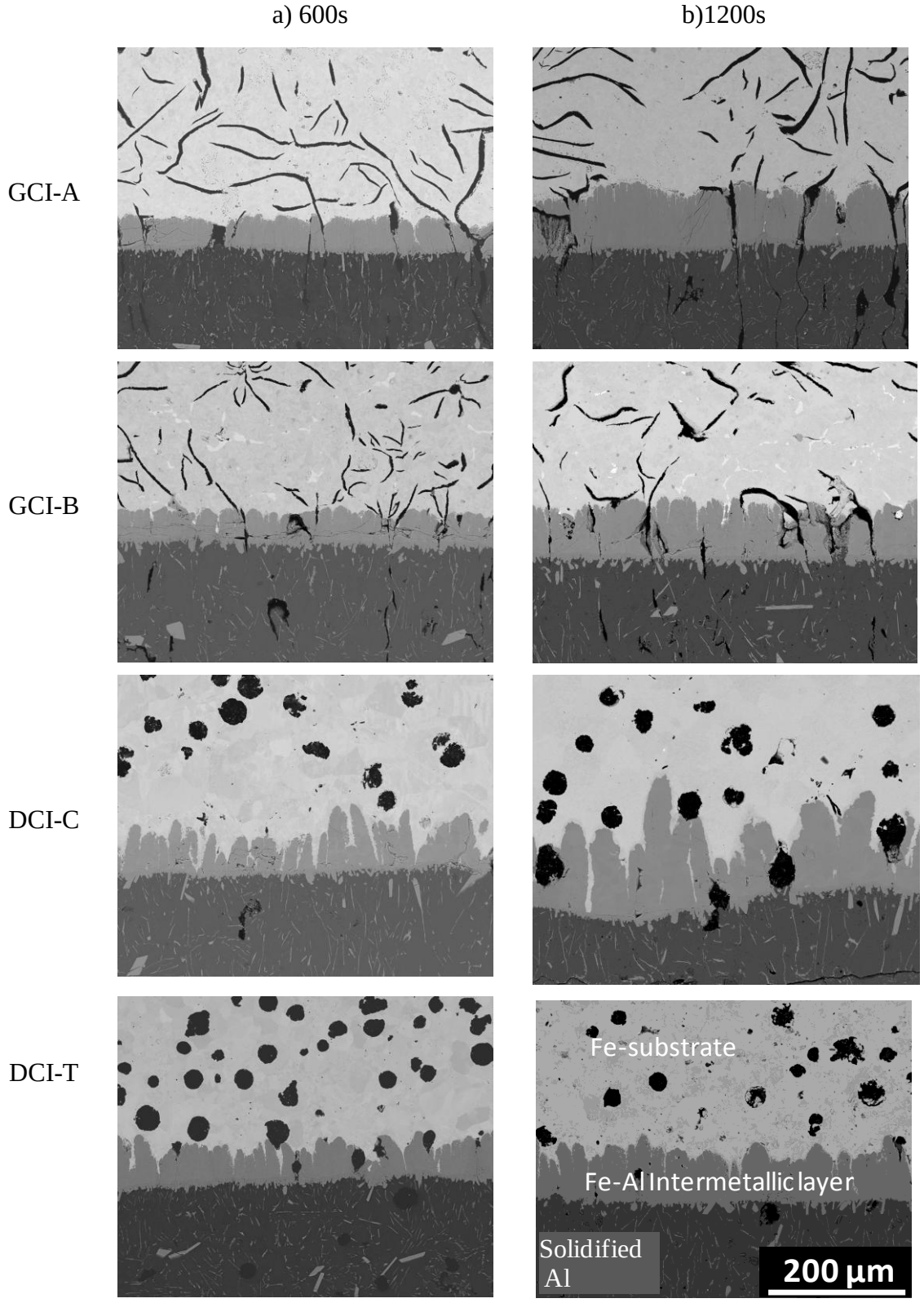

Figure 4.60 - Morphology of the intermetallic layers of various cast iron alloys at 850°C, a) 600s-static, b) 1200s-static.

Figure 4.61 illustrates X_{max} and X_{min} of an intermetallic layer. $\overline{X}_{max}$ and $\overline{X}_{min}$ for each alloy were calculated from four measurements for each dimension on two SEM images (850°C-

1200s-static). Figure 4.62 shows the measured $\overline{X}_{max}$ and $\overline{X}_{min}$ of GCIs, DCIs and CS, arranged in ascending order of their corrosion rates.

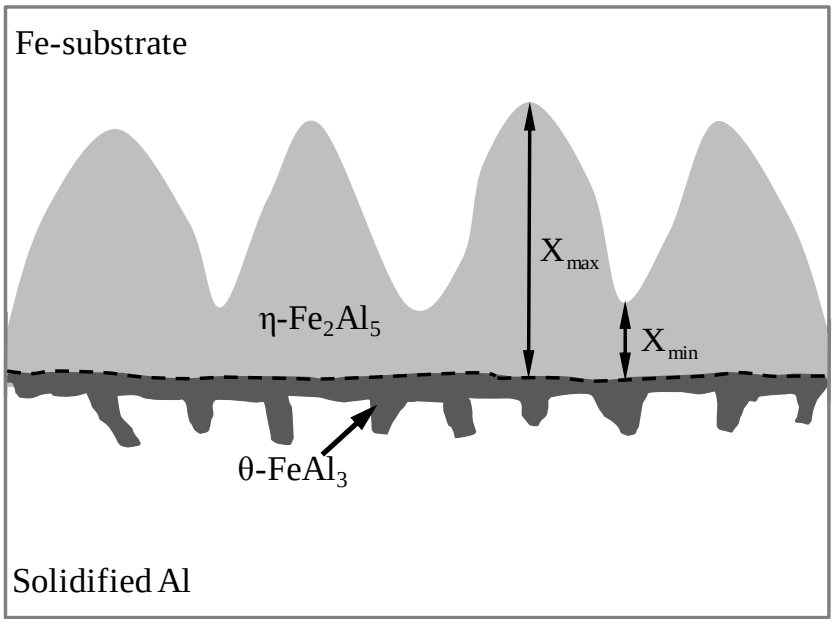

Figure 4.61 - A schematic showing X_{max} and X_{min} of an intermetallic layer.

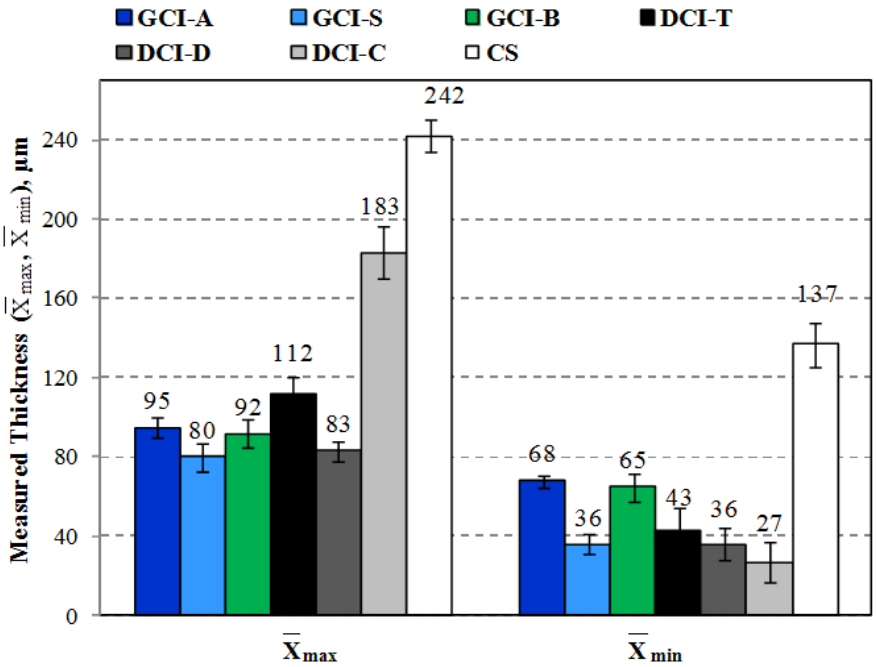

Figure 4.62 - Measured values of $\overline{X}_{max}$ and $\overline{X}_{min}$ of GCIs, DCIs and CS. (Arranged left to right in ascending order of corrosion rates)

Compared to GCIs, DCIs generally have higher $\overline{X}_{max}$ and lower $\overline{X}_{min}$. CS showed higher $\overline{X}_{max}$ and $\overline{X}_{min}$ values than cast irons. Among GCIs, a relatively lower value of $\overline{X}_{min}$ of GCI-S was attributed to the presence of cementite particles in its matrix as cementite particles act as barriers to intermetallic layer growth and were found to create regions of thinner intermetallic layer (Figure 4.20). The higher liquid Al corrosion rates of DCIs than GCIs appeared to be related to the relative values of $\overline{X}_{max}$ and $\overline{X}_{min}$.

4.6.2 3D Morphology of the Intermetallic Layer

After exposure to static liquid Al, specimens of CS, DCIs and GCIs were deep etched with 50% HNO_3 for two hours at room temperature. HNO_3 dissolves Fe, but it does not corrode the η-Fe_2Al_5 compound and the solidified Al. The deep-etching method worked well for steel and DCIs. However, being inert with HNO_3, the inter-connected graphite flakes in GCIs cannot be removed and thus true morphology of the intermetallic compounds of GCIs could not be revealed.

4.6.2.1 CS

Figure 4.63 shows a CS specimen (850°C-1200s-static); the Fe-Al intermetallic layer appears continuous. Figure 4.64 and Figure 4.65 show the 3D SEM images of the intermetallic layer of a deep-etched CS specimen (850°C-1200s-static). The η-Fe_2Al_5 phase can be seen as individual columns, which grew in a direction perpendicular to the specimen surface in contact with liquid Al. The outer surface of the cast steel (η-Fe_2Al_5) columns exhibited a uniform and smooth appearance, Figure 4.65. The thin line projections on the η-Fe_2Al_5 surface are expected to be the regions of relatively higher growth of η-Fe_2Al_5 across the grain boundaries of the steel substrate.

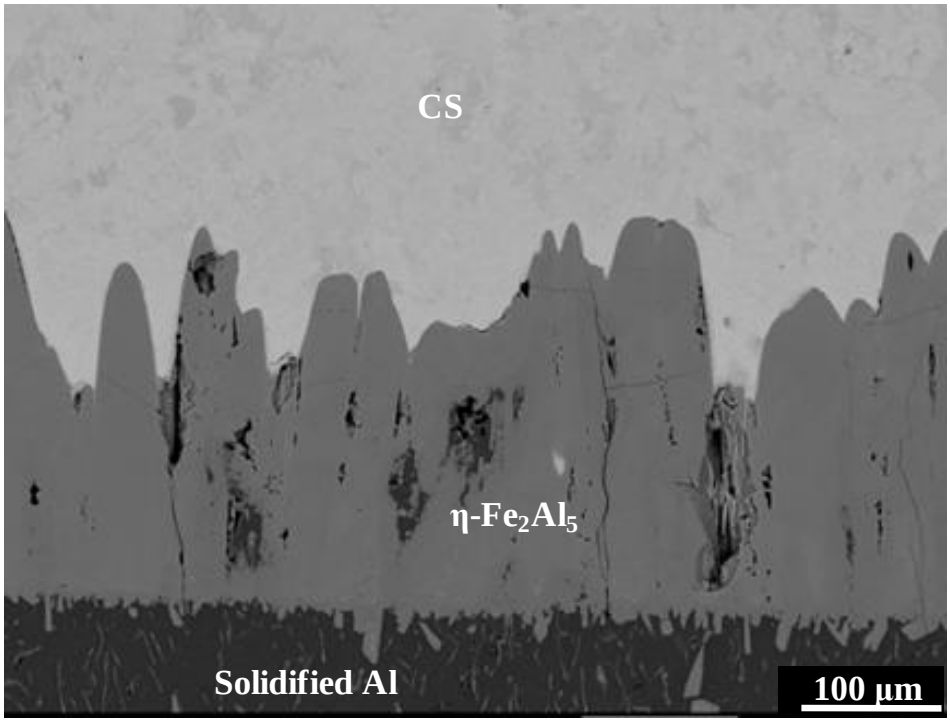

Figure 4.63 - Cross-section of an intermetallic layer of a CS specimen (850°C-1200s-static).

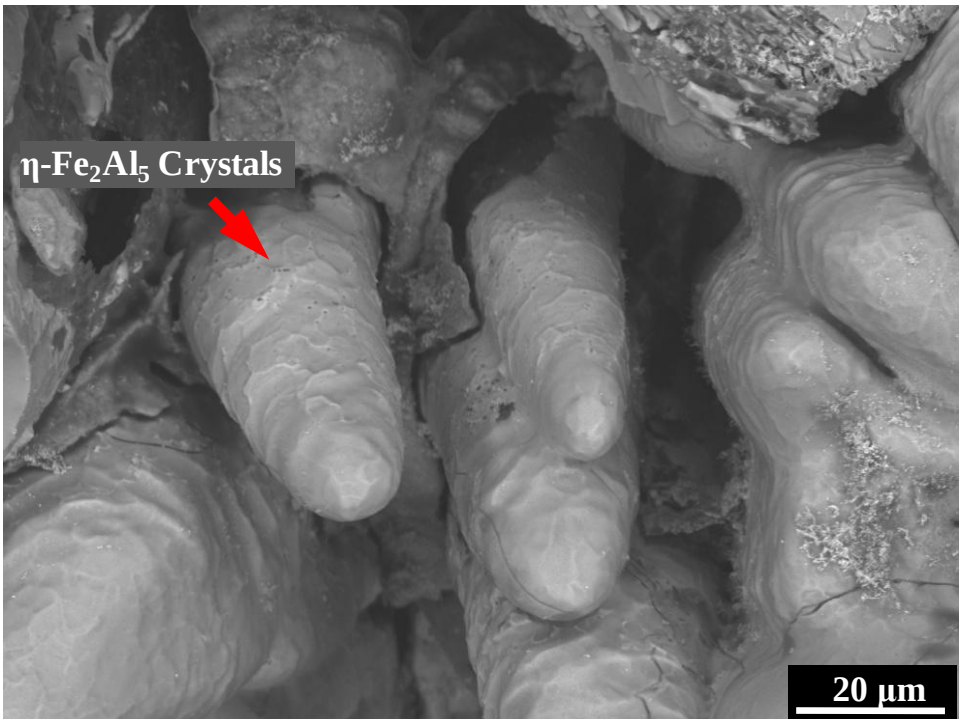

Figure 4.64 - A deep-etched 3D image of the η-Fe_2Al_5 intermetallic layer on CS specimen (850°C-1200s-static).

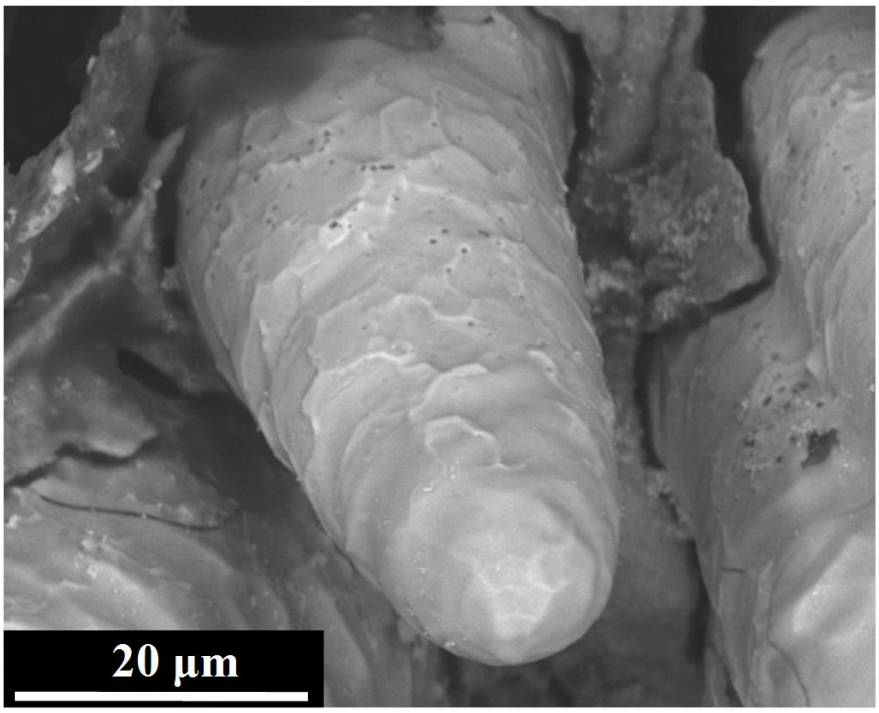

Figure 4.65 - SEM image showing the surface morphology of the η-Fe_2Al_5 columns.

4.6.2.2 DCI-T

Figure 4.66 shows a specimen cross-section of a DCI-T specimen (750°C-1200s-static). Serrations are visible on the η-Fe_2Al_5/substrate boundary. These may be due to Si build up at the Fe/η-Fe_2Al_5 interface. The 3D columnar structure of η-Fe_2Al_5 (DCI-T) is shown in Figure 4.67 and Figure 4.68. The removal of Fe after etching may have led to such morphology because Fe dissolves in HNO_3 leaving the Si rich colonies and η-Fe_2Al_5. Thus the remaining outer structure is possibly the η-Fe_2Al_5 consisting of colonies of the Fe_3(Al, Si) phase. It was difficult to distinguish between the η-Fe_2Al_5 and Fe_3(Al, Si) phase because of their similar colour contrast. However, EDS results indicated the existence of higher Si content in the slightly darker regions (~2 at.%-bright, ~7 at.%-dark) (Figure 4.69, Figure 4.70), and these can be the colonies of Fe_3(Al, Si) phase. These results are only an indication of the presence of Si since the accuracy of EDS results can be affected by the non-planar/uneven surfaces, and the existence of products of etching (such as oxides and nitrates of Fe) at the outer η-Fe_2Al_5 surface.

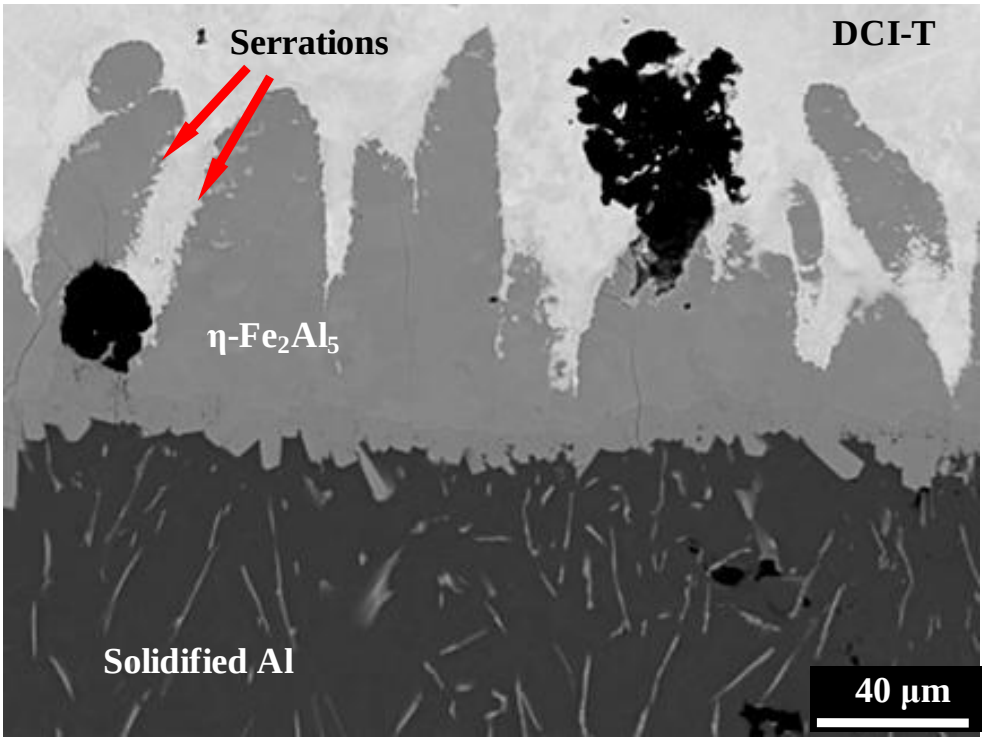

Figure 4.66 - A 2-D image of a DCI-T specimen (750°C-1200s-static).

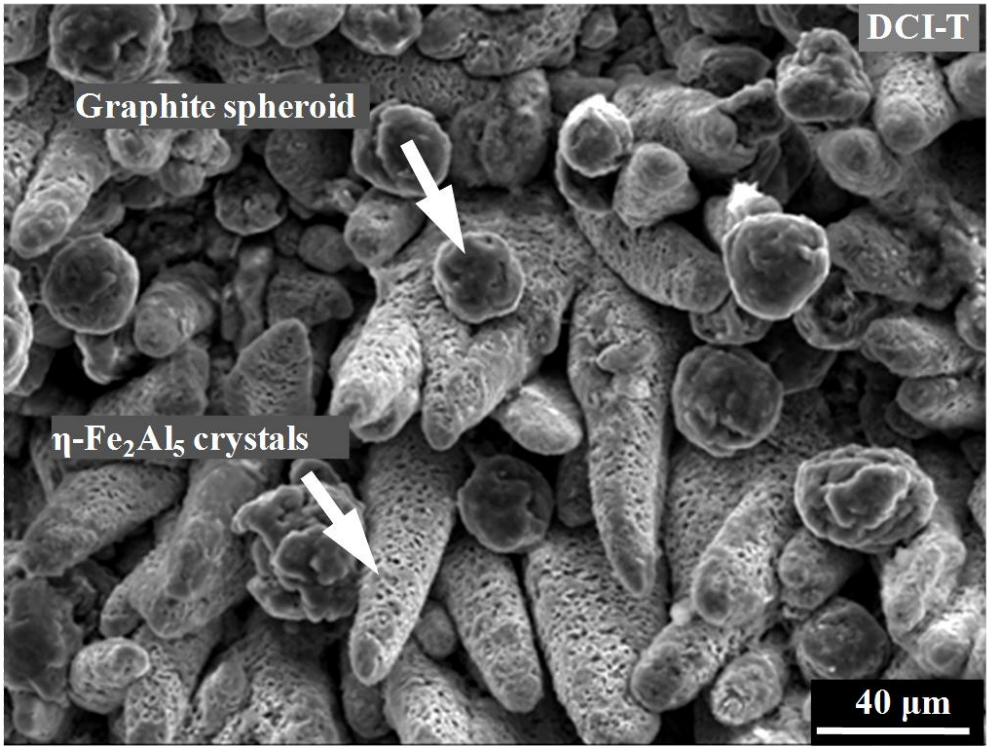

Figure 4.67 - Morphology of η-Fe_2Al_5 columns on a DCI-T specimen (750°C-1200s-static).

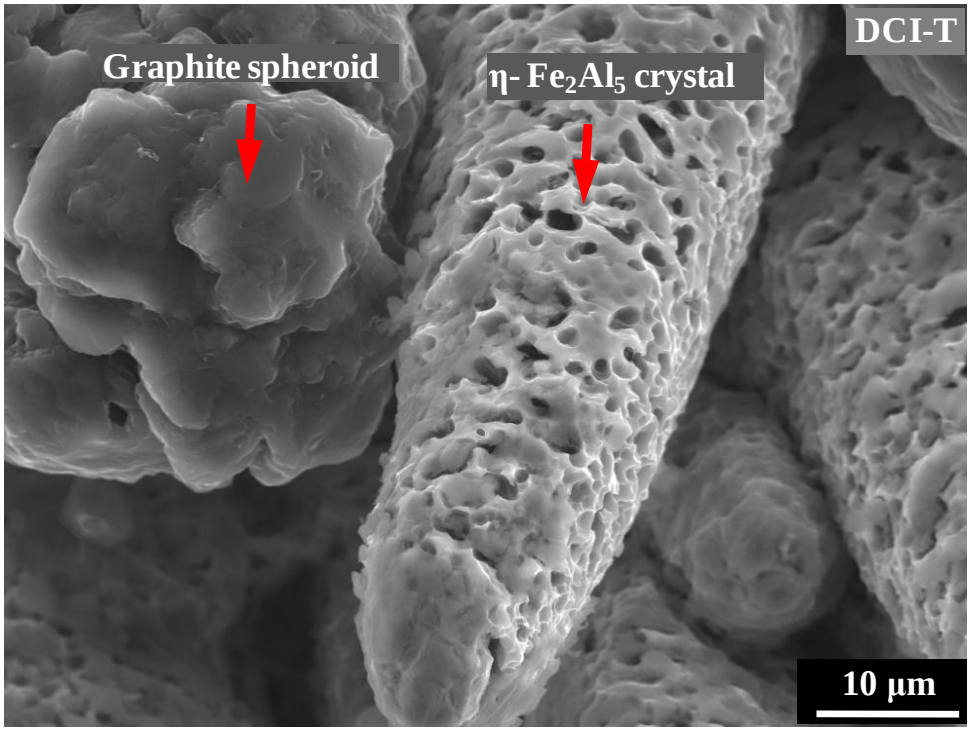

Figure 4.68 - A magnified image of a η-Fe_2Al_5 column on a DCI-T specimen (750°C-1200s-static).

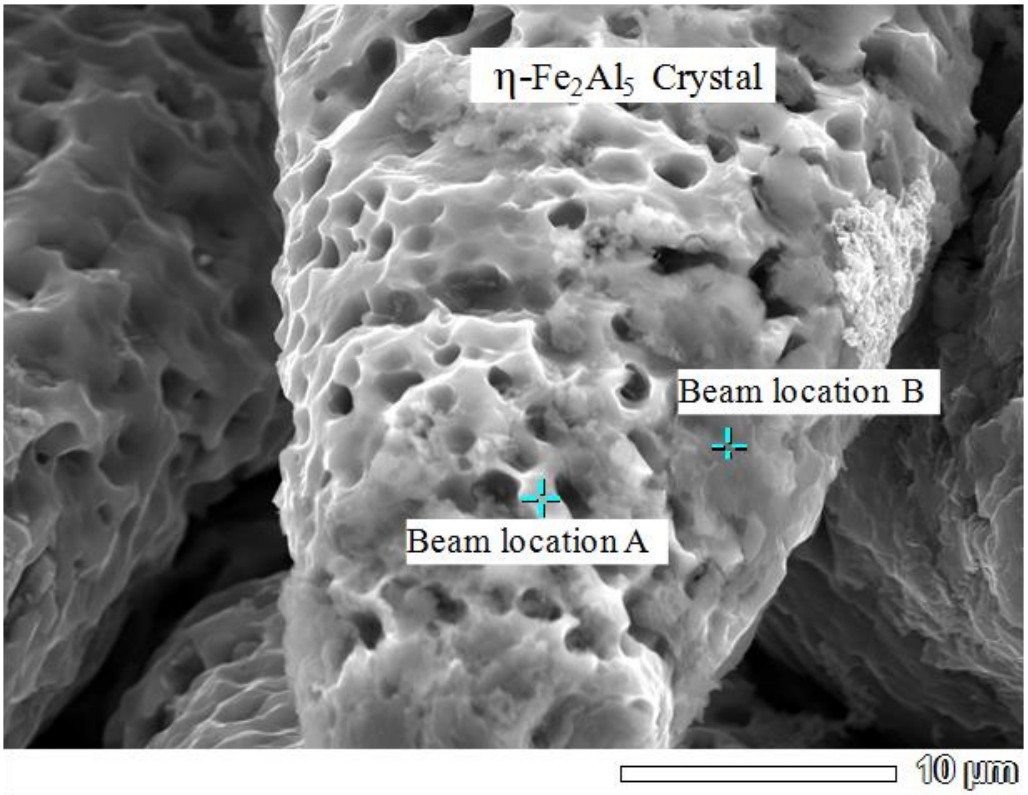

Figure 4.69 - An SEI image showing beam locations for EDS analysis on DCI-T specimen (750°C-1200s- static).

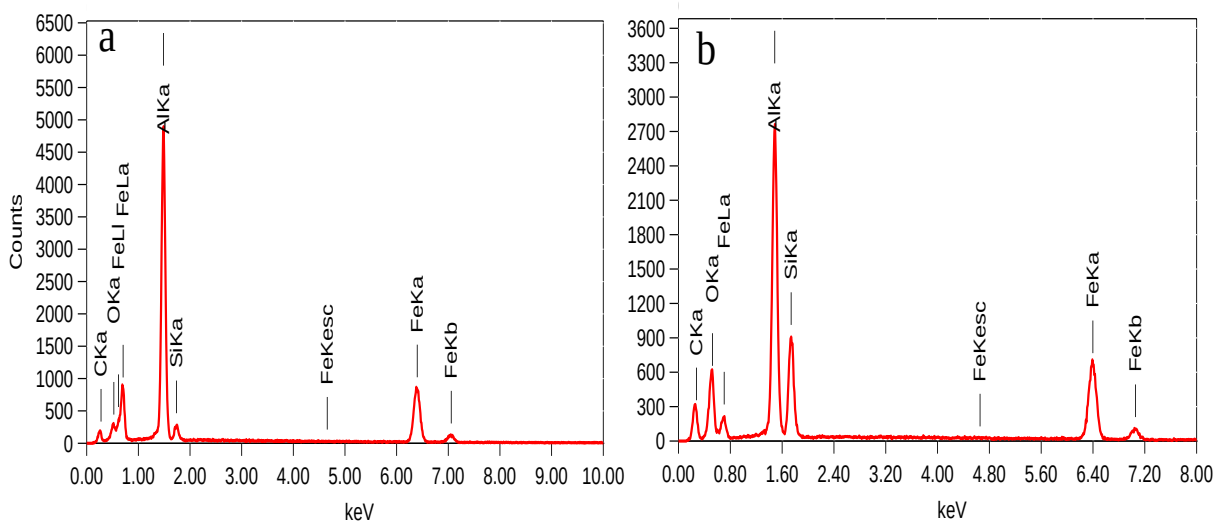

Figure 4.70 - EDS spectrums at beam locations shown in Figure 4.69, a) A, b) B.

4.6.2.3 DCI-C

Figure 4.71 shows the intermetallic layer morphology of DCI-C (950°C-1200s-static). The formation of a compound layer is evident over the η-Fe_2Al_5 columns. This compound layer was characterized as Fe_3Si (Section 4.3.1.3.1).

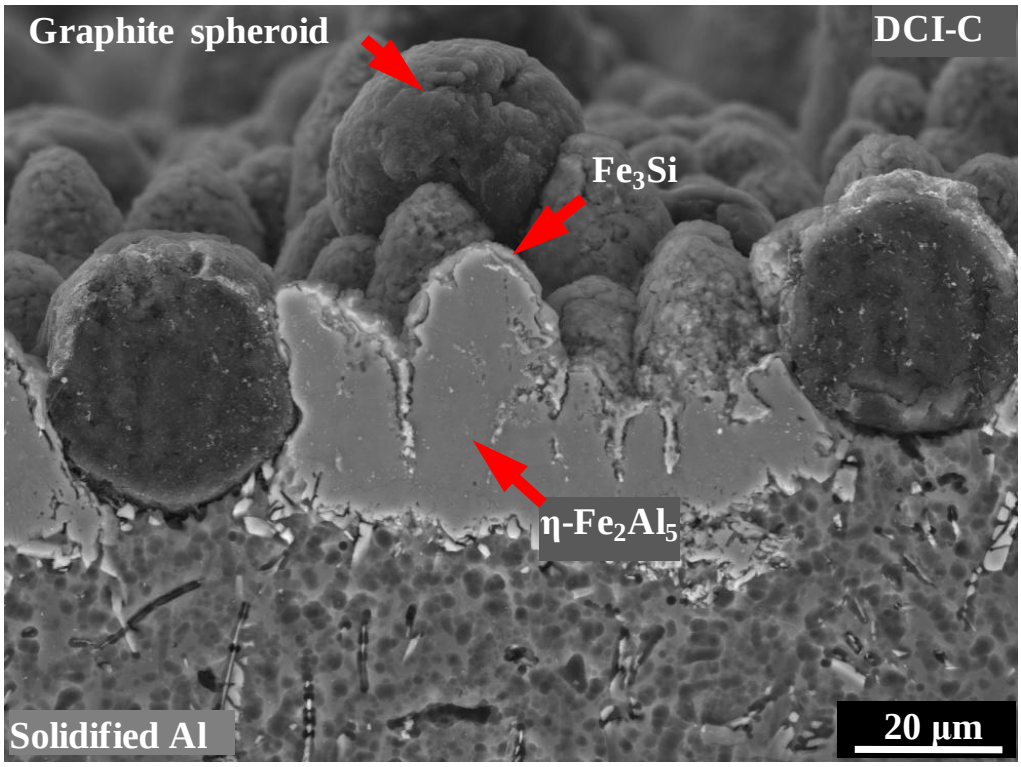

Figure 4.71 - Cross-section of a deep-etched DCI-C specimen (950°C-1200s-static).

Similar to η-Fe_2Al_5, the Fe_3Si phase also remained unetched by HNO_3. Fe_3Si in the form of discrete rounded platelets constitutes a crust like morphology and lies over the η-Fe_2Al_5 columns, Figure 4.71 and Figure 4.72. Figure 4.73 shows the EDS spectrum of Fe_3Si layer; however, the results in a deep-etched condition are only an indication of high Si concentration.

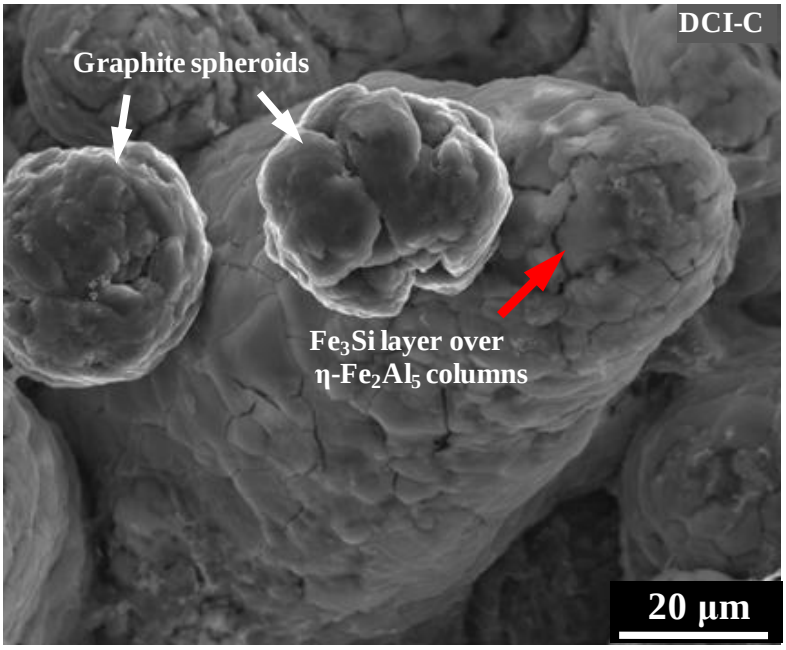

Figure 4.72 - A magnified view of a η-Fe_2Al_5 crystal with a Fe_3Si layer on a DCI-C specimen (950°C-1200s-static).

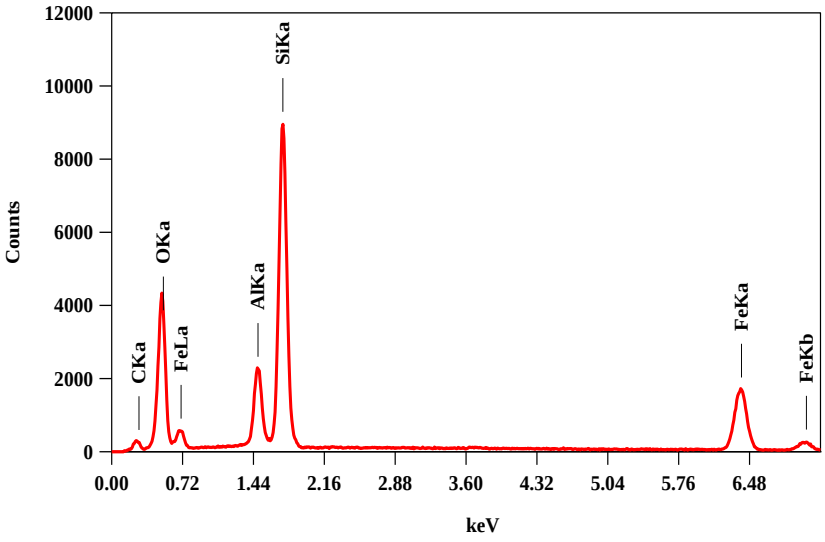

Figure 4.73 - An EDS spectrum of the Fe_3Si layer in deep etched condition on a DCI-C specimen (950°C-1200s-static).

Chapter References

[1] S.G. Denner, R.D. Jones, R.J. Thomas, Iron and Steel International, 48 (1975) 241-252.

[2] A. Bouayad, C. Gerometta, A. Belkebir, A. Ambari, Materials Science Engineering A, A363 (2003) 53-61.

[3] T. Heumann, S. Dittrich, Zeitschrift Fuer Metallkunde, 50 (1959) 617-625.

[4] R.W. Richards, R.D. Jones, P.D. Clements, H. Clarke, International Materials Reviews, 39 (1994) 191-212.

[5] P. Villars, L.D. Calvert, Pearson's Handbook of Crystallographic Data for Inter-

metallic Phases, 2nd ed., ASM International, Materials Park, Ohio, 1991.

[6] D. Balloy, J.C. Tissier, M.L. Giorgi, M. Briant, Metallurgical and Materials Transactions A, 41 (2010) 2366-2376.

[7] H. Baker, ASM Handbook-Alloy Phase Diagrams, ASM International, Materials Park, Ohio, 1992.

[8] T. Maitra, S.P. Gupta, Materials Characterization, 49 (2003) 293-311.

[9] H.R. Shahverdi, M.R. Ghomashchi, S. Shabestari, J. Hejazi, Journal of Materials Processing Technology, 124 (2002) 345-352.

[10] V.I. Dybkov, Reaction Diffusion and Solid State Chemical Kinetics, The IPMS Publications, Kyiv, 2002.

[11] V.N. Eremenko (Ed.), The Physical Chemistry of Inorganic Materials, Vol. 3, Kiev, 1988.

[12] V.N. Yeremenko, Y.V. Natanzon, V.I. Dybkov, Journal of Materials Science, 16 (1981) 1748-1756.

[13] C. Xa, W. Gao, Materials Research Innovations, 3 (2000), 231-235.

CHAPTER 5 : DISCUSSION

Introduction

To understand the liquid Al corrosion characteristics of cast irons and steels, firstly, the corrosion rates of these materials were discussed with regard to compositions and microstructures. It was recognized that there are two aspects to understand the mechanisms and behaviour of corrosion of ferrous alloys in Al melts. One is the advance of substrate/η-Fe_2Al_5 interface towards the Fe-substrate, and other the dissolution and/or spallation of the Fe-Al intermetallic layer into the melt. In order to understand these characteristics of cast irons and steels, intermetallic compound formation at substrate/η-Fe_2Al_5 interfaces was analysed in detail and compared with the corrosion rates of these materials. Subsequently, the intermetallic layer growth characteristics of steel and cast irons were analyzed and compared with the corrosion rates. Last section describes the effect of Si on dissolution, growth and nature of the intermetallic layers of cast irons.

5.1 Liquid Al Corrosion Resistance of Cast Irons and Steels

5.1.1 Cast Irons and Corrosion Resistance

The obtained cast iron microstructures chiefly depend upon the amount and type of each compositional constituent added, and many other variables such as cooling rate and inoculation [1]. Therefore, achieving the desired cast-microstructures of cast irons requires a tight control of these variables. Cast irons can be regarded as natural composites with graphite particles embedded in a matrix of Fe, and the Fe matrix can comprise various phases such as pearlite, ferrite, and cementite. Thus cast irons generally present an extremely complex metallurgical system. The liquid Al corrosion resistance of cast irons could depend upon the following factors:

a) Cast irons comprise various phases such as ferrite, pearlite and cementite. Each of these phases can have different corrosion resistance. The fraction and high temperature stability of these phases chiefly relies upon cast iron composition. Moreover, the different alloying elements present in these phases may have different interdiffusion potential with Al, which can also influence the corrosion rate.

b) Graphite particles could act as a physical barrier to the liquid Al attack. Cast irons comprise graphite of various shapes and their fraction and morphology are primarily controlled by the alloy composition.

The effect of these factors on liquid Al corrosion resistance of cast irons is discussed in the following sections.

5.1.2 GCIs

5.1.2.1 Effect of Microstructure and Composition

The amount of ferrite, pearlite, cementite and graphite in a cast iron can be controlled by selecting a chemical composition. However, while holding at 850°C or 950°C, pearlite and cementite can start to transform into austenite and also result in a greater graphite volume in cast irons [1]. Thus the fraction of pearlite and cementite present in experimental alloys before testing is indicative of C present in the cast iron matrix. The stability of cementite and pearlite at elevated temperatures chiefly relies upon the chemical composition of cast iron.

Being dependent upon several factors (Section 5.1.1), the liquid Al corrosion resistance of cast irons could present a complex relationship to the cast iron composition. This may be a reason that, previous research efforts presented in [2-3], were unable to establish a relationship between the liquid Al corrosion resistance of GCIs and chemical composition. Figure 5.1(a) shows an example of the ranking of GCIs according to the liquid Al corrosion resistance, data is taken from [3]. These materials were tested at 900ºC for 6 hours, details

are in Section 2.3. They [3] only compared the corrosion resistance of cast irons against the chemical composition; no attempts were made to reveal the effect of cast iron microstructure. It is to be noted that, those investigations were carried out using static Al melt. Compared to the average value of the corrosion rate, present results of 850ºC-static conditions showed a large difference in the corrosion rates of two specimens of each GCI (Figure 4.1). However, the introduction of forced flow melt conditions depicted a clear picture of the corrosion resistance of GCIs. Moreover, the details of the surface condition and number of specimens for each test were not noted in [3]. In the present work, the as-cast surfaces of cast irons were found to differ to a larger extent than the bulk, and made the comparison of corrosion resistance difficult, details are found in Appendix B. Thus in the current work, specimens with finished surfaces was used. If the specimens with as-cast surfaces were used for the results presented in [3], comparison of the corrosion resistance of GCIs could be more difficult.

In the results from literature, Figure 5.1(a), P containing cast irons were excluded because mechanical properties of cast irons deteriorate even with small additions of P. In the current work, the cast irons were alloyed with only those alloying elements which are well established to improve the high temperature properties of cast irons, details are found in Section 2.1. Looking at the results from literature [3], a correlation between the chemical composition and corrosion resistance of cast irons cannot be established, for example GCI-1 and GCI-2 have similar corrosion resistance but entirely different chemical composition. Similarly, the composition of GCI-6 is close to GCI-8 but GCI-8 dissolved at a higher rate. Other example is GCI-11 and GCI-12, being different chemical compositions showed a similar corrosion resistance. In the literature [3], the microstructures of cast irons were not investigated.

In the present work, the liquid Al corrosion resistance of cast irons was analysed with respect to the fractions of microstructural constituents and chemical composition. Figure 5.1(b) shows the results obtained from the current work, the test conditions were 950ºC-3000s-0.48 m/s. Figure 5.2 shows the average fractions of various phases in GCIs from current work. The alloying elements in cast irons basically control the amount of C in the form of graphite and Fe-C phases. Thus firstly, the liquid Al corrosion rates are discussed with respect to the phase fractions.

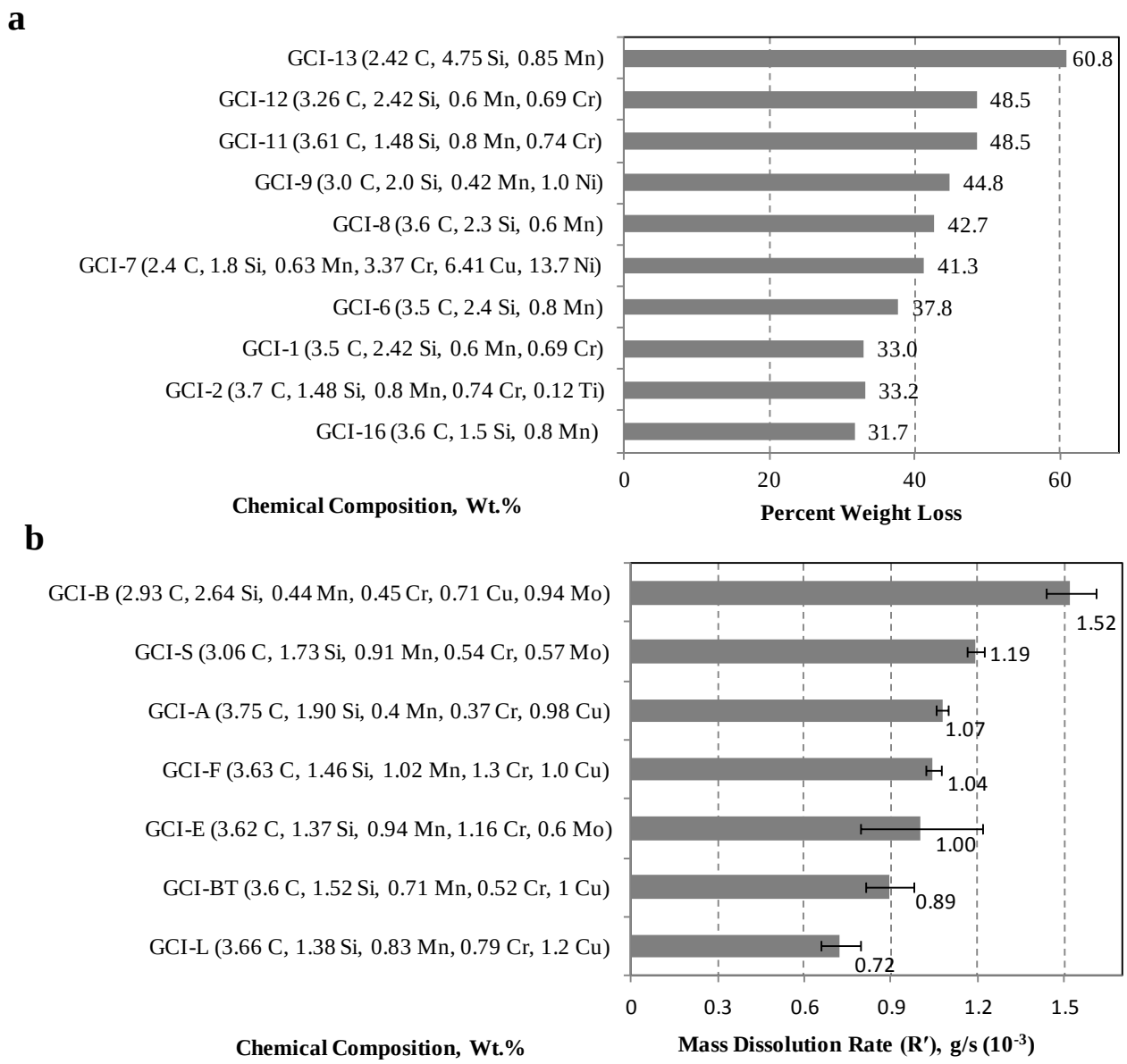

Figure 5.1 - Comparing the chemical composition and corrosion resistance of GCIs from literature and current work, a) 900°C-21600s-static [3], b) 950°C-3000s-0.48 m/s.

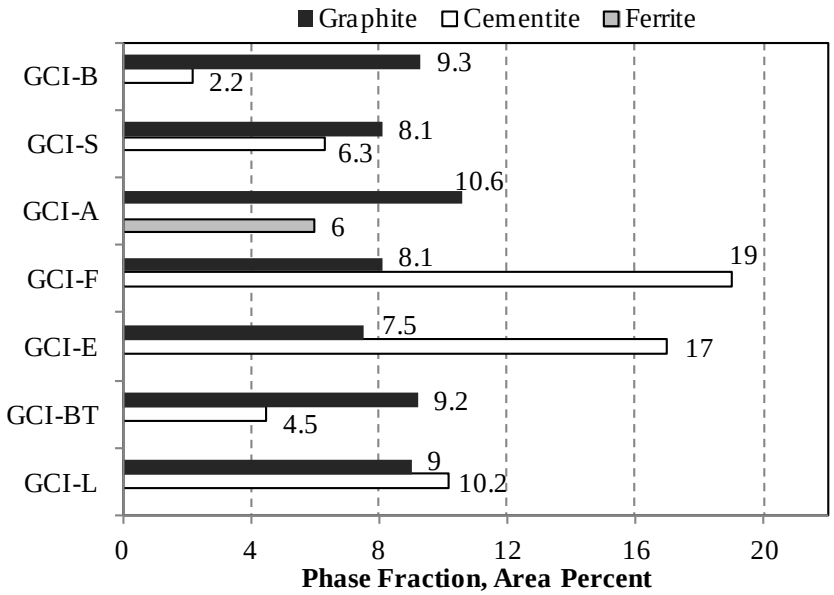

Figure 5.2 - Average fraction of graphite, cementite and ferrite in GCIs from current work.

Considering the top three alloys in Figure 5.1(b), the corrosion rate of GCI-A was found to be the lowest, followed by GCI-S and GCI-B, in that order. Theoretically, an increasing graphite flake volume should enhance the corrosion resistance of GCIs. Moreover, in literature [4-5], it was suggested that cementite is more resistant to liquid Al corrosion than ferrite and pearlite. Figure 5.3 shows the microstructures of GCI-A and GCI-S. GCI-A comprises the highest graphite fraction and GCI-S has a significantly higher cementite fraction than GCI-B. On the other hand, GCI-A microstructure contains ferrite, but no cementite. A better corrosion resistance of GCI-A was attributed to a higher graphite volume. A significantly lower corrosion rate of GCI-S than GCI-B was credited to a greater cementite fraction in GCI-S.

Both graphite and cementite improved the corrosion resistance of GCIs. Thus the next step was to know which phase; cementite or graphite is more effective in reducing the rate of liquid Al corrosion of GCIs. Thus in Series-II alloys mainly the fractions of cementite and graphite were varied. GCI-A has no cementite, GCI-F has the highest cementite fraction among GCIs, but a lower graphite fraction (1.4 times) than GCI-A. The introduction of a

higher cementite fraction at the expense of reduced graphite volume in GCI-E and GCI-F showed no significant improvement in the liquid Al corrosion resistance. Compared to GCI-F, GCI-BT (with a higher graphite volume but lower cementite content) dissolved more slowly. A further reduction in corrosion rate was achieved by imparting approximately the same graphite fraction as GCI-BT but with an increased amount of cementite in GCI-L (Figure 5.2). It is to be noted that fractions of cementite and graphite in GCI-L were in an approximate ratio of 1:1 by area.

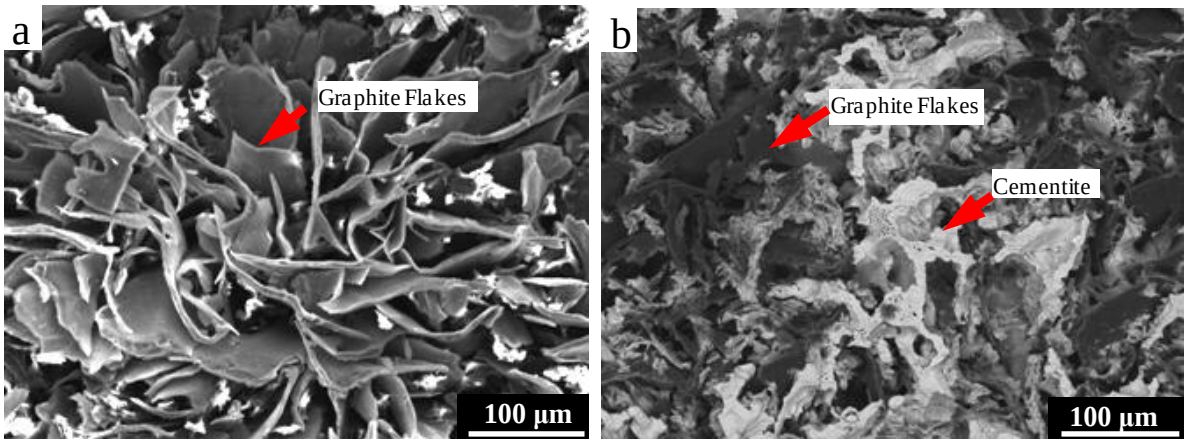

Figure 5.3 - BSE images of cast iron microstructures, a) GCI-A, b) GCI-S (deep-etched with 50% HNO_3 for 2 hours).

These results showed that a higher graphite volume is a primary requirement for corrosion resistant GCIs; however, the liquid Al corrosion resistance can be further enhanced by introducing cementite in microstructure. Thus increasing the fraction of both graphite and cementite can enhance the corrosion resistance. However, at a fixed C content, if the graphite volume increases, the C in the form of cementite and/or pearlite decreases. Thus to achieve a corrosion resistant cast iron it should have a sufficient C content to meet the requirements of the higher volumes of both of graphite and cementite. Alloying elements in cast irons help to distribute the C in the required form. Based upon the analysis of the

corrosion rates, microstructure and chemical composition data, the alloying elements added to cast irons were divided into two categories, which are described in the following sections.

5.1.2.1.1 Graphite Promoters

Si and C primarily control the amount of each phase in cast irons by changing the carbon equivalent (CE). Raising the CE helps the C to come out of solid solution as graphite flakes instead of cementite [1]. It is noted that the cast irons (both in literature and current work, Figure 5.1) with highest Si content dissolved at the highest rate. Unfortunately, both materials, in addition to being richest in Si, also have lowest C in each class of materials. Since the alloying elements are present in combination, the extent of the effect of increasing Si and decreasing C cannot be revealed. However, the current work supports that increased C in the form of graphite flakes is beneficial to enhance the corrosion resistance of GCIs. Contrastingly, increasing Si contents were found to weaken the cast iron substrate against liquid Al corrosion. The effect of a higher Si content is expected to become more dominant with a decrease in C because of a lower graphite fraction.

Niinomi *et al.* [6] found that the addition of Si (3 wt.%) to pure iron leads to a substantial increase in material loss in liquid Al melts. Due to the absence of C in pure iron, Si cannot affect the liquid Al corrosion resistance by increasing/decreasing the amount of cast iron phases (ferrite, pearlite, cementite and graphite). Therefore, in addition to increasing the amount of ferrite, there may be another inherent mechanism by which Si enhances the liquid Al corrosion rates of cast irons. Such effects of Si are discussed in Section 5.7.

5.1.2.1.2 Cementite and Pearlite Promoters

Alloying elements such as Cr and Mn affect the iron-graphite eutectic temperature and iron carbide eutectic temperature of cast irons, which controls the distribution of C in the form of cementite, pearlite, ferrite and graphite. The addition of Cr and Mn strongly promote

cementite and pearlite in cast irons. Cu is of dual character: it promotes pearlite as well as graphite [7].

Introduction of cementite to cast iron substrates was found to enhance the liquid Al corrosion resistance. GCI-BT performed better than GCI-E and GCI-F. Both GCI-E and GCI-F contained about 1.2 wt.% Cr and 1 wt.% Mn, which imparted a lower graphite flake fraction and a higher cementite fraction (approximately 3 times) than GCI-BT. The modified alloy GCI-L that exhibited the lowest material loss contained a higher cementite (approximately 2 times) fraction and a similar graphite fraction to GCI-BT. GCI-L alloy has higher contents of Cr and Mn than GCI-BT. GCI-L also has slightly higher Cu and C contents. The elements such as Cr and Mn bind the C in the form of cementite and pearlite and make the matrix strong against liquid Al corrosion. Cu provides high temperature stability to pearlite and it also substitutes for Si to some extent leading to more graphitization.

The addition of Cu + Mo and Cu + Cr combinations in GCI-E and GCI-F, respectively, led to almost similar dissolution rates. GCI-E and GCI-F have similar base composition thus substitution of Cu by Mo showed no significant effect. However, the phase fractions of cementite and graphite were found to be slightly lower in GCI-E than that of GCI-F.

The major impact of alloying elements on corrosion rates was found to result from the fraction of each phase (ferrite, pearlite, cementite and graphite) in the cast iron microstructure. In contrast to Si, increased C in GCIs is beneficial, whether it contributes to the formation of graphite flakes or increases the amount of cementite. The presence of different alloying elements in ferrite, pearlite and cementite may also directly influence the corrosion resistance of cast irons. However, due to the predominance of the effect of the

cementite and graphite fractions, the direct influence of alloying elements (except Si and C) on liquid Al corrosion resistance could not be revealed.

5.1.2.2 Optimum Composition

In order to enhance the corrosion resistance, as a rule of thumb, Si content in cast irons should be kept as low as possible and C at the highest. However, a reduction in Si content can lead to a lower graphite volume; on the other hand, a higher amount of C can promote ferrite and/or eliminate cementite. The detrimental effects of increased C content (or carbon equivalent) can be balanced by increasing the amounts of cementite promoters such as Mn and Cr. On the basis of current findings, a GCI with a high liquid Al corrosion resistance can be achieved with the composition stated in Table 5.1.

Table 5.1 - Recommended composition range for GCIs for a high liquid Al corrosion resistance.

C	Si	Mn	Cr	Cu
3.7-3.8	1.35-1.45	0.8-0.9	0.7-0.8	1-1.2

The recommended composition is similar to GCI-L with a relatively higher C content. A higher C content was recommended to introduce a higher graphite flake fraction than GCI-L. On the other hand, a higher C content decreases the tensile strength and impact resistance of GCIs [1]. However, it is generally agreed that a higher C content contributes to a better thermal fatigue resistance of GCIs [8], which is also a desired property for tapping pipes and other similar applications.

5.1.2.3 Effect of Temperature and Flow Conditions

Corrosion resistance of Series-I alloys was extensively studied to reveal the effect of changing temperature and flow conditions. Figure 4.1 shows the obtained corrosion rates at different exposure conditions of flow and temperature of liquid Al. In general, GCI-A showed the best corrosion resistance and GCI-S performed better than GCI-B.

To know the effect of changing temperature and flow conditions, the relative increases in corrosion rates of GCIs with a change in exposure conditions are shown in Figure 5.4. With a rise in temperature (850°C to 950°C) under static conditions, Figure 5.4(a), GCI-A showed a significantly lower increase in corrosion rate than GCI-S and GCI-B; however, under forced flow, Figure 5.4(b), the material loss of the former increased by a larger amount than the latter alloys. With a change in flow conditions from static to forced, at 850°C, GCI-A showed a significantly lower increase than GCI-S and GCI-B, Figure 5.4(c); however, at 950°C all materials showed similar levels of increase Figure 5.4(d).

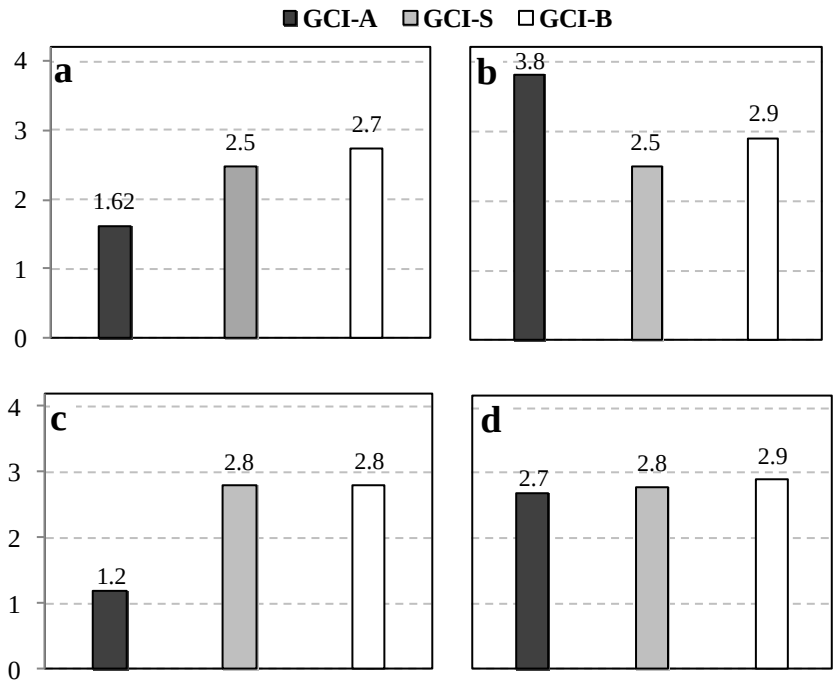

Figure 5.4 - Ratios of corrosion rates of Series-I GCIs under different changes of conditions of liquid Al exposure, a) Static, 950°C to 850°C, b) Forced, 950°C to 850°C, c) 850°C, forced to static, d) 950°C, forced to static.

With the rise in temperature (850°C-950°C) under static conditions, a higher graphite volume was believed to reduce the increase in corrosion rate of GCIs. Similar effect of graphite flakes is expected in the case of a change in melt conditions from static to dynamic at 850°C. However, comparing the rise in temperature under forced flow, a greater graphite fraction seems incapable of reducing the material loss to a similar extent at 950°C as it does

at 850°C. As mentioned before, ferrite is the weakest phase of GCIs to liquid Al corrosion, which is related to its low C content. The CE of GCI-A is significantly higher than GCI-S and GCI-B, thus at the exposure temperature, the depletion of C from the matrix of the former should occur at a greater rate than the later alloys [1]. This difference of C depletion should be greater at 950°C than at 850°C. With increase in temperature, this should result into the weakening of the matrix of GCI-A to a greater extent than GCI-S. With rise in temperature, under static melt conditions, a greater graphite volume can effectively resist the increasing corrosion rate, but under forced flow a weaker matrix possibly overrides the beneficial effect of graphite flakes.

Both GCI-S and GCI-B showed similar levels of increase with increasing severity of exposure conditions. This was attributed to the balancing effect of a greater cementite fraction in GCI-S and comparatively more graphite volume in GCI-B. Although, GCI-B has a higher CE than GCI-S, but the alloying elements (Cr, Cu) in GCI-B tends to bind the C in the form of pearlite and cementite.

5.1.3 DCIs

5.1.3.1 Effect of Composition and Microstructure

Among DCIs, DCI-T exhibited the lowest rate of material removal, followed by DCI-D and DCI-C, in that order (Figure 4.3). DCIs contain similar contents of C but different Si contents. The graphite fraction in all DCIs was found to be approximately the same, thus the microstructural variables were only the ferrite and pearlite fractions. Figure 5.5 shows the Si content and fractions of ferrite and pearlite in DCIs. Comparing DCI-T and DCI-C, a higher amount of Si in DCI-C resulted in greater ferrite content, which was suggested to dissolve at a higher rate than cementite or pearlite [4]. In other words, a higher C content of cast iron matrix at exposure temperatures means greater resistance to liquid Al corrosion.

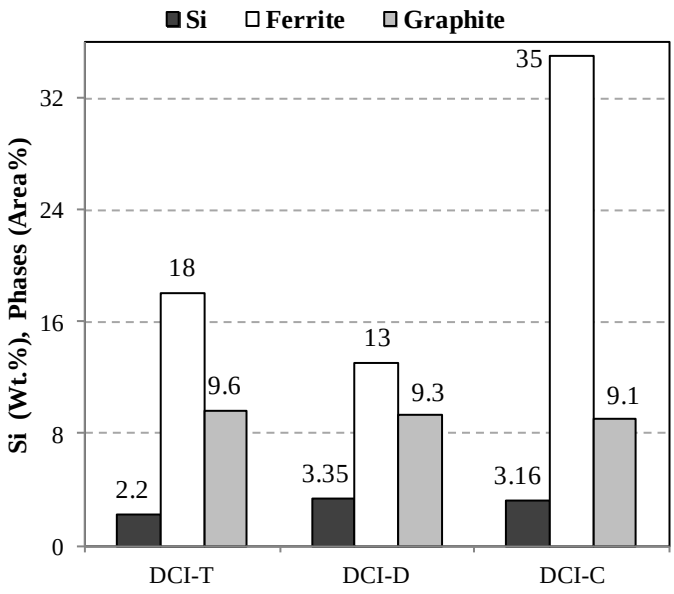

Figure 5.5 - Si content and average fractions of ferrite and graphite (balance pearlite) in DCIs.

DCI-D contains the highest amount of Si among DCIs, and it was alloyed with Cu and Cr. Addition of Cr and Cu can offset the tendency of Si to form ferrite. Thus a higher pearlite fraction in DCI-D than DCI-C can contribute to a higher liquid Al corrosion resistance. Thus the conclusion follows that the introduction of a pearlitic matrix by the addition of alloying elements is able to offset the effect of increased Si to some extent.

Compared to DCI-T, DCI-D with a higher Si content was found to dissolve at a higher rate in spite of containing a higher pearlite fraction. Higher Si contents in cast irons increase the graphitization (on the other hand, C depletion from matrix) at elevated temperatures [1]. Being richer in Si, the CE of DCI-D is higher than DCI-T. Thus holding at experimental temperatures, the C depletion from DCI-D matrix should be occurring at a higher rate than DCI-T. Moreover, as mentioned before (Section 5.1.2.1.1), considering the findings of Niinomi *et al.* [6], in addition to increasing the amount of ferrite, there may be another inherent mechanism by which Si reduces the corrosion of cast irons in liquid Al, details are in Section 5.7

Similar to GCIs, the corrosion resistance of DCIs can be enhanced by introducing more pearlite and/or cementite and reducing the addition of Si. DCIs are named after their high ductility, but the introduction of cementite and pearlite reduces their ductility and impact strength.

5.1.3.2 Effect of Temperature and Flow Conditions

Figure 5.6 shows the relative increases in corrosion rates with changing conditions of liquid Al exposure. With all type of changes in exposure conditions, DCI-T and DCI-D showed similar changes, but DCI-C behaved differently. Under static melt conditions, with a rise in temperature (850°C-950°C), DCI-C showed the smallest increase in corrosion rate with increase in temperature, Figure 5.6(a). Similar results were found with increase in temperature under forced flow conditions, Figure 5.6(b).

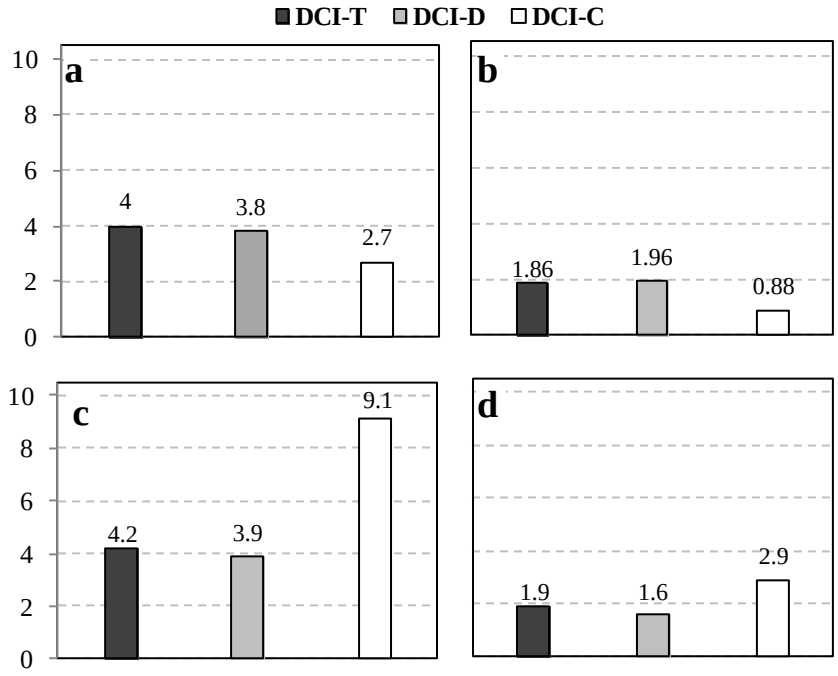

Figure 5.6 - Ratios of corrosion rates of DCIs under different changed conditions of liquid Al exposure, a) Static, 950°C to 850°C, b) Forced, 950°C to 850°C, c) 850°C, forced to static, d) 950°C, forced to static.

DCI-C has more ferrite and is unalloyed. Thus theoretically, compared to DCI-C, pearlite in DCI-D and DCI-T matrixes should slowly decompose at 850°C compared to at 950°C,

which may lead to a higher relative increase in corrosion rates of latter alloys compared to the former. In other words, compared to DCI-C, DCI-T and DCI-D should have more C in matrix at 850°C than at 950°C.

At 850°C, with a change in exposure conditions from static to forced, DCI-C showed a larger increase than DCI-T and DCI-D, Figure 5.6(c). Similar results were found at 950°C (static to forced flow, Figure 5.6(d)); however, all materials showed small increase as compared to 850°C-forced flow. This may be due to the higher vulnerability of ferrite or low C matrix to corrosion under forced flow. It is to be noted that DCI-C under forced flow showed a lower corrosion rate at 950°C than at 850°C, Figure 4.3. Possible microstructural mechanisms leading to such behaviours are discussed in Section 5.3.2.1. Since all DCIs have similar graphite fractions, the effect of fraction of graphite on liquid Al corrosion resistance could not be revealed.

5.1.4 Steels

Liquid Al corrosion resistance of steels was found to increase with increasing C content. These findings are consistent with Hwang *et al.* [4] where a carbon steel with 0.45 wt.% C performed approximately 2 times better than a 0.2 wt.% C steel. The dissolution in that case was determined using the rotating disc method. In the present work, under flow assisted corrosion conditions, the C content increase from 0.2 wt.% (CS) to 0.4 wt.% C (AISI 4140) showed a dramatic decrement (approximately 12 times) in the corrosion rate. However, a further increase to 1.1 wt.% C (AISI W1) exhibited a relatively small decrease in the corrosion rate.

CS microstructure is mainly ferritic thus has the highest corrosion rate. The as-received microstructures of AISI 4140 and AISI W1 steels were found to differ to a great extent. The AISI 4140 steel was found to possess a typical microstructure of tempered martensite, while

the AISI W1 consisted of fine cementite globules distributed in a ferrite matrix. During holding at the exposure temperature, martensite, cementite and ferrite should be transforming into austenite. C in AISI 4140 steel matrix is more uniformly dispersed in the form of martensite, while AISI W1 steel comprises ferrite and isolated cementite globules. The existence of ferrite in AISI W1 steel (1.1 wt.% C) can be a reason that being significantly richer in C, it showed a relatively small increase in corrosion resistance compared to AISI 4140 (0.45 wt.% C). Moreover, addition of Mn to pure Fe has been found to increase the liquid Al corrosion resistance [6]. Thus compared to AISI W1 steel, a higher Mn (by 0.45 wt.%) content in 4140 may have contributed to its liquid Al corrosion resistance.

5.1.5 Comparing DCIs, GCIs and Steel

Section 4.2 describes the obtained corrosion rates of cast irons and steels. GCIs dissolved at a slower rate than the DCIs. The low carbon steel (CS, 0.2 wt.% C), dissolved at a significantly higher rate than the cast irons. The difference between the corrosion rates of GCIs and DCIs could be explained by the fact that GCIs have a lower fraction of ferrite compared to DCIs. Current work clearly showed that cementite improves the corrosion resistance of cast irons, and ferrite or a low carbon matrix has the opposite effect. GCIs comprise an interconnected network of graphite flakes, which are inert with liquid Al and difficult to pull out of the matrix compared to isolated spheroidal graphite found in DCI. Figure 5.7 shows the examples of two types of graphite morphologies at the substrate/Al interfaces on the specimens obtained from dynamic corrosion tests.

The interconnected network of graphite lamellas in GCIs provides a physical barrier against liquid Al corrosion, and GCIs also have the added advantage of cementite and pearlite. In DCIs, the graphite spheroids initially can provide protection against liquid Al attack;

however, when the matrix adjacent to the spheroids gets corroded these are likely to fall out from the matrix leaving a cavity behind. Thus their protection seems to be not as effective as graphite flakes.

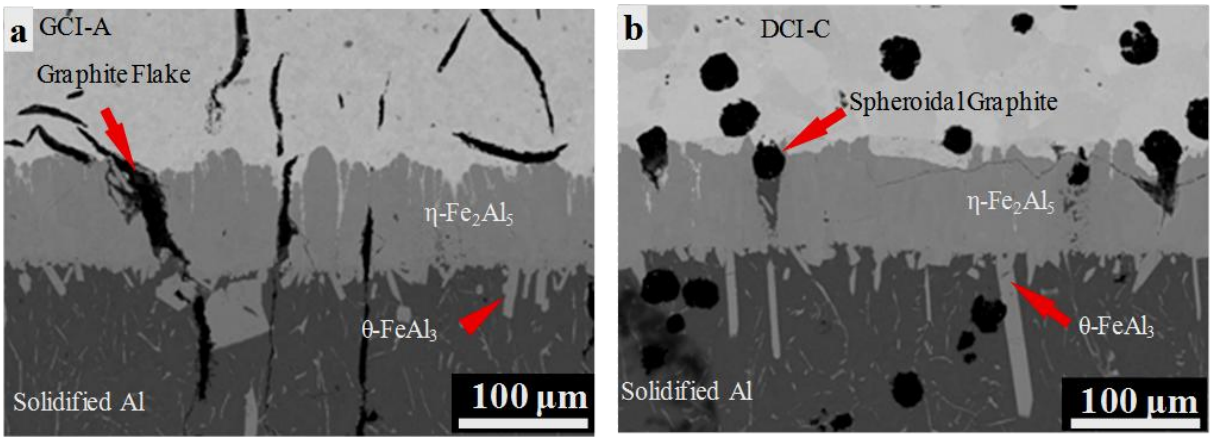

Figure 5.7 - Graphite particles at the substrate/Al interface, a) GCI-A (950°C-1200s-0.48 m/s), b) DCI-C (850°C-1200s-0.48m/s).

Although, cast irons possess graphite particles, the AISI 4140 and AISI W1 steels performed significantly better than some cast irons. Figure 5.8 shows the corrosion rates (R′) of AISI 4140 steel, GCI-B and DCI-T.

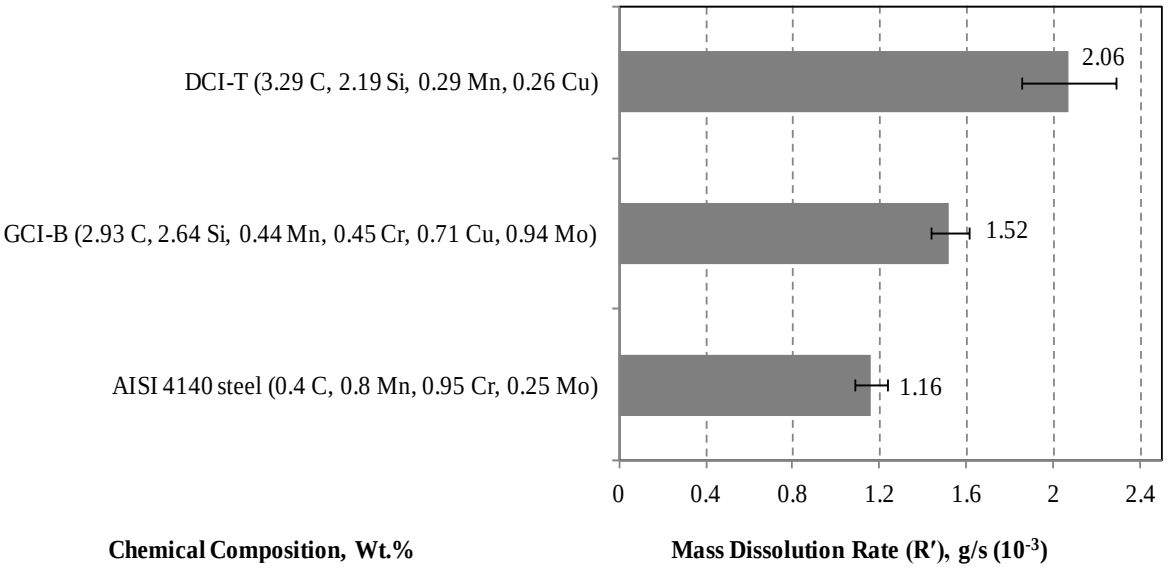

Figure 5.8 - Mass dissolution rates (R′) of selected cast irons and steel at 950°C-0.48 m/s.

AISI 4140 steel showed approximately 1.3 and 1.7 times slower rate of corrosion than GCI-B and DCI-T, respectively. In a previous work [2], a carbon steel (0.37 wt.% C) performed approximately 1.5 times better than a high Si (4.5 wt.%) GCI, these alloys were exposed to static liquid Al at 690°C for 72 hours. This difference was attributed [2] to the higher amount of ferrite in GCI than the carbon steel.

In addition to the as-cast microstructure of cast irons, Si can also affect the microstructural transformations at exposure temperatures. The as-cast microstructure of GCI-B was pearlitic with cementite particles, and as-cast DCT-T comprised pearlite and ferrite. The AISI 4140 steel has no Si and the GCI-B and DCI-T contains Si in significantly larger amounts. GCI-B contained higher Si than GCI-T; however, graphite flakes and pearlite with cementite have contributed to a higher corrosion resistance of GCI-B than GCI-T. As mentioned before, Si depletes C from cast iron matrixes at exposure temperatures [1], thus an increase of Si reduces the corrosion resistance of cast iron matrix. In the absence of Si and graphite, C remains in the matrix of the 4140 steel at exposure temperatures leading to a higher corrosion resistance than high Si cast irons. Other effects of Si on liquid Al corrosion are discussed in Section 5.7.

5.1.6 Effect of Boronizing

Liquid Al corrosion resistance of cast irons under dynamic corrosion conditions was increased (7-8 times) with boronizing treatment, details are found in Appendix D. An effective boronizing treatment generally requires a finished surface [9] but in industrial practice, the tapping pipes are used in as-cast condition. The as-cast surface of cast irons was found to differ to a large extent than the bulk, and found to be more resistant to the liquid Al corrosion (3-6 times) than a finished surface (Appendix B). Thus before recommending the

boronizing treatment for tapping pipes, issues such as economic viability and obtaining uniform boride layers need to be addressed.

5.2 Liquid Al Corrosion Characteristics of Ferrous Alloys

Before discussing the underlying mechanisms of liquid Al corrosion of GCIs, DCIs and steels, it is important to understand the common characteristics of compound formation and mechanisms of corrosion of ferrous alloys in Al melts. Based upon the current research findings, the common characteristics of liquid Al corrosion of cast irons and steels are discussed in this section.

5.2.1 Mechanisms of Liquid Al Corrosion

Immediately after immersion into liquid Al, Fe-Al intermetallic compounds form on the surface of ferrous alloys and, simultaneously, the ferrous substrate starts to dissolve into liquid Al. In all the investigated ferrous materials, η-Fe_2Al_5 and θ-$FeAl_3$ appeared as primary reaction compounds. The predominant appearance of η-Fe_2Al_5 to the exclusion of other phases has been attributed to its anomalously high vacancy concentration; resulting in a greater Fe/Al diffusion within η-Fe_2Al_5 thus it grows rapidly [10].

The corrosion mechanisms based upon the formation and growth kinetics of intermetallic compounds are difficult to establish because complete characterization of the formation and growth of θ-$FeAl_3$ has not been achieved in the past. It has been commonly found that θ-$FeAl_3$ exists in the form of a thin layer and as lath-shaped particles [11-12]. However, the formation of these two types of morphologies was difficult to establish and the origin of the lath-shape morphology of θ-$FeAl_3$ remains unclear, details are found in Section 2.2.2. Moreover, it is difficult to establish whether θ-$FeAl_3$ in the form of layer and/or particles grows during ongoing interaction with liquid Al or during solidification of Al around the

corroded specimen. The work presented in this section is an attempt to discover the underlying mechanisms of θ-$FeAl_3$ formation and growth.

The only way to determine the corrosion mechanisms is to observe the Fe-Al interaction zone after solidification, which may not present the actual situation while the Fe-liquid Al interaction proceeds. This limitation is a primary barrier to determine the exact corrosion mechanisms. Moreover, the mechanisms of flow induced corrosion may vary at different flow speeds, such as cavitation corrosion, mass-transport controlled or phase-transport controlled [13]. However, in a generalized case, the corrosion of ferrous substrates in Al melts can be considered to result from one or more mechanisms as discussed below. It is difficult to evaluate the contribution of each of the listed mechanisms towards the corrosion of a ferrous substrate in liquid Al melts. Figure 5.7 shows the examples of corrosion of ferrous alloys in liquid Al.

a) Both the η-Fe_2Al_5 and θ-$FeAl_3$ phases simultaneously form by the Fe-substrate/liquid Al interaction or the former grows first and then interacts with liquid Al to form θ-$FeAl_3$. Simultaneously, the θ-$FeAl_3$ phase may break away owing to the presence of convection currents in Al melt.
b) Both η-Fe_2Al_5 and θ-$FeAl_3$ or only η-Fe_2Al_5 may dissolve and/or spall into Al melt, which may be the principal mode of corrosion under forced flow melt conditions. However, η-Fe_2Al_5 may be simultaneously transforming into θ-$FeAl_3$ during dissolution.
c) Fe atoms diffuse directly into liquid Al owing to the existence of a concentration gradient between the intermetallic layer and Al melt.

In the current work, the typical growth direction of θ-$FeAl_3$ crystallites was found be perpendicular to the specimen surface (Figure 4.7 and Figure 4.9). Relatively smaller size particles in the solidified Al layer appeared as broken pieces of the large particles that were

grown at η-Fe_2Al_5 surface. If θ-$FeAl_3$ crystals form during solidification, these should precipitate by a eutectic reaction at 655°C (Figure 2.5). Growth and disintegration of large θ-$FeAl_3$ particles into smaller pieces seems less probable during the short period of solidification. At 950°C, θ-$FeAl_3$ has a larger negative (- 93862 J/mol) Gibbs free energy of formation compared to η-Fe_2Al_5 (- 87348 J/mol) [14] and the calculated surface free energies of these compounds are similar (differ by less than 1%) [15]. In Fe-Al interaction at 690°C, Ryabov [16] suggested that θ-$FeAl_3$ was initially formed being lowest in Fe content. Moreover, there is a basis for hypothesizing that these intermetallics can grow simultaneously. Both phases were found to exist at the Fe-Al interface even for a one second contact time between Fe and liquid Al [17]. According to another opinion [15], when the surface energies of two compounds (η-Fe_2Al_5, θ-$FeAl_3$) are close, the preferred growth of η-Fe_2Al_5 can be due to the kinetic hindrances to the formation of θ-$FeAl_3$ because the latter phase has significantly larger number of atoms per unit cell (η-Fe_2Al_5-24 atoms [18], θ-$FeAl_3$-100 atoms [19]). However, θ-$FeAl_3$ formation is thermodynamically favoured over η-Fe_2Al_5. Thus the nucleation and growth of θ-$FeAl_3$ is possible during ongoing liquid Al interaction with Fe-substrate.

Significantly smaller size particles (Figure 4.8) were also found uniformly dispersed within the solidified Al. These particles can form during solidification because the Al melt contains some amount of dissolved Fe. Also, with the passage of time, the large θ-$FeAl_3$ crystals may start to dissolve into the melt leading to the smaller sized particles.

In agreement with the literature, the orthorhombic crystals of η-Fe_2Al_5 were found to grow preferentially in the [001] direction, which is the shortest axis of the η-Fe_2Al_5 unit cell. In the current work, the preferred growth direction of θ-$FeAl_3$ was found to be the [010] direction of its monoclinic unit cell, which is also the shortest axis of the θ-$FeAl_3$ unit cell

(Figure 4.13). Similarly to the faster Al/Fe diffusion in η-Fe_2Al_5 along c-axis [10], the diffusion of Al/Fe can be faster along the b-axis of θ-$FeAl_3$ leading to a significantly higher growth along this direction. A high rate of Al/Fe interdiffusion can lead to the growth of lath shape θ-$FeAl_3$ particles in a direction normal to the η-Fe_2Al_5 surface. The thin θ-$FeAl_3$ stratum that appears continuous in optical or SEM images was identified using EBSD as polycrystalline. Therefore, the thin layer actually comprises growing θ-$FeAl_3$ particles or the remaining roots of fractured θ-$FeAl_3$ particles. The majority of dispersed θ-$FeAl_3$ crystals may be attached to the η-Fe_2Al_5 during interaction. It was therefore believed that θ-$FeAl_3$ can form during ongoing corrosion of ferrous alloys in Al melts.

Corrosion mechanisms of the ferrous materials based upon the formation and growth of η-Fe_2Al_5 and θ-$FeAl_3$ phases can be divided into two stages as described below, Figure 5.9 shows a schematic of the dissolution of Fe into liquid Al under static melt conditions.

5.2.1.1 Nucleation and Reaction

Immediately after immersion of a ferrous substrate into liquid Al, the nucleation of η-Fe_2Al_5/θ-$FeAl_3$ at the Fe surface starts. Thermodynamically, θ-$FeAl_3$ should form first and, moreover, it requires lower amount of Fe than η-Fe_2Al_5. On the other hand, a higher kinetic hindrance of θ-$FeAl_3$ as proposed by [15] can lead to a slower growth rate than η-Fe_2Al_5. However, evidence presented in [17] shows that both η-Fe_2Al_5 and θ-$FeAl_3$ phases were present at the Fe/Al interface even for one second contact time with liquid Al, which indicates that both phases can form simultaneously. Thus the nucleation and reaction to form η-Fe_2Al_5 and θ-$FeAl_3$ phases occurs in a very short time after exposure to liquid Al. In this short period of interaction, the reaction between Fe and Al atoms governs the compound formation, and the growth of the intermetallic layer occurs at a faster rate than the subsequent period of interaction [20]. The possible explanation of the columnar morphology

of η-Fe_2Al_5 can be the nucleation of individual crystallites at the Fe substrate and their subsequent growth. At the initial stage, considering a η-Fe_2Al_5 nuclei as an arrangement of a few unit cells, and their possible preferred alignment along the direction of higher diffusion (c-axis). This nuclei will tend grow in a along its initial direction of higher diffusion leading to the columnar morphology. Due to the fast reaction between Fe and Al, the number of η-Fe_2Al_5 nuclei should be high and due to their competitive growth they tend to grow in directions other than the specimen normal. Only those crystals which have their growth direction aligned along the normal to the specimen surface grow to a greater depth while the growth of other crystals can be hindered by the neighbouring crystals. Thus a common growth direction of η-Fe_2Al_5 was found normal to the substrate surface.

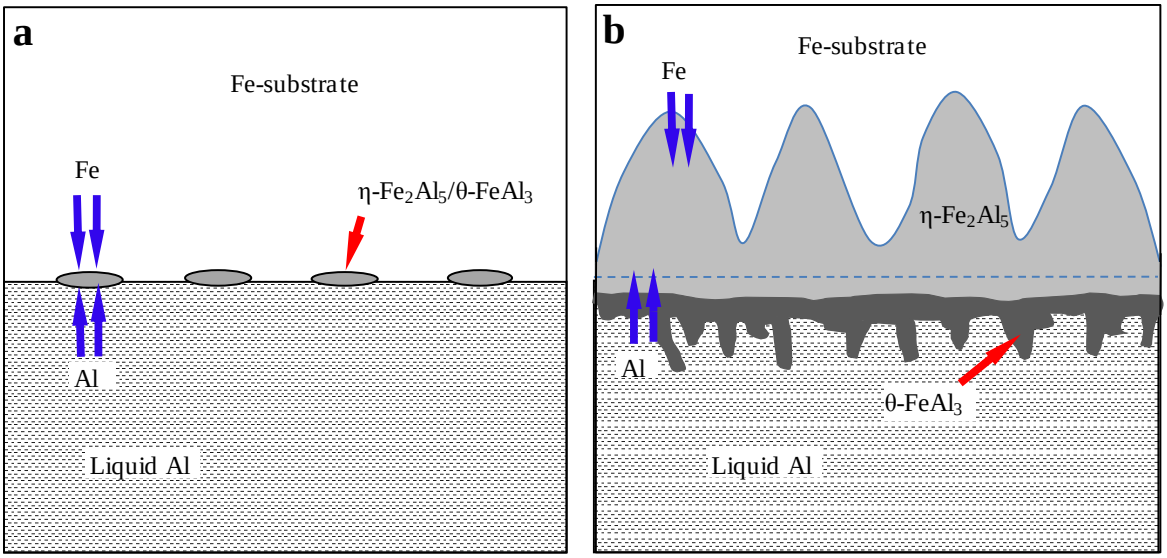

Figure 5.9 - Schematic of the dissolution of Fe into liquid Al, a) nucleation and reaction, b) growth and dissolution.

5.2.1.2 Growth and Dissolution

After the reaction controlled growth of Fe-Al intermetallics, the growth of η-Fe_2Al_5 and θ-$FeAl_3$ compounds proceeds by the diffusion of the Fe and Al atoms in the opposite directions through the bulk of these phases. The diffused atoms react at the respective interfaces and the growth of the intermetallic layer continues. This phenomenon is

commonly known as the reaction-diffusion mechanism [20] of compound formation. A model describing the growth of η-Fe_2Al_5 and θ-$FeAl_3$ in Fe/Al couples was found in [20]. In accordance with Heumann and Dittrich [10] about the predominant diffusion of Al in the lattice of η-Fe_2Al_5, it has been suggested [20] that the growth of η-Fe_2Al_5 mainly occurs due to Al diffusion. During interaction with liquid Al, η-Fe_2Al_5 may be transforming into θ-$FeAl_3$ in the abundance of Al and/or forming due to the interaction of diffused Fe and Al at the η-Fe_2Al_5/Al interface. In accordance with the current findings, the θ-$FeAl_3$ crystals of various lengths can form at the η-Fe_2Al_5/liquid Al interface.

Simultaneously, with the growth of the η-Fe_2Al_5 intermetallic layer, the θ-$FeAl_3$ crystals also tend to grow in size. With the ongoing dissolution and/or spallation, the η-Fe_2Al_5/θ-$FeAl_3$ interface becomes rough and uneven, and then the growth of individual θ-$FeAl_3$ crystallites can be hindered by competitive growth of neighbouring crystals. In agreement with [12], the hardness of η-Fe_2Al_5 was found in the 800-1000 H_v range. The hardness of θ-$FeAl_3$ cannot be measured accurately because they were found to fracture during hardness testing (Figure 5.10). This showed that the θ-$FeAl_3$ particles are very brittle thus easily able to disintegrate, and the convection currents present in static or flowing liquid Al can act as the driving force. Moreover, the particles with greater breadth were found to grow to larger sizes, which may be due to their greater mechanical strength. The growth of crystals increases the aspect (length/breadth) ratio, which results in more stresses at the roots of θ-$FeAl_3$ crystallites, finally causing their disintegration. With the ongoing interaction of Fe/Al atoms at the η-Fe_2Al_5/θ-$FeAl_3$ surface, the θ-$FeAl_3$ particles form and then disintegrate, and the growth-spallation cycle continues.

Similar to static conditions, η-Fe_2Al_5 and θ-$FeAl_3$ were found in the specimens from dynamic corrosion tests, Figure 5.7 shows the examples. However, under dynamic corrosion

conditions, both η-Fe_2Al_5 and θ-$FeAl_3$ are likely to spall off into the melt due to their brittleness. In accordance with the parabolic law of intermetallic layer growth (Section 2.2.3), the spallation of these layers would facilitate intermetallic compound formation at a higher rate due to the increased Fe/Al diffusion, and simultaneously faster corrosion in forced flow conditions.

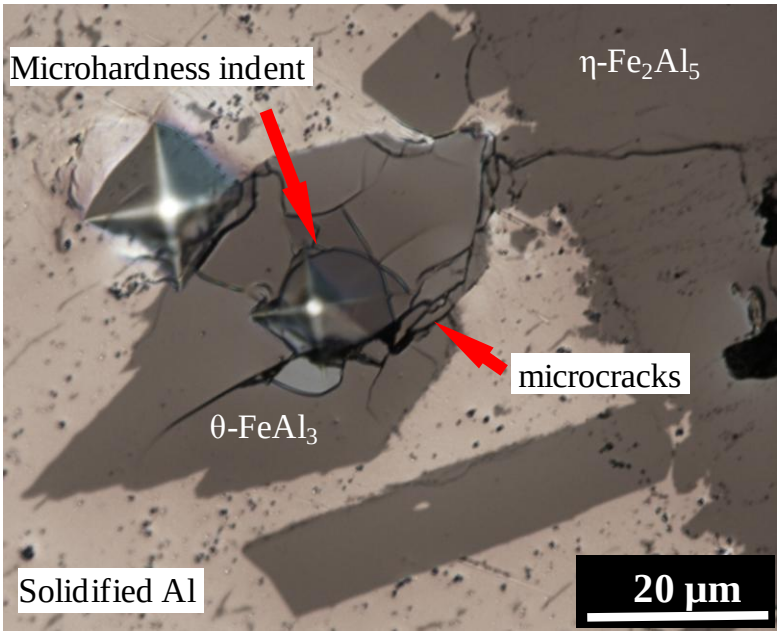

Figure 5.10 - A θ-$FeAl_3$ particle that was fractured during microhardness testing (CS, 950°C-60s-static).

5.2.2 Si Enrichment

Si enrichment (SEP) was found at the substrate/η-Fe_2Al_5 interfaces of cast irons and AISI W1 steel specimens (Figure 4.14, Figure 4.15 and Figure 4.34). Balloy *et al.* [2] also reported the formation of a SEP on GCI specimens exposed to liquid Al at 690°C for 72 hours. Maitra and Gupta [21] determined that the Si solubility in η-Fe_2Al_5 is 2.0-4.6 at.% in the 800°C-900°C range. In contrast, the Si solubility in α-Fe or γ-Fe is sufficiently higher than η-Fe_2Al_5. Therefore, during the formation of η-Fe_2Al_5, the excess Si can enrich the Fe substrate ahead of the growing η-Fe_2Al_5 crystals [2]. However, in the present work, the Si content in AISI W1 is significantly lower (0.4 wt.% or 0.8 at.%) than cast irons (> 1.6

wt.%), but a SEP was found. The Si content of 0.8 at.% is well below the solubility limits of η-Fe_2Al_5 reported by [21]. Thus a lower solubility of Si in η-Fe_2Al_5 is not a necessary condition for the occurrence of SEP. Based upon these findings, the SEP may result from the relatively slower rate of diffusion of Si than Fe. AISI 4140 steel has no Si and in CS the Si content is significantly low (0.2 wt.%) thus no SEP was detected in the specimens of these materials.

Balloy *et al.*[2] reported the formation of a SEP on a high Si (4.5 wt.%) ferritic GCI samples exposed to liquid Al. Moreover, it was suggested that the diffusion of Si towards the Fe-substrate can be prevented by the graphite flakes present in the GCI matrix. However, in the present work, it is concluded that the extent of Si enrichment primarily depends upon the Si content of the cast iron substrate (Figure 4.16). Furthermore, the Si concentration within the η-Fe_2Al_5 was found to be higher in the cast irons containing higher Si content.

5.2.3 Concentration Distribution of Alloying Elements

In all the experimental materials, the concentration of alloying elements (Cr, Mo, Mn) within the η-Fe_2Al_5 phase was found to be lower than in the Fe-substrates (Figure 4.17). Dybkov [22] postulated that the corrosion of 18-10 stainless steel by molten Al was "non-selective dissolution" based upon the hypothesis that the metallic bonds between Fe, Cr and Ni have approximately the same strength. Thus all the alloying elements should pass into the melt in those ratios in which they are present in the Fe-substrate. Dybkov also suggested that the alloying elements can easily substitute for the Fe of η-Fe_2Al_5 to form $(Cr,Ni)_2Al_5$ phases. If this is the case, then similar to Fe, the concentration of alloying elements present in η-Fe_2Al_5 should be lower than the Fe-substrate.

In contrast to Si, enrichment of other alloying elements (such as Cr, Mn, and Mo) at the Fe/ η-Fe_2Al_5 interface was not detected. Considering the suggestion of [22] these elements may

be diffusing at a similar rate to Fe and/or their solubility in η-Fe_2Al_5 is sufficiently high to prevent their enrichment at the Fe-substrate/Al interface. Moreover, small amounts (< 2.5 wt.%) of these elements in the experimental alloys may be a reason that their direct effect on the compound formation was not found. However, a change in composition affects the microstructure and phase stability in cast irons and steels, which can induce a change in corrosion rates and the mechanisms that facilitate liquid Al corrosion. This conclusion directed the interest towards the effect of C, Si on the mechanisms governing the liquid Al corrosion of cast irons and steels.

5.3 Alloy Specific Mechanisms of Compound Formation and Liquid Al Corrosion

Depending upon the substrate composition and conditions of liquid Al exposure, various secondary intermetallic compounds (other than η-Fe_2Al_5 and θ-$FeAl_3$) appeared at the Fe-substrate/η-Fe_2Al_5 interfaces of experimental materials. In this section, the formation mechanisms and the effects of these new phases or phase compositions are discussed with respect to the corrosion rates.

5.3.1 GCIs

In addition to the SEP, the current work explored the formation of Al_4C_3 and κ-Fe_3AlC phases in the intermetallic layers of GCIs. Since the existence of Al_4C_3 and κ-Fe_3AlC phases was confirmed for the first time, the formation of these phases is discussed first.

5.3.1.1 Cementite Transformation to Al_4C_3 and Fe-Al Phases

The corrosion rates of GCIs were found to diminish with increasing cementite fraction (Figure 5.1 and Figure 5.2). Cementite particles in GCI matrix were found to act as barriers to the advance of intermetallic layer towards substrate (Figure 4.20), thus it was concluded that cementite dissolves slowly and contributes to suppressing the liquid Al corrosion rate of

cast irons. A significant contribution of the present work is the exploration of the mechanism of cementite transformation to Al_4C_3 and Fe-Al phases.

There is sparse information on the formation of Al_4C_3 in Fe-Al couples. So-called "white spots" in the reaction (η-Fe_2Al_5) layer between 1040 steel and Al-7 wt.% Si alloy were found to have high (2.8 wt.%) C contents and were suggested to contain Al_4C_3 particles [23]. Likewise, the existence of Al_4C_3 was also detected in Al-cementite composites synthesized by mechanical alloying [24]. Recently, Balloy *et al.* [2] observed tiny particles (< 5μm long) in the intermetallic layer of carbon steel (0.38 wt.% C) after 72 hours immersion in liquid Al at 690°C. Owing to the small particle size, phase identification could not be made, and this phase was suggested to be graphite or Al_4C_3 [2]. To date there are no reports on the morphology, and complete identification of an Al_4C_3 phase formed between ferrous substrate(s) and liquid Al.

Under ordinary melt conditions, the formation of Al_4C_3 in graphite/liquid Al couples only occurs above 1000°C [25-27]. Poor wetability of graphite by liquid Al was suggested to prevent the Al/C interaction to form Al_4C_3. Above 1000°C, the contact angle between Al and graphite was found to decrease with increasing temperature, and attained values below 90º above 1100 °C [25, 27]. From the present work, it is interesting to note that in GCI-liquid Al interaction, the formation of Al_4C_3 is possible at 750°C, which is significantly lower than the temperature required to form this phase by graphite-liquid Al interaction.

At high temperatures, Al has a high potential for reaction with the elements such as C, Si, Fe and O. The Gibbs free energy of reaction (ΔG_f) between Al and these elements is given in Table 5.2. Thermodynamically, the Al_2O_3 is the most favourable phase to form among the listed phases and the formation of Al_4C_3 should be preferred to the Fe-Al phases. However, in a study [23] where carbon steel and liquid Al interaction was studied under atmospheric

air, only the existence of a few 1-2 μm long Al_2O_3 particles entrapped in the η-Fe_2Al_5 intermetallic layer was reported [23]. In contrast, no such particles were found in the current work. However, O in the melt is not abundantly available as at the melt surface exposed to atmospheric air because the formation of Al_2O_3 layer at the melt surface minimizes the further possible oxidation of the Al melt. Thus the possibility of Al_2O_3 formation in the Fe/Al interaction zone is negligible.

Table 5.2 - Gibbs free energy of formation of various phases at 950°C.

Phase	(ΔG_f), J/mol	Ref.
Al_2O_3	- 1346602	[28]
Al_4C_3	- 148788	[28]
θ-$FeAl_3$	- 93862	[14]
η-Fe_2Al_5	- 87348	[14]
β_2-FeAl	- 44107	[14]
κ-Fe_3AlC	-95179	[29]

Exposure of ferrous alloys to liquid Al leads to the formation of the intermetallic layer at the Fe/Al interface. In contrast, liquid Al does not react with graphite due to the poor wetability of graphite by liquid Al. Thus the presence of η-Fe_2Al_5 reaction layer over the cast iron substrate facilitates the cementite (C)/Al interaction to form Al_4C_3. This is a possible explanation of the formation of Al_4C_3 in Fe-liquid Al couples at the temperatures lower compared to the graphite-liquid Al couples.

Cementite in GCI matrix was found as a major source of Al_4C_3 formation. For relatively short (< 2400s) exposure periods at 750°C, 850°C and 950°C, the Al_4C_3 particles were observed in contact with the cementite surface and extending towards the η-Fe_2Al_5 phase (Figure 4.21). Considering the reaction-diffusion mechanism of compound formation, the diffused Al through the η-Fe_2Al_5 phase layer can react with cementite to form Al_4C_3 and η-Fe_2Al_5. After extended periods of liquid Al exposure at 950°C, the α-Fe(Al, Si) solid

solution and β_2-FeAl layers grew at the advancing η-Fe_2Al_5/cast iron interface and the Al_4C_3 particles were observed in the β_2-FeAl phase (Figure 4.25) instead of extending from the cementite surface. Figure 5.11 shows a schematic of various phases formed by GCI/liquid Al interaction for extended periods of immersion.

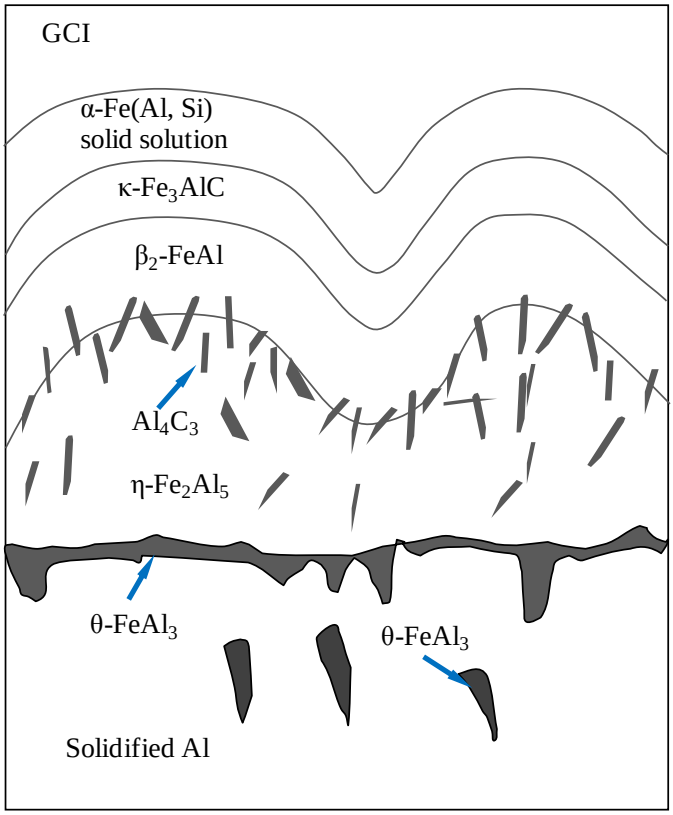

Figure 5.11 - A schematic representing various phases formed by GCI/liquid Al interaction.

Calculated sections of ternary Fe-Al-C phase diagram, Figure 5.12 and Figure 5.13, clearly define the concentration and temperature conditions of the occurrence of Al_4C_3. However, there are discrepancies in literature as described in [30], for the existence of phases and the location of phase boundaries. Moreover, Si additions to Fe-Al-C alloys increase the stability of Al_4C_3 during annealing, and previous work [30] concluded that the addition of silicon supports the formation of Al_4C_3. Thus, presence of Si in cast irons of current investigation can help to promote the formation of Al_4C_3. The solubility of Si in β_2-FeAl is higher than the other Fe-Al intermetallics [21] and the Si atoms replace Al atoms in this compound. It was

supposed [26] that the effects of Al and Si add together and in the presence of Si, the phase boundaries such as (α+C)/(α+C+Al_4C_3) should then shift towards the lower Al content [30]. Thus in the presence of Si, as in the present case, the phase boundaries in the sections of ternary Fe-Al-C phase diagram should be taken as an approximation only. However, the Al rich corner of isothermal Fe-Al-C diagram at 800°C (Figure 5.13) shows the existence of α-Fe and Al_4C_3, which is in agreement with the current findings.

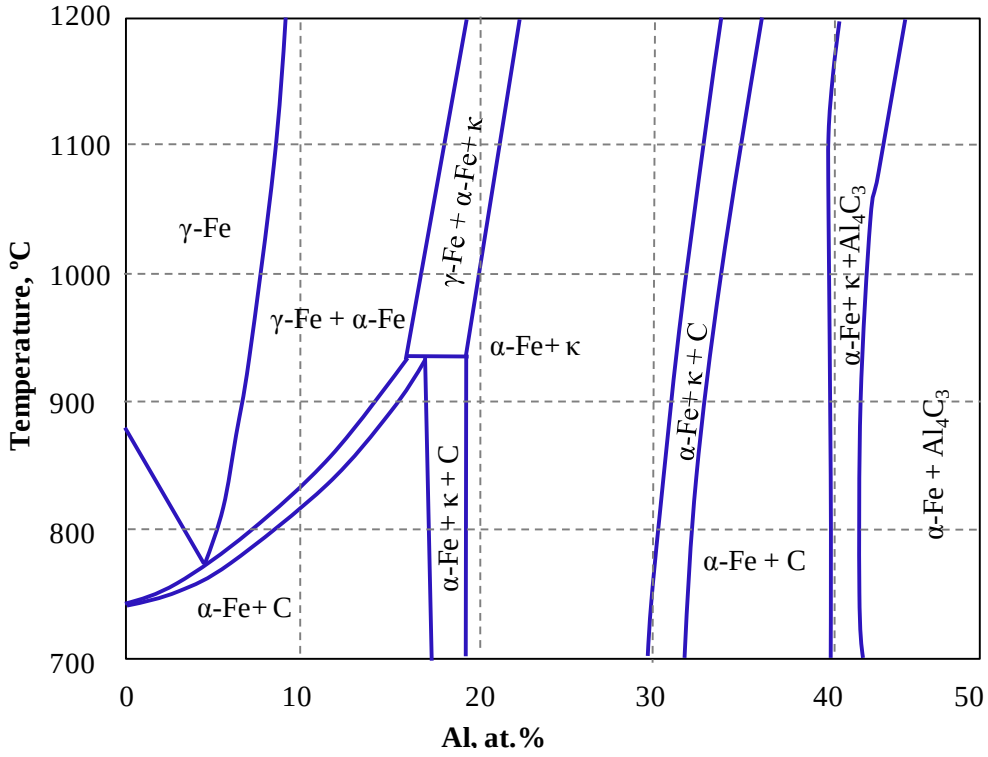

Figure 5.12 - A section of the ternary Fe-Al-C phase diagram at 5 at.% C. [After [31]]

From the available section of the Fe-Al-C ternary phase diagram (Figure 5.12) at 5 at.% C, the occurrence of Al_4C_3 requires at least about 40 at.% Al. After extended periods of immersion, the α-Fe(Al, Si) solid solution, κ-Fe_3AlC and β_2-FeAl layers grew at the cast iron/η-Fe_2Al_5 interface, chemical compositions of these phases are listed in Table 4.2. Among these phases only β_2-FeAl or η-Fe_2Al_5 contain the required amount of Al to form Al_4C_3, thus the Al_4C_3 particles were only observed within these phases.

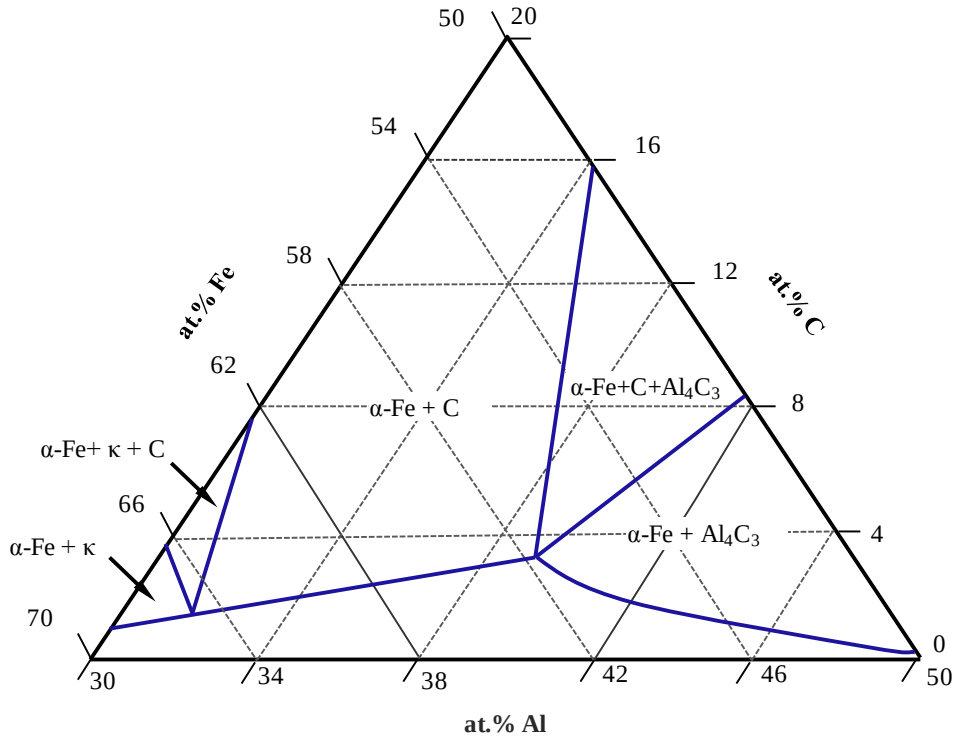

Figure 5.13 - An isothermal section of ternary Fe-Al-C phase diagram at 800°C. [After [30]]

With increasing exposure time of cast irons at 950°C, the carbon enrichment of γ-Fe should be increasing due to the decomposition of cementite and pearlite, but on the contrary, Si tends to deplete the carbon from matrix and leads to graphitization [1]. The alloying elements such as Mn, Cr and Cu increase the high temperature stability of cementite and pearlite [1]. Thus the decomposition of cementite and pearlite, and the carbon enrichment of γ-Fe depend upon the overall cast iron composition [1]. Due to the C enrichment of γ-Fe with time at 950°C, a sufficient amount of C can be available even in the areas free from cementite, thus the Al_4C_3 particles can even form at the substrate/η-Fe_2Al_5 interfaces free from cementite. It is to be noted that the isothermal Fe-Al-C phase diagram, Figure 5.13, shows the existence of Al_4C_3 at the C concentration as low as 1 at.%.

Considering the possible parabolic kinetics of the intermetallic layer growth, for long interaction times, the diffusion paths of Al atoms become complex. Therefore, for extended immersion times, in the lack of supply of Al, the formation of Fe rich phases such as β_2-

FeAl or β_1-Fe_3Al could dominate the strong growth kinetics of η-Fe_2Al_5. Moreover, due to the slow diffusion of Si compared to Fe, the presence of α-Fe(Al, Si) solid solution layer was found between cast iron substrate and η-Fe_2Al_5. Thus for extended exposure times and due to slow Al diffusion, the Al_4C_3 formation appeared to start by Al-C interaction in the β_2-FeAl phase. This also suggests that before being converted into Al_4C_3, the substrate C diffuses through the α-Fe(Al, Si) solid solution, κ-Fe_3AlC and β_2-FeAl phase layers.

5.3.1.2 κ-Fe_3AlC Formation

In high C steels, a thin C-enrichment zone ahead of the advancing η-Fe_2Al_5 serrations has been suggested, for example [32]. Whereas, owing to the lack of experimental verification Richards *et al.* [33] disregarded the formation of such a layer and suggested this as α-Fe solid solution. However, the present study confirmed the existence of a C-enrichment zone ahead of the growing η-Fe_2Al_5 columns, which is in agreement with [23]. Moreover, the existence of κ-Fe_3AlC has been found and confirmed for the first time in the cast iron-liquid Al interaction.

κ-Fe_3AlC was found in the intermetallic layers of GCI-S and GCI-A. The thickness of the κ-Fe_3AlC was increased with increasing time at exposure temperature (Figure 4.25). Thus at short exposure times the κ-Fe_3AlC zone may be too thin to detect. Figure 5.14 shows a unit cell of κ-Fe_3AlC [34]. The κ-Fe_3AlC unit cell structure can be viewed as $L1_2$-Fe_3Al structure with only the difference of C atom at the octahedral position. The presence of the C atom at the centre of the κ-Fe_3AlC leads to an energetically destabilized structure thus the κ phase often exists as $Fe_3AlC_{0.5}$ [34]. This could be the reason that only about 12 at.% C is detected in the κ-Fe_3AlC layers of GCIs. Nevertheless, EDS is not a very accurate method for determining the amount of light elements such as C.

The ternary Fe-Al-C phase diagrams, Figure 5.12 and Figure 5.13, show the existence of κ-Fe_3AlC over a wide range of composition and temperature. This indicates that κ-Fe_3AlC can exist at the temperature (950°C) used for the immersion tests. Also, the thermodynamic potential (ΔG) of the formation of κ-Fe_3AlC is also relatively high (Table 5.2). Existence of κ-Fe_3AlC and Al_4C_3 has been reported [35] in cast irons containing Al as the alloying element. Formation of κ-Fe_3AlC was reported between 10-16 wt.% Al and between 25-26 wt.% Al, the existence of Al_4C_3 was detected [35].

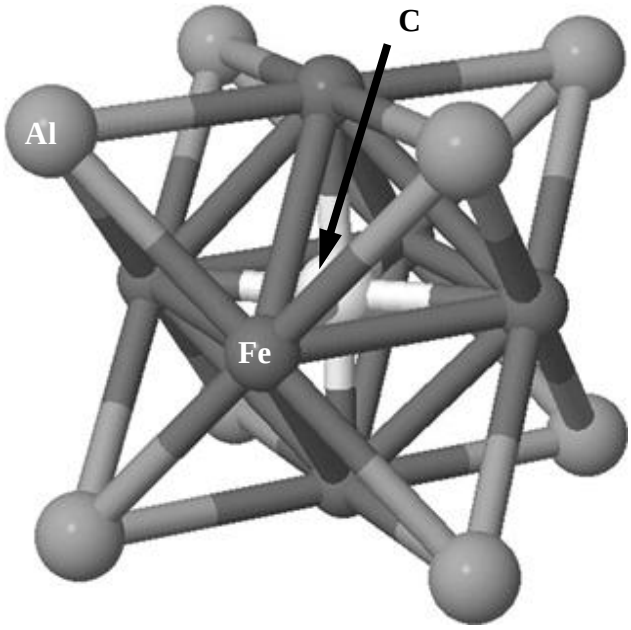

Figure 5.14 - Pervoskite (κ) structure of Fe_3AlC [34].

Owing to the low solubility of C in Fe-Al compounds, the diffusion of C through Fe-Al intermetallics is suggested to be slow [32, 36]. The slower diffusion of C than Fe in β_2-FeAl and η-Fe_2Al_5 is a possible cause of its enrichment in the form of κ-Fe_3AlC. Compared to C, the Si solubility in α-Fe or γ-Fe is much greater, and at high temperatures, Si tends to deplete C from cast iron matrix [37]. Thus in cast iron/liquid Al interaction, the growing η-Fe_2Al_5 enriches the adjacent cast iron substrate with Si, the substrate C is forced out of the solid solution, and C then tends to diffuses through the α-Fe(Al, Si) solid solution and β_2-FeAl layers. Diffusion of C through the α-Fe(Al, Si) solid solution layer believed to be faster

than the β_2-FeAl layer since the existence of κ-Fe_3AlC detected between the two phases. Moreover, the growth of κ-Fe_3AlC with time at exposure temperature indicated that for shorter immersion times this layer may be too thin to detect. The Al concentration of the α-Fe(Al, Si) solid solution was found to be significantly (approximately 3 times) lower than κ-Fe_3AlC (Table 4.2), which may be due to the inhibition of Al diffusion by κ-Fe_3AlC. During the formation of the intermetallic layer, while Si enriches the Fe-substrate, part of the C diffusing towards the η-Fe_2Al_5 transforms into Al_4C_3, while some amount of C combines with Al and Fe to form κ-Fe_3AlC.

Alternatively, there may be a possibility of κ-Fe_3AlC formation during cooling of cast iron specimens after the immersion test. In Fe-Al interaction, the Al concentration was found to increase from the substrate to the η-Fe_2Al_5 phase, and starting from η-Fe_2Al_5, the formation of Fe-rich phases such as, ζ-$FeAl_2$, β_2-FeAl and β_1-Fe_3Al is possible. If β_1-Fe_3Al forms in pure Fe and liquid Al interaction its location should be similar to κ-Fe_3AlC in cast irons. Among these phases the β_1-Fe_3Al is the richest in Fe, and according to Fe-Al phase diagram (Figure 2.5) this phase cannot form at higher (> 600°C) temperatures. Also, the ΔG of formation of β_1-Fe_3Al was found to be positive above 730°C [14]. During cooling, the excess C rejected from α-Fe(Al, Si) solid solution and β_2-FeAl phase layers may combine with Fe and Al to form the κ-Fe_3AlC phase instead of β_1-Fe_3Al.

5.3.1.3 Si-enrichment, Al_4C_3, κ-Fe_3AlC and Corrosion Resistance

During solidification of cast irons, higher Si content in cast irons promotes ferrite and leads to a larger volume fraction of graphite. Increasing Si content in cast irons also accelerates the decomposition of pearlite and cementite at annealing temperatures (> 600°C) and increases graphitization [1, 37]. From the present results, it is believed that SEP forms due to the slower diffusion of Si than Fe; however, a greater Si content in SEP has shown no

positive effect in suppressing the corrosion rate of cast irons (Figure 4.1, Figure 4.3 and Figure 4.16). EDS analysis in Figure 4.25(d) identified a lower C content in the α-Fe(Al, Si) solid solution layer than the adjacent GCI-A substrate. Therefore, under the conditions of increasing Si content ahead of the advancing η-Fe_2Al_5, C could be depleted from this zone. In a previous investigation [4] and in the present work a lower C content (higher ferrite fraction) in ferrous alloys was found to be least resistant to liquid Al corrosion. Thus the existence of a low C zone (due to Si-enrichment) ahead of the advancing η-Fe_2Al_5 was ascertained to facilitate the corrosion of cast irons in Al melts.

In GCIs, cementite was identified as a barrier to intermetallic compound growth, and therefore enhances the liquid Al corrosion resistance of cast irons. For relatively short interaction times (< 2400s) cementite particles were observed in contact with the η-Fe_2Al_5 phase (Figure 4.21). With the passage of time at exposure temperature, Si-rich (α-Fe(Al, Si) solid solution and β_2-FeAl) layers grew between cementite and the η-Fe_2Al_5 phase (Figure 5.15). Thus no cementite particles were seen in contact with η-Fe_2Al_5 in GCI-S specimen (950°C-7200s-static). As mentioned before, a high Si concentration ahead of the growing intermetallic layer can facilitate the transformation of cementite. After 7200s of exposure at 950°C, two Si-rich layers were evident, α-Fe(Al, Si) solid solution and β_2-FeAl. However, adjacent to the cementite particle only β_2-FeAl was seen, and the α-Fe(Al, Si) solid solution layer appears to be involved in the transformation of cementite into β_2-FeAl and Al_4C_3 (Figure 5.15).

The combined effect of temperature and long exposure time is expected to complete the cementite (Fe_3C) → austenite (γ-Fe) + graphite (C) transformation. However, the cementite particles within the GCI-S matrix were found intact even after 2 hours interaction at 950°C

(Figure 5.14). This suggests that the transformation $Fe_3C \rightarrow \gamma$-Fe + C, was very slow compared to the $Fe_3C \rightarrow Al_4C_3 + \beta_2$-FeAl/$\eta$-$Fe_2Al_5$ transformation in GCI-S specimens.

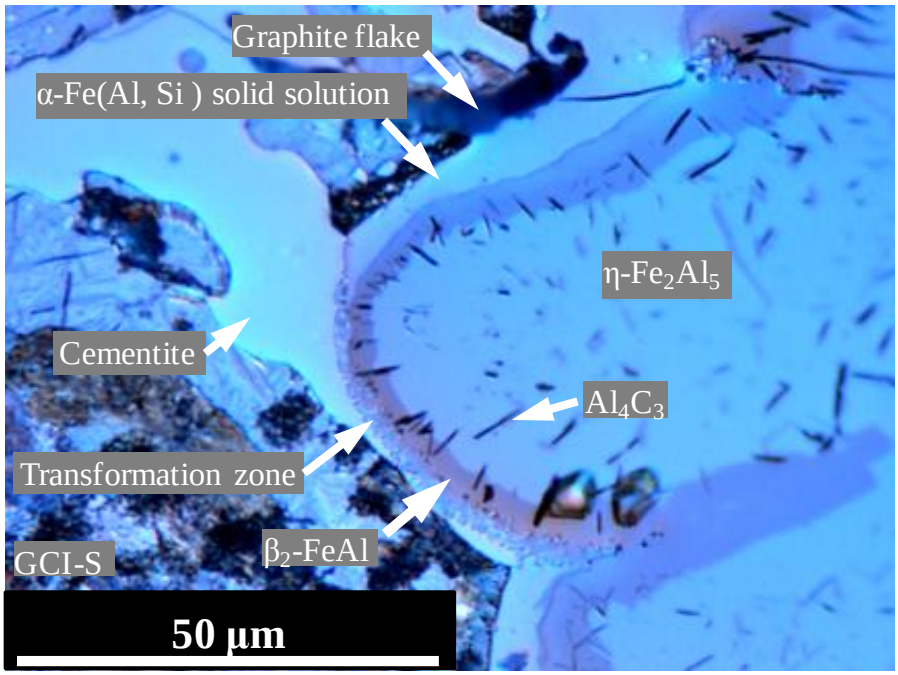

Figure 5.15 - Optical image showing cementite, α-Fe(Al, Si) solid solution and β_2-FeAl layers on a GCI-S specimen (950°C-7200s-static).

Figure 5.16 shows a plot of the Si content in GCIs versus thickness of the κ-Fe_3AlC layer, and Figure 5.2(b) shows the phase fractions in GCIs. For GCI-S, the κ-Fe_3AlC layer was found to be thicker than in GCI-A, and the formation of κ-Fe_3AlC was not detected in the high Si GCI-B alloy.

The extent of κ-Fe_3AlC formation appeared to be related to the amount of C in the cast iron matrix (‘matrix’ refers to the Fe-C phases except graphite). GCI-S matrix has relatively a lower Si, and higher Cr and Mn contents than GCI-A. This elemental combination led to a relatively higher amount of C in the matrix of GCI-S in the form of cementite and pearlite. During holding at 950°C, the transformation of ferrite, cementite and pearlite into γ-Fe starts. Consequently, at the exposure temperature, the C enrichment of GCI-S matrix should be higher than GCI-A and GCI-B. Accordingly, the thicker κ-Fe_3AlC zone was found in

GCI-S. GCI-B contains about 2.6 wt.% Si, at the exposure temperature, the C diffusion from γ-Fe to graphite particles should occur at a highest rate in GCI-B. Thus the availability of C in GCI-B matrix at 950°C is expected to be lower than the solubility limits of Fe-Al phases or the κ-Fe_3AlC layer of GCI-B was too thin to detect.

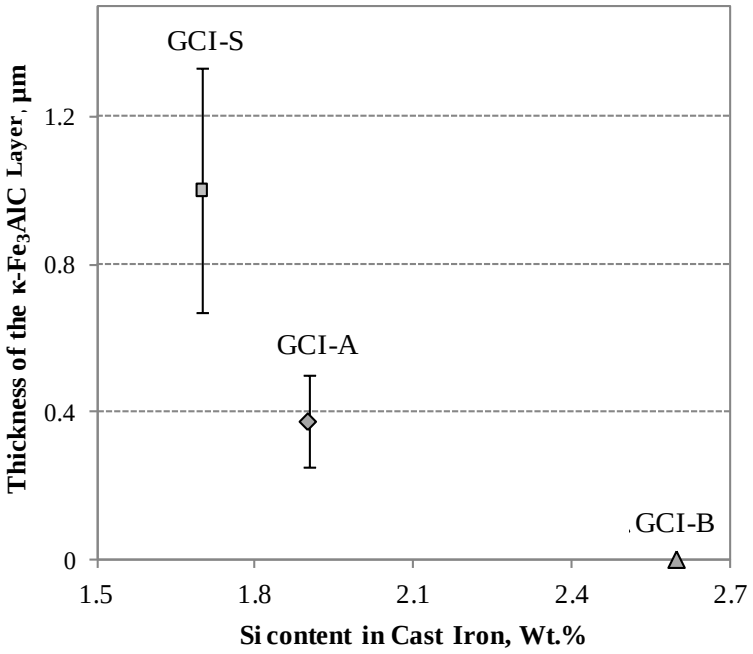

Figure 5.16 - Si content of cast irons versus thickness of κ-Fe_3AlC layer in GCIs.

A higher graphite flake volume in GCIs was found to enhance the liquid Al corrosion resistance, and the alloy GCI-S contained cementite and a lower graphite flake volume than GCI-A. At 950°C, the corrosion resistance of GCI-S was close to that of GCI-A, and both of these materials outperformed the GCI-B alloy, Figure 4.1. Thus the GCI-S matrix was believed to possess a greater liquid Al corrosion resistance than the GCI-A matrix. The formation of a thicker κ-Fe_3AlC layer therefore corresponded to a better liquid Al corrosion resistance of the cast iron matrix.

The phase fraction of Al_4C_3 in GCI-S was found to be approximately 1.5 times higher than GCI-A, and GCI-B showed only negligible amount of Al_4C_3 formation, Table 4.4.

Formation of Al_4C_3 and κ-Fe_3AlC phases consumes some diffusing Al; consequently, the formation of Fe-Al phases should slow down and thus the corrosion rate decrease. Moreover, inter-diffusion paths of Fe and Al may become more difficult with a greater amount of Al_4C_3 particles.

The formation of κ-Fe_3AlC and Al_4C_3 phases were found to depend upon the C content of cast iron matrix. Thus the corrosion resistance of cast iron matrix can be enhanced by the introduction of C in the form of cementite and pearlite. From these findings, it is confirmed that C and Si are the major compositional constituents that control the rate and mechanisms of liquid Al corrosion of cast irons. Addition of other alloying elements (being present in small amounts, ~ 1 wt.%) controls the amount of C in various phases in cast irons thus were believed to indirectly affect the corrosion resistance and mechanisms of liquid Al corrosion.

5.3.2 DCIs

5.3.2.1 Si-enrichment and Corrosion Resistance

Similar to GCIs, a higher Si content accelerates the rate of C depletion from the matrix of DCIs [1]. Thus during liquid Al corrosion of DCIs at exposure temperatures, Si enrichment was believed to facilitate the liquid Al corrosion by weakening the matrix by the depletion of C ahead of growing η-Fe_2Al_5. Si content of DCIs is sufficiently high, accordingly, they have low amount of C in their matrix. Thus during ongoing liquid Al corrosion, due to the Si enrichment of DCI substrate (SEP), the available carbon from the matrix tends to diffuse through the Fe-Al phases, but this C content is expected to be below the solubility limits of η-Fe_2Al_5. Therefore, no C enrichment zone was found at the interface between DCIs and η-Fe_2Al_5.

In the experimental DCIs, the graphite fraction was approximately the same, the only major variable was Si content. At the substrate/η-Fe_2Al_5 interface, DCI-T with comparatively low

Si (2.2 wt.%) showed the formation of $Fe_3(Al, Si)$, while the alloys (DCI-C and DCI-D) with higher Si contents (3.1-3.3 wt.%) showed the formation of Fe_3Si (Table 4.5). Figure 5.17 shows a schematic of phases formed at the corrosion interfaces of DCIs.

In addition to the C depletion form DCI matrix at exposure temperatures, the formation of Si-rich phases may also affect the mechanisms of corrosion. In the present work, in cast iron/liquid Al couples, the existence Fe_3Si was recognized for the first time thus its formation and possible effects on liquid Al corrosion are explained in detail. Balloy *et al.* [2] also reported the formation of an Al free SEP (13 wt. % Si approx.) in the specimens of a ferritic GCI (4.5 wt.% Si) the and suggested this as an α-Fe(Si) solid solution. They [2] noted that due to the formation of Al free α-Fe(Si) solid solution, Al diffusion to cast iron substrate may be lower than the diffusion of Fe to Al side. However, how Si enrichment at the GCI/ η-Fe_2Al_5 interface can affect the liquid Al corrosion was not explained in Balloy *et al.*'s work.

Comparing the corrosion rates and Si concentration of SEP, DCI-C and DCI-D with higher Si concentration of SEP corroded more rapidly compared to DCI-T. In SEP of DCI-C and DCI-D, only a negligible amount (about 0.35 at.%) of Al was detected. Since the three elements - Fe, Al and Si - were involved in the diffusion interaction while the formation of phases proceeds - the formation of binary Fe_3Si phase in the intermetallic layers of DCIs is unexpected.

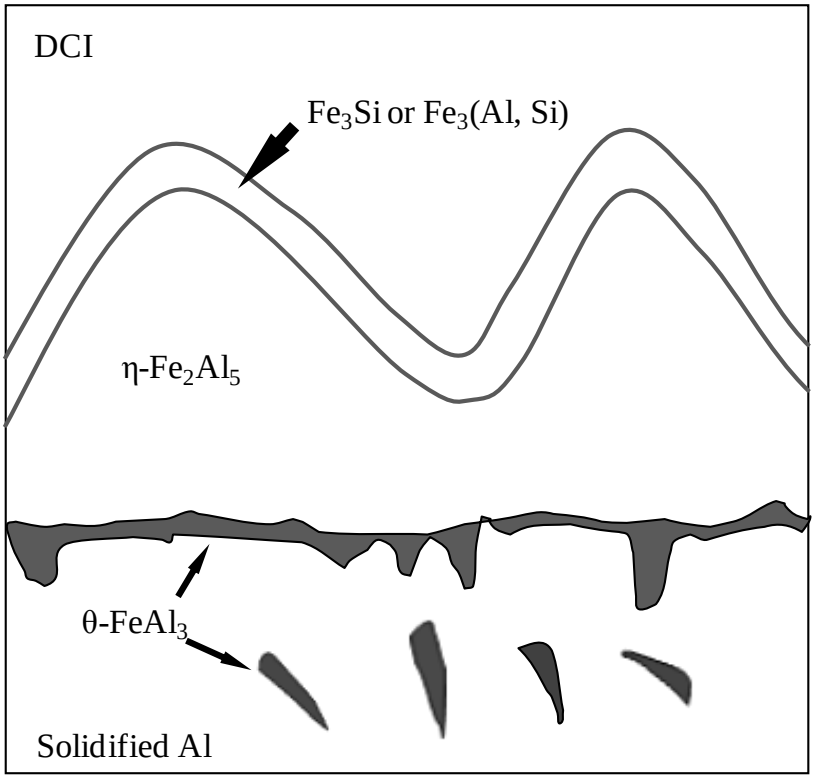

Figure 5.17 - A schematic of the corrosion phases formed in DCIs.

The binary Fe-Si phase diagram (Figure 5.18) shows that Fe_3Si can exist over fairly wide ranges of composition and temperature. Zhang and Ivey [38] determined the free energy of formation of Fe_3Si phase taking into account the chemical and magnetic interactions. The configurational free energy (ΔA) was found to decrease with increasing Si content in Fe_3Si from 12 to 25 at.%. Therefore, the stoichiometric Fe_3Si is expected to form preferentially. In DCIs, the Si content of the SEP was found to increase with increasing Si content in the cast iron matrix. However, the Si concentration of SEP was drastically increased with increasing Si content of cast irons from 2.6 wt.% to 3.2 wt.% (Figure 4.16). Therefore, in the case of high Si cast irons, it is likely that the thermodynamic potential (ΔA) favours the formation of near stoichiometric Fe_3Si.

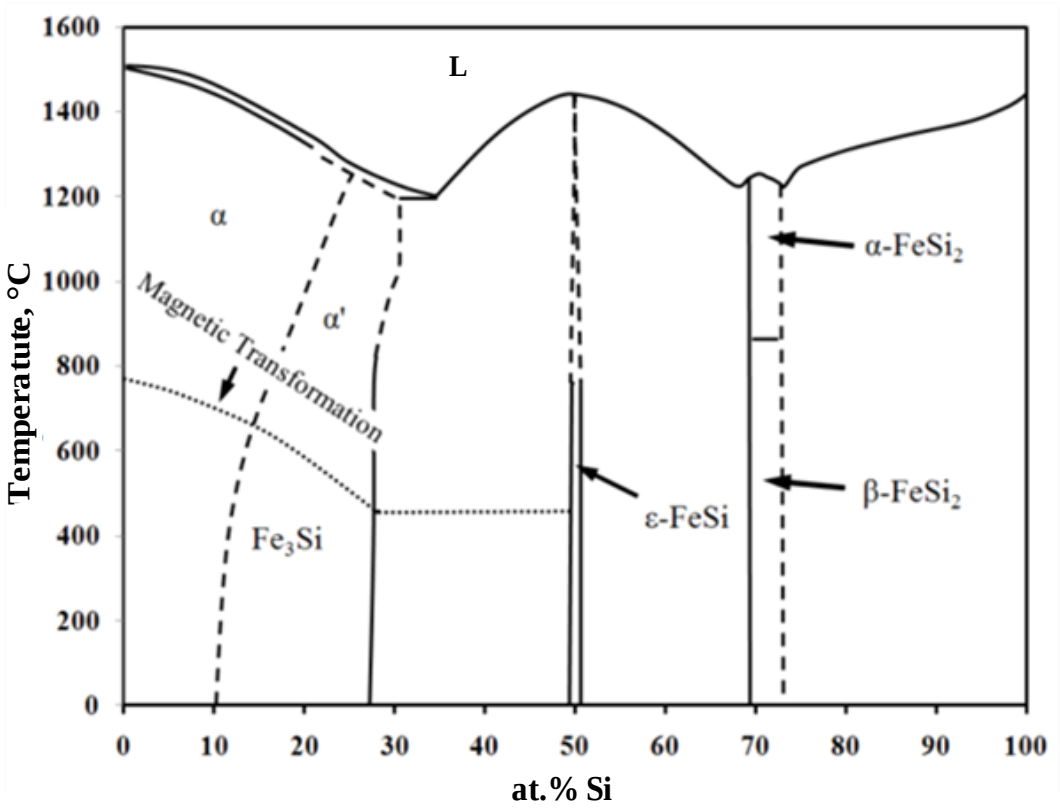

Figure 5.18 - A simplified Fe-Si binary phase diagram. [After [19]]

Furthermore, Cowdery and Kayser [39] measured the crystal structures and lattice parameters of Fe-Al-Si alloys of various compositions; $Fe_3Al_xSi_{1-x}$ ($0 \leq x \leq 1$). These alloys were found to have $D0_3$ structures with lattice parameters varying between 5.65A° (Fe_3Si) to 5.79A° (Fe_3Al). In the $D0_3$ structure of Fe_3Si (Figure 5.19) the Fe (A) atoms have specific sites, while Fe (B) and Si (C) atoms can substitute for each other depending upon the alloy composition [40]. In the $Fe_3Al_xSi_{1-x}$ ($0 \leq x \leq 1$) alloys, the C atomic sites can be occupied either by Al or Si maintaining the $D0_3$ symmetry [36]. Therefore, non-stoichiometric Fe_3Si or Fe_3(Al, Si) may exist in the Fe-Al-Si intermetallic layers of DCIs, with Al substituting for the Si atoms.

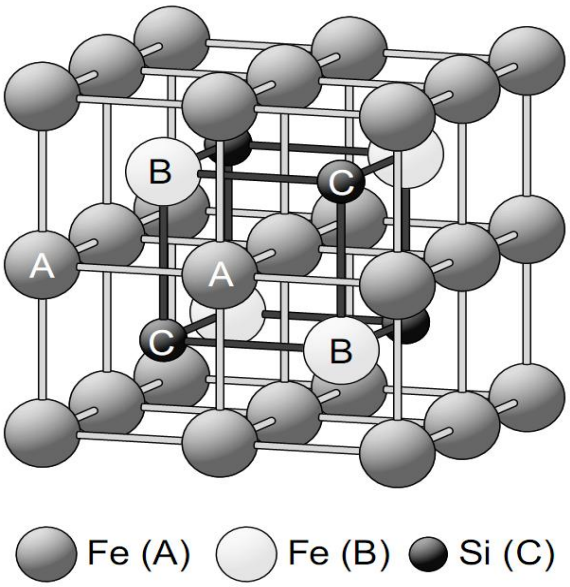

Figure 5.19 - $D0_3$ structure of Fe_3Si [40].

Previous Mössbauer studies [41] showed that the Fe diffusion in stoichiometric Fe_3Si is fast and becomes slower in alloys with increasing Fe contents. Diffusion coefficients of Fe in Fe-Si alloys were determined by Gude and Mehrer [42] (Table 5.3) and show an increase in diffusion coefficient as the Fe-Si alloys approach the stoichiometric ($Fe_{75}Si_{25}$) composition. In agreement with these findings, Zhang and Ivey [38] found that at 720°C, the diffusivity of Fe for $Fe_{80}Si_{20}$ was five to ten times slower than that of stoichiometric $Fe_{75}Si_{25}$. Therefore, the diffusion rates of Fe through the near stoichiometric Fe_3Si layers of DCI-C and DCI-D could be higher than through the non stoichiometric Fe_3(Al, Si) or α-Fe(Al, Si) solid solution layers of other experimental cast iron alloys. With the higher diffusion rates of Fe through the SEP, η-Fe_2Al_5 formation should occur at a higher rate, which can facilitate a high corrosion rate.

Table 5.3 - Diffusion coefficients of Fe in Fe-Si alloys [42].

Alloy composition	Temperature (K)	Diffusion coefficient (m^2s^{-1})
$Fe_{76}Si_{24}$	639	2.11×10^{-17}
$Fe_{79}Si_{21}$	688	7.83×10^{-18}
$Fe_{82}Si_{18}$	733	5.3×10^{-18}

From the analysis of corrosion rates under forced flow conditions (Figure 4.3), DCI-C showed an unexpected decrease in dissolution rate with an increase in temperature from 850°C to 950°C. However, under static melt conditions, the dissolution rate was found to increase with the rise in temperature from 850°C to 950°C. To understand this behaviour, the intermetallic layers of DCI-C were investigated. DCI-C specimen cross-sections (850°C-1200s-0.48 m/s) and (950°C-1200s-0.48 m/s) are shown in Figure 5.20. At 850°C, the η-Fe_2Al_5 layer was found to be smoother and thicker compared to 950°C. Another major difference was the formation of the Fe_3Si layer in the 850°C specimen, while in the 950°C case, only the colonies of the Fe_3(Al, Si) phase were found dispersed along the growing η-Fe_2Al_5 projections. Figure 5.20(c) and (d) show the magnified images of areas 'c' and 'd' in Figure 5.20 (a) and (b), respectively.

The rate of Fe diffusion was found [38, 42] to increase as Fe-Si alloys approach the stoichiometric Fe_3Si, which increases the η-Fe_2Al_5 growth leading to a higher corrosion rate. Thus the formation of near stoichiometric Fe_3Si at 850°C could be facilitating a high corrosion rate of DCI-C compared to at 950°C (where the existence of Fe_3(Al, Si) phase was evident). The formation of Fe_3Si and a higher diffusion rate of Fe through this compound further support the conclusion of current work (Section 5.2.2) that SEP occurs due to relatively slower diffusion rate of Si than Fe.

Figure 5.21 shows the Fe_3Si intermetallic layers under 850°C-static and 950°C-static conditions of liquid Al. Under forced flow conditions at 850°C, the Fe_3Si exhibited an appearance dissimilar to that observed in static immersion tests at 850°C and 950°C. Under forced flow conditions at 850°C, Fe_3Si showed an equi-axed appearance, Figure 5.20(c), while under static conditions no such morphology was evident (Figure 5.21). Figure 5.19(c) shows significantly smaller sized equi-axed Fe_3Si grains towards the substrate side. This

indicates that these grains may nucleate towards the substrate side and then the grain growth occurs due to further Si enrichment and holding at a high temperature. However, the reasons behind such distinct morphologies of Si-rich layers at different conditions of temperature and flow remain unexplained.

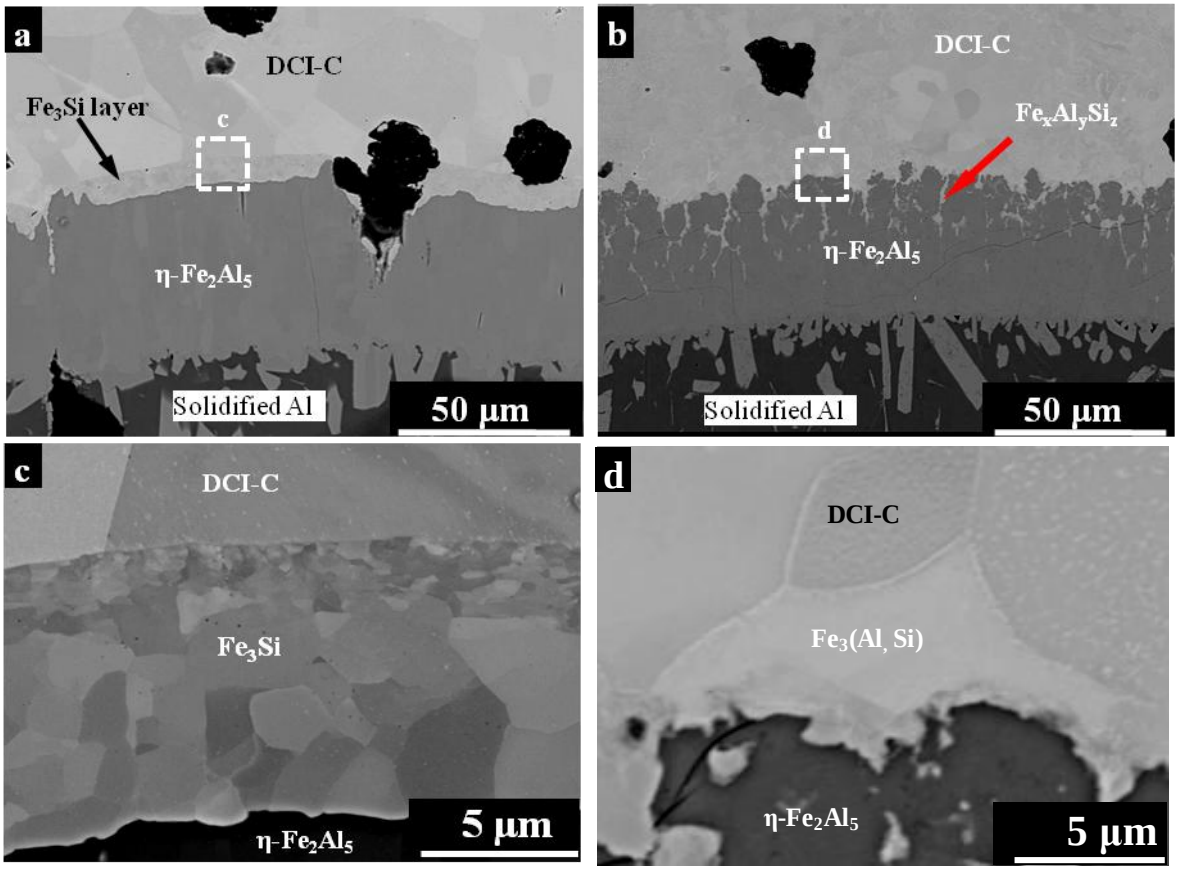

Figure 5.20 - BSE images of intermetallic layers on DCI-C specimens, a) 850°C-1200s-0.48 m/s, b) 950°C-1200s-0.48 m/s, c) magnified area 'c' (d) magnified area'd'.

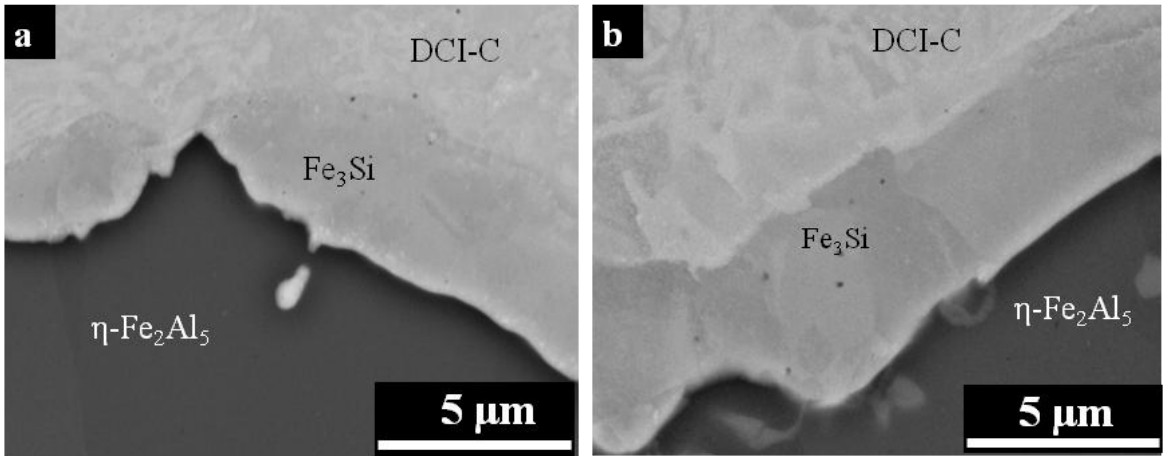

Figure 5.21 - BSE images of SEP on the DCI-C specimens, a) 850°C-1200s-static, b) 950°C-1200-static.

5.3.2.2 Al_4C_3

Existence of Al_4C_3 was rarely observed in DCI specimens (Figure 4.31). The major reason is the absence of cementite particles in DCIs, which were found to be the major source of C for Al_4C_3 formation in the case of GCIs. Moreover, the DCIs contain significantly lower pearlite fraction than GCIs. During holding DCIs at 850°C, pearlite can partially or fully transform into γ-Fe, and this transformation rate chiefly relies upon cast iron composition. The liquid Al remained in contact with DCI-T substrate during the entire time of pearlite to γ-Fe transformation and the isothermal Fe-Al-C phase diagram, Figure 5.13, indicates that Al_4C_3 formation is possible at a C concentration as low as 1 at.%. Thus the origin of these particles may be the interaction of Al with C from γ-Fe or the cementite lamellae of remaining pearlite.

5.3.3 Steels

In addition to η-Fe_2Al_5 and θ-$FeAl_3$, β_1-Fe_3Al was found in CS specimen (950°C-2400s-static), Figure 4.32. The existence of β_1-Fe_3Al has also been reported by Kobayashi and Yakou [43] in solid Fe-Al diffusion couples subjected to long-term annealing at 1000°C. In the present work, no distinguishable β_1-Fe_3Al layer was detected at 850°C and for shorter (< 2400s) interaction times at 950°C. The parabolic law of diffusion suggests that the growth rate of the η-Fe_2Al_5 intermetallic layer diminishes with time. With the passage of time, the diffusion paths of Al atoms become complex and the availability of Al atoms reduces at the Fe/η-Fe_2Al_5 interface. In the shortage of Al atoms, the possibility of formation of Fe-rich phases, such as β_1-Fe_3Al, β_2-FeAl increases. However, the binary Fe-Al phase diagram shows that (Figure 2.5) β_1-Fe_3Al cannot exist above 600ºC, and thus this phase should form by cooling below this temperature. Moreover, ΔG of β_1-Fe_3Al was found to be positive above 730ºC [14].

Since only the η-Fe_2Al_5 and θ-$FeAl_3$ phases should form at experimental temperatures at the CS/liquid Al interface, the mechanism of corrosion of CS believed to be simple compared to AISI 4140 and AISI W1 steels.

The AISI 4140 and AISI-W1 steels showed C-enrichment ahead of the growing η-Fe_2Al_5. This could be attributed to low solubility of C in η-Fe_2Al_5 or a slower diffusion rate of C than Fe is responsible for this phenomenon. The formation of β_2-FeAl, κ-Fe_3AlC and α-Fe(Al, Si) solid solution was detected in AISI-W1 specimens (Table 4.6). The sequence of these layers was found to be similar to GCIs. The mechanisms of formation of κ-Fe_3AlC and Al_4C_3 phases are explained in Section 5.3.1. Since the Si content of AISI W1 is low (0.4 wt.% Si), the Si enrichment of SEP of AISI W1 steel (2.4 wt.% Si) was found to be lower than GCIs (3.6 wt.% Si). These results indicate that the low solubility of Si in η-Fe_2Al_5 is not a necessary condition for the Si enrichment as it occurred at the AISI W1 steel substrate with as low as 0.4 wt.% Si. The Si enrichment should be occurring due to the slower diffusion of Si compared to Fe.

AISI 4140 steel is Si free and AISI-W1 steel has a significantly higher C content than the former, thus no distinguishable β_2-FeAl, κ-Fe_3AlC and α-Fe(Al, Si) solid solution layers were detected (Figure 4.33 and Figure 4.34) in AISI 4140 steel. Moreover, the amount of Al_4C_3 formation in AISI 4140 steel was found to be lower compared to AISI-W1 steel. No Al_4C_3 or C enrichment was found in the case of CS (0.2 wt.% C).

These findings reconfirmed a conclusion of the current work (Section 5.3.1.3) that the formation of a thicker κ-Fe_3AlC layer and a higher fraction of Al_4C_3 occurs in the case of substrates having higher C content. The corrosion rates of steels under current investigation are given in Figure 4.5. Similar to GCIs, a thicker κ-Fe_3AlC and a higher Al_4C_3 fraction corresponded to a better corrosion resistance of the steel substrate. Formation of κ-Fe_3AlC

and Al_4C_3 was believed to reduce the corrosion by consuming some of the diffusing Fe and Al and hindering the Fe/Al interdiffusion. In the case of AISI-W1 steel, Si enrichment can accelerate the depletion of C from steel matrix ahead of advancing η-Fe_2Al_5. Due to the formation of a low C zone at the steel substrate, the η-Fe_2Al_5 may be forming at a higher rate and thus facilitating the liquid Al corrosion of the steel substrate. Thus the Si enrichment at the AISI W1 substrate may be a reason for a relatively small increase in corrosion rate with increase in C content of steel substrate from 0.4 wt.% (AISI 4140) to 1.1 wt.% (AISI W1).

5.3.4 Comparison of Corrosion Compounds in Ex-service and Laboratory Materials

Comparison of the formed intermetallic compounds can be used to judge the similarities of corrosion mechanisms under laboratory and industrial service conditions. In ex-service and laboratory GCIs, the intermetallic phases observed most frequently are η-Fe_2Al_5 and θ-$FeAl_3$ and less frequently, β_2-FeAl, ζ-$FeAl_2$, κ-Fe_3AlC and Al_4C_3. The formation of the latter phases may be hampered by the non-equilibrium conditions. However, certain phases may be present in very small quantities and thus could not be detected by scanning electron microscopy. The formation of β_1-Fe_3Al was found under specific material and experimental conditions. The laboratory CS specimens obtained from the 950°C-2400s-static immersion test contained β_1-Fe_3Al; however, it was not found in any of the after-service specimens. The infrequent formation of the Fe-rich Fe-Al phases can also be explained on the basis of the available literature. Naoi and Kajihara [44] suggest that the Fe/Al interdiffusion coefficient is more than two orders of magnitude smaller for β_2-FeAl, ζ-$FeAl_2$ and θ-$FeAl_3$ than for η-Fe_2Al_5. Yan and Fan [45] conducted tests by immersing H21 tool steel specimens in liquid Al for long durations. The η-Fe_2Al_5 and θ-$FeAl_3$ phases appeared as the first reaction products. After extended (9 hours) periods of immersion into liquid Al, ζ-$FeAl_2$ formed and its thickness was found to increase with exposure time while the η-Fe_2Al_5 thickness remained constant [45]. These studies suggest that the Fe-rich phases such as β_2-

FeAl, ζ-$FeAl_2$ grow more slowly than η-Fe_2Al_5 and θ-$FeAl_3$. In other words, these phases only grow when there is a lack of Al diffusion.

After-service tapping pipes may be retained at ambient temperature for several months. This could help in achieving equilibrium between the intermetallic layers, leading to the formation of a wider range of compounds from the Fe-Al system. For example, ζ-$FeAl_2$ was only found in an after-service GCI. Al_4C_3 and κ-Fe_3AlC phases were found in both after-service and laboratory GCI specimens. However, the formation of κ-Fe_3AlC under laboratory conditions was detected only after extended periods of liquid Al exposure at 950°C.

β_2-FeAl, Al_4C_3 and κ-Fe_3AlC phases were observed in laboratory and after-service GCIs. This suggests that the GCI employed as bottom tapping pipe material corrodes in a similar manner to laboratory materials. Laboratory CS also shows a similar behaviour of liquid Al corrosion to after-service CS. In both the after-service and laboratory specimens, only θ-$FeAl_3$ particles were found dispersed in the solidified Al, which suggests that θ-$FeAl_3$ is the major contaminant of liquid Al melts.

5.4 Intermetallic Layer Growth

When a ferrous alloy is exposed to liquid Al, Fe-Al intermetallic compounds appear at the substrate-Al interface and these tend to grow with the increasing exposure time. The available literature (Section 2.2.3) relating to the intermetallic layer growth was found to be confined to steels and pure Fe, and only a very few studies considered the dissolution as well as the growth of the Fe-Al intermetallic layer. In the present work, several cast iron alloys were compared for the first time in terms of dissolution and growth kinetics of the intermetallic compounds. The recorded growth of intermetallic layers of Series-I materials is described in Section 4.4.

5.4.1 Comparing GCIs, DCIs and CS

At 750°C and 850°C, GCIs generally exhibited a lower mean intermetallic layer thickness (x) than DCIs, and CS showed a significantly larger x than the former alloys (Figure 4.54). Among the three test temperatures, at 850°C, most alloys showed highest x at 1200s (Figure 4.55). At this set of conditions, the relative effect of the dissolution and/or spallation of the layer believed to be small and thus the intermetallic layer grows to a maximum.

At all the temperatures, GCIs showed an increase in x with the increasing t; however, DCIs and CS showed negative deviations to this trend. The corrosion specimens of these alloys from static immersion tests showed one major difference: the GCI specimens exhibited a significantly greater thickness of solidified Al layer than that of CS and DCIs. Figure 5.22 shows the examples of solidified Al layers of each alloy type (950°C-1200s-static).

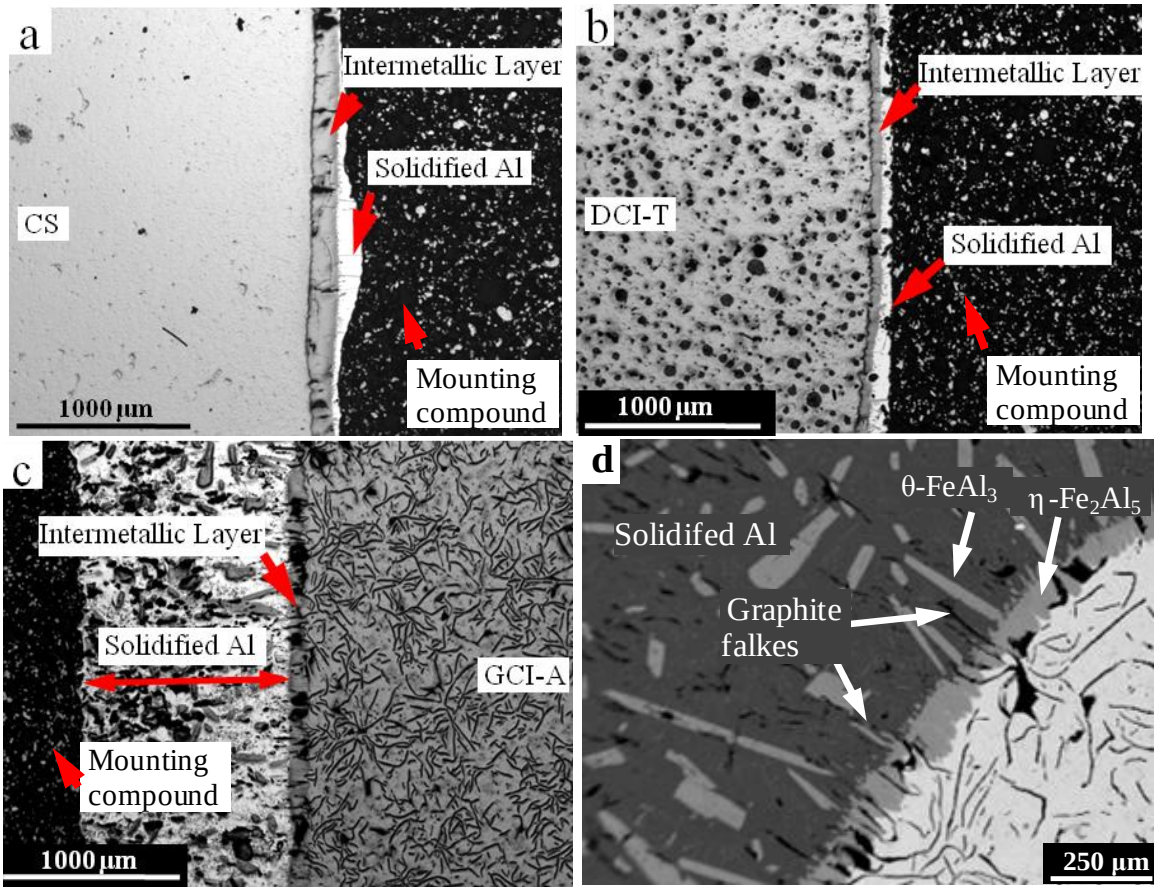

Figure 5.22 - Solidified Al layer on test specimens (950°C-1200-static), a) cast steel (CS), b) DCI-T, c) GCI-A, d) a magnified cross-section of GCI-A.

The greater thickness of solidified Al layers on GCI specimens could be due to: i) the mechanical support provided by the graphite flakes, which were found extending towards the solidified Al, ii) the graphite flakes may also support the growing θ-$FeAl_3$ crystals, which further support the solidifying Al. Therefore, the graphite flakes contribute to reducing the spallation of the intermetallic layers and reduce material loss of GCIs compared to DCIs and CS.

Among DCIs, DCI-C and DCI-D showed a decrease in x at 2400s at 850°C and 950°C. Only DCI-T showed intermetallic layer growth at 950°C, whereas DCI-C and DCI-D exhibited thinning of the intermetallic layers with increasing time even less than 1200s. With the rise in exposure temperature from 750°C to 950°C, a decrement in x suggests that for DCI-C and DCI-D the ratio of the spallation and/or dissolution to the formation of the compound layer could be to be higher at 950°C.

It is to be noted that GCI-S has the lowest Si content among GCIs and showed the highest relative increase in x with rise in temperature. Also, DCI-T, which exhibited an increasing x with time at 850°C, contained lower amounts of Si compared to DCI-C and DCI-D. Therefore, the decreasing x with time at 950°C is related to higher Si contents in DCI-C and DCI-D. The materials (DCI-C, DCI-D and CS) that showed thinning of the intermetallic layer with increasing exposure time at 850°C, were also found to dissolve at a higher rate than GCIs and DCI-T (Section 4.2).

Table 4.7 shows the time exponents (n) of power law growth of intermetallic layers of cast irons and steel. In agreement with literature, most alloys showed values of n between 0.25 and 0.5. However, current results showed that a decrease in n with rise in temperature (750°C- 950°C) was more pronounced in the case of alloys having higher corrosion rates.

This indicates that the dissolution and/or spallation of the intermetallic layer should be relatively higher at the higher exposure temperature.

5.4.2 GCIs

As mentioned before, at 1200s, compared to the other temperatures, most alloys showed a maximum x at 850°C. This exposure condition may be more favourable for formation of η-Fe_2Al_5 at a higher rate relative to its dissolution and/or spallation. Thus x at this set of conditions was taken as a representative of the aggressiveness of liquid Al to form η-Fe_2Al_5. For convenience x at 850°C-1200s-static was designated as x_h. Figure 5.23 shows a plot between x_h and cementite fraction in GCIs. The x_h of GCIs was varied inversely with the increasing cementite fraction. Compared to pearlite or ferrite, the decomposition of cementite into Fe-Al compounds was found to be relatively slow (Section 4.3.1.2), which tends to limit the thickness of the intermetallic layer.

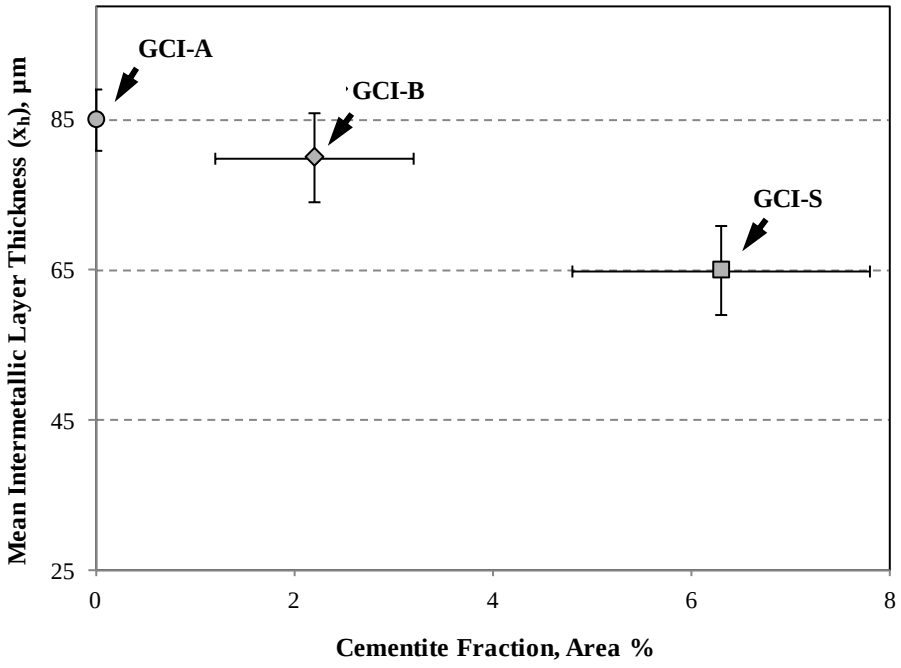

Figure 5.23 - Mean Intermetallic layer thickness (x_h) versus cementite fraction in GCIs.

5.4.3 DCIs

In DCIs, x_h varied directly with the ferrite fraction, Figure 5.24 shows a plot between x_h ferrite fractions in DCIs. The fraction of each Fe-C phase (ferrite, pearlite and cementite) depends upon the chemical composition of cast irons. Exposure of DCIs to 850°C should initiate the transformation of these phases to austenite, thus the phase fraction measured before exposure is indicative of the C present in cast iron matrix. Both DCI-C and DCI-D have high Si (> 3 wt.%) and Si promotes ferrite in cast irons [1]; however, the addition of Cu and Cr to DCI-D has lead to a lower amount of ferrite than DCI-T. DCI-C alloy has the highest amount of ferrite or low carbon matrix at exposure temperatures, which was found to be the least resistant to the liquid Al corrosion, thus the DCI-C intermetallic layer grows fast.

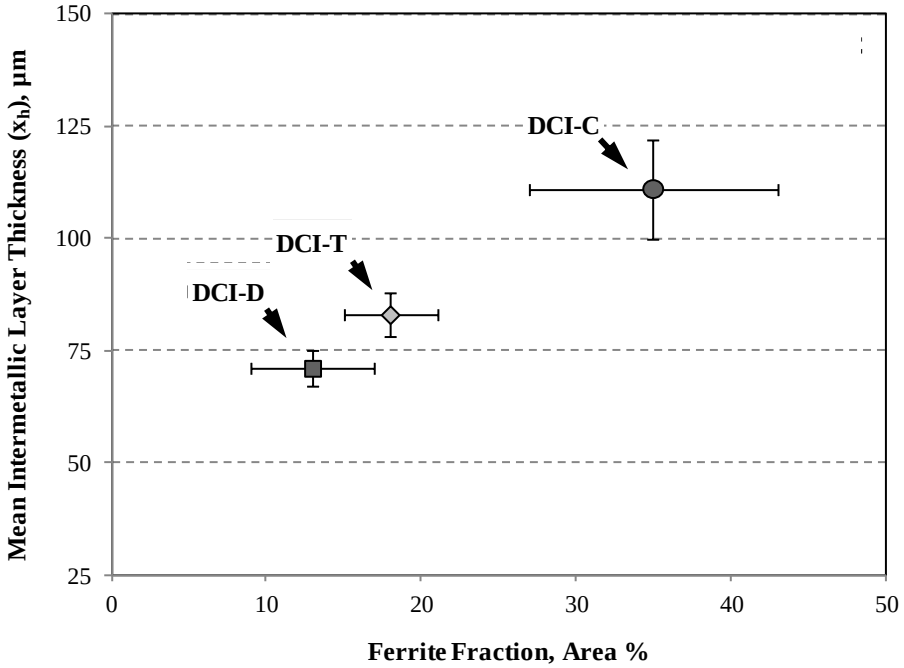

Figure 5.24 - Mean Intermetallic layer thickness (x_h) versus ferrite fraction in DCIs.

5.4.4 CS

At the three test temperatures, CS showed an increasing x with increasing t; however, a decrease in x was observed at 2400s at 850°C (Figure 4.55). In general, thicker intermetallic

layers are expected at higher temperatures. However, most CS specimens showed a complete reversal with the lowest x at 950°C. Since CS has the highest corrosion rate among the alloys under current investigation, the increased dissolution and/or spallation of the intermetallic layer at 950°C can lead to such behaviour. However, unlike DCIs, with increasing time at 950°C, the thinning of the intermetallic layers was not observed in the case of CS.

5.5 Intermetallic Layer Growth and Dissolution Kinetics

The diffusion of Fe and spallation (and/or dissolution) of the intermetallic layer are the primary mechanisms of material loss from Fe-substrates in Al melts. In order to reveal the role of spallation and/or dissolution of the intermetallic layer, the observed intermetallic layer thickness (x) was compared with the dissolution under static melt conditions (Method-II) (Figure 4.59). The extent of dissolution of ferrous alloys was linear with time.

As a general consideration, the observed thickness of the intermetallic layer at any instant is a balance between its advance towards the substrate and spallation and/or dissolution into the melt. Yeremenko *et al.* [46] suggested that the growth rate of the intermetallic layer in a saturated solution (liquid Al saturated with Fe) can be given by Equation 5.1.

$$\frac{dx}{dt} = \frac{k_1}{x} \tag{5.1}$$

In an undersaturated solution, after immersion, the diffusion boundary layer rapidly forms at the solid Fe-liquid Al interface; thus, the concentration of Fe near the solid surface was regarded as being equal to the saturation concentration. Thus k_1 was assumed to be independent of the degree of saturation of liquid metal, and dissolution in a saturated solution does not occur [46]. Considering the dissolution of the intermetallic layer in an

undersaturated Al melt, Yeremenko *et al.* revised Equation 5.2 to include the dissolution rate (d′):

$$\frac{dx}{dt} = \left(\frac{k_1}{x} - d' \right) \tag{5.2}$$

They [43] noted that the decreased x can contribute to increased growth of the intermetallic layer. As the dissolution rate (d′) increases, x should decrease, and Equation 5.2 suggests that with a decrease in x, the compound formation rate increases. Thus, the observed thickness (x) of the intermetallic layer is not a simple difference between the growth and dissolution of the intermetallic layer.

In solid state Fe-Al diffusion couples, the intermetallic layer growth has been found to follow the parabolic growth law [43], and there are no reports of negative deviations. However, in the case of Fe-liquid Al systems, for extended exposure periods, a decrease in x can be understood because in agreement with the reaction-diffusion mechanism [20], the growth rate of the intermetallic layer reduces with time. Concurrently, the dissolution and/or spallation rate remains constant thus thinning of the intermetallic layers can take place.

The intermetallic layer growth rate varies inversely with x (Equation 5.2). However, Equation 5.2 does not account for the growth and dissolution during the reaction controlled regime (initial short period of immersion). An increased rate of compound formation should result when x decreases by a high dissolution. Moreover, with a further decrease in x, the growth of Fe-Al compounds can occur at a higher rate because the compound formation may become reaction dominant (a faster growth regime than diffusion controlled growth). In high Si DCIs (Si > 3 wt.%), with increasing immersion time at 950°C, x for the subsequent period of interaction decreased less than or remain nearly equal to the intermetallic thickness at the initial exposure period (60s). Thus a high dissolution rate can cause a small x, which

was further believed to enhance the formation rate of the intermetallic layer and simultaneously, the dissolution and/or spallation of the intermetallic layer continues.

Both dissolution and intermetallic layer growth occur simultaneously. Considering Equation 5.2, when $\frac{k_1}{x} = d'$, $\frac{dx}{dt} = 0$ and reach steady state.

All GCIs showed an increase in x with increasing t, while DCIs and CS generally showed a maxima and then x decreased with increasing t. In GCIs, the equilibrium between the growth and dissolution may not be achieved up to the maximum exposure period. At 950°C, DCI-C showed maxima in x at 60s and for DCI-T it was at 1200s. These results suggest that the equilibrium between the growth and dissolution of the intermetallic layer may have attained in a short exposure time for the alloys having higher dissolution rates. The results presented here also affirmed the suggestion of Yeremenko *et al.* [46] that the growth of the intermetallic layer cannot be considered independent of the dissolution.

According to Yeremenko *et al.* [46], in the solid-liquid systems such as Fe-liquid Al, it is impossible to avoid the formation of intermetallic compounds by increasing the dissolution rate. Nucleation and reaction between Fe and Al are sufficiently fast at exposure temperatures [43] that the thickness of the intermetallic layer can decrease by dissolution, but it may not vanish completely. Thus there is a possibility of a minimum intermetallic layer thickness (x_{min}) even under high dissolution rates. Current work showed that the occurrence of x_{min} depends upon the type and composition of ferrous alloy and the conditions of liquid Al exposure. It was found that the alloys with higher corrosion rates show x_{min} in shorter immersion periods.

The negative deviations from the parabolic growth law and decreasing trends of x with increasing t were more readily observed in the cases of alloys having higher corrosion rates.

These findings indicate that formation and dissolution (and/or spallation) of the intermetallic layer are the primary modes of liquid Al corrosion of ferrous materials.

5.6 Comparing Intermetallic Layer Growth and Corrosion Rates

In order to judge the performance of ferrous alloys in liquid Al melts, two types of characteristics of intermetallic layers of were compared with the corrosion rates, first is the mean intermetallic layer thickness at a single set of temperature and time and second the x-t behaviour at different temperatures.

5.6.1 Mean Intermetallic Layer Thickness at 950°C

A simple approach for judging the performance of ferrous alloys can be x at a single set of conditions. Current findings suggest that dissolution and/or spallation of the intermetallic layer contributes to the material loss from Fe-substrates. Compared to lower temperatures, at 950°C, thinning of the intermetallic layer with increasing exposure time was commonly observed in the cases of alloys having higher corrosion rates. Thus x at this temperature was used to relate to the corrosion resistance. For this purpose x at 950°C-2400s-static was used, x at these exposure conditions was designated as x_d. The x_d of ferrous alloys was compared with their corrosion rates under forced flow of liquid Al at 950°C, same ranking of corrosion resistance of cast iron alloys was found under static melt conditions (Figure 4.1 and Figure 4.3). Figure 5.25 shows x_d and mass dissolution rates (R′) of cast irons and steel under dynamic corrosion conditions (950°C-0.48m/s). The corrosion rate generally followed the inverse relationship to x_d. However, for CS, x_d was found to be highest among these alloys but also the highest corrosion rate. The CS microstructure was mainly ferritic (0.2 wt.% C), which promoted the intermetallic layer growth at a relatively higher rate. Moreover, CS is different from cast irons in terms of graphite particles and Si content. A higher Si content promotes the thinning of intermetallic layers at 950°C, Section 5.4.1. When there are several

factors affecting the intermetallic layer thickness, it is difficult to know the effect of each of these factors. However, the effect of higher C in cast irons and a significantly higher Si may have contributed to a lower x_d of cast irons. A higher C content of Fe-substrate can cause the η-Fe_2Al_5 at a slower rate and a higher Si may lead to the thinning of intermetallic layers. There is also a conflict between GCI-A and GCI-S. However, x_d and R′ of GCI-B can be clearly differentiated from these alloys. The difference between the corrosion rates of GCI-A and GCI-S under static melt conditions at 950°C was found to be small (Figure 4.1) thus similar can be the case of x. Thus when the corrosion resistance of two GCIs is close, it is difficult to judge their corrosion performance on the basis of intermetallic layer thickness (x_d).

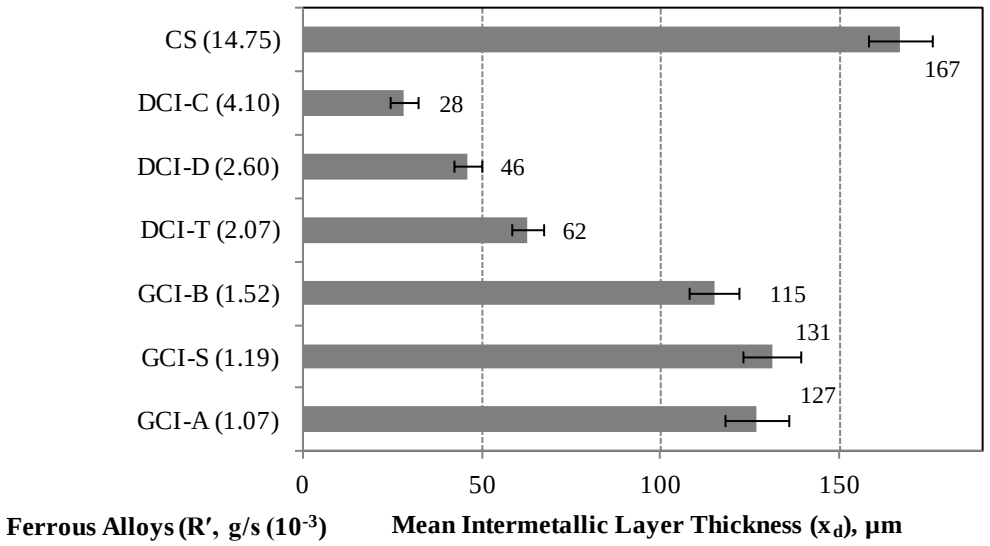

Figure 5.25 - a) Mean intermetallic layer thickness at 950°C-2400s-static (x_d), Method-II, and mass dissolution rate (R′) 950°C-0.48 m/s, Method-I.

5.6.2 Intermetallic Layer Growth Behaviour at 750°C and 950°C

Intermetallic layer growth of each alloy at 750°C and 950°C was compared with their ranking according to the corrosion rates (Figure 4.56 and Figure 5.25). A lower growth rate or a decrease in x with a rise in temperature (750-950°C) reflected a greater susceptibility to corrosion. In other words, a larger area confined between the Log(x)-Log(t) trend-lines for

750°C (above) and 950°C (below) indicated a higher corrosion resistance. For example, DCI-C has the lowest corrosion resistance among cast irons, and x of DCI-C decreases with time at 950°C and the majority of data points at 750°C showed greater x than at 950°C. GCI-A was found to be an exception to this trend: it has a lower corrosion rate compared to GCI-S but showed a larger area between 750°C-950°C trend lines but these difference were relatively small. There is a complex effect of phases present and Si content in cast irons on liquid Al corrosion rates such as GCI-A comprises ferrite, which can enhance the corrosion rate but a higher graphite fraction than GCI-S has the opposite effect. Thus it is not possible to reveal the effect of each factor when the corrosion resistance and x-t behaviour of two cast irons are close. However, a higher amount of Si and ferrite in GCI-A can be a possible explanation because ferrite promotes the formation of intermetallic layer, on the other hand at higher temperatures a greater Si content leads to the thinning of intermetallic layers.

In literature, the x-t behaviour of carbon steels studied by Sasaki *et al.* [47] showed a similarity with the present observations on cast irons, with a rise in temperature the two high C steels designated as C45 and C88 (0.45 wt.% C and 0.88 wt.% C, respectively) showed a larger area between the 700°C and 850°C trend lines than a low C steel (C05, 0.05 wt.% C). At 850°C, the C05 and C45 steels showed negative deviations from parabolic behaviour while the C88 steel followed the parabolic behaviour at the three test temperatures, for details see Figure 2.8. However, corrosion rates of these materials were not investigated in Sasaki *et al.*'s work. Considering the present findings, a higher C content in steels reduces the corrosion rate. Thus the deduced x-t behaviour that relates the corrosion rates to the thinning of intermetallic layers (with a rise in temperature) may be applicable to steels as well.

These findings suggest that x_d or x-t (750°C-950°C) behaviour in static melt conditions can be used to judge the performance of ferrous alloys under static or flow assisted liquid Al corrosion. However, the x-t behaviour was believed to be more robust than evaluating x at a single set of conditions. Current work found that both x and corrosion rates are interrelated and strongly depend on the chemical composition of ferrous alloys. However, when there is a small difference between the corrosion resistances of two materials and/or they differ to large extent in terms of chemical composition and phases present, the stated x-t (750°C-950°C) behaviour versus-corrosion relationship may not be applicable.

5.7 Role of Si in Liquid Al Corrosion of Ferrous Alloys

5.7.1 Dissolution and Growth of Intermetallic Layers

It is well known that Si addition to molten Al strongly reduces the intermetallic layer thickness, details are found in Section 2.2. However, the mechanism by which Si reduces the growth of the Fe-Al alloy layer remains controversial. One point of view suggests that Si atoms occupy the structural vacancies in the η-Fe_2Al_5 phase resulting in reduced Al diffusivity, and as a result Si containing η-Fe_2Al_5 grows more slowly than Si free η-Fe_2A1_5 [10, 48]. On the other hand, Komatsu *et al*. [49] and Ueda *et al.* [50] suggested that the presence of Si in Al melts does not inhibit the intermetallic layer growth, but accelerates its dissolution into liquid Al. Moreover, Komatsu *et al.* concluded that presence of Si in Fe substrates does not affect the corrosion rate; however, an increase (approximately 15 %) of corrosion rate at 1 and 3 wt.% Si additions to pure Fe was clearly seen in Komatsu *et al.*'s work. It is to be noted that in the present work, the Si content in cast irons was between 1.4 - 3.5 wt.%.

Niinomi and Ueda [5] found that that the addition of Si (3 wt.%) to pure Fe decreases the intermetallic layer thickness. In an another publication, Niinomi *et al.* [6] reported that the

addition of Si (3 wt.%) to pure Fe results in an increase in the liquid Al corrosion rate. Considering the results of [5-6, 49-50], it was recognized that addition of Si to pure Fe increases the corrosion rate and results into thinner intermetallic layers. With increasing Si content, thinning of the intermetallic layers and higher dissolution rates were also found in the present investigation. However, Si present in cast irons also affects the microstructure, and thus the corrosion rate and compound formation. It is to be noted that the Fe/Al interdiffusion rate should be higher for a greater corrosion rate. Thus the conclusion follows that the suggestion of [10, 48] of Si reducing the diffusion of Al and/or Fe through η-Fe_2Al_5 does not hold in the case of Si present in Fe-substrates. In agreement with the Komatsu *et al.*'s [49] findings, similar may be the case of Si addition to Al melts.

In the present case of cast irons, higher Si contents promote ferrite, which can contribute to a higher rate of the compound formation. For example, compared to other alloys, a higher Si content in DCI-C led to a higher ferrite fraction, which does result into higher rates of compound formation as found at 850°C. However, a relatively higher dissolution rate and thinning of the intermetallic layers of DCI-C was found at 950°C. Also at 850°C, thinning of the intermetallic layers with increasing exposure time were more readily observed in the cases of alloys having higher Si and higher corrosion rates, Figure 4.55. Figure 5.26 (a) shows a relationship between x and Si content in cast irons at 950°C-1200s-static. In the case of pure Fe, Si cannot affect the intermetallic layer growth and corrosion rates by varying the fractions of ferrite, cementite and pearlite as it does in cast irons. As mentioned before, the literature reported that Si addition to pure Fe reduces the intermetallic layer thickness. Thus the conclusion follows that Si containing intermetallic layers are more vulnerable to dissolution and/or spallation leading to the higher corrosion rates. As discussed in Section 5.5, when the thickness of intermetallic layer decreases by dissolution its formation should occur at a higher rate. Simultaneously, the formation and spallation of the

intermetallic layer continues. Figure 5.26 (b) shows dissolution in terms of dissolved thickness (d_{Fe2Al5}) versus Si content in each cast iron alloy.

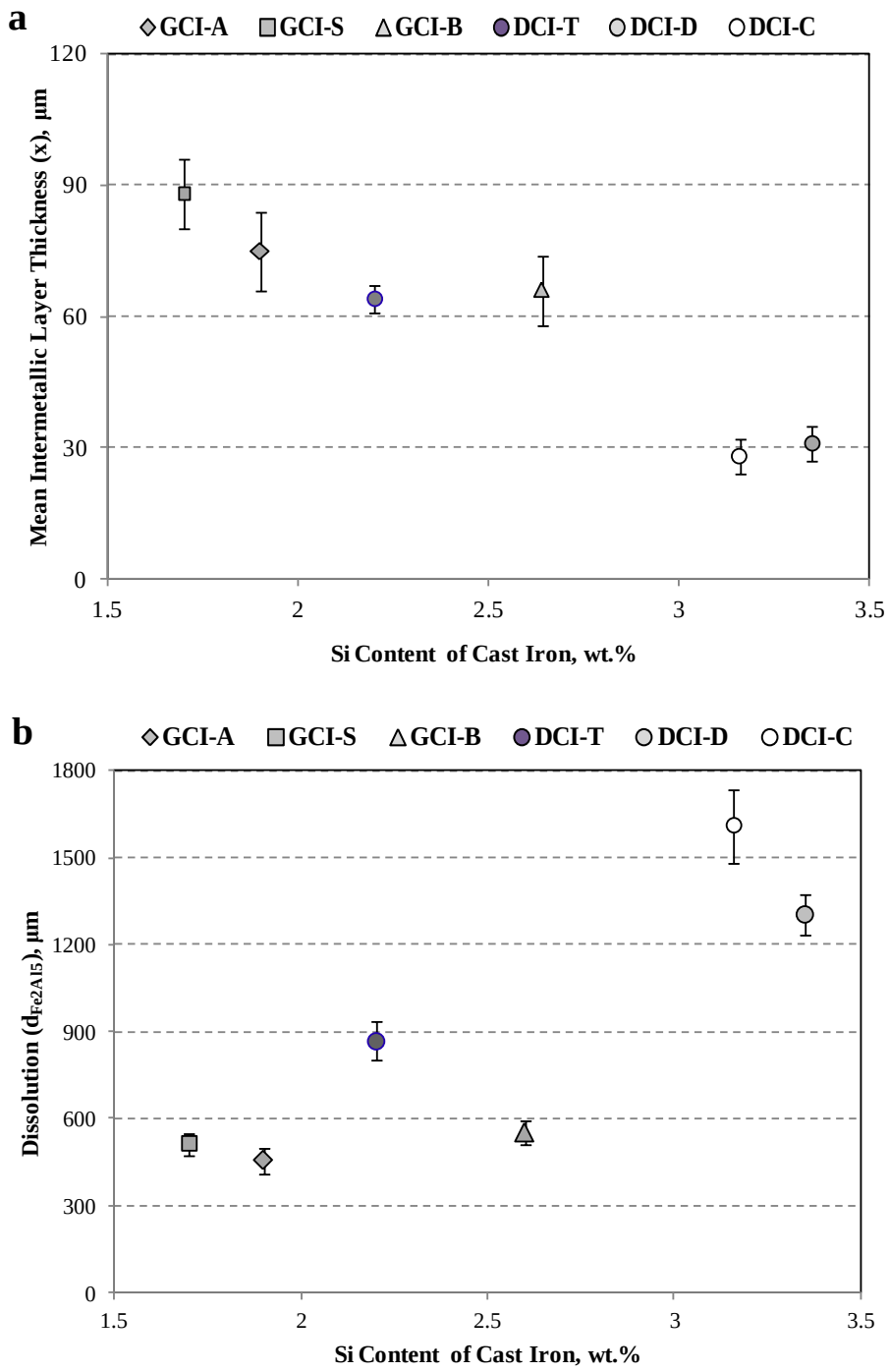

Figure 5.26 - a) Mean intermetallic layer thickness versus Si content in cast irons (950°C-1200s-static), b) Dissolution versus Si content in cast irons (950°C-1200s-static).

Data presented shows that the intermetallic layer thickness varied inversely and the dissolution tends to increase with increasing Si content. Thus Si in cast irons was believed to act in two ways:

a) Si promotes ferrite and depletes C from cast iron matrix at exposure temperatures, which contributes to higher rates of compound formation and liquid Al corrosion.
b) Si leads to a higher dissolution and/or spallation rate of the intermetallic compounds, which is reflected by the higher dissolution and thinning of the intermetallic layers of high Si DCIs.

In addition, the formation of SEP at the cast iron/η-Fe_2Al_5 interfaces were also believed to affect the liquid Al corrosion as discussed in Section 5.3.1.3 and Section 5.3.2.1. Considering these aspects, for improving the liquid Al corrosion resistance of cast irons, the Si content should be minimized. Moreover, similar to cast irons increasing Si content may also negatively impact the liquid Al corrosion resistance of steels.

5.7.2 Morphology of Intermetallic Layers

To investigate the mechanisms by which Si increases the dissolution and/or spallation tendency of intermetallic layers, the morphology of the intermetallic layers of cast irons was investigated in detail (Section 4.6). The morphology of the intermetallic layer was found to vary with the substrate composition and alloy type. The DCIs showed more serrated morphology and uneven intermetallic layers than GCIs. The nature of the intermetallic layers was determined from the average maximum ($\overline{X}_{max}$) and average minimum ($\overline{X}_{min}$) intermetallic layer thickness, Figure 4.62.

As a general consideration, a lower value of $\overline{X}_{min}$ suggests that liquid Al was closer to the substrate and the intermetallic layer is difficult to sustain in liquid Al. On the other hand, a

higher value of $\overline{X}_{max}$ can be attributed to formation of intermetallic layer at a greater rate. Generally, $\overline{X}_{min}$ of cast irons showed a decrease with increasing Si while $\overline{X}_{max}$ showed the opposite trend. For example, DCI-C is richer in Si than DCI-T and $\overline{X}_{max}$ of DCI-C was found to be significantly higher than DCI-T and $\overline{X}_{min}$ followed the opposite trend. A lower value of $\overline{X}_{min}$ may correspond to the higher tendency of spallation and/or dissolution. On the other hand, a higher $\overline{X}_{max}$ value suggests that the intermetallic layer formation in DCI-C occurred at a greater rate. Thus more serrated and uneven morphology of the intermetallic layer of DCIs may be directly related to their higher Si content than GCIs.

CS showed highest $\overline{X}_{max}$ and $\overline{X}_{min}$ values and also has the highest corrosion rate. This trend is not consistent with cast irons. CS is mainly ferritic and has a negligible Si content (0.2 wt.%) compared to cast irons. Moreover, the compositional constituents in CS are similar to cast iron matrixes except the graphite inclusions. Since Si addition to pure Fe was found [5] to reduce the intermetallic layer thickness, and the current work showed that $\overline{X}_{min}$ decreases with increasing Si. Thus a higher value $\overline{X}_{min}$ of CS was attributed to a significantly lower Si content, and a ferritic microstructure can promote the intermetallic layer formation at a higher rate leading to a higher $\overline{X}_{max}$. Moreover, the graphite particles can also affect the growth and spallation of the intermetallic layer; however, the affect of the Si content appeared to dominate the both characteristics.

In the present work, the deep etching technique was successfully used to reveal the true morphology of the intermetallic layers of cast irons and steel, Section 4.6.2. $Fe_3(Al, Si)$ or Fe_3Si compounds can create discontinuities at the surface of η-Fe_2Al_5 columns of DCIs. Compared to DCIs, the η-Fe_2Al_5 compound structure of CS was found to be uniform and free from structural imperfections which may be reflected by considerably thicker

intermetallic layers. The structural imperfections created by the formation of $Fe_3(Al, Si)$ or Fe_3Si phases may cause stress concentrations, which decrease the physical strength of the η-Fe_2Al_5 columns resulting in the increased spallation under natural or forced convection.

Si concentration at the cast iron substrate/η-Fe_2Al_5 interface varied directly with the substrate Si content. Also, within the bulk of η-Fe_2Al_5, Si concentration was found to be higher for high Si cast irons (Section 4.3.1.1). Thus a higher Si content within the bulk of the η-Fe_2Al_5 phase may also affect the spallation tendency of the intermetallic layer. However, it is difficult to reveal the possible contribution of each factor (higher Si concentration at substrate/η-Fe_2Al_5 interface and within the bulk of η-Fe_2Al_5) to the spallation tendency.

The results of present investigation identified that the liquid Al corrosion resistance of a ferrous alloy depends upon the rate of formation and spallation tendency of the η-Fe_2Al_5 layer. For example, the higher dissolution rates of high Si cast irons were attributed to the mechanically weaker and/or enhanced tendency of dissolution of Si containing η-Fe_2Al_5. The case of θ-$FeAl_3$ may be similar. Similarly to η-Fe_2Al_5, the rate of formation and/or the physical strength θ-$FeAl_3$ may vary with the chemical composition of ferrous alloy. However, the formation rate and spallation and/or dissolution tendency of θ-$FeAl_3$ cannot be determined because of the fragility of the θ-$FeAl_3$ phase.

Chapter References

[1] J.R. Davis, ASM Speciality Handbook-Cast Irons, ASM International, Materials Park, Ohio, 1996.

[2] D. Balloy, J.C. Tissier, M.L. Giorgi, M. Briant, Metallurgical and Materials Transactions A, 41 (2010) 2366-2376.

[3] F.A. Mountford, T.J. Glover, Foundry Trade Journal, 120 (1966) 849-852.

[4] S.H. Hwang, J.H. Song, Y.S. Kim, Materials Science and Engineering A, 390 (2005) 437-443.

[5] M. Niinomi, Y. Ueda, Transactions of the Japan Institute of Metals, 23 (1982) 709-717.

[6] M. Niinomi, Y. Ueda, M. Sano, Transactions of the Japan Institute of Metals, 23 (1982) 780-787.

[7] J.F. Janowak, R.B. Gundlach, American Foundry Society Transactions, 90 (1982) 847-863.

[8] K. Roehrig, American Foundry Society Transactions, 86 (1978) 75-88.

[9] U. Sen, S. Sen, F. Yilmaz, Journal of Materials Processing Technology, 148 (2004) 1-7.

[10] T. Heumann, S. Dittrich, Zeitschrift Fuer Metallkunde, 50 (1959) 617-625.

[11] A. Bouayad, C. Gerometta, A. Belkebir, A. Ambari, Materials Science Engineering A, A363 (2003) 53-61.

[12] H.R. Shahverdi, M.R. Ghomashchi, S. Shabestari, J. Hejazi, Journal of Materials Processing Technology, 124 (2002) 345-352.

[13] F. Balbaud-Célérier, F. Barbier, Journal of Nuclear Materials, 289 (2001) 227-242.

[14] E.G. Ivanov, Metal Science and Heat Treatment, 21 (1979) 449-452.

[15] V.I. Nizhenko, Powder Metallurgy and Metal Ceramics, 43 (5-6) (2004) 273-279.

[16] V.R. Ryabov, Fusion Welding of Aluminium to Steel, Scientific Thoughts, Nauk, Dumuka, Kiev, (1969) 232-258.

[17] V.N. Eremenko (Ed.), The Physical Chemistry of Inorganic Materials, Vol. 3, Kiev, 1988.

[18] R.U. Burkhardt, Y.U. Grin, M. Ellner, Acta Crystallographica, B50 (1994) 313-316.

[19] M. Hansen, Constitution of Binary Alloys, McGraw-Hill Book Company, New York, 1958.

[20] V.I. Dybkov, Reaction Diffusion and Solid State Chemical Kinetics, The IPMS Publications, Kyiv, 2002.

[21] T. Maitra, S.P. Gupta, Materials Characterization, 49 (2003) 293-311.

[22] V.I. Dybkov, Journal of Materials Science, 25 (1990) 3615-3633.

[23] T.S. Shih, S.H. Tu, Materials Science Engineering A, 454-455 (2007) 349-356.

[24] D. Chaira, S. Sangal, B.K. Mishra, Materials and Manufacturing Processes, 22 (2007) 492-496.

[25] A. Banerji, W. Reif, Metallurgical Transactions A, Physical Metallurgy and Materials Science, 17 A (1986) 2127-2137.

[26] J.C.R. Manning, T.B. Gurganus, Journal of the American Ceramic Society, 52 (1969) 115-118.

[27] J.V. Naidich, J.N. Chuvashov, Journal of Materials Science, 18 (1983) 2071-2080.

[28] P.C. Hayes, Process Principles in Minerals and Materials Production, Hayes Publishing Company, Sherwood, 1993.

[29] P. Maugis, J. Lacaze, R. Besson, J. Morillo, Metallurgical and Materials Transactions A, 37 (2006) 3397-3401.

[30] P. Kratochvil, F. Dobe, V. Vodickova, Intermetallics, 17 (2009) 39-45.

[31] H. Ohtani, M. Yamano, M. Hasebe, Iron and Steel Institute of Japan, 44 (10) (2004) 1738-1747.

[32] N.W. Ageew, O.I. Vher, Institute of Metals - Advance Papers, Institute of Metals Meeting, London, 44 (2) (1930) 83-95.

[33] R.W. Richards, R.D. Jones, P.D. Clements, H. Clarke, International Materials Reviews, 39 (1994) 191-212.

[34] D. Connetable, P. Maguis, Intermetallics, 16 (2008) 345-352.

[35] N.N. Aleksandrov, L.V. Il'Icheva, Metal Science and Heat Treatment, (1963) 646-650.

[36] S.G. Denner, R.D. Jones, R.J. Thomas, Iron and Steel International, 48 (1975) 241-252.

[37] Y.N. Malinochka, Metal Science and Heat Treatment, (1963) 640-646.

[38] Y. Zhang, D.G. Ivey, Journal of Materials Science, 33 (1998) 3131-3135.

[39] S.J. Cowdery, F.X. Kayser, Materials Research Bulletin, 14 (1979) 91-99.

[40] U. Starke, J. Schardt, W. Weiss, W. Meier, C. Polop, P.L. De Andres, K. Heinz, Europhysics Letters, 56 (2001) 822-830.

[41] B. Sepiol, G. Vogl, Diffusion in ordered Fe-Si alloys, Switzerland, (1995) 149-159.

[42] A. Gude, H. Mehrer, Philosophical Magazine A, 76 (1) (1976) 1-29.

[43] S. Kobayashi, T. Yakou, Materials Science and Engineering A, 338 (2002) 44-53.

[44] D. Naoi, M. Kajihara, Materials Science and Engineering A, 459 (2007) 375-382.

[45] M. Yan, Z. Fan, Journal of Materials Science, 35 (2000) 1661-1667.

[46] V.N. Yeremenko, Y.V. Natanzon, V.I. Dybkov, Journal of Materials Science, 16 (1981) 1748-1756.

[47] T. Sasaki, T. Yakou, K. Mochiduki, K. Ichinose, The Iron and Steel Institute of Japan International, 45 (2005) 1887-1892.

[48] J.E. Nicholls, Corrosion Technology, 11 (1964) 16-21.

[49] N. Komatsu, M. Nakamura, H. Fujita, Journal of Japan Institute of Metals, 18 (1968) 474-482.

[50] Y. Ueda, M. Sano, M. Niinomi, Journal of the Japan Institute of Metals, 42 (1978) 549-555.

CHAPTER 6 : CONCLUSIONS

The primary purpose of the present research program was to enhance the service life of cast iron/steel tapping pipes used to transfer liquid Al from smelting cells. In order to achieve this goal, research was focused on developing the cast iron and steel alloys with better liquid Al corrosion resistance. Moreover, the formation and growth characteristics of intermetallic compounds were studied to better understand the dissolution mechanisms and to predict the relative corrosion behaviour of ferrous alloys. The most significant contribution of the present work is the identification of the factors and mechanisms affecting the liquid Al corrosion resistance of cast irons and steels. The conclusions derived from this work are described in the following sections.

6.1 Liquid Al Corrosion Resistance and Chemical Composition

Review of the literature indicated that there is no known correlation between the cast irons composition and liquid Al corrosion resistance. The current work successfully differentiated liquid Al corrosion resistance of cast irons and steels according to the microstructure and/or chemical composition. The following conclusions were drawn:

- Both increasing the temperature of the liquid Al and introducing forced flow conditions significantly accelerated the material loss of ferrous alloys. The liquid Al corrosion resistance of GCIs under static and dynamic corrosion environments was found to be exceptionally better than DCIs. This was mainly due to the presence of interconnected graphite flakes in GCIs compared to the isolated spheres in the case of DCIs. Moreover, cementite present in GCIs also contributed to their enhanced corrosion resistance.

- The key to obtaining GCIs with enhanced corrosion resistance was identified as the effect of alloying elements on the amount of each phase (ferrite, pearlite, cementite and

graphite) present in the microstructure. The increased amount of C in the form of graphite flakes enhances the liquid Al corrosion resistance of GCIs, which can be further improved by the introduction of cementite. No increase in corrosion resistance was found by increasing cementite fraction at the expense of a decreased graphite flake fraction in GCIs. Among the GCIs under current study, the best corrosion resistance was obtained when both graphite and cementite were present in an approximate ratio of 1:1 by area.

- Contrary to C, the material loss of cast irons tends to increase with increasing Si content because Si promotes ferrite and depletes C from cast iron matrixes at exposure temperatures. Thus in order to maintain the matrix corrosion resistance, Si content should be minimized; however, a small amount Si (> 1 wt.%) is generally required to promote graphite flakes in GCIs.

- A GCI with a high liquid Al corrosion resistance can be obtained with C 3.7-3.8, Si 1.35-1.45, Mn 0.8-0.9, Cr 0.7-0.8 and Cu 1-1.2 (in wt.%). Furthermore, a higher amount of C may be used to enhance the corrosion resistance. When increasing C in GCIs, Mn and Cr contents should also be higher than the stated values so that the amount and high temperature stability of cementite can be maintained. However, the drawbacks are reduced toughness and strength of cast irons.

- Similar to GCIs, alloying the DCIs with cementite and pearlite forming elements such as Mn, Cr and Cu yields improvements to corrosion resistance, and increasing Si has the opposite effect. However, a relatively high Si content is often required in DCIs for improving their high temperature properties and to promote ferrite for high ductility. The elements such as Mn, Cr and Cu can be useful to offset the effect of increased Si to some extent.

- A higher amount of C in steel was also found to improve the liquid Al corrosion resistance. A steel with 0.4 wt.% C showed a significant improvement in the liquid Al corrosion resistance compared to a 0.2 wt.% C steel, while a further increase to 1.1 wt.% C showed a relatively small increase. It was also found that carbon steels ($\geq$ 0.4 wt.% C) can be more resistant to flow assisted liquid Al corrosion than high Si (> 2 wt.%) DCIs and GCIs. The absence of Si (or significantly lower Si contents) in steels was believed to enhance their corrosion resistance compared to cast irons because Si weakens the cast iron matrix by promoting ferrite and depleting carbon from cast iron matrix at exposure temperatures.

6.2 Intermetallic Compounds and Liquid Al Corrosion Resistance

In order to determine the effect of intermetallic compounds on liquid Al corrosion resistance, the substrate-Al interfaces of steel and cast iron alloys were investigated utilizing SEM, EDS and EBSD.

- In all the ferrous alloys under investigation, η-Fe_2Al_5 was the major phase of the intermetallic layers, while θ-$FeAl_3$ remained the minor phase. Moreover, all the intermetallic compounds of the Fe-Al binary system (formed under the equivalent temperature range) were detected. The compounds η-Fe_2Al_5, θ-$FeAl_3$, β_2-FeAl and β_1-Fe_3Al were found in laboratory specimens, while ζ-$FeAl_2$ was only detected in an after-service GCI.

- The orthorhombic η-Fe_2Al_5 phase was found to grow in a [001] direction, which is consistent with the existing literature. Current work reported for the first time that the preferred crystallographic growth direction of θ-$FeAl_3$ is [010]. It was conjectured that, like η-Fe_2Al_5, θ-$FeAl_3$ has faster diffusion of Fe/Al in the [010] direction leading to the lath shaped morphology of θ-$FeAl_3$ particles. Also the morphology of the thin θ-$FeAl_3$

layer was found to be polycrystalline. It was believed that formation and spallation of θ-$FeAl_3$ particles forms an active part of the process of dissolution of ferrous alloys into liquid Al melts.

- Si enrichment (SEP) was found ahead of the growing η-Fe_2Al_5 projections. A previous work suggested that the Si enrichment can be due to the low solubility of Si in η-Fe_2Al_5. In the present work, it was identified that the low Si solubility of η-Fe_2Al_5 is not a necessary condition for the formation of SEP. SEP can result from the relatively slower diffusion of Si than Fe. The Si concentration of SEP was found to rise with the increasing Si content in the cast iron matrix and also the corrosion rate. The Si enrichment was believed to facilitate the corrosion by depleting the C ahead of the growing η-Fe_2Al_5.

- The existence of near stoichiometric Fe_3Si (SEP) was recognized for the first time in Fe-liquid/solid Al couples. This phase was found to form in high Si (> 3 wt.%) DCIs. Also these alloys corroded at a greater rate than the cast irons with lower Si contents. The Fe diffusion in stoichiometric Fe_3Si is known to be faster than the non-stoichiometric Fe_3Si (with lower Si content), which can facilitate a higher corrosion rate of high Si cast irons.

- The current research reported formation of κ-Fe_3AlC in Fe-liquid Al couples for the first time. The fraction of this phase increased with the carbon present in the cast iron or steel matrix. Moreover, a higher thickness of the ternary κ-Fe_3AlC compound layer corresponded to a better liquid Al corrosion resistance of a cast iron or steel matrix.

- The existence of Al_4C_3 has been confirmed for the first time in Fe-liquid Al systems. Intermetallic layers of cast irons and steels exposed to liquid Al have been found to contain Al_4C_3. Thus all ferrous alloys containing cementite may be susceptible to the formation Al_4C_3 when exposed to liquid Al. The present work identified that in a

cementite/liquid Al interaction, the Al_4C_3 formation is possible at temperatures 750°C-950°C. However, according to the literature, in the case of graphite/liquid Al couples, the Al_4C_3 formation occurs at temperatures ≥1000°C.

- The literature indicated that the presence of higher C in steels reduces the corrosion rate, which was attributed to the increase in cementite content in the steel microstructure. Unfortunately, the identification of the underlying mechanisms could not be achieved in the past. The present research explored the mechanism of cementite transformation into Al_4C_3 and Fe-Al phases (at the cast iron/liquid Al interface), which occurred at a significantly higher rate compared to its transformation to austenite or graphite. It was conjectured that the formation of carbon rich phases, Al_4C_3 and κ-Fe_3AlC, consumes a part of the diffused Al and complicates the Fe/Al diffusion paths, therefore reducing the corrosion rate.

6.3 Intermetallic Layer Growth and Dissolution

The kinetics of dissolution and intermetallic layer growth were also determined to predict the effect of microstructure and chemical composition on the mechanisms controlling the corrosion rate of cast irons and steels.

- Liquid Al temperature played an important part in the growth of Fe-Al intermetallic layers formed on ferrous substrates. Increasing the temperature was found to accelerate the material loss and change the growth of the intermetallic layers of cast irons and steel.

- At 750°C, 850°C and 950°C, the intermetallic layer thickness of GCIs increased with increasing exposure time, whereas the DCIs and steel showed negative deviations from this behaviour. Graphite flakes in GCIs possibly provide mechanical support to the intermetallic layer, which was believed to suppress the liquid Al corrosion and leads to the thicker intermetallic layers with rise in temperature (750°C-950°C).

- At 750°C and 850°C, the time exponents (n) for the power law growth of intermetallic layers of ferrous alloys were varied between 0.32-0.54 (t = 60s-1200s), and the value of n for a low carbon cast steel (CS) and a high Si ferritic DCI (DCI-C) was close to 0.5. With a rise in temperature to 950°C, a large decrease in n was found especially in the case of DCIs.

- A thinner layer and/or a decrease in growth rate of the intermetallic layer with a rise in temperature (750°C-950°C) reflected the higher susceptibility of a cast iron to liquid Al corrosion. This type of relationship can be utilized to predict the relative corrosion resistance of ferrous alloys in static and forced flow conditions of liquid Al.

- The thinning and/or decrease in the growth rate of the intermetallic layers with a rise in temperature was found to vary directly with increasing Si contents in cast irons, which indicated that increasing Si additions affect the properties of the intermetallic layer. As the available literature suggested that a decrease in intermetallic layer thickness can enhance the compound formation rate. With a decrease in intermetallic layer thickness a higher corrosion rate is expected. Therefore, Si not only weakens the cast iron matrix against liquid Al corrosion by promoting ferrite or low carbon matrix at exposure temperatures, it also leads to enhanced susceptibility of the intermetallic layer to dissolution and/or spallation.

- Under static melt conditions, the dissolution of ferrous alloys was found to be a linear function of exposure time. Thinning of the intermetallic layer was observed with increasing exposure time in the cases of alloys having higher dissolution rates. Dissolution and/or spallation of the intermetallic layer are believed to be the cause of the negative deviations of the intermetallic layer growth from the parabolic law. These

findings also suggest that the dissolution and/or spallation of the intermetallic layer can be the primary mode of liquid Al corrosion.

- 3-D characterization of deep-etched specimens showed the true morphology of the intermetallic layers of steel and DCIs. The surface morphologies of η-Fe_2Al_5 columns for both types of ferrous alloys were found to be entirely different. The presence of Si in cast irons changes the surface morphology of the interfacial layer by forming iron rich Fe-Al-Si or Fe-Si phases. The existence of these phases made the η-Fe_2Al_5 surface discontinuous, which may be related to the fragility or poor mechanical strength of the intermetallic layer causing a higher tendency to spallation. However, there may be another physical or chemical phenomenon by which Si present in the bulk and/or at the outer surface of η-Fe_2Al_5 enhances the spallation and/or dissolution tendency of the intermetallic layer.

CHAPTER 7 : RECOMMENDATIONS TO INDUSTRY AND FUTURE WORK

7.1 Materials Recommendations

Based upon the results of liquid Al corrosion resistance and thermal fatigue characteristics of several ferrous alloys, the materials recommended for trials in actual industrial service are described in the following sections.

7.1.1 Bottom Tapping Pipe

An experimental GCI (GCI-L) exhibited an approximately 20% lower corrosion rate than the existing bottom tapping pipe material (GCI-BT). Based upon the outcomes of the current work (Section 6.1), the recommended composition (GCI-R) for bottom tapping pipes is listed in Table 7.1. GCI-R composition has similar composition to GCI-L except slightly higher contents of C, Mn and Cr.

Table 7.1 - Current and recommended compositions (wt.%) for bottom tapping pipes.

	C	Si	Mn	Cr	Cu
Current (GCI-BT)	3.6	1.5	0.7	0.5	1.0
Recommended (GCI-R)	3.7-3.8	1.35-1.45	0.8-0.9	0.7-0.8	1-1.2

Compared to GCI-L and GCI-BT, higher C content in GCI-R combined with higher amounts of Cr, Mn additions will increase the cementite fraction with a similar or greater amount of graphite. The GCI-R composition is expected to perform better than the current material (GCI-BT). Finally, the service performance will best determine the suitability of the new composition for bottom tapping pipes.

7.1.2 Top Tapping Pipe

The liquid Al corrosion rate of AISI 4140 steel was found to be significantly (approximately 12 times) lower than CS (AS 2074 steel), which is currently used as the top tapping pipe

material in Smelting Lines 1-3 at NZAS. The recommended steel composition (CS-R) is given in Table 7.2. CS-R has C and Mn contents similar to AISI 4140 steel and the rest of the chemical composition is kept similar to CS standard specification (AS 2074). In CS, Mo and Cr were used to improve properties such as resistance to oxidation and high temperature strength. Si content should be minimized as it may negatively impact the liquid Al corrosion resistance. However, Si is commonly used as deoxidizer in steel making and it improves the fluidity of molten steel.

Table 7.2 - Current and recommended compositions (wt.%) for top tapping pipes.

Steels	C	Mn	Mo	Cr	Si
Current (AS 2074)	0.20	0.5-0.8	0.45-0.65	1-1.5	0.6 max.
Recommended (CS-R)	0.40	Other alloying elements can be as in AS 2074 steel, Si should be kept as low as practically possible			

While the thermal fatigue study (Appendix-A) suggests that high Si DCIs are suitable candidates for top tapping pipes, the liquid Al corrosion resistance of cast irons was found to decrease with increasing Si contents. Thus the high Si DCIs cannot be recommended for tapping pipe applications.

AISI 4140 steel also showed liquid Al corrosion resistance superior to the DCI-T composition employed in reduction Line 4. The existing DCI-T alloy is more resistant to failure by liquid Al corrosion than Lines 1-3 CS tapping pipes; however, it fails through thermal fatigue cracking. Thus, the successful implementation of CS-R for Lines 1-3 could also replace the DCI-T pipes (Line-4) and the CS back spouts. The CS-R composition for top tapping pipes is anticipated to perform exceptionally well in service.

7.2 Future Work

- GCIs have proved to be the best ferrous materials to combat liquid Al corrosion. In the present work, the liquid Al corrosion resistance of various GCIs was compared only on the basis of the amounts of ferrite, graphite and cementite. It would be interesting to further reveal the effect of morphology, size and distribution of graphite flakes and cementite particles on material removal rate in liquid Al melts.

- Heat treatments can cause various types of microstructural and physical changes in cast irons, such as changing the phase fractions and internal oxidation, which may be studied to achieve a cast iron with a better performance in service. In the present work, the range of Si content in cast iron alloys was only varied between 1.38-3.35 (wt.%). Efforts may be made to determine the critical amounts of Si at which the corrosion rate will be minimum or maximum. Likewise, the increased amount of carbon in steels is beneficial in enhancing the liquid Al corrosion resistance. However, the optimum amount of carbon associated with the least dissolution in liquid Al melts is yet to be determined.

- Findings presented in this thesis identified that, higher Si additions in cast irons change the nature of intermetallic layers leading to a higher tendency towards spallation/dissolution in liquid Al. However, the inherent mechanism(s) by which Si causes such changes is not completely understood, which may be a challenge for future research.

- In the current research, all the materials were selected for comparison under the constraints of two desirable properties (liquid Al corrosion resistance and thermal fatigue) and the final product cost. Considering the available literature on the high temperature properties of cast irons and the cost of high alloy cast irons, only low alloy compositions of cast irons/steels were studied. Therefore, only the effects of low alloy additions of Mo,

Cr and Cu were revealed, and higher amounts of these elements may influence the liquid Al corrosion in a different way. Also the other pearlite and/or carbide promoting elements such as V and Ti can be given a trial. However, a relatively higher cost of these elements may be a constraint in employing the V and/or Ti alloyed cast irons to industrial applications.

- In addition to the modifications in the chemical composition, external factors such as the design features of tapping pipes and the casting design (position and size of risers, gates etc.) can also affect the service life of tapping pipes. For example, during solidification, the formation of shrinkage cavities can act as stress raisers leading to the eventual origin of cracks during service. Research endeavours may be made to address the effect of pipe design and casting design factors, which can further help in enhancing the service life of tapping pipes and similar types of hardware used in the Al industry.

APPENDIX A : THERMAL FATIGUE RESISTANCE OF GRAY AND DUCTILE CAST IRONS

Thermal fatigue often causes failure in applications including brake drums and rotors, ingot moulds, exhaust manifolds, cylinder heads of high performance diesel engines, moulds used for glass and pig iron castings. Selecting a cast iron for thermal cycling conditions is largely a matter of trial and error because resistance to thermal fatigue is a complex, extrinsic material property that depends on intrinsic properties such as thermal conductivity, thermal expansivity, modulus of elasticity and high temperature strength. Furthermore, cast irons have complex microstructures consisting of graphite in various shapes and a variety of matrix structures, which makes the selection of cast iron for a particular application under thermal fatigue difficult.

This appendix describes the various test apparatuses that were developed to assess the thermal fatigue resistance of cast irons for tapping pipe applications. Finally, the obtained results on the thermal fatigue resistance of candidate ferrous alloys are discussed. It is anticipated that the present research effort will provide another piece to the puzzle of the thermal fatigue resistance of cast irons.

A.1 Literature Review

A.1.1 Types of Thermal Fatigue Failures

It is important to know the type of failures that occur by thermal stresses. Cast iron components when subjected to temperature cycling may fail in the following ways:

a) Cracks first appear in the hot zone of the component and may eventually propagate through the section as observed in brittle materials like GCIs [1].
b) Severe distortion which ultimately renders the component useless. This type of failure is usually found in DCI components [1].

c) Gross cracking through the entire section during the first few cycles. These failures emanate from the mismatching of materials selected, improper design and random thermal cycling [1].

d) Lowering of the mechanical properties of materials owing to metallurgical variations such as microstructural changes and internal oxidation, which can lead to premature failure of the components [1].

A.1.2 Material Properties Affecting the Thermal Fatigue Resistance of Cast Irons

There are several material properties upon which the thermal fatigue resistance of cast irons depends. The most important of these are described as follows:

A.1.2.1 Thermal Diffusivity

The temperature gradient induced in a material depends upon the rate of distribution of heat, which is known as thermal diffusivity (k) and expressed as:

$$k = \frac{K}{\rho C_p} \tag{A.1}$$

where K is the thermal conductivity, ρ is the density and C_p the specific heat capacity.

k of metals usually decreases with temperature. For cast irons, k decreases by a factor of two when the shape of graphite is changed from flake-like to spherical, because in the case of GCIs, the dispersion of highly conductive graphite flakes provides easy pathways for heat flux leading to a higher K [2].

A.1.2.2 Thermal Expansion

Cast irons have a complex internal structure, typically a composite of carbon steel and graphite clusters of various types. The thermal expansion (α) of cast irons is much more complex than many other materials, because the volume fractions of ferrite, pearlite, austenite and graphite changes during heating. This change in volume fraction primarily depends upon

the increase in the C content of ferrite and austenite during heating. The change in C content causes a lattice expansion, which also influences α. It is assumed that graphite loses contact with the iron matrix owing to the lower density of graphite relative to cast iron. The iron can now be considered to contain pores instead of graphite, and the thermal expansion can compared to that of steel. In addition, C content in austenite increases with temperature. The austenite lattice expands with the increasing C content and the expansion thus consists of two parts (a) thermal expansion and (b) austenite expansion [2].

A.1.2.3 Elastic Modulus and Strength

The low elastic modulus (E) of a material means a temperature gradient (ΔT) will create stresses (σ) of low magnitude (Equation A.2) [3]. In general, a material with high E and high α is assumed to have low resistance to thermal fatigue, but at the same time it may have an adequate strength.

$$\sigma = E\alpha\Delta T \qquad \text{(A.2)}$$

It is shown that E and α are lower and k is higher for a cast iron with flake graphite as opposed to compacted or spheroidal morphologies. Thus, GCIs are believed to possess a higher fatigue resistance than CGIs or DCIs [1].

A.1.2.4 Oxidation and Phase Transformations

DCIs appear to be more suitable for use at higher temperatures because they are more oxidation resistant than GCIs and because a ferritic grade can be used to overcome the problem associated with pearlite decomposition. The oxidation rate at the surface of DCI is about the same as that of GCIs of similar Si content; however, the internal oxidation is negligible [1].

The ferrite to austenite transformation temperature is largely a function of Si content, and generally lies between 700^{o}C and 900^{o}C. Thermal cycling of cast irons in this temperature

region causes partial or complete austenization and retransformation to a new structure takes place depending upon the cooling rate [1].

A.1.2.5 Growth

When cast irons are subjected to prolonged periods of continuous or cyclic heating, they have a tendency to swell, which may occur due to factors such as the decomposition of carbides, structural change of pearlite to ferrite and graphitization. Growth can be reduced either by producing a ferritic matrix with no pearlite or by stabilizing the carbides so as to prevent their breakdown into ferrite and graphite [1].

A.1.2.6 Creep

Creep is primarily important where the component is constrained, implying that the component is not free to expand or contract under thermal loading. However, these constraints may be external or internal depending upon the component design and prevailing service conditions. During alternating heating and cooling cycles, materials creep under the effect of induced compressive and tensile stresses. Under constrained specimen tests, the GCIs with greatest resistance to creep were found to be most resistant to thermal cycling [4].

A.1.3 Thermal Fatigue Resistance of Cast Irons

For a particular service application, suitability of a cast iron depends upon several factors as discussed in previous sections. In cast irons, strength, E and K are closely interrelated owing to their dependence on graphite flake size and morphology. Higher graphite content in GCIs increases K, decreases E and reduces strength. For example, a pearlitic GCI with A-type graphite has good K and low E but comparatively low strength. On the downside, the pearlitic GCIs have limited structural stability and low resistance to oxidation. However, they are economically attractive, so the bulk of cast irons used under thermal cycling conditions

are in fact GCIs [1]. As mentioned before, ferritic DCIs are structurally stable and almost immune to internal oxidation. Drawbacks are high E, low K and a higher cost than GCIs [1].

The literature on the thermal fatigue of gray and DCIs comprises several investigations, which were carried out using a variety of thermal fatigue test methods, thermal cycling conditions, specimen geometry and microstructures of cast irons. The majority of studies were focused upon the thermal fatigue resistance of GCIs only [1, 4, 5-6], and only a few studies considered the DCIs [1, 6]. Table A.1 summarizes the results obtained by various researchers and are arranged in descending order of thermal fatigue resistance of the cast irons. This review of the literature demonstrates the lack of information available for selecting a type of cast iron for a particular application under thermal fatigue.

a) Rukadikar and Reddy [5] found that the thermal fatigue resistance of GCIs largely depends upon graphite morphology, degree of pearlite refinement and chemical composition. High C cast irons were found to have superior thermal fatigue resistance and alloy additions such as Mo, Mo+Cr and Cr+3 wt.% Cu imparted good thermal fatigue resistance to GCIs.

b) Roehrig [1] found that in the temperature range of 590°C-200°C, alloying with Mo and Cr improves performance. In the temperature range of 690°C-240°C, DCIs outperformed the GCIs, while the compacted graphite irons exhibited intermediate thermal fatigue resistance between GCIs and DCIs.

c) Shea [6] found that an unalloyed DCI having 3.62 wt.% C and 2.64 wt.% Si exhibited the best thermal fatigue resistance followed by a GCI alloyed with Cr, Mo and Sn. Thermal resistance of a GCI containing Cr, Mo and Al was found to be very poor. Shea concluded that graphite morphology has a greater effect on the thermal fatigue resistance than the matrix microstructure.

d) Gundlach [4] found that a low C (3.2 wt.% C) GCI with Mo and Cr alloying elements showed superior thermal fatigue resistance compared to the cast irons with higher C contents. It was concluded that thermal fatigue was very much dependent on the resistance to creep and, to a lesser extent, on the tensile strength.

Table A.1 - Summary of the literature on the thermal fatigue resistance of cast irons.

Test conditions	Alloys under test (In descending order of thermal fatigue resistance)								Results
	Type	Composition Wt.% (Balance Fe)							Cycles to first major crack
		C	Si	Mn	Mo	Cr	Cu	Others	
Rukadikar and Reddy [5]	GCI	3.93	1.06	0.7	1.0	--	--	--	40
T_{max}= 700°C		3.00	1.98	0.7	0.3	0.7	--	--	40
T_{min} = 40°C		3.93	1.06	0.7	--	1.0	3.1	--	39
Disc with a central hole.		3.00	1.98	0.7	1.0	--	--	--	36
Molten salt heating-water		3.93	1.06	0.7	0.3	0.72	--	--	32
cooled		3.93	1.06	0.7	--	--	--	--	30
Roehrig [1]	GCI	3.40	1.66	0.58	0.4	0.50	--	--	1550
T_{max}= 590°C		3.45	1.68	0.63	0.3	0.30	0.87	0.97Ni	1475
T_{min} = 200°C		3.44	1.69	0.58	0.3	0.21	0.30	0.77Ni	1325
Disc with a central hole		3.45	1.74	0.59	--	0.49	0.59	0.6 Ni	1075
Cycled in fluidized bed		3.43	1.65	0.60	--	--	--	--	925
alumina									
Roehrig [1]	DCI	3.7	2.17	--	--	--	--	--	800
T_{max}= 690°C		3.7	2.17	--	0.2	--	--	--	800
T_{min} = 240°C	CGI*	3.7	1.80	--	0.4	0.20	--	--	510
Disc with a central hole		3.7	1.80	--	--	0.20	--	--	460
Cycled in fluidized bed		3.7	1.80	--	--	0.20	--	--	380
alumina		3.7	1.80	--	0.5	0.20	--	--	380
	GCI	3.7	2.17	--	0.2	0.26	--	--	370
		3.84	1.65	--	--	0.15	--	--	220
Shea [6]	Steel	0.84	2.06	0.66	0.2	0.29	--	--	180
T_{max}= 850°C	DCI	3.62	2.64	0.48	--	--	--	--	50
T_{min} = 65°C	GCI	3.93	2.37	0.78	0.3	0.22	--	0.21Sn	22
Disc shape specimens		3.49	2.37	0.84	0.2	0.24	--	--	12
Induction heating-water		3.48	0.60	0.88	0.2	0.23	--	2.37Al	5
cooled		3.50	2.38	0.83	0.7	0.30	1.51	--	5

Test conditions	Type	Composition Wt. % (Balance Fe)							Results
		C	Si	Mn	Mo	Cr	Cu	Other	
Gundlach [4]	GCI	3.26	1.56	0.63	0.76	0.20	0.10	0.11Ni	511[#]
T_{max}= 540°C		3.40	1.76	0.65	0.48	0.31	0.11	0.11Ni	288[#]
T_{min} = 100°C		3.43	1.66	0.58	0.39	0.50	0.12	0.1Ni	221[#]
Test bar with ends fixed.		3.44	1.69	0.58	0.38	0.21	0.30	0.1Ni	178[#]
Induction heating-water cooled		3.45	1.68	0.63	0.30	0.30	0.87	0.97Ni	139[#]
		3.44	1.74	0.76	--	0.12	1.48	0.3V	124[#]
		3.45	1.74	0.59	--	0.49	0.59	0.6Ni	78[#]
		3.43	1.65	0.57	--	0.11	--	0.1 Ni	51[#]
		3.39	1.75	0.64	--	0.30	0.11	0.1Ni	48[#]

[*]Compacted graphite iron, [#] number of cycles to fracture

According to Roehrig [1], where low cooling rates exist, high strength pearlitic GCIs or DCIs alloyed with Si and Mo are best with regard to resistance to cracking and distortion. GCIs with high graphite content give the best performance in the conditions where rapid cooling and heating cause severe thermal gradients within the component. It was suggested that increasing the C content up to 4 wt.% can be advantageous. Where medium cooling rates exist, ferritic ductile and compacted graphite irons have the highest resistance to cracking [1].

The majority of the studies described above were carried out under a maximum cycle temperature of 700°C. However, in the present application, tapping pipes are frequently exposed to flowing liquid Al at temperatures of up to 950°C. Considering the service conditions of tapping pipes, only a few thermal fatigue studies were found in which cast irons were subjected to such a high temperature (> 900°C):

a) Chou *et al.* [7] compared the thermal fatigue resistance of CGI and GCI for the cast iron moulds used for pig iron casting, (for compositional details see Table A.2). The higher temperature of the mould surface was found to reach between 850°C-1000°C and after pouring the molten pig iron, the outer surface of the mould was cooled by water spray to

accelerate the removal of the pig iron casting. Laboratory and field trials were performed to judge the performance of the two types of cast irons.

Table A.2 - Compositions and test results of cast irons under investigation [7].

Cast Irons	Chemical composition (Wt.%)						Cycles to failure
	C	Si	Mn	P	S	Mg *	
GCI	3.93	2.29	0.56	0.085	0.011	--	> 500
CGI	3.4	2.95	0.57	0.031	0.016	0.023	223

*Balance Fe

The laboratory test consisted of partial immersion of machined rectangular (50 mm x 80 mm x 150 mm) blocks into a salt bath at 1000°C for 4.5 minutes, followed by submersion in water. The thermal fatigue resistance was compared by the summation of crack length, which showed the superiority of GCI over the CGI. In field tests where the cast iron moulds were mounted in a pig iron casting machine, the CGI failed after 223 cycles, while the GCI survived even after 500 cycles. The hot face region of the CGI contained much more martensite than the GCI. The inferior thermal fatigue of CGI compared to the GCI was mainly attributed to the excessive martensite formation after the thermal fatigue cycles.

b) In another investigation, Lee and Lee [8] studied the thermal fatigue of GCI, DCI and CGI. Cast moulds of various compositions of these alloys were mounted in a pig iron casting machine. The failure of the mould was judged by the cracking of the mould that led to leakage of molten iron. Table A.3 contains the best alloys in each category of cast irons. The CGI showed substantially better thermal fatigue resistance compared to GCI, which is in contradiction to the previous results of Chou et al. [7] where the thermal fatigue trials were carried out under similar test conditions. Therefore, no conclusive remarks can be drawn from the literature about the type of cast iron most suitable for service under such industrial conditions. Both investigations included only unalloyed cast

irons, and it is possible that the thermal fatigue resistance of each type of cast iron could be improved by alloying.

Table A.3 - Compositions and test results of cast irons under investigation [8].

Cast irons	Chemical composition (Wt.%)						Cycles to failure
	C	Si	Mn	P	S	Mg *	
CGI	3.59	2.53	0.16	0.010	0.002	0.009	5000
DCI	3.50	2.40	0.31	0.015	0.009	0.035	2031
GCI	3.11	2.24	0.49	0.027	0.019	---	1519

*Balance Fe

A.1.4 Evaluation of Thermal Fatigue Resistance

Mathematical relationships have been developed [9-12] to calculate the thermal stress and to compare the thermal fatigue resistance of materials. According to a basic relationship [9], the thermal stress induced in a component can be given by:

$$\sigma = [(E\alpha\Delta T)/(1-\nu)]F \quad (A.3)$$

where ν is Poisson's ratio and F is the geometry factor. Equation A.3 suggests that the thermal stress is proportional to α, E, ΔT. Furthermore, ΔT is inversely proportional to k of a material.

Various relationships, Equation A.4, Equation A.5 and Equation A.6 have been proposed to compare the thermal fatigue of materials by calculating thermal fatigue index (R_1, R_2, R_3); a higher value of a thermal fatigue index indicates a better thermal fatigue resistance of a material.

a) Radon *et. al* [10]

$$R_1 = \frac{(1-\nu)K}{\alpha E} \quad (A.4)$$

b) Hasselman [11]

$$R_2 = \frac{(1-\nu)K(TS)}{\alpha E} \tag{A.5}$$

c) Lee and Chen [12]

$$R_3 = \frac{(1-\nu)K(TS)^{1/2}(BHN)^2 K_{IC}^{1/2}}{\alpha E} \tag{A.6}$$

where TS is tensile strength, BHN is Brinell hardness value and K_{IC} is the fracture toughness.

Considering the equations above, various researchers (for example [13]) have obtained controversial results with respect to the service life of cast irons used in different environments. Literature on the thermal fatigue of cast irons indicates that there is a complex interaction between the mechanical properties, maximum test temperature, and heating and cooling conditions. The material properties vary with temperature, and the actual values at operating temperature should be considered while evaluating the thermal fatigue resistance. Moreover, the data concerning each of these properties for a range of cast iron compositions at a range of elevated temperatures (600°C-1000°C) is difficult to obtain. In fact, the available literature is only limited to 600°C [14]. For this reason, it is difficult to evaluate theoretically the thermal fatigue resistance of cast irons for a particular application.

A.2 Service Conditions

The periodic flow of liquid Al (at about 950°C) through the tapping pipes creates an irregular temperature distribution in circumferential, longitudinal and radial directions resulting in differential expansion, which therefore induces complex stress conditions. Moreover, the thermal stress conditions could become more severe when liquid Al contacts the regions along the pipe where the bath is unable to solidify, details are found in Chapter 1. As a general consideration, the pipe sections at lower temperatures remain in tension, and hot

zones experience compression. Consequently, hot zones experience creep in compression and the cold sections experience creep in tension. After cooling of a section, stresses are reversed. As a result, a dimensional discrepancy exists, which can still be absorbed by creep, but may eventually lead to the progressive opening of cracks.

A.3 Experimental Methods and Materials

A.3.1 Materials

The thermal fatigue tests were performed after comparing the Series-I ferrous alloys for their liquid Al corrosion resistance. Compared to cast irons, the literature shows that steels possess higher strength [14] and better thermal fatigue resistance [6]. However, since corrosion and cost were emphasized, only the GCIs and DCIs were tested under thermal fatigue. Out of the six alloys tested for liquid Al corrosion, only two alloys with better liquid Al corrosion resistance from each category of cast irons were compared under thermal fatigue. For a quick reference, the compositions of cast irons are listed in Table A.4.

Table A.4 - Chemical compositions (wt.%) of cast irons tested for thermal fatigue.

Alloy	C	Si	Mn	Cr	Cu	Mo	S	P	Mg *
GCI-A	3.75	1.90	0.4	0.37	0.98	0.00	0.03	0.02	0.00
GCI-S	3.06	1.73	0.91	0.54	0.00	0.57	0.01	0.02	0.00
DCI-D	3.54	3.35	0.21	0.18	0.87	0.03	0.00	0.04	0.06
DCI-T	3.29	2.19	0.29	0.01	0.26	0.03	0.00	0.01	0.04

*Balance Fe

A.3.2 Test Methods

A.3.2.1 Test Method with Similar Stress Conditions to Industrial Application

For producing similar stress conditions to tapping pipes, a specialized thermal fatigue test apparatus (Figure A.1) was developed to achieve the thermal stresses similar to actual service conditions.

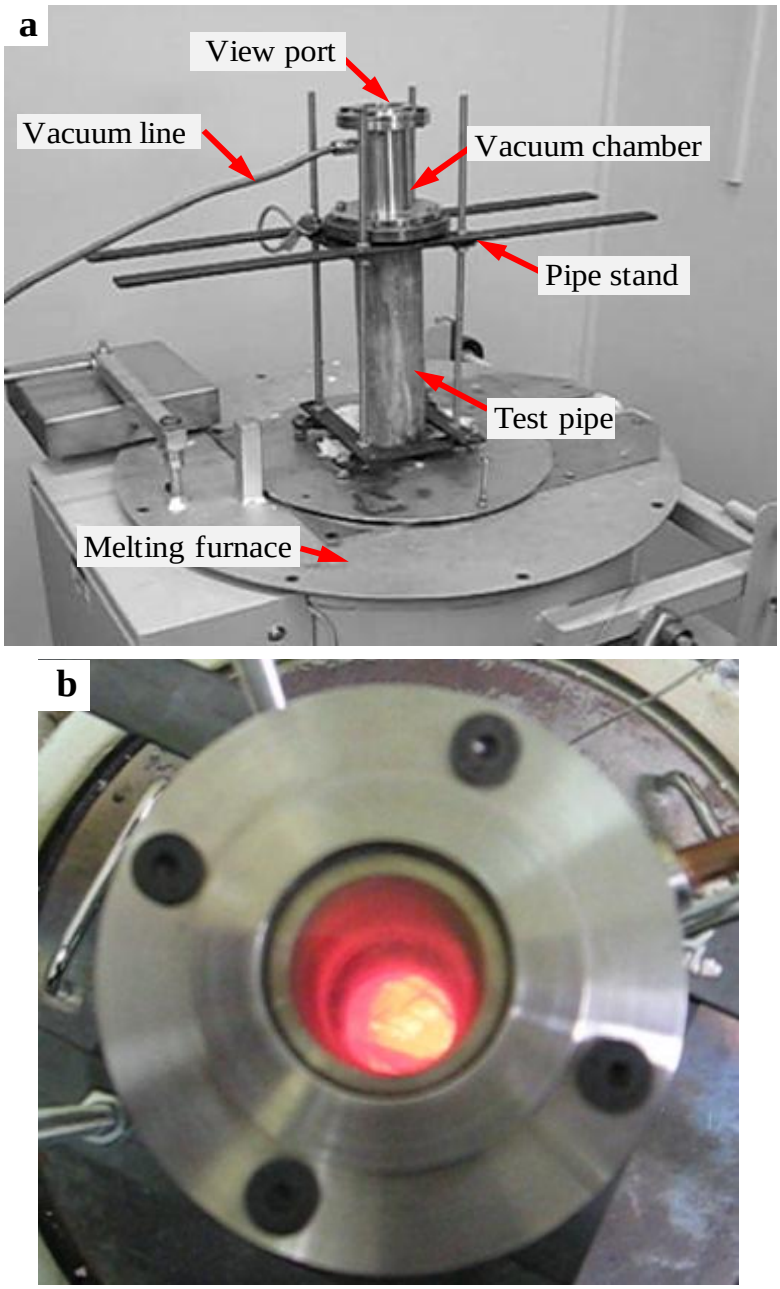

Figure A.1 - a) Thermal fatigue test apparatus, b) a view of rising liquid Al inside the test pipe.

Test pipes of 450 mm length, 70 mm outer diameter and with 15 mm wall thickness were cast to compare the thermal fatigue resistance of candidate materials. In this apparatus, liquid Al is drawn inside a test pipe to a specified height by applying a vacuum for a specific period of time and over a specified number of cycles. A specialized apparatus (Figure A.2) was designed and built to control the vacuum inside the test pipes.

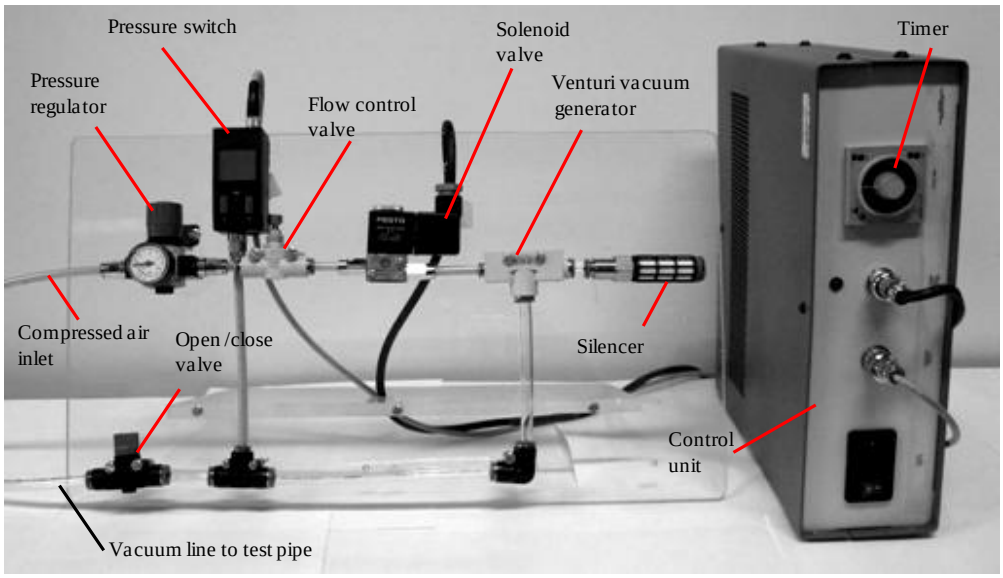

Figure A.2 - Automated vacuum control apparatus.

The pressure regulator and flow control valve control the magnitude of the vacuum being produced. The pressure switch acts as a vacuum sensor and a safety cut off. If the liquid Al crosses its maximum level in the pipe, the pressure switch sends a signal to the control unit to cut-off the vacuum. A viewing hub was incorporated through which the rising liquid Al was observed in order to set the experimental parameters. This apparatus was found to be successful in consistently cycling the liquid Al through the test pipes. For testing, liquid Al was maintained at 950 ± 10°C; and the melt temperature after each cycle was dropped to 860 ± 10°C. Each thermal cycle comprised 12s for maintaining the liquid Al inside the test pipe and 600s for heating the melt in the furnace. The thermal fatigue set up with thermocouple locations and temperature data is shown in Figure A.3 and Figure A.4, respectively.

GCI-A pipe was tested for a total of 70 hours (410 cycles) spanning 7 days. After the test, the pipe was visually inspected. No cracks were found throughout the pipe section; however, shortening of the pipe length (by 3.5 cm) was observed due to the corrosion caused by the cyclic flow of liquid Al.

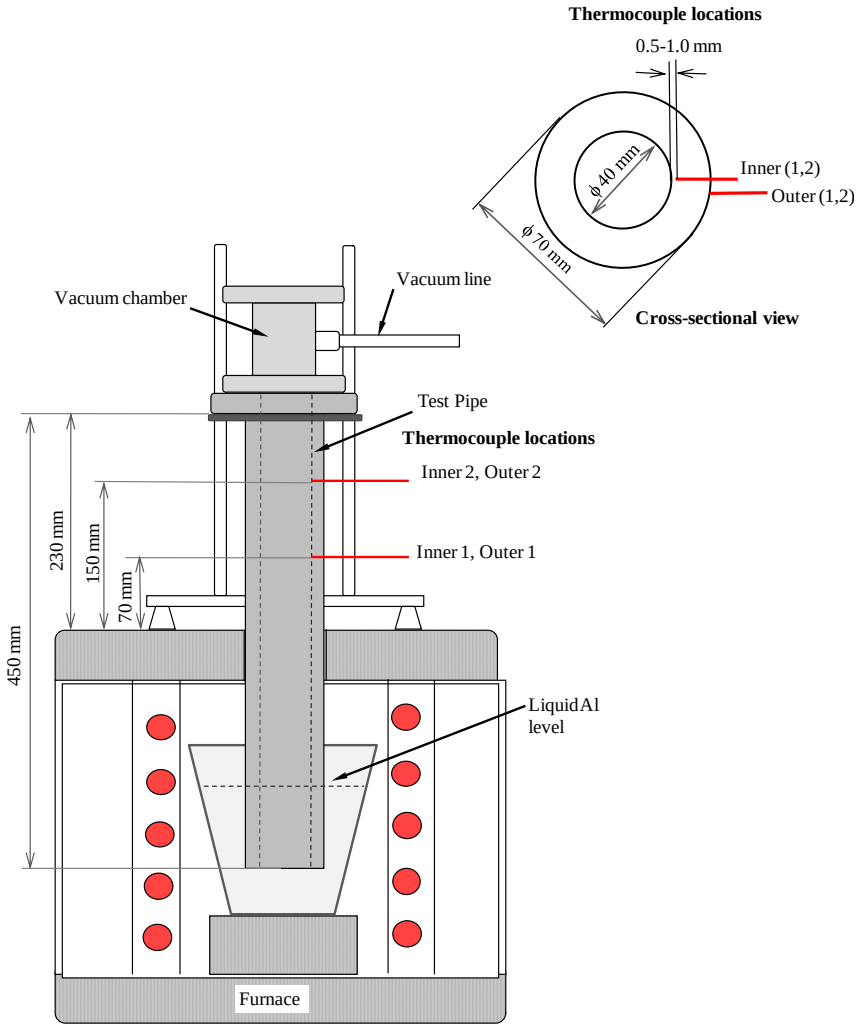

Figure A.3 - A schematic showing the thermocouple positions on the test pipe cross-section for temperature data logging.

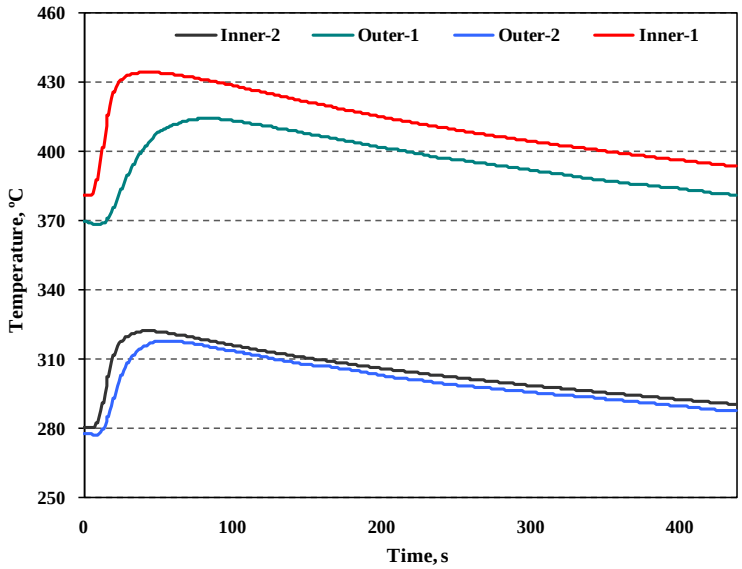

Figure A.4 - Temperature versus time profile for the thermocouple locations shown in Figure A.3.

The shortening of the pipe length with further cycling was found to be a constraint on testing for longer time durations. The limitation of not achieving the expected service temperatures was found to be the major reason behind the unsuccessful implementation of this test apparatus.

A.3.2.2 Alternate Test Methods

Two alternate test methods were developed to subject the cast iron alloys to variable heating and cooling rates to access their resistance to failure by thermal fatigue. Unfortunately, these test methods could not reproduce the thermal stress conditions of tapping pipes. In the first test method, cylindrical pipe specimens were mainly subjected to radial thermal gradients (Test method-I). While in the second set up, the specimens were subjected to non-uniform radial and circumferential temperature gradients (Test method-II). The thermal stress conditions of the Test method-I and Test method-II were designated as TSC-I and TSC-II, respectively. The geometry of the test piece should resemble the component in actual service for a good simulation of the stress condition [4]. Therefore, cylindrical pipe specimens were machined from as-cast pipes (dimensions D_o = 70 mm, D_i = 40 mm, L = 450 mm) of cast irons. Figure A.5 shows a photograph of a test specimen with labelled dimensions. Specimens of same geometry were used for both of the test methods. Table A.5 shows the summary of the thermal fatigue test methods.

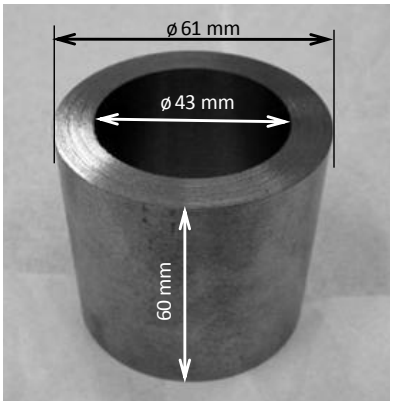

Figure A.5 - Specimen for the thermal fatigue comparison of cast iron alloys.

Table A.5- Summary of the Test Method-I and Test Method-II.

	Cycle temperature °C		Heating method	Cooling method	Specimen movement
	T_{max}	T_{min}			
Test Method-I	950	120	Electric resistance furnace maintained at 1070°C	Water spray at the entire outer surface	Manual
Test method-II	900	500	Electric resistance furnace maintained at 920°C	Air jet at a localized position	Automated

A.3.2.2.1 Test Method-I

The hot specimen was quenched by water spray on the outer surface in the apparatus shown in Figure A.6. This comprised nine water sprayers, which were connected to the water supply under controlled pressure (0.4 bar), and the flow was maintained at 2.2 litres/minute. The entire outer specimen surface was sprayed with water at 18-20°C, while the inner surface remained at a higher temperature.

A typical thermal heating cycle was approximately 400s long, which included heating for 330s followed by quenching for 40s and then placing the specimen in ambient air for 20s to dry the moisture. Temperature was measured by two K-type thermocouples of 1 mm diameter placed into holes drilled (1.1 mm diameter). Figure A.7 shows the thermocouple locations, and Figure A.8 shows the time-temperature logging of the thermal cycles.

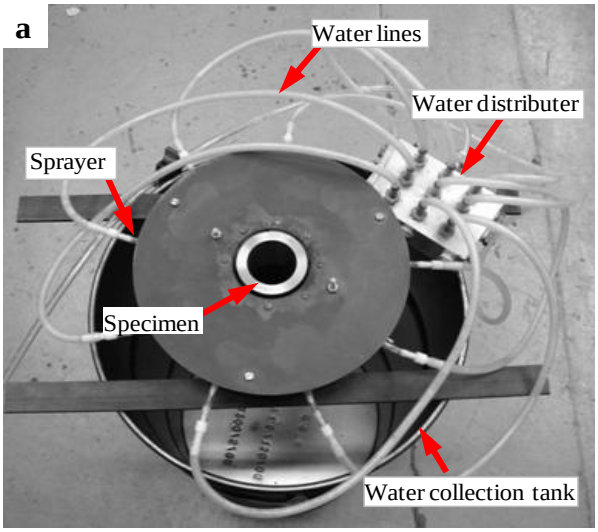

Figure A.6 - Test Method -I thermal fatigue test apparatus.

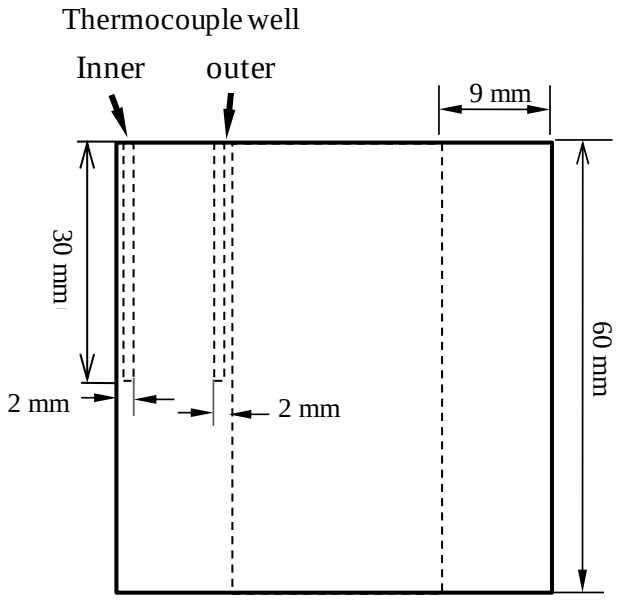

Figure A.7 - Thermocouple locations on the specimen cross-section for temperature data logging.

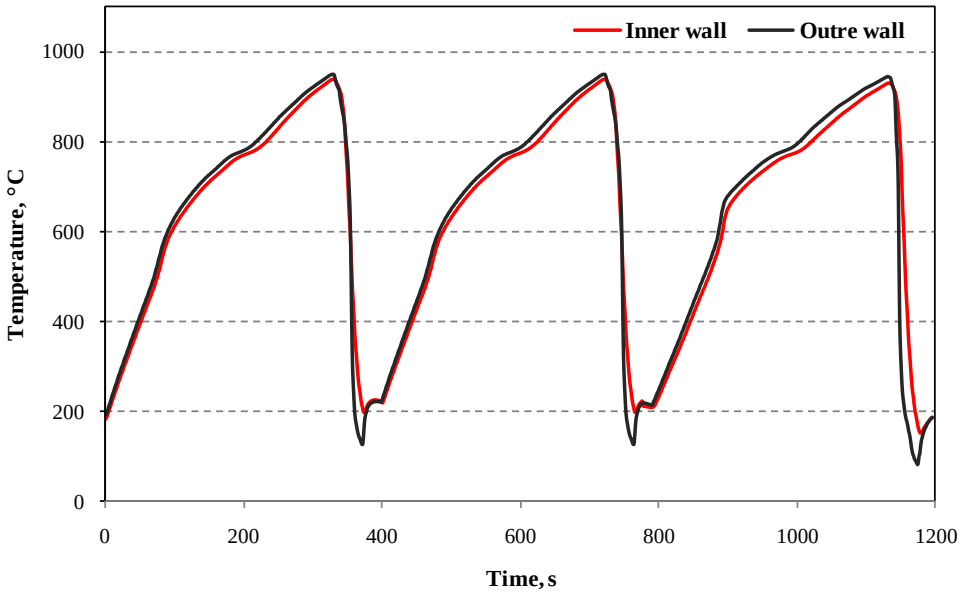

Figure A.8 - Thermal cycle logging for the thermocouple locations shown in Figure A.7.

The average heating rate at the outer specimen surface was found to be 2.5°C/s, and the average cooling rate was 13.8°C/s. Each specimen was subjected to 45 thermal cycles. Specimens were inspected after the initial 15 cycles and then after 10 cycle increments. At each inspection, the oxide layer (0.2 - 0.5 mm thick) was removed from the specimen surface by grinding with 240 and 600 grit SiC papers in order to reveal the cracks. In addition, the

removal of the oxide layer helps to minimize its effect on the cooling rate for different alloys under investigation, because the GCIs are more susceptible to oxidation compared to DCIs.

A.3.2.2.2 Test Method-II

A specialized apparatus (Figure A.9) was designed and built to achieve the TSC-II conditions. In this apparatus for continuous cycling for longer times, the test specimens were moved pneumatically. An air cylinder was operated by a solenoid valve, which was controlled by an automated timer. The control apparatus was used for automation with a few modifications compared to the thermal fatigue apparatus consisting cycling of liquid Al cycling through the test pipes.

To maintain the inner surface of the specimens at a higher temperature, specimens were filled with loosely heaped sand and sealed with FIBERFRAX® paste. Considering the large amount of oxidation of cast irons, which occurred at 950°C (Test method-I), the maximum cycle temperature was limited to 900°C.

The outer surface of the specimen was cooled by means of a compressed air jet (4 mm diameter) at a constant pressure of 4 bar. Figure A.10 and Figure A.11 show the positions of the thermocouples and cooling air jet. The total cycle time was 360s, which included 300s for heating, 50s of cooling and 10s for specimen movement. For temperature data logging, three K-type thermocouples (1 mm) were used (Figure A.10). Figure A.12 shows the time-temperature profiles. The outer specimen surface (cooling side) was subjected to an average heating rate of 1.3°C/s and a cooling rate of 8.1°C/s.

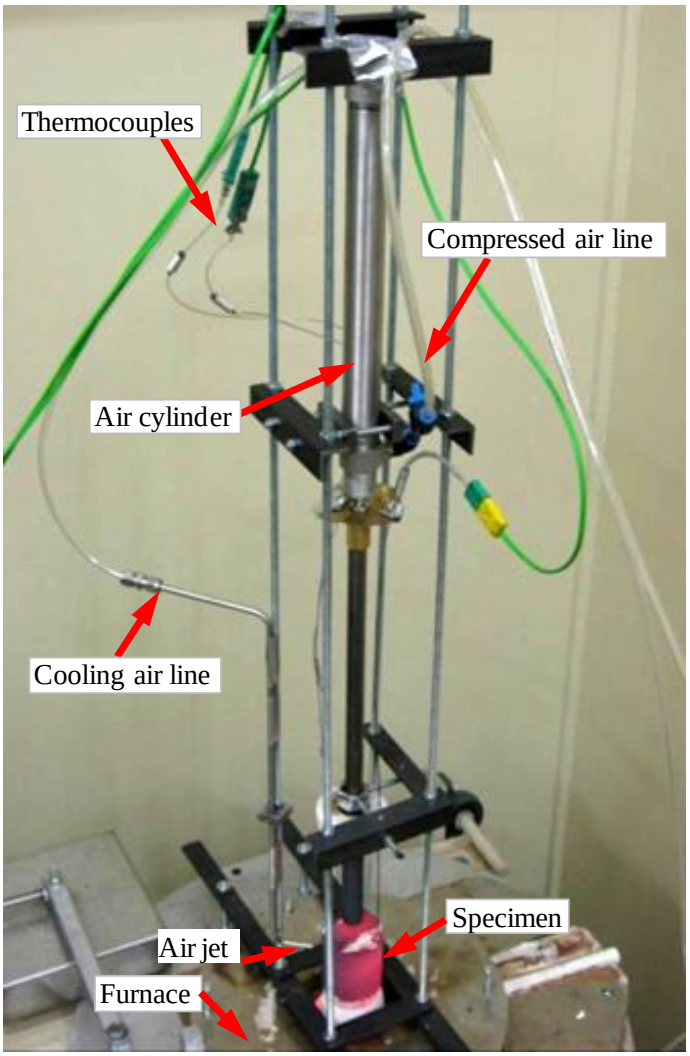

Figure A.9 - Thermal fatigue test apparatus-II.

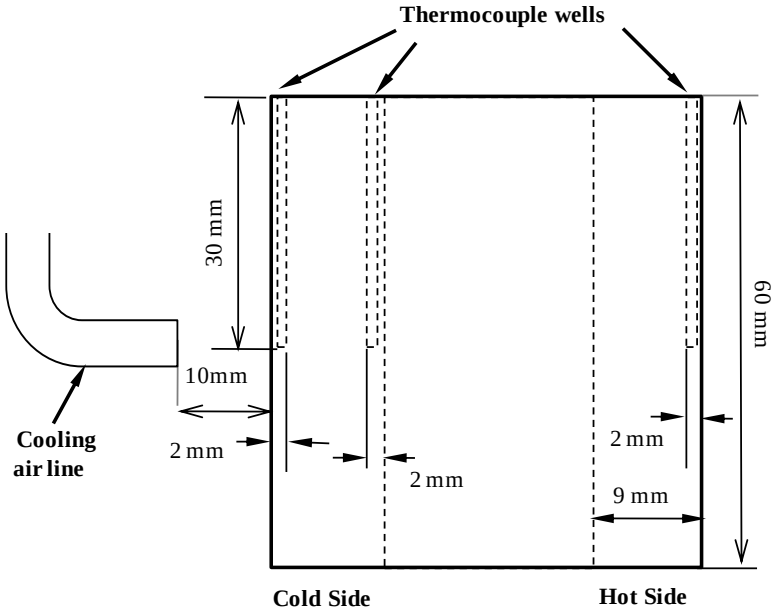

Figure A.10 - A schematic of thermocouple locations for temperature data logging.

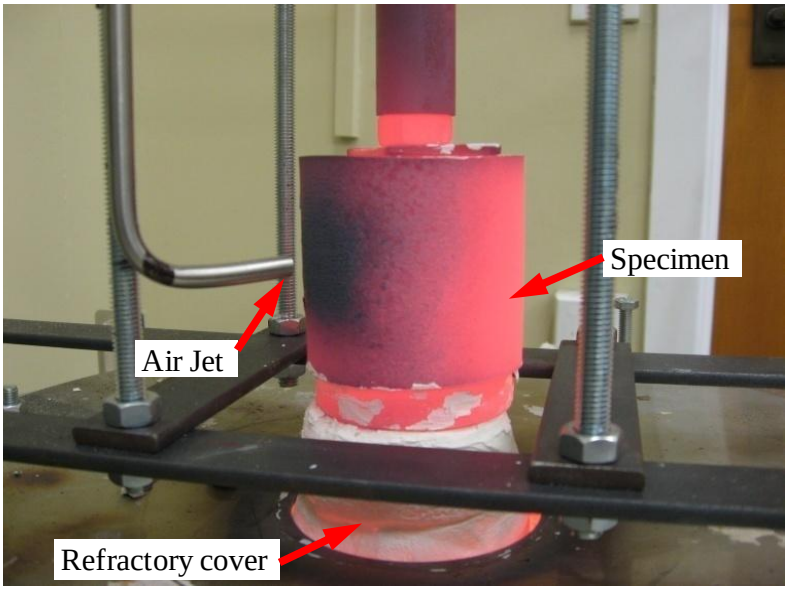

Figure A.11 - A closer view of a thermal fatigue specimen during a test.

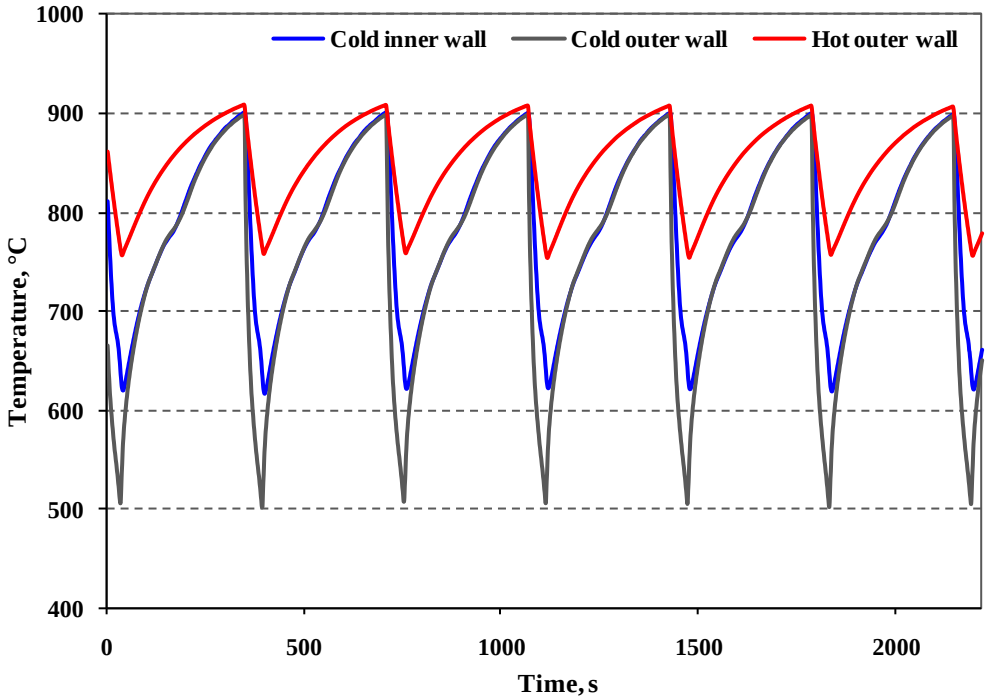

Figure A.12 - Time-temperature profiles at three different locations on the specimen section shown in Figure A.10.

A.4 Results and Discussion

A.4.1 Test Method- I

Cast iron alloys GCI-A, GCI-S, DCI-D and DCI-T showed differing behaviour under thermal fatigue cycling. Figure A.13 and Figure A.14 show GCI and DCI specimens, respectively,

after 45 thermal cycles. Images on the left show the bottom face of the specimens and on the right optical stereo-micrographs show examples of typical crack patterns.

GCI-A showed the initiation of several cracks on the inner corner of the bottom face, while no cracks were found on its outer cylindrical surface. Moreover, an inter-connected crack network (commonly known as “craze cracks”) was found on the inner surface of GCI-A. The GCI-S specimen exhibited no cracks on its bottom face, while only two minor cracks were found on its outer cylindrical surface.

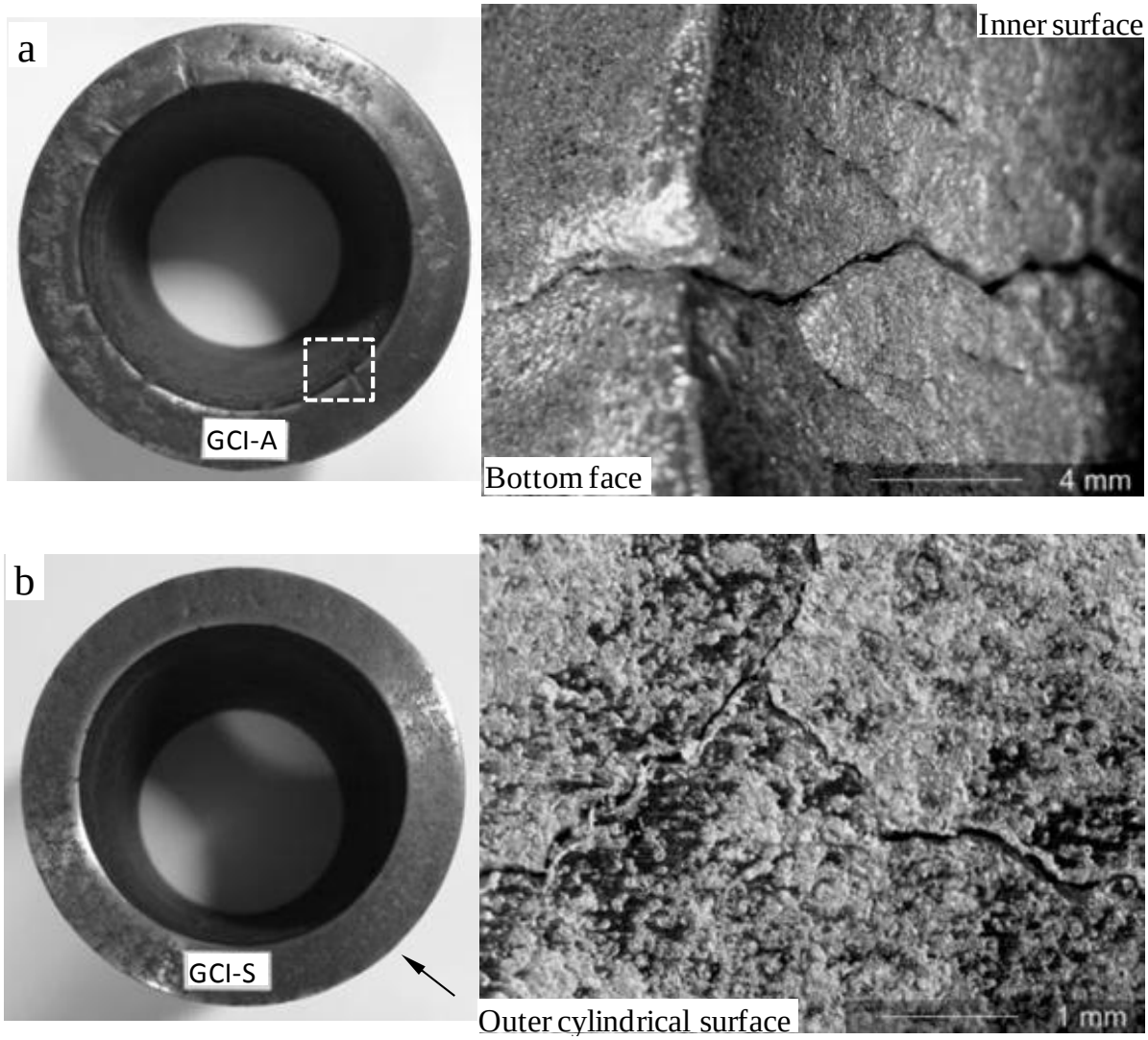

Figure A.13 - Bottom faces of GCI specimens and optical stereo-micrographs of crack patterns after 45 thermal cycles, a) GCI-A, b) GCI-S.

The DCI-D specimen showed the least amount of surface oxidation and also no cracking at its bottom face; however, a number of minor cracks were found on its outer cylindrical surface distributed around its diameter and located approximately midway along the specimen height.

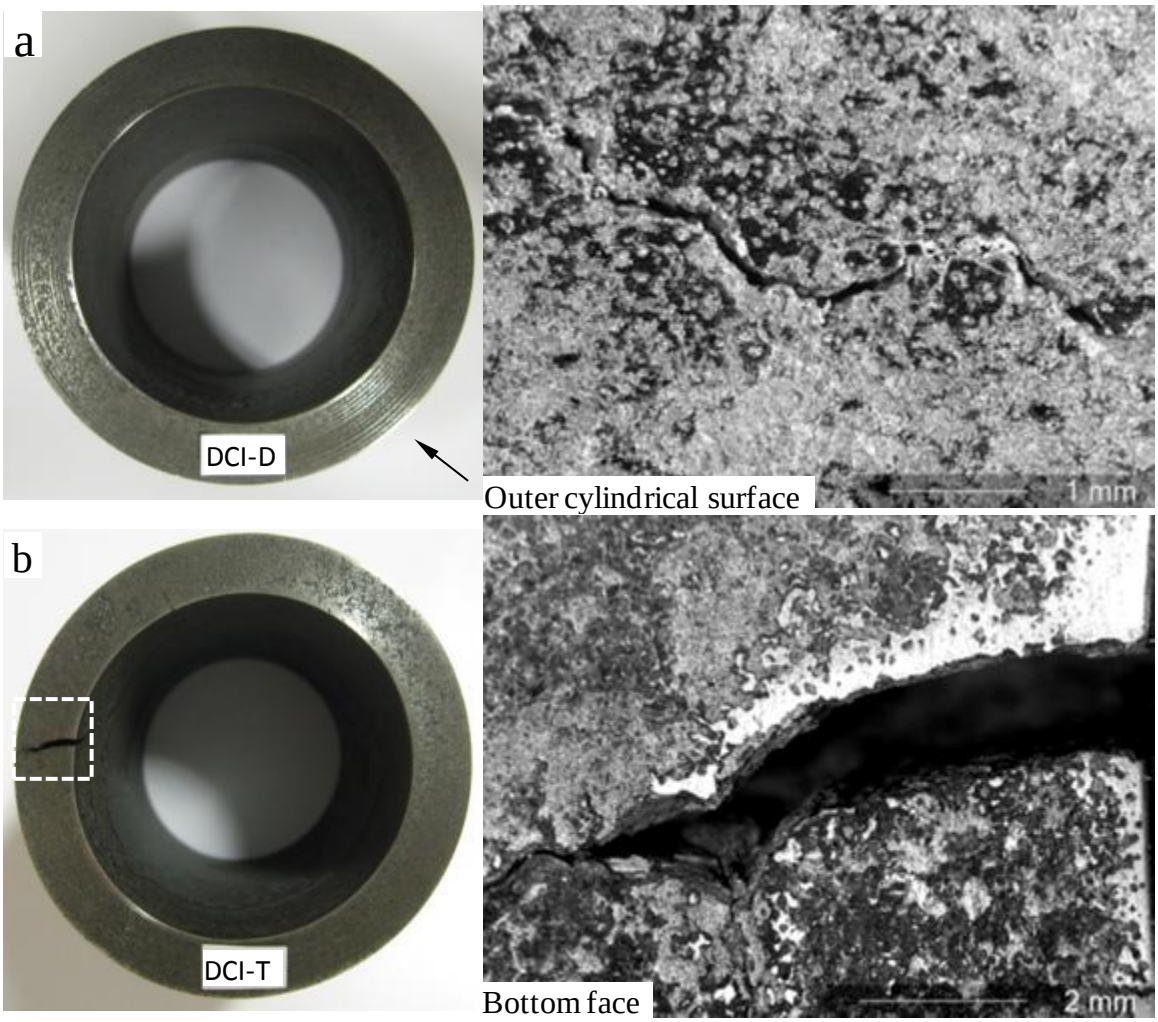

Figure A.14 - Cast iron specimens and crack patterns after 45 thermal cycles, a) DCI-D, b) DCI-T.

In the case of DCI-T, a major crack opening on the bottom inner corner can be seen in Figure A.14 (b), while only one minor crack was found on its outer surface.

The thermal fatigue resistance of these materials was compared in terms of the total surface crack area, which was evaluated from the following relationship:

$$\sum C_a = \sum C_l C_w \qquad (A.7)$$

where C_a is the crack area, C_l is the crack length and C_w is the maximum width of the crack. Table A.6 shows the obtained results.

Table A.6 - Measured total crack area after 45 thermal cycles.

Location of cracks	Total crack area, mm^2 (number of cracks)			
	GCI-A	GCI-S	DCI-T	DCI-D
Bottom face	22 (8)	Nil	11(2)	Nil
Outer cylindrical surface	Nil	1.2(2)	1.5(1)	12.4(17)
Inner cylindrical surface	craze cracks	Nil	Nil	Nil
Total crack area ($\sum C_a$)	>>22	1.2	12.5	12.4

GCI-S has demonstrated the best fatigue thermal fatigue resistance of all cast irons under investigation. The thermal fatigue resistance of DCI-D and DCI-T was found to be between GCI-S and GCI-A. However, DCI-D and DCI-T showed different modes of failure under thermal fatigue.

When the outer surface of the hot specimen is quickly cooled by the water spray, it tends to arrest its shape in an expanded state. Under such conditions, the outer part of the cylindrical specimen being at a low temperature has higher strength and tends to deform the high temperature inner material in each thermal cycle. It has been observed that during cooling some part (height) of each specimen was remained above (~ 5 mm) the water spray area. Therefore, compared to the top section of the specimen, the bottom section experienced faster cooling. Thus, the bottom diameter of each specimen experienced a greater increase in dimension compared to the top diameter.

The change in specimen dimensions after thermal cycling is commonly known as distortion. In the present case, distortion (Δ_D) of test specimens was determined in-terms of change in outer bottom diameter:

$$\Delta_D = \left(\frac{D_f - D_i}{D_i} \right) 100 \qquad \text{(A.8)}$$

where D_f is the outer bottom diameter after thermal cycling and D_i the initial outer bottom diameter.

Figure A.15 shows the relationship between the number of thermal cycles and the extent of distortion in the outer bottom diameter. The GCIs showed significantly lower distortion than DCIs. GCI-S exhibited a minimum distortion among the cast irons tested, showing a significant change in dimensions in the first 15 cycles only. GCI-A distorted by a substantially greater extent compared to GCI-S. DCI-T showed the highest distortion of all the cast irons under investigation, closely followed by DCI-D.

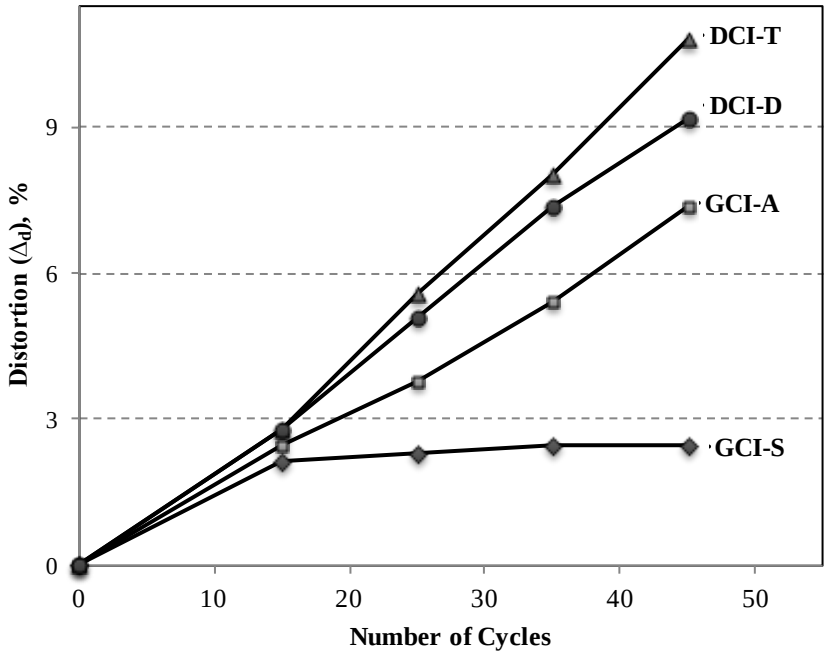

Figure A.15 - Distortion of the bottom diameter of specimens versus the number of thermal cycles.

GCI-S showed the best resistance to cracking and also exhibited the least distortion of the cast irons under investigation. However, different alloys of cast irons showed different modes of failure, such as craze cracking in GCI-A, distortion and one major crack in DCI-T.

GCI-S is alloyed with Cr and Mo. GCI-A has higher C content than GCI-S, and is alloyed with Cu and Cr (Table A.4). There is general agreement that higher C content improves the thermal fatigue resistance of GCIs [1]. However, this finding is based upon the results of thermal fatigue investigations at maximum cycle temperatures < 750°C. The GCIs with higher C content are less resistant to oxidation and grow at a higher rate. Also, Lee and Lee [8] compared the thermal fatigue resistance of various alloys of GCIs under a pig iron casting environment and found that the thermal fatigue resistance of GCIs decreases with increasing C contents. Possibly, in GCI-A, oxidation occurring along the graphite flakes caused progressive opening of cracks, which resulted in its inferior thermal fatigue resistance. It is also well known that the addition of Mo and Cr reduces growth, improves the oxidation resistance, creep strength and tensile strength of GCI [1]. Therefore, in addition to being lower in C, GCI-S has the advantage of Cr and Mo additions.

Thermal fatigue resistance of DCI-D and DCI-T falls between those of GCI-A and GCI-S. DCI-D showed a number of minor cracks on the outer surface, and DCI-T showed progressive opening of cracks at the specimen corner, where the stress concentration should be the highest. The DCIs have low K compared to GCIs; however, they possess higher E and ductility. Under the application of the thermal gradient, the bulk of the specimen deforms owing to good ductility and higher E, leading to stress build up at sharp corners which have lower strength. Therefore, at the regions of stress concentration, the thermal fatigue resistance of DCIs can be adversely affected.

Thermal conductivity (K) of cast irons was found to decrease with increasing Si content [15]. Therefore, being higher in Si, thermal diffusivity (k) (Equation A.1) of DCI-D is less than DCI-T. Owing to its low k the transient temperature gradient generated during quenching can

be highest among the alloys under investigation. This could be a major factor contributing to the origin of multiple cracks at the outer surface of the DCI-D specimen facing fast cooling.

A.4.2 Test Method-II

Figure A.16 shows the photographs of specimens after 300 thermal fatigue cycles. GCIs exhibited major crack openings at the inner specimen surface running lengthwise at both sides of the area cooled by the air jet. In GCI-A the cracks were only visible at the inner surface, while in GCI-S a crack spread deeply leading to the separation of the specimen wall. Moreover, several minor crack openings can be seen on the top surface of GCI-S. The DCIs showed different behaviour to GCIs. These alloys had no cracks at the inner surface. DCI-T exhibited a typical crack pattern originating at the impingement spot of the cooling air jet (Figure A.16(c)). DCI-D showed no cracks on its inner or outer surface. Results based upon the total surface crack ($\sum C_a$) area are listed in Table A.7.

DCIs performed significantly better than GCIs with DCI-D having no signs of cracking after 300 cycles. The measured crack area of GCI-A was found to be higher than GCI-S. However, a major crack passed through the wall of GCI-S. Therefore, practically speaking, the thermal fatigue resistance of GCI-S is inferior to GCI-A under test method-II conditions.

Cracking at the area of fast cooling is not of primary importance to the present investigation, because no fast cooling occurs in the case of tapping pipe applications. The main purpose of cooling from one face is to create a circumferential temperature gradient. The area between the fast cooling region and the hot end of the specimen is of specific interest to the present investigation as it is where thermal deformation occurs during each thermal cycle.

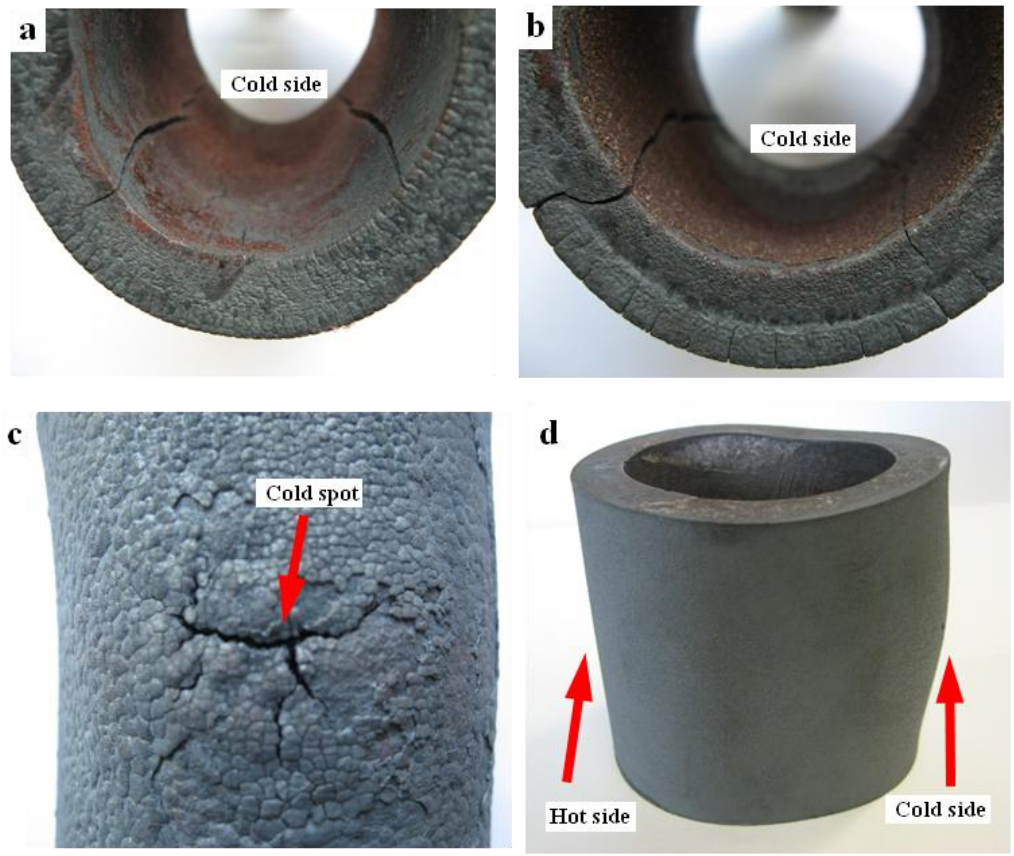

Figure A.16 - Cracking and distortion of specimens after 300 thermal fatigue cycles, a) GCI-A, b) GCI-S, c) DCI-T, d) DCI-D.

Table A.7 - Measured crack area on the specimen surface after 300 thermal cycles.

Cast Iron	$\sum C_a$, mm^2 (number of cracks)
GCI-A	253 (4)
GCI-S	167 (9)
DCI-T	33 (7)
DCI-D	Nil

Since in the present work, GCIs and DCIs exhibited different behaviour in the two test methods applied. Moreover, selecting a comparison criterion appeared to be major factor in determining the thermal fatigue resistance of cast irons. It is difficult to set a common failure criterion because different cast iron alloys may possess unique thermal fatigue characteristics under a particular thermal fatigue condition.

After thermal fatigue cycling the specimens became oval thus percentage dimetrical distortion (Δ_{Dm}) was determined in terms maximum (D_{max}) and minimum (D_{min}) diamaters of

the specimen. Similarly, percentagte longitudinal distortion (Δ_{Dl}) was also determined. Figure A.17 shows a schematic of the parameters for evaluating Δ_{Dm} and Δ_l, Equation A.9 and Equation A.10 are the respective mathematical expressions. Figure A.18 shows the obtained results.

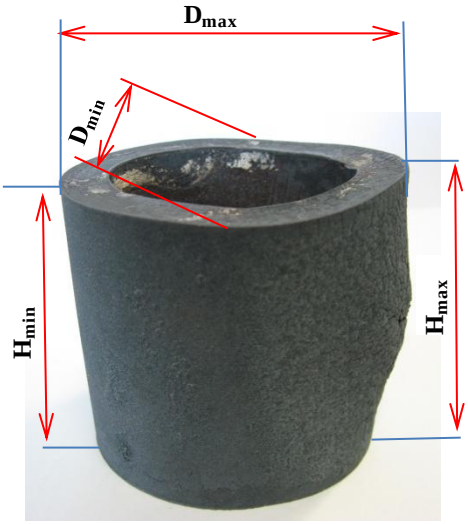

Figure A.17 - Schematic for measuring distortion; various parameters are marked on a DCI-T specimen.

$$\Delta_{Dm} = \left(\frac{D_{max} - D_{min}}{D_i} \right) 100 \quad \text{(A.9)}$$

$$\Delta_l = \left(\frac{H_{max} - H_{min}}{H_i} \right) 100 \quad \text{(A.10)}$$

where H_i is the specimen initial specimen height and D_i the initial diameter.

During each thermal cycle, a large temperature difference was induced across the circumference of the specimen, which deformed the specimen shape from circular to oval. Δ_{Dm} in DCIs was found to be greater than GCIs, whereas Δ_l followed the opposite trend. Δ_{Dm} was increased with increasing Si content in DCIs. Lower Δ_{Dm} in cast iron alloys was typically correlated with the greater vulnerability to cracking under thermal cycling. Therefore, a material that is unable to deform under thermal stresses ultimately leads to the opening of cracks to accommodate the stresses.

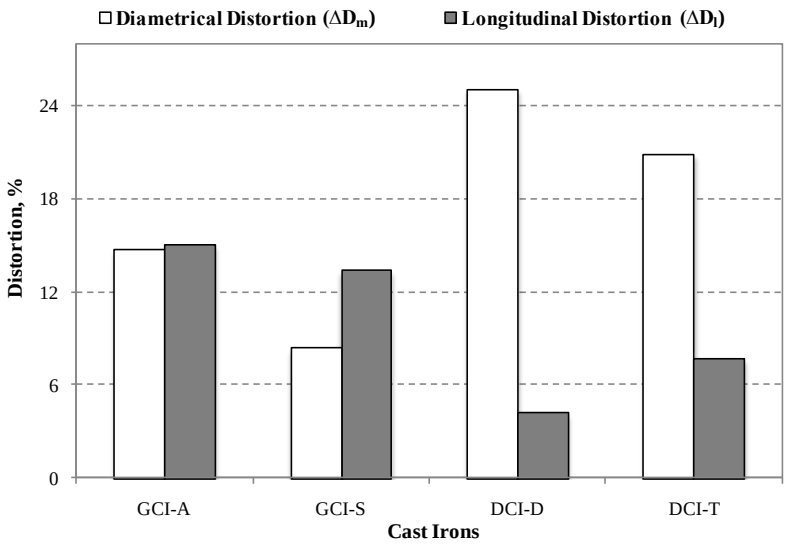

Figure A.18 - Diametrical and longitudinal distortion in cast irons after 300 thermal cycles.

Δ_l appears to be related to the growth of cast irons. DCIs grow at a slower rate compared to GCIs and in GCIs growth increases with increasing C content [14]. Therefore, compared to GCI-S, GCI-A should grow more because of higher internal oxidation and graphitization occurring during thermal cycling. During each cycle the cooling caused by the air jet tends to arrest the material shape in the expanded condition, and growth further adds to the increasing dimension of the surface experiencing a large thermal gradient.

A.5 Final Thoughts

Under TSC-I conditions with large thermal gradients and fast cooling (13.8 °C/s), a Cr and Mo alloyed low C cast iron (GCI-S) performed substantially better than a high carbon Cr+Cu alloyed GCI (GCI-A). The major difference was believed to be the higher oxidation rate of GCI-A compared to GCI-S, because a higher carbon equivalent (CE) led to higher graphite volume, which should further increase by subjecting the cast iron to a high temperature. Graphite flakes can provide easy paths for oxidation that ultimately lead to the progressive opening of cracks. It was difficult to compare the thermal fatigue resistance of two DCIs with different Si contents, because their degradation modes were found to be entirely different.

Under TSC-II condition and relatively lower cooling rates (8.1°C/s), DCIs performed significantly better than GCIs. The high Si cast iron, DCI-D, outperformed all the alloys under investigation. Practically, the resistance to thermal fatigue fracture of GCI-S was found to be slightly inferior to GCI-A; however, under TSC-I, GCI-S outperformed of all the cast irons under investigation.

Because the GCIs and DCIs behaved differently, comparison of thermal fatigue resistance is difficult. Under TSC-I and TSC-II conditions the DCI-T alloy showed cracking; however, owing to its good ductility the cracks did not propagate to a large extent. In ferritic DCIs, elevated temperature brittleness [16] and embrittlement by cycling heating [17] have been reported and are believed to be caused by magnesium assisted sulphur segregation and MgO segregation at grain boundaries, respectively. Moreover, this type of behaviour may also be related to structural imperfections or other obscure reasons related to the particular chemical composition.

These findings indicate that, where the lower cooling rates exist, DCIs can perform better than GCIs because ductile cast irons can absorb thermal stresses by deformation. This finding is also consistent with the literature [1]. Moreover, under lower cooling rates a better thermal fatigue resistance in DCIs can be achieved by increasing the Si content.

A.6 Conclusions

- Replication of the thermal fatigue conditions of tapping pipes on a laboratory scale was unsuccessful owing to the relatively low maximum temperature and the practical constraints of testing the pipes for longer durations. Therefore, alternative test methods were used to access the thermal fatigue resistance of cast irons.

- GCI-S, a low C cast iron alloyed with Cr and Mo, showed the greatest thermal fatigue resistance under the conditions of severe quenching and predominant radial temperature gradients. Relatively higher C contents, as in GCI-A, were found to be a major factor behind the inferior thermal fatigue resistance of GCIs, because a higher graphite volume provides easy paths for oxidation, leading to the progressive opening of cracks. Under the same test conditions, the ductile cast irons showed poor thermal fatigue resistance. This could be attributed to their low K and high E, which lead to higher stresses in the regions of stress concentration and surfaces facing fast cooling.

- Under both circumferential and radial thermal gradients and relatively lower cooling rates, DCIs performed significantly better than GCIs. DCI-D, a high Si ductile cast iron outperformed all the alloys under investigation. Both GCIs failed in a similar manner and the resistance to thermal fatigue fracture of GCI-S was found to be inferior to GCI-A.

- High Si DCIs appeared to be most promising for tapping pipe applications in terms of thermal fatigue. However, the corrosion resistance of high Si DCIs was found to be inferior.

Appendix References

[1] K. Roehrig, American Foundry Society Transactions, 86 (1978) 75-88.
[2] H. Fredriksson, P.A. Sunnerkrantz, P. Ljubinkovic, Materials Science and Technology, 4 (1988) 222-226.
[3] G.E. Dieter, Mechanical Metallurgy, McGraw-Hill Book Company, New York, 1986.
[4] R.B. Gundlach, American Foundry Society Transactions, 87 (1979) 551-450.
[5] M.C. Rukadikar, G.P. Reddy, International Journal of Fatigue, 9 (1987) 25-34.
[6] M.M. Shea, American Foundry Society Transactions, 04 (1978) 23-30.
[7] J.M. Chou, J.L. Lee, Y.C. Ko, Journal of Materials Science, 25 (1990) 2971-2974.
[8] J.L. Lee, S.C. Lee, Metallurgical and Materials Transactions A, 26A (1995) 1431-1439.
[9] I. Minkoff, The Physical Metallurgy of Cast Iron, John Wily & Sons Inc., New York, 1983.
[10] J.C. Randon, D.J. Burns, P.P. Benham, Journal of the Iron and Steel Institute, 204 (1966) 928-935.
[11] D.P.H. Hasselman, Journal of the American Ceramic Society, 46 (11) (1963) 535-540.

[12] S.C. Lee, S.C. Chen, Journal of Materials Science, 21 (1989) 210-223.
[13] Y.J. Park, R.B. Gundlach, M. Thoas, I.F. Janowk, American Foundry Society Transactions, 93 (1985) 415-422.
[14] J.R. Davis, ASM Speciality Handbook-Cast Irons, ASM International, Materials Park, Ohio, 1996.
[15] D. Holmgren, Thermal Conductivity of Cast Iron, PhD Thesis, Chalmers University of Technology, Sweden, 2006.
[16] R.N. Wright, T.R. Farrell, American Foundry Society Transactions, 137 (1985) 853-866.
[17] H.M. Lin, T.S. Lui, L.H. Chen, Materials Transactions, 45 (2004) 569-576.

APPENDIX B : EFFECT OF SURFACE CONDITION ON LIQUID Al CORROSION RESISTANCE OF CAST IRONS

This appendix describes the liquid Al cossosion behaviour of cast iron specimens with unfinished and finished surfaces. At the initial stage of comparing the liquid Al corrosion resistance, as-machined cylindrical cast iron specimens with one as-cast bottom face were used. The as-cast surface was kept so that a factor of the actual service surface can be considered. For subsequent dissolution testing, the specimens in finished condition were utilized because the unfinished specimens of GCI-S and DCI-T (two entirely different ferrous alloys) were found to dissolve at similar rates.

Figure B.1 shows the two types of specimens, and Figure B.2 shows the dissolution rates of GCI-S and DCI-T after exposure to liquid Al (850°C-0.48 m/s). The test durations for finished and unfinished specimens were 3.9 x 10^3s and 10.2 x 10^3s, respectively. For unfinished specimens, in addition to the similar dissolution rates of GCI-S and DCI-T, there was a large variation in the material loss of two specimens of each alloy, shown by the error bars. With the finished sufaces, the material loss of GCI-S and DCI-T specimens was increased by the factors of 3 and 6, respectively.

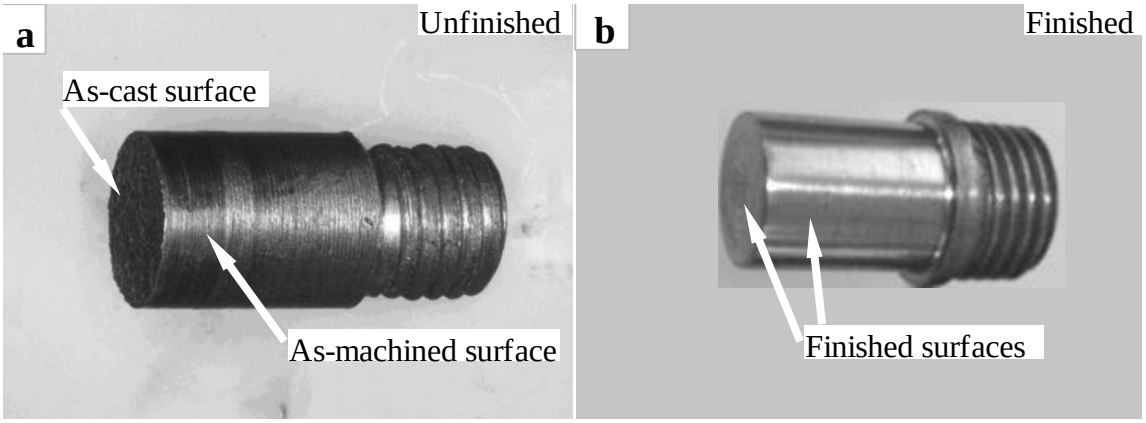

Figure B.1 - a) As-machined specimen with one as-cast surface, b) specimen with all the surfaces finished (finished using 240 and 600 grit SiC papers, in order).

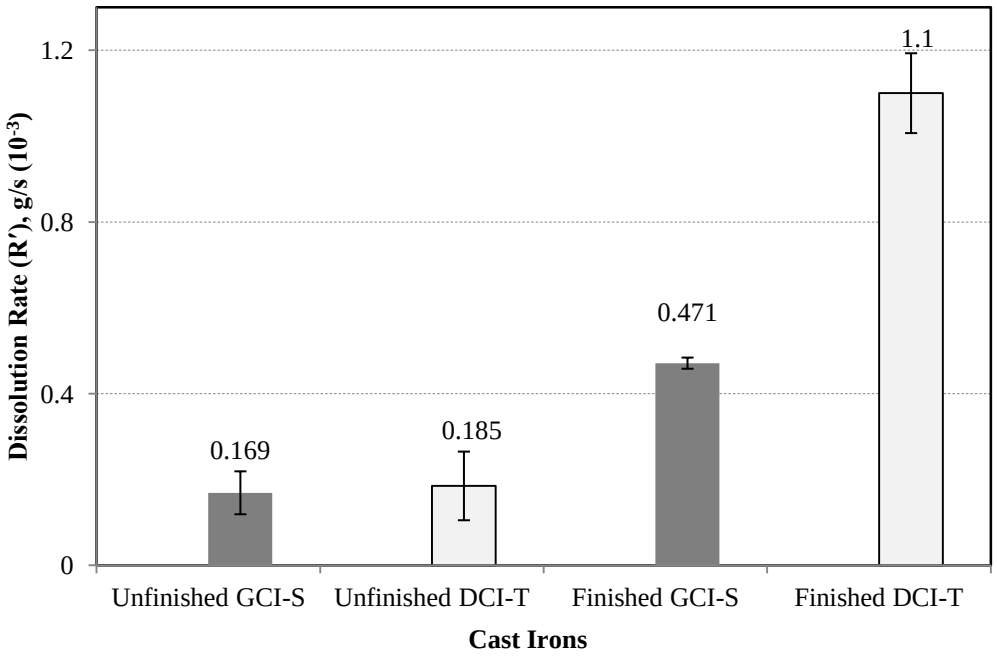

Figure B.2 - Mass dissolution rates (R′) of unfinished and finished specimens of cast irons (850°C-0.48m/s).

In order to reveal the inherent causes of difference in dissolution rates, the specimens in both surface conditions were exposed to liquid Al (850°C-900s-0.48 m/s). After exposure, the specimens with as-cast/unfinished surface showed the solidification of Al at random locations, as shown in Figure B.3. Figure B.4 shows the light optical image of the cross-section of specimen in Figure B.3. The random solidification of Al over the specimen surface signifies that the liquid Al had attacked at the localized sites. The regions at which iron and liquid Al come in contact in least possible time an Fe-Al intermetallic layer forms. The Fe-Al intermetallic layer provides bonding between the Fe-substrate and Al, leading to the solidification of Al over the interaction zones.

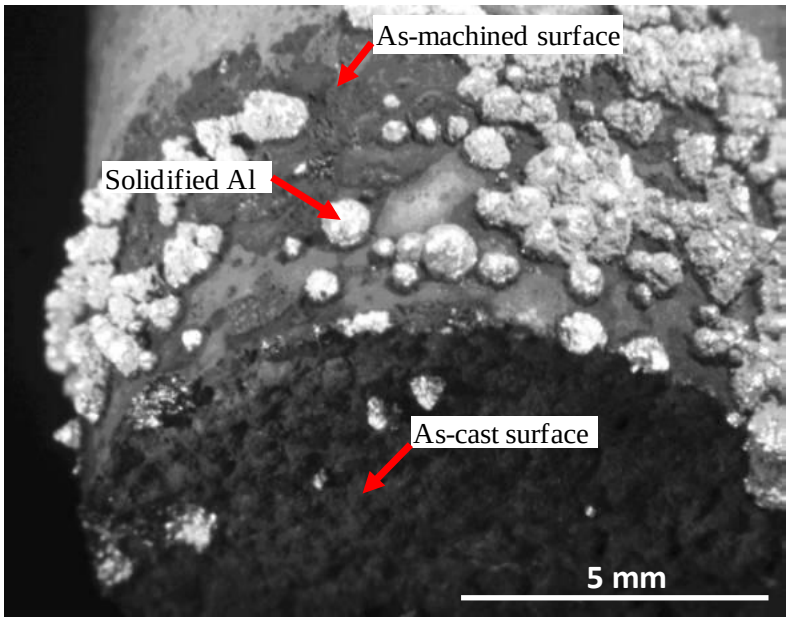

Figure B.3 - Solidified Al mounds over the reaction zones on an unfinished DCI-T specimen (850°C-900s-0.48m/s).

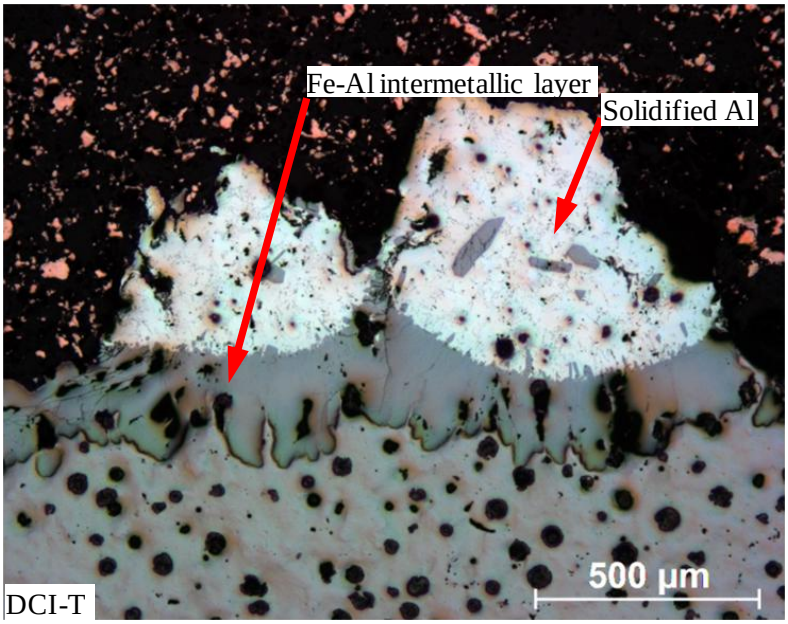

Figure B.4 - Optical image showing the merger of two reaction pits on the specimen surface shown in Figure B3.

Figure B.5 (a) shows the finished DCI-T specimen after immersion (850°C-900s-0.48m/s) and Figure B.5 (b) shows the light optical image of the DCI-T specimen cross-section. The specimens with finished surfaces exhibited the solidification of Al over the entire specimen surfaces, which revealed that the specimen was attacked more severely compared to the

specimens with unfinished surface. Thus the as-cast and rough/unfinished ferrous substrates could delay the Fe/Al nucleation, which lead to the occurrence of liquid Al corrosion only at random locations. The possibility of air trapped in the pores of a rough surface and forming Al_2O_3 has been suggested [1], which could inhibit the Fe-Al interaction. Initial reaction on the specimen surface starts at random locations and with ongoing liquid Al corrosion - these pits can merge - leading to large pits or a common corrosion surface.

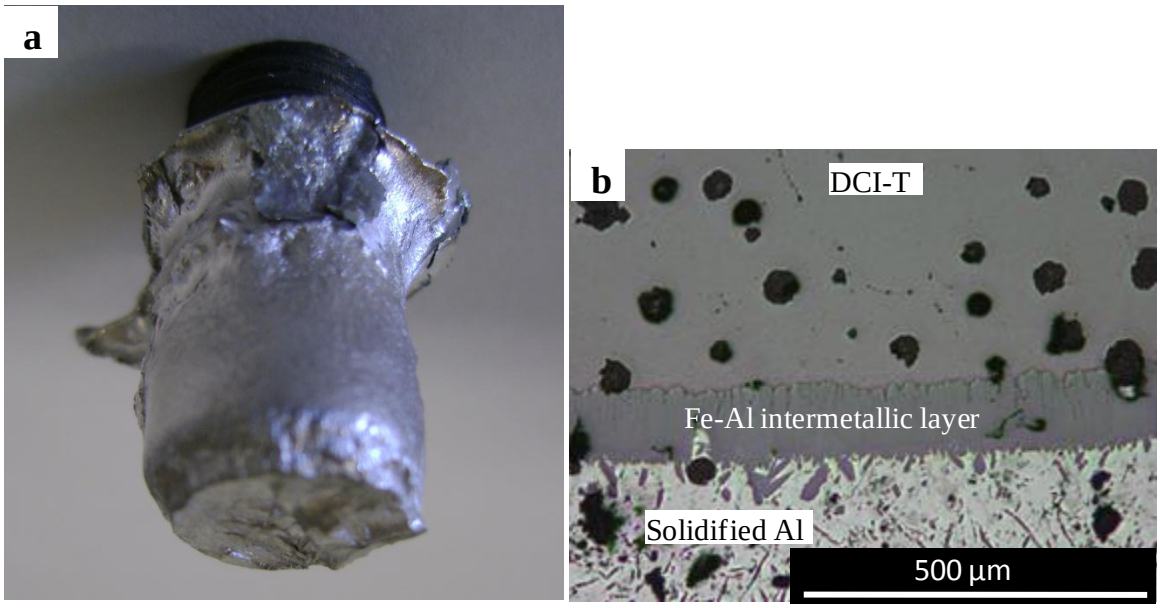

Figure B.5 - a) Finished DCI-T specimen (850°C-900s-0.48m/s) after withdrawal from the melt, b) light optical image showing the continuous intermetallic layer at the cross-section of specimen shown in Figure B5(a).

Moreover, the large differences in the dissolution rates of the two types of specimens could be explained by the fact that the as-cast surfaces of cast irons were found to be entirely different to the bulk. Figure B.6 and Figure B.7 show the light optical images of as-cast surfaces of GCI-S and DCI-T specimens, respectively. In GCI-S, high cooling rates at the mould/casting interface lead to the formation of cementite in the form of a layer about 100 µm thick.

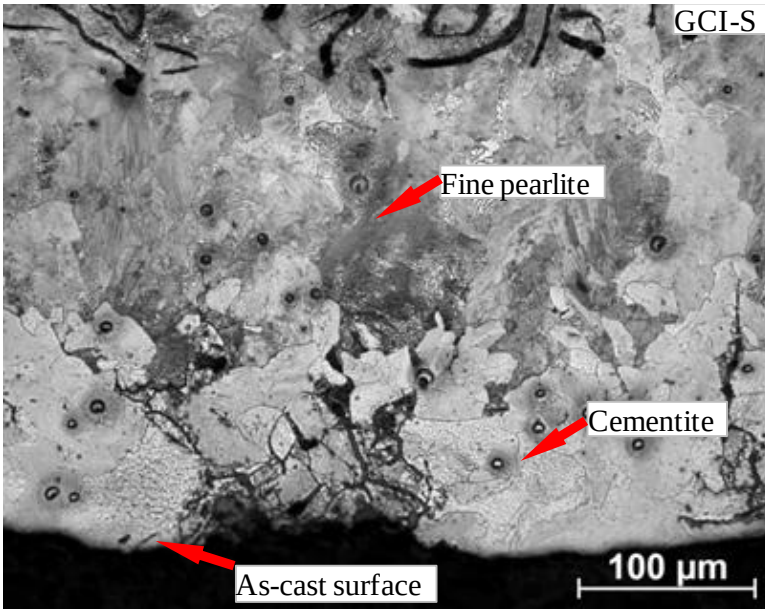

Figure B.6 - As-cast surface of GCI-S.

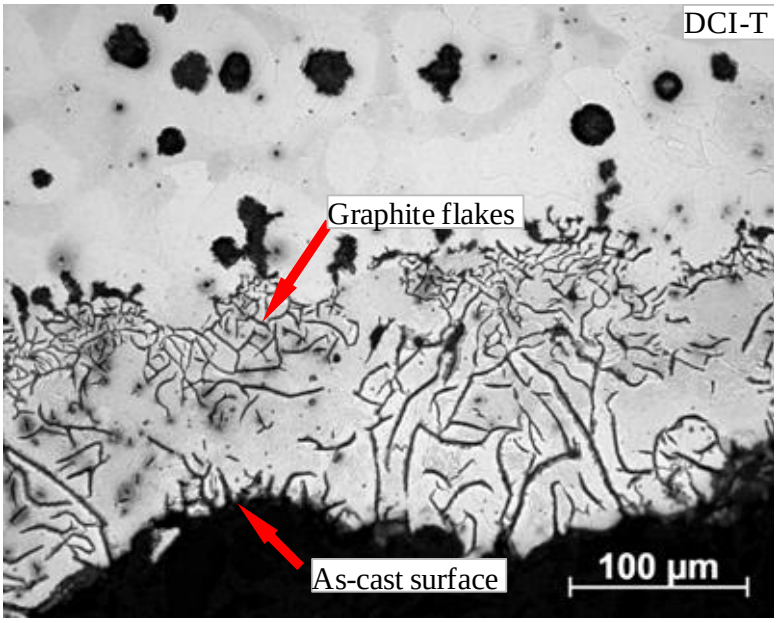

Figure B.7 - Formation of graphite flakes at the as-cast surface of DCI-T.

At the surface of the as-cast block of DCI-T, the formation of a ~ 200 µm thick layer containing the graphite flakes can be seen. Flake graphite structures at the surface of a DCI casting can occur as the consequence of surface reactions with contaminants in the sand, usually sulphur. This structure can become even more pronounced when the Mg content in the DCI decreases [2].

Conclusion

The present research identified that the cementite and flake graphite structure enhances the liquid Al corrosion resistance of cast irons. Thus both the unfinished and as-cast surfaces can reduce the material loss of cast iron substrates. However, in the long run, when the liquid Al penetrates the surface layer, the dissolution resistance of the bulk of a material determines the service life of a component.

Appendix References

1. T.S. Shih, S.H. Tu, Materials Science and Engineering A, 454-455 (2007) 349-356.
2. G.M. Goodrich, American Foundry Society Transactions, 30 (1997) 669-683.

APPENDIX C : CHARACTERISTICS OF THE DYNAMIC CORROSION TEST APPARATUS

In order to determine the characteristics of dynamic corrosion test apparatus, the material loss was determined by two methods: firstly by the mass loss and secondly by the semi-instantaneous dissolution.

C.1 Mass Loss

The decrease in mass of each specimen is a direct indication of the relative corrosion resistance of ferrous alloys over each immersion period. Time and mass loss for temperature stabilization period was excluded from the total values. Figure C.1 and Figure C.2 show the mass loss-time relationship for the ferrous alloys under forced flow conditions of liquid Al at 850°C and 950°C respectively. These tests were performed at a rotation velocity of 0.48 m/s, error-bars show the variation in mass loss of two specimens of each alloy. As expected, all the ferrous materials degraded progressively with increasing exposure time.

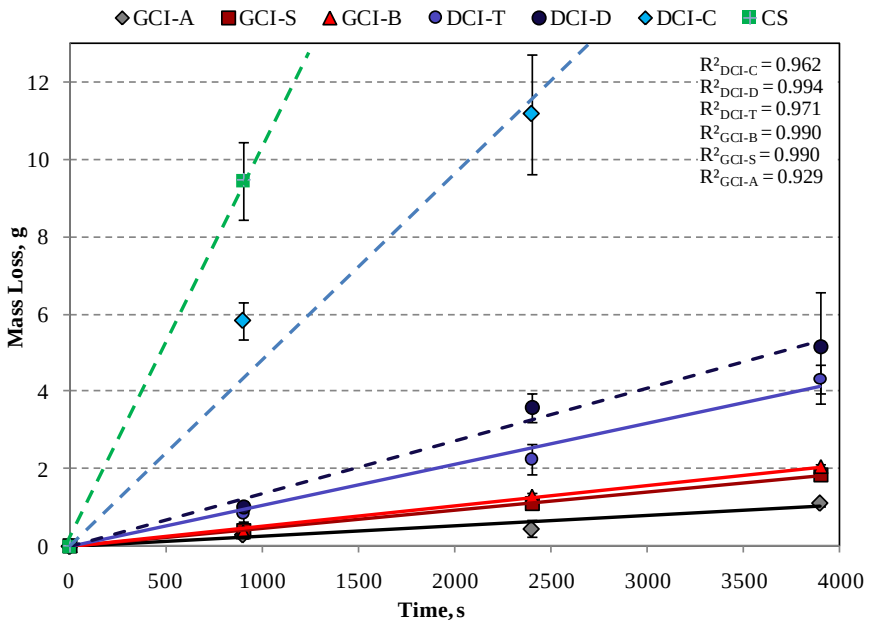

Figure C.1- Mass loss versus time plot for the ferrous alloys exposed to liquid Al (850°C-0.48 m/s), R^2 values show goodness of fit.

Figure C.1 identifies a linear relationship of mass loss with time at 850°C for GCIs and DCIs. Thus a kinetic constant of the material dissolution can be obtained from the slope of each trend-line representing the relationship of mass loss per unit of time. The listed R^2 values show goodness of the linear fit for each alloy. In general, the alloys with lower dissolution rates are closer to the ideal linear fit. The CS and DCI-C specimens eroded completely during experiment, thus only one and two data points are plotted for these alloys.

As expected, increasing the melt temperature to 950°C accelerated the material loss of all the ferrous alloys, except DCI-C. Data points for CS lie beyond the presented scale thus only a trend line is shown. The results presented (950°C-0.48m/s) in Figure C.2 identified two different regimes of material dissolution. All the alloys showed an initial high mass dissolution followed by a subsequent region of relatively lower mass dissolution. The dissolution rate constant obtained from a linear fit of the entire set of data points is designated R, while R_1 and R_2 are the rate constants in the initial fast and subsequent slower mass dissolution regimes, respectively.

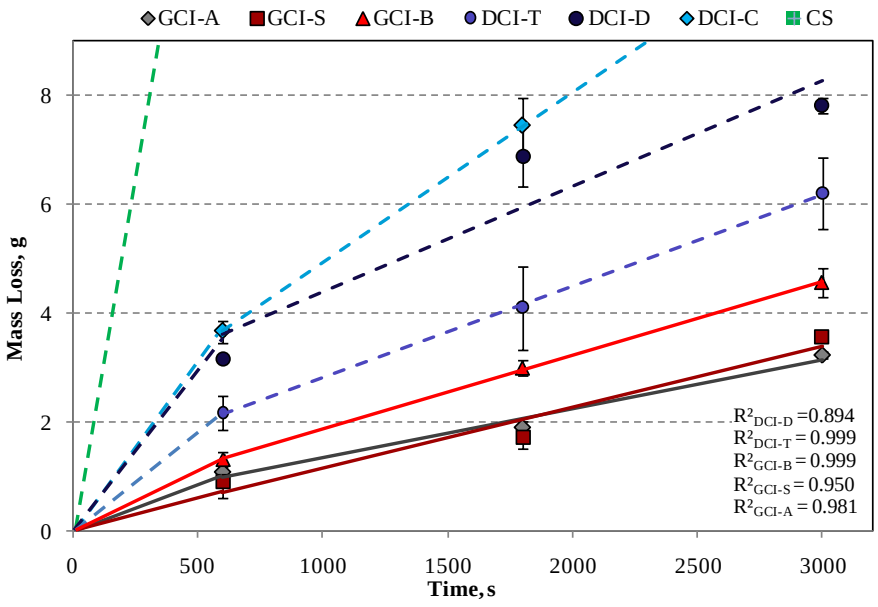

Figure C.2 - Mass loss versus time plot of various ferrous alloys exposed to liquid Al (950°C-0.48 m/s), R^2 values show goodness of fit for slower mass loss regime ($600 \leq t \leq 3000$s).

The values of R, R_1 and R_2 listed in Table C.1 in ascending order clearly identify the ranking of the mass dissolution of ferrous alloys. Moreover, the large differences in the R_1 and R_2 at 950°C indicate that the material dissolution is not only affected by the liquid Al temperature, but also the exposure time.

Table C.1- Mass dissolution rate constants of ferrous alloys at (850°C-0.48m/s) and (950°C-0.48m/s).

Mass dissolution rate, g/s x 10^{-3}	Ferrous alloys								
	Temperature (°C)	Time (s)	GCI-A	GCI-S	GCI-B	DCI-T	DCI-D	DCI-C	CS
R	850	0-3900	0.271	0.488	0.533	1.112	1.434	4.90	10.51
R_1	950	0-600	1.786	1.477	2.196	3.617	5.256	6.103	14.75
R_2	950	600-3000	0.900	1.200	1.354	1.679	1.944	3.153	---
R	950	0-3000	1.091	1.136	1.578	2.166	2.994	4.333	

C.2 Semi-instantaneous Dissolution

During the dissolution progression, the specimen surface area in contact with liquid Al decreases. In order to consider the effect of decreasing surface area, the semi-instantaneous dissolution rate was determined. The semi-instantaneous dissolution was defined as the volume loss per unit mean area (λ):

$$\lambda = 2\left(\frac{V_f - V_i}{A_f + A_i}\right) \tag{C.1}$$

V is the volume of specimen, A is the surface area of the specimen in contact with liquid Al, and subscripts i and f denote initial and final specimen parameters respectively. If the specimen remains cylindrical with height h, the final approximate specimen diameter (d_f) is

$$d_f = \left[d_i^2 - \left(\frac{4m}{\pi\rho h}\right)\right]^{1/2} \tag{C.2}$$

ρ is the density of ferrous alloy, m is the dissolved mass, d_i is the initial specimen diameter.

A value of 7225 kg/m^3 was utilized for the density of cast irons [1] and for steel the standard value of 7800 kg/m^3 was taken. The calculated dissolved material volume per mean area for each alloy is a relative measure of the component service life under a similar liquid Al degradation environment. The volume loss per mean area versus time plots under forced flow conditions at the temperatures of 850°C and 950°C are given in Figure C.3 and Figure C.4, respectively. At 850°C, all the alloys exhibited a linear relationship between volume loss per mean area and exposure time. The slope of each line represents the semi-instantaneous dissolution rate (Δ) in terms of material volume removed per area per time.

However, at 950°C, the regions of two different regimes of material dissolution can still be identified. Thus, similar to mass dissolution analysis, three rate constants were determined: Δ for the entire time range, and Δ_1 and Δ_2 for the initial fast and subsequent stabilized dissolution regimes, respectively. Table C.2 shows the Δ, Δ_1 and Δ_2 values at 850°C and 950°C.

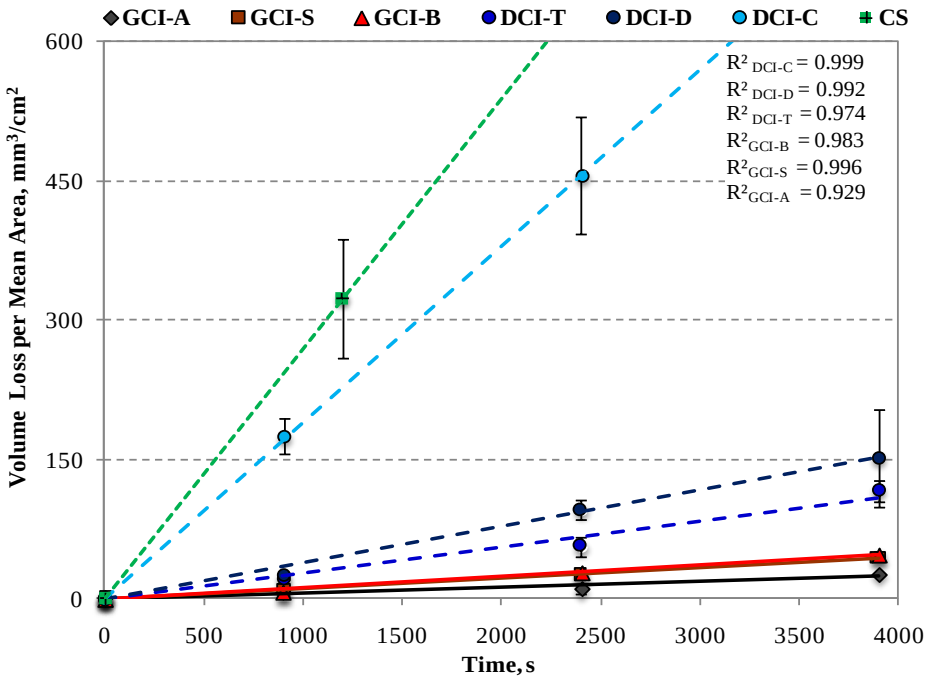

Figure C.3 - Relationship between volume per loss mean area and exposure time (850°C-0.48m/s), R^2 values show goodness of fit for the entire data.

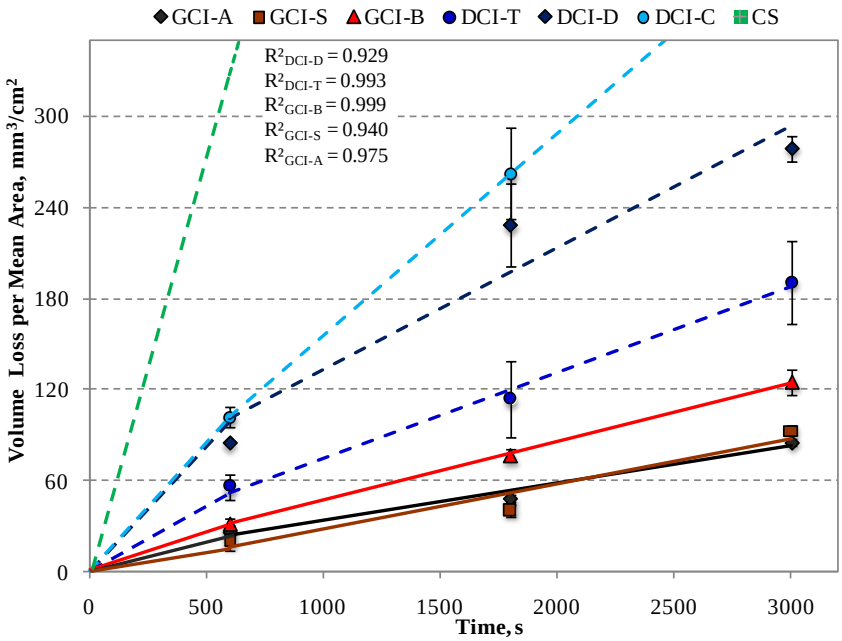

Figure C.4 - Volume loss per mean area versus time plot (950°C-0.48m/s), R^2 values show goodness of fit for the stabilized dissolution regime ($600 \leq t \leq 3000$s).

Table C.2 - Semi-instantaneous dissolution rates of ferrous alloys exposed to liquid Al at (850°C-0.48m/s) and (950°C-0.48 m/s).

Semi-instantaneous dissolution rate, $mm^3cm^{-2}s^{-1} \times 10^{-4}$		T(°C)	t (s)	Ferrous Alloys						
				GCI-A	GCI-S	GCI-B	DCI-T	DCI-D	DCI-C	CS
	Δ	850	0-3900	62	110	119	279	389	1908	2700
	Δ_1	950	0-600	437	352	532	923	1425	1705	5463
	Δ_2	950	600-3000	240	300	380	560	800	1330	--
	Δ	950	0-3000	284	291	423	643	1031	1483	--

Again, increasing the liquid Al temperature (850°C to 950°C) accelerated the material loss in the initial period (Δ_1) compared to the subsequent period of exposure (Δ_2). However, for the alloys having high dissolution rates, the Δ_1/Δ_2 ratio is significantly smaller than R_1/R_2.

APPENDIX D : EFFECT OF BORONIZING ON LIQUID Al CORROSION RESISTANCE OF STEEL AND CAST IRONS

After boronizing, the cylindrical specimens were cut perpendicular to the longitudinal axis and subsequently mounted and polished to observe the morphology of the formed boride layers. Figure D.1 shows optical images of the boride layers of DCI-T, GCI-S and CS. All the three alloys exhibited a similar type of morphology, with two boride layers formed at the specimen surface. The literature suggests that layers are Fe_2B and FeB [1], although the boride layers were not fully characterized in the present work.

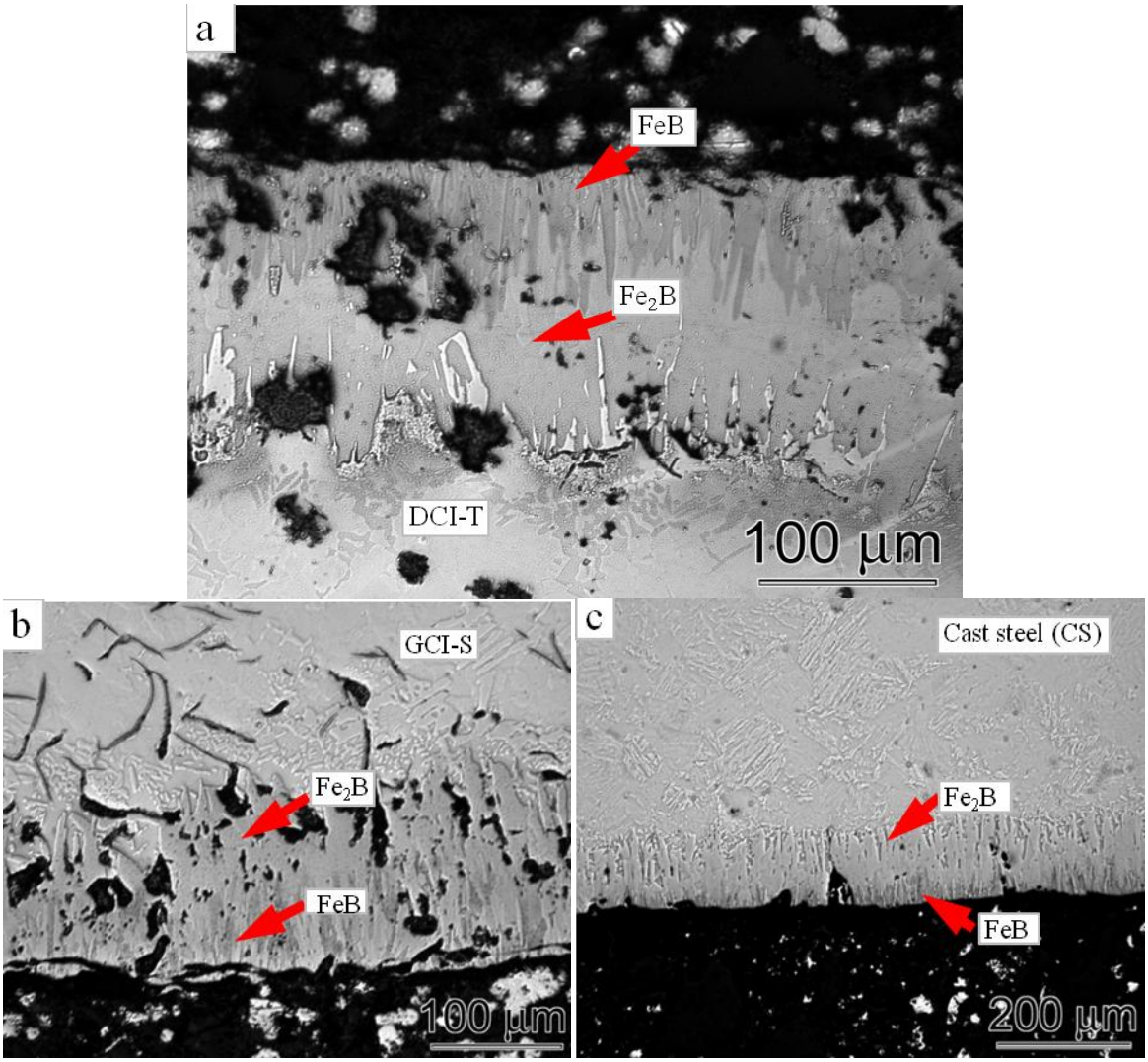

Figure D.1 - Formed boride layers after the boronizing treatment at 950°C for 4 hours, a) DCI-T, b) GCI-S, c) CS.

The liquid Al corrosion resistance of selected ferrous alloys, GCI-S, GCI-T and CS was also investigated after a boronizing surface treatment (Section 3.3). Figure D.2 shows the mass dissolution rates for the non-boronized (finished) and boronized test specimens (950°C-2400s-0.48 m/s). The test durations for non-boronized and boronized specimens were 600s and 2400s, respectively. All the boronized alloys showed improved liquid Al corrosion resistance. With boronizing treatment, the dissolution rate of CS was decreased to about 2 times; however, the entire boronized CS specimens were dissolved during the test.

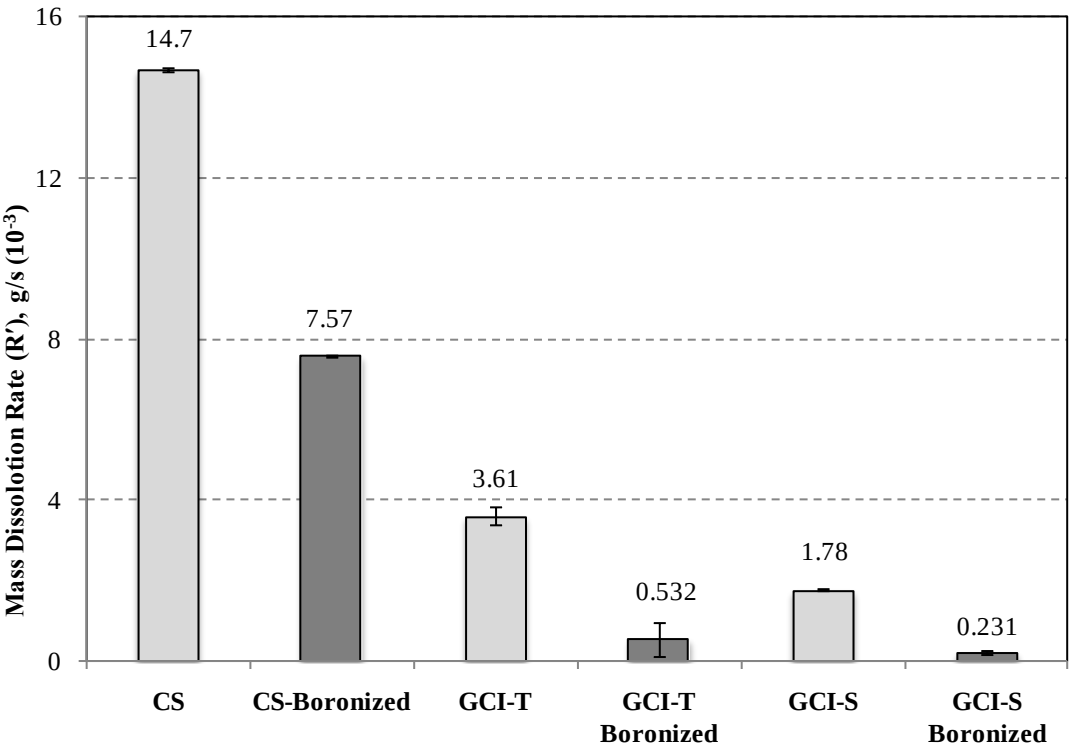

Figure D.2 - Effect of boronizing surface treatment on the mass dissolution rates (R′) of cast irons and steel (950°C-0.48m/s).

Boronizing DCI-T and GCI-S decreased the weight dissolution rate by the factors of 7 and 8, respectively. With boronizing, a significantly greater decrease in the dissolution rates GCI-S and DCI-T compared to CS was found. This can be attributed to the inferior liquid Al corrosion resistance of the bulk of CS, since when the liquid Al penetrates the boride layer

and starts to corrode the substrate, the material loss of CS should occur at a higher rate than cast irons.

Conclusion

With boronizing surface treatment, the liquid Al corrosion rate can be controlled. An effective boronizing treatment generally requires a finished surface. However, presently the tapping pipes are used in as-cast condition. It has been shown that as-cast, unfinished surfaces can be more resistant to liquid Al attack than the finished surfaces (Appendix-B). Although, the test conditions were different (in terms of temperature) to compare the liquid Al corrosion resistance of unfinished and boronized specimens, the boronizing treatment appeared to be more effective than the unfinished surfaces. However, the successful application of boronizing surface treatment to tapping pipes requires overcoming some barriers, such as obtaining uniformity in the protective boride layer and the total process cost.

Appendix References

[1] S. Sen, U. Sen, C. Bindal, Vacuum, 77 (2005) 195-202.